UTS UNIVERSITY OF TECHNOLOGY SYDNEY

Dynamic Behaviour of Ballasted Railway Track with Special Reference to Transition Zones

by Piyush Punetha

Thesis submitted in fulfilment of the requirements for the degree of

Doctor of Philosophy

under the supervision of Dr. Sanjay Nimbalkar and
Prof. Hadi Khabbaz

University of Technology Sydney
Faculty of Engineering and Information Technology (FEIT)

January 2022

CERTIFICATE OF ORIGINAL AUTHORSHIP

I, *Piyush Punetha* declare that this thesis, is submitted in fulfilment of the requirements for the award of *Doctor of Philosophy*, in the *School of Civil and Environmental Engineering (Faculty of Engineering and Information Technology, FEIT)* at the University of Technology Sydney.

This thesis is wholly my own work unless otherwise referenced or acknowledged. In addition, I certify that all information sources and literature used are indicated in the thesis.

This document has not been submitted for qualifications at any other academic institution.

This research is supported by the Australian Government Research Training Program.

Signature: Production Note:
Signature removed prior to publication.

Date: 10/01/2022

Dedicated to

My Parents

मेरे माता-पिता

को समर्पित

ABSTRACT

The poor performance of transition zones in railway tracks has long been a subject of concern for the rail infrastructure managers. These zones are the discontinuities along a railway line that are highly susceptible to differential settlement due to an abrupt variation in the support conditions over a short span. Consequently, these regions require frequent maintenance to ensure adequate levels of passenger safety and comfort. The rapid deterioration of track geometry in these zones is primarily ascribed to limited understanding of the underlying mechanism and scarcity of adequate tools to assess the severity of the potential issue. Therefore, a comprehensive evaluation of their behaviour is paramount to improve the design and ensure adequate service quality. With this objective, a novel methodology is developed which can predict the dynamic behaviour of the transition zones under train-induced repeated loading and assess the suitability of different countermeasures in improving the track performance.

To this end, an integrated approach is first developed by combining track loading, resiliency, and settlement models to evaluate the transient and irrecoverable response of the substructure layers of a standard ballasted railway track. The track substructure layers (ballast, subballast, and subgrade) in this model are simulated as an array of lumped masses that are connected by elastic springs and viscous dampers. The irrecoverable response of the track is evaluated using the empirical settlement models for substructure layers. The accuracy of the method is validated by comparing the predicted results against the field investigation data reported in the literature. Subsequently, the practical applicability of the aforementioned method under different traffic loading and soil conditions is improved by replacing the empirical approach with a mechanistic approach, in which, plastic slider elements are employed to predict the inelastic deformation in the substructure layers. To validate the approach, the predicted results are compared with the in-situ measurements reported in the literature. A good agreement between the predicted results and the field data verified the accuracy of the novel geotechnical rheological track model. A parametric investigation is conducted which highlights the significant influence of axle load, train speed, and granular layer thickness, on the accumulated settlement in the track layers.

The novel geotechnical rheological track model is then applied to an open-track bridge transition by incorporating the inhomogeneous support conditions associated with the critical zone and the adequacy of different countermeasures to mitigate the differential track settlements is examined. The approach is successfully validated with published field data and predictions from the finite element (FE) analysis. The results revealed that an increase in axle load exacerbates the track geometry degradation problem. The results also show that the performance of transition zones with weak subgrade can be improved by increasing the granular layer thickness. Interpretation of the predicted differential settlement for different countermeasures exemplified the practical significance of the proposed methodology.

Subsequently, the influence of principal stress rotation (PSR) experienced by the soil elements during a train passage is incorporated in the geotechnical rheological model. The results revealed that PSR causes significant cumulative deformation in the substructure layers, and disregarding it in the analysis leads to inaccurate predictions. Finally, the adequacy of using three-dimensional (3D) cellular geoinclusions to improve the performance of critical zones is investigated using the proposed methodology and FE analyses. A novel semi-empirical model is first developed to evaluate the magnitude of improvement provided by these inclusions under the 3D stress state. The proposed model is successfully validated against the experimental data. This model is then incorporated in the geotechnical rheological model and the effectiveness of 3D geoinclusions in improving the performance of an open track-bridge transition is investigated. The results show that the geoinclusions significantly reduce the magnitude of differential settlement and therefore, have a huge potential to be used in the transition zones to improve track performance.

The essential contribution of this thesis is that it provides reliable, practical, and adaptable techniques to assist the practising railway engineers in analysing the performance of various sections of ballasted railway tracks, identifying the most effective method to improve the track performance, planning the maintenance operations, and improving the design. The developed techniques are available in the form of MATLAB codes, which can readily be converted into an application that can be used by railway engineers. Nonetheless, the outcomes of this study have huge potential to influence the real-world

design implications of track transition zones. The approaches developed in this study are original, simple yet elegant, and can enhance, if not fully replace, present complex track modelling procedures for anticipating the behaviour of critical zones and adopting appropriate mitigation strategies.

ACKNOWLEDGEMENTS

It is a great pleasure to express my indebtedness to my principal supervisor, Dr. Sanjay Nimbalkar, whose encouragement and continuous support have allowed me to complete this thesis. He is a perfectionist and possesses immense knowledge in the field of Geotechnical Engineering. His patience, understanding, invaluable suggestions, critical comments and continual motivation helped me throughout the PhD journey and assisted me in realising my true potentials.

I sincerely thank my co-supervisor Prof. Hadi Khabbaz for his invaluable guidance, suggestions and constant motivation that helped me in completing this thesis. Moreover, I am also grateful to the candidature assessment panel members A/Prof. Behzad Fatahi, Dr. Nadarajah Gowripalan and Dr. Mina Mortazavi for providing valuable suggestions to improve the quality of my thesis.

I appreciate the support rendered by the academic and non-academic staff at the School of Civil and Environmental Engineering, Faculty of Engineering and Information Technology (FEIT) at UTS. I am also thankful to the high-performance computing (iHPC) team, and IT support team of FEIT for their assistance throughout my candidature at UTS. I am incredibly fortunate to have shared the PhD journey with my colleagues Naveen, Adnan, Navid, Yang, Praveen, Vasant, Amin, Akshay, Maria, Fulin, Lan, Xiaoqing, Derek, Wenkui, Yazan, Amir, Idris, Jiantao, Minh, Syed, Zhijie, Tran *et al*.

I wish to thank UTS for granting me the International Research Scholarship and Faculty of Engineering and Information Technology Scholarship to cover the tuition fees and living expenses throughout the candidature.

I am greatly indebted to my family, who have encouraged me in all my endeavours. They have been a constant source of love, support and strength throughout my PhD journey. Even though I was unable to meet them for the past three-and-half years due to the border closures because of the COVID-19 pandemic, they understood the situation and allowed me to focus only on my PhD. I warmly appreciate their understanding and generosity.

LIST OF PUBLICATIONS RELATED TO THIS RESEARCH

Journal Articles (Published):

1. **Punetha, P.** & Nimbalkar, S. 2022, Performance improvement of ballasted railway tracks using three-dimensional cellular geoinclusions', *Geotextiles and Geomembranes*. (in press) [**IF: 5.839** (2021)] [link]
2. **Punetha, P.** & Nimbalkar, S. 2022, 'Geotechnical rheological modeling of ballasted railway tracks considering the effect of principal stress rotation', *Canadian Geotechnical Journal*. (in press) **[IF: 4.167** (2021)**]** [link]
3. **Punetha, P.,** Nimbalkar, S. & Khabbaz, H. 2021, 'Simplified geotechnical rheological model for simulating viscoelasto-plastic response of ballasted railway substructure', *International Journal for Numerical and Analytical Methods in Geomechanics*, vol. 45, no. 14, pp. 2019-47. **[IF: 4.229** (2021); Citations: **3** (Google scholar)**]** [link]
4. **Punetha, P.**, Maharjan, K. & Nimbalkar, S. 2021, 'Finite element modeling of the dynamic response of critical zones in a ballasted railway track', *Frontiers in Built Environment*, vol. 7, 660292. [Citations: **2** (Google scholar)] [link]
5. **Punetha, P.**, Nimbalkar, S. & Khabbaz, H. 2020, 'Analytical evaluation of ballasted track substructure response under repeated train loads', *International Journal of Geomechanics*, vol. 20, no. 7, 04020093. [**IF: 3.819** (2020); Citations: **8** (Google scholar)] [link]
6. **Punetha, P.**, Nimbalkar, S. & Khabbaz, H. 2020, 'Evaluation of additional confinement for three-dimensional geoinclusions under general stress state', *Canadian Geotechnical Journal*, vol. 57, no. 3, pp. 453-461. **[IF: 3.725** (2020); Citations: **16** (Google scholar)**]** [link]

Conference Papers (Published):

7. **Punetha, P.** & Nimbalkar, S. 2021, 'Mathematical modeling of the short-term performance of railway track under train-induced loading', *Advances in Transportation Geotechnics IV*., Springer. [link]
8. **Punetha, P.** & Nimbalkar, S. 2021, 'Prediction of extra confinement offered by cellular inclusion under three-dimensional stress state', *Challenges and Innovations in Geomechanics*, Springer. [link]

9. **Punetha, P.** and Nimbalkar, S. 2021, 'Performance improvement of ballasted railway tracks for high-speed rail operations'**,** *Challenges and Innovations in Geomechanics*, Springer [Citations: **2** (Google scholar)]. [link]

Book Chapter (Published):

10. Nimbalkar, S., **Punetha, P.** & Kaewunruen, S. 2020, 'Performance improvement of ballasted railway tracks using geocells: present state of the art', in Sitharam, T.G. et al. (eds), *Geocells. Springer Transactions in Civil and Environmental Engineering*, Springer, Singapore. [Citations: **7** (Google scholar)] [link]

All the aforementioned papers have been published during my PhD candidature.

Journal Articles (Under review):

11. **Punetha, P.** & Nimbalkar, S. 2022, 'An innovative rheological approach for predicting the behaviour of critical zones in a railway track', *Acta Geotechnica*.

To be Submitted:

12. **Punetha, P.** & Nimbalkar, S. 2022, 'Dynamic behaviour of geocell reinforced ballasted rail tracks with special reference to transition zones'.

STATEMENT OF CONTRIBUTION OF AUTHORS

The chapters of this thesis contain material from 8 journal articles (6 published, 1 under review and 1 to be submitted) and 1 book chapter (published).

1. **Punetha, P.** & Nimbalkar, S. 2022, Performance improvement of ballasted railway tracks using three-dimensional cellular geoinclusions', *Geotextiles and Geomembranes*. [Status: Accepted (in press)]

Author	Statement of contribution	Thesis chapters
Piyush Punetha	Literature review, conceptualisation, methodology, validation, manuscript writing: original draft.	Chapter 6 (Part-B)
Sanjay Nimbalkar	Conceptualisation, resources, methodology, supervision, manuscript witing: review and editing	

2. **Punetha, P.** & Nimbalkar, S. 2022, 'Geotechnical rheological modeling of ballasted railway tracks considering the effect of principal stress rotation', *Canadian Geotechnical Journal*. https://doi.org/10.1139/cgj-2021-0562 [Status: Accepted (in press)]

Author	Statement of contribution	Thesis chapters
Piyush Punetha	Literature review, conceptualisation, methodology, validation, manuscript writing: original draft.	Chapter 5
Sanjay Nimbalkar	Conceptualisation, resources, methodology, supervision, manuscript witing: review and editing	

3. **Punetha, P.,** Nimbalkar, S. & Khabbaz, H. 2021, 'Simplified geotechnical rheological model for simulating viscoelasto-plastic response of ballasted railway substructure', *International Journal for Numerical and Analytical Methods in Geomechanics*, vol. 45, no. 14, pp. 2019-47. https://doi.org/10.1002/nag.3254 (Status: Published)

Author	Statement of contribution	Thesis chapters
Piyush Punetha	Literature review, conceptualisation, methodology, validation, manuscript writing: original draft.	Chapter 2 and Chapter 3 (Part-B)
Sanjay Nimbalkar	Conceptualisation, resources, methodology, supervision, manuscript witing: review and editing	
Hadi Khabbaz	Methodology, manuscript witing: review and editing	

4. **Punetha, P.**, Maharjan, K. & Nimbalkar, S. 2021, 'Finite element modeling of the dynamic response of critical zones in a ballasted railway track', *Frontiers in Built Environment*, vol. 7, 660292. https://doi.org/10.3389/fbuil.2021.660292 (Status: Published)

Author	Statement of contribution	Thesis chapters
Piyush Punetha	Literature review, conceptualisation, methodology, validation, manuscript writing: original draft.	Chapter 7
Krijan Maharjan	Methodology, manuscript writing: review and editing	
Sanjay Nimbalkar	Conceptualisation, resources, methodology, supervision, manuscript witing: review and editing	

5. **Punetha, P.**, Nimbalkar, S. & Khabbaz, H. 2020, 'Analytical evaluation of ballasted track substructure response under repeated train loads', *International Journal of Geomechanics*, vol. 20, no. 7, 04020093. https://doi.org/10.1061/(ASCE)GM.1943-5622.0001729 (Status: Published)

Author	Statement of contribution	Thesis chapters
Piyush Punetha	Literature review, conceptualisation, methodology, validation, manuscript writing: original draft.	Chapter 2 and Chapter 3 (Part-A)
Sanjay Nimbalkar	Conceptualisation, resources, methodology, supervision, manuscript witing: review and editing	
Hadi Khabbaz	Methodology, manuscript witing: review and editing	

6. **Punetha, P.**, Nimbalkar, S. & Khabbaz, H. 2020, 'Evaluation of additional confinement for three-dimensional geoinclusions under general stress state', *Canadian Geotechnical Journal*, vol. 57, no. 3, pp. 453-461. https://doi.org/10.1139/cgj-2018-0866 (Status: Published)

Author	Statement of contribution	Thesis chapters
Piyush Punetha	Literature review, conceptualisation, methodology, validation, manuscript writing: original draft.	Chapter 6 (Part-A)
Sanjay Nimbalkar	Conceptualisation, resources, methodology, supervision, manuscript witing: review and editing	
Hadi Khabbaz	Methodology, manuscript witing: review and editing	

7. **Punetha, P.** & Nimbalkar, S. 2022, 'An innovative rheological approach for predicting the behaviour of critical zones in a railway track', *Acta Geotechnica*. (Status: Under review)

Author	Statement of contribution	Thesis chapters
Piyush Punetha	Literature review, conceptualisation, methodology, validation, manuscript writing: original draft.	Chapter 4
Sanjay Nimbalkar	Conceptualisation, resources, methodology, supervision, manuscript witing: review and editing	

8. Punetha, P. & Nimbalkar, S. 2022, 'Dynamic behaviour of geocell reinforced ballasted rail tracks with special reference to transition zones', *Computers and Geotechnics*. (Status: To be submitted)

Author	Statement of contribution	Thesis chapters
Piyush Punetha	Literature review, conceptualisation, methodology, validation, manuscript writing: original draft.	Chapter 7
Sanjay Nimbalkar	Conceptualisation, resources, methodology, supervision, manuscript witing: review and editing	

9. Nimbalkar, S., **Punetha, P.** & Kaewunruen, S. 2020, 'Performance improvement of ballasted railway tracks using geocells: present state of the art', in Sitharam, T.G. et al. (eds), *Geocells. Springer Transactions in Civil and Environmental Engineering*, Springer, Singapore. https://doi.org/10.1007/978-981-15-6095-8_11 (Status: Published)

Author	**Statement of contribution**	**Thesis chapters**
Sanjay Nimbalkar	Conceptualisation, resources, methodology, supervision, manuscript witing: review and editing	Chapter 2 and Chapter 6 (Part-A)
Piyush Punetha	Literature review, conceptualisation, methodology, manuscript writing: original draft.	
Sakdirat Kaewunruen	Manuscript witing: review and editing	

TABLE OF CONTENTS

LIST OF FIGURES

LIST OF TABLES

LIST OF NOTATIONS

Latin Symbols:

A_b Equivalent area of ballast at a particular depth (m^2)

A_b^s Equivalent shear area of ballast (m^2)

A_d Maximum normal operating cant deficiency angle (rad)

A_f Fourier amplitude

A_g Equivalent area of subgrade at a particular depth (m^2)

A_g^s Equivalent shear area of subgrade (m^2)

A_s Equivalent area of subballast at a particular depth (m^2)

A_s^s Equivalent shear area of subballast (m^2)

A_y Angle of lateral ramp discontinuity (rad)

a, a^r Equivalent radius of sleeper-ballast contact area in softer and stiffer side (m)

a^* Empirical coefficient

a' Material parameter for subgrade

a_h Cyclic hardening parameter

a_o, b_o Locomotive and track maintenance factors

a_t Number of wheels considered

b Intermediate principal stress ratio

b^*, b' Empirical coefficients

b_g Material parameter for subgrade

b_{ps} Intermediate principal stress ratio at plane-strain condition

b_{sl} Sleeper width (m)

b_t Track width (m)

C Coefficient in Japanese standard

c Cohesion (N/m^2)

c_b, c_s, c_g Viscous damping coefficients for ballast, subballast and subgrade (Ns/m)

c_b^r Viscous damping coefficient for ballast in the stiffer side (Ns/m)

c_b^s, c_s^s, c_g^s Shear damping coefficients for ballast, subballast and subgrade (Ns/m)

$c_b^{s,r}$ Shear damping coefficient for ballast in the stiffer side (Ns/m)

D Dilatancy

D_g Diameter of geoinclusion opening (m)

D_p Plastic dilatancy

D_r Dilatancy rate

D_w Train wheel diameter (m)

d_s Diameter of soil specimen in triaxial test (m)

$dF^r_{b,n}$ Force increment acting on ballast layer in the stiffer side (N)

$dF_{g,n}$, $dF_{s,n}$, $dF_{b,n}$ Force increment acting on subgrade, subballast and ballast (N)

$d\hat{p}$ Hydrostatic stress increment in characteristic stress space

dp_i Image mean effective stress increment (N/m^2)

$d\hat{q}$ Deviatoric stress increment in characteristic stress space

dt Time step (s)

E Young's modulus of infill (N/m^2)

E_b, E_s, E_g Resilient modulus of ballast, subballast and subgrade (N/m^2)

E^r_b Resilient modulus of ballast in the stiffer side (N/m^2)

E_i Initial Young's modulus (N/m^2)

E_m Young's modulus of geoinclusion (N/m^2)

E_R Resilient modulus (N/m^2)

E_r Young's modulus of rail (N/m^2)

E_{sec} Secant Young's modulus (N/m^2)

e, e_0 Current and initial void ratio

e_c Void ratio on critical state line at the current mean effective stress

F Frequency (Hz)

F_{wr} Wheel-rail contact force (N)

f_c, f_r, f_t Current, reference and transitional surfaces

f_g, f_s, f_b Yield surface for subgrade, subballast and ballast

G Wheel-rail contact constant (m/N$^{2/3}$)

g Acceleration due to gravity (m/s^2)

g_p Potential function

g_t Centre-to-centre distance between the rails (m)

H Hardening parameter in Nor-sand model

H_L Lateral load (N)

H_m Influence height of planar geosynthetic (m)

H_{mean} Mean lateral load (N)

H_w Crosswind force (N)

h Vertical distance from rail top to centre of gravity of train (m)

h_b, h_s, h_g Ballast, subballast and subgrade thickness (m)

h_b^r Ballast thickness in the stiffer side (m)

h_{bL}, h_{sL}, h_{gL} Overlap height in ballast, subballast and subgrade along longitudinal direction (m)

h_{bt}, h_{st}, h_{gt} Overlap height in ballast, subballast and subgrade along transverse direction (m)

h_d Cant or superelevation deficiency (m)

h_{eb}, h_{es} Equivalent thickness of ballast and subballast layers (m)

h_{gl} Granular layer thickness (m)

h_i Thickness of i^{th} substructure layer (m)

h_{se} Superelevation (m)

I_r Moment of inertia of rail (m^4)

i_1, i_2 Empirical parameters for calculating dynamic amplification factor

K Coefficient representing the internal friction

K_1, K_2, K_3, K_4 Fitting parameters that depend on type and physical state of the soil

K_j Track stiffness at joint (N/m)

K_y Effective lateral rail stiffness per wheel (N/m)

k Track modulus (N/m^2)

k^r Track modulus for stiffer side of the transition (N/m^2)

k^*, k_1^*, k_2^*, k_3^* Empirical parameters

k_0 Lateral earth pressure coefficient

k_1, k_2, k_3, k_4 Empirical parameters

$k_1^b, k_2^b, k_3^b, k_4^b$ Empirical parameters for calculating ballast deformation

$k_1^s, k_2^s, k_3^s, k_4^s$ Empirical parameters for calculating subballast deformation

k_b, k_s, k_g Stiffness of ballast, subballast and subgrade (N/m)

k_b^r Stiffness of ballast in the stiffer side (N/m)

k_b^s, k_s^s, k_g^s Shear stiffness of ballast, subballast and subgrade (N/m)

$k_b^{s,r}$ Shear stiffness of ballast in the stiffer side (N/m)

k_c Ratio of circumferential strain to the radial strain in the geocell

k_p Stiffness of rail pad (N/m)

k_p^r Rail pad stiffness in the stiffer side (N/m)

$k_{\sigma,2}$, $k_{\sigma,3}$ Normalised additional confinement

L Characteristic length (m)

l_c Distance between rail top and centre of gravity of train (m)

l_e Effective length of sleeper (m)

l_g Gauge width (m)

l_{sl} Sleeper length (m)

l_w Distance between centre of rails and the resultant wind force (m)

M Critical stress ratio

$\widehat{M}$ Critical stress ratio in characteristic stress space

M_i Critical stress ratio corresponding to image state

M_{itc} Critical stress ratio corresponding to the image state for triaxial compression

M_m Mobilised modulus of geocell (N/m)

M_p Peak stress ratio

M_t Tensile stiffness of the geocell (N/m)

M_{tc} Critical stress ratio under triaxial compression

M_u Effective lateral unsprung mass per axle (kg)

M_y Effective lateral rail mass per wheel (kg)

m, n Empirical coefficients

m^* Material parameter for subgrade

m_b, m_s, m_g Vibrating mass of ballast, subballast and subgrade (kg)

m_b^r Vibrating mass of ballast in the stiffer side (kg)

N Number of load cycles

N_d Number of days

N_{lim} Number of load cycles required to reach stable zone

N_{limit} Number of load repetitions required to reach the resilient state

N_v Volumetric coupling coefficient

P_a Atmospheric pressure (N/m^2)

p Mean effective stress (N/m^2)

p_i Image mean effective stress (N/m^2)

p_{ic}, p_{im} Hardening parameters

$\hat{p}_{xg}$ Intersection of potential function with $\hat{p}$ axis

$\hat{p}_{xt}$, $\hat{p}_{xc}$, $\hat{p}_{xr}$ Intersection of transitional, current and reference surfaces with $\hat{p}$ axis

Q, Q_a Static wheel and axle load (N)

Q_d Design wheel load (N)

Q_{dy} Dynamic component of load (N)

Q_{qs} Quasi-static wheel load (N)

$Q_{r,n}$ Vertical rail seat load at n^{th} sleeper (N)

Q_t Tensile load (N)

Q_{tv} Total vertical wheel load (N)

q Deviatoric stress (N/m^2)

$\hat{q}$ and $\hat{p}$ Deviatoric and hydrostatic stress invariants in the characteristic stress space

R Parameter that controls the magnitude of plastic volumetric strain increment

R_c Radius of curvature of track (m)

R_i Parameter that controls the magnitude of plastic strain accumulation

R_s Stress ratio

R_w Nominal radius of the wheel (m)

r Spacing ratio

S Sleeper spacing (m)

$s_{1\alpha}$, $s_{2\alpha}$ Constitutive parameters to account for the effects of principal stress rotation

s_b, s_s Settlement of ballast and subballast (m)

s_g, s_{gl} Settlement of subgrade and granular layers (m)

$\boldsymbol{s}_{ij}$ Deviatoric stress tensor

s_t Settlement of track substructure (m)

s_v^r Vertical resilient deformation (m)

T Cumulative tonnage (kg)

$\boldsymbol{T}_n^s$ Average shear stress vector

T_x, T_y Tensile stresses in planar geosynthetic along x and y directions (N/m)

t Time instant (s)

t_g Thickness of geoinclusion (m)

t_u Factor that depends on the upper confidence limit

V Train speed (m/s)

V_m Maximum normal operating speed (m/s)

W_u Unsprung weight at one wheel (N)

W_{vd} Vertical deformation (m)

W_{wr} Deformation at the wheel-rail contact point (m)

w Vertical track deflection (m)

w_b Vertical displacement at ballast top (m)

w_{bm} Mean value of track displacement in stiffer zone (m)

w_t Vertical track displacement (m)

x Distance along longitudinal direction (m)

x_n^j Distance of n^{th} sleeper from j^{th} wheel (m)

Z Plastic softening parameter

z Depth (m)

$z_{b,n}, \dot{z}_{b,n}, \ddot{z}_{b,n}$ Displacement, velocity and acceleration of ballast below n^{th} sleeper

$z_{b,n}^p, \dot{z}_{b,n}^p$ Plastic displacement and velocity of ballast below n^{th} sleeper

$z_{s,n}, \dot{z}_{s,n}, \ddot{z}_{s,n}$ Displacement, velocity and acceleration of subballast below n^{th} sleeper

$z_{s,n}^p, \dot{z}_{s,n}^p$ Plastic displacement and velocity of subballast below n^{th} sleeper

$z_{g,n}, \dot{z}_{g,n}, \ddot{z}_{g,n}$ Displacement, velocity and acceleration of subgrade below n^{th} sleeper

$z_{g,n}^p, \dot{z}_{g,n}^p$ Plastic displacement and velocity of subgrade below n^{th} sleeper

$z_g^{ve}, z_s^{ve}, z_b^{ve}$ Viscoelastic displacement in subgrade, subballast and ballast (m)

Greek Symbols:

α Stress distribution angle for ballast (°)

α^* Empirical parameter

α' Coefficient relating track irregularities, train suspension and speed

α^r Stress distribution angle for ballast in the stiffer side (°)

α_0 Reference stress distribution angle in ballast (°)

α_m Bonding coefficient for planar geosynthetic

α_v Angle between major principal stress direction and vertical (°)

β Stress distribution angle for subballast (°)

β' Coefficient accounting for the movement of train along a curve

β_0 Reference stress distribution angle in subballast (°)

Γ Critical void ratio at p = 1 kPa

$\hat{\Gamma}$, $\hat{N}$ Void ratio of critical state line and normal compression line at $\hat{p}$=1 kPa

γ Stress distribution angle for subgrade (°)

γ' Coefficient that depends on speed and design of train, and track condition

$\Delta\sigma$ Increase in stress (N/m^2)

$\Delta\sigma'_2$, $\Delta\sigma'_3$ Effective additional confining stress in the direction of σ'_2 and σ'_3 (N/m^2)

$\Delta\sigma_3$ Additional confining stress in the direction of σ_3 (N/m^2)

$\Delta\sigma_x$, $\Delta\sigma_y$ Additional confining pressure along x and y directions (N/m^2)

$d\boldsymbol{\varepsilon}_{ij}^p$, ε_v^p Plastic strain increment and cumulative plastic volumetric strain

$d\varepsilon_v$, $d\varepsilon_q$ Volumetric and deviatoric strain increments

$d\varepsilon_v^p$, $d\varepsilon_q^p$ Plastic volumetric and deviatoric strain increments

$d\varepsilon_z^p$ Plastic strain increment in vertical direction

δ_{ij} Kronecker delta

δ_t Factor that depends on the track condition

$\varepsilon_0/\varepsilon_r$, ρ_p, β_p Fitting parameters

ε_1, ε_2, ε_3 Major, intermediate and minor principal strains

ε_1^e, ε_2^e, ε_3^e Resilient components of major, intermediate and minor principal strains

ε_1^p, ε_2^p, ε_3^p Plastic components of major, intermediate and minor principal strains

$\varepsilon_{1,1}^p$ Plastic axial strain after the first load cycle

ε_a Axial strain

ε_a^p Accumulated plastic axial strain

ε_b^p, ε_s^p, ε_g^p Cumulative plastic strain in ballast, subballast and subgrade

ε_c Circumferential strain

ε_q Deviatoric strain

ε_r Radial strain

ε_t Tensile strain

ε_x, ε_y Strain along x and y directions

ε_x^m, ε_y^m Strains in geosynthetic in x and y directions

ε_z^p Cumulative plastic strain in vertical direction

η Stress ratio

$\hat{\eta}$ Stress ratio in characteristic stress space

η_v Factor that depends on the speed of vehicle

θ Bulk stress (N/m^2)

$\theta_1 + \theta_2$ Total dip angle of the rail joint (rad)

$\mathcal{I}$ Tensorial invariant

Λ_s, Λ_g Scalars

λ, κ Slope of critical state line and swelling line in e–ln p space

ν_b, ν_s, ν_g Poisson's ratio of ballast, subballast and subgrade

ν_b^r Poisson's ratio of ballast in the stiffer side

ν_i Poisson's ratio of infill

ν_m Poisson's ratio of geoinclusion material

ξ, A Dimensionless material parameters

ρ_b, ρ_s, ρ_g Density of ballast, subballast and subgrade (kg/m^3)

ρ_b^r Density of ballast in the stiffer side (kg/m^3)

σ_1, σ_2, σ_3 Major, intermediate and minor principal stresses (N/m^2)

σ_{bb}^r Vertical stress at the bottom of substructure layer in the stiffer side (N/m^2)

$\sigma_{C,2}$, $\sigma_{C,3}$ Circumferential stresses in the direction of σ'_2 and σ'_3 (N/m^2)

σ_c Confining pressure in triaxial tests (N/m^2)

σ'_c Effective confining pressure (N/m^2)

σ_{cyc} Cyclic deviator stress (N/m^2)

σ_d Deviator stress (N/m^2)

σ'_d Effective deviatoric stress (N/m^2)

σ_{di} Deviator stress at which slope of E_R versus σ_d curve changes (N/m^2)

σ_g Compressive strength of the soil (N/m^2)

$\boldsymbol{\sigma}_{ij}$ Stress tensor

$\hat{\boldsymbol{\sigma}}_{ij}$ Characteristic stress tensor

σ_j	Principal stress (N/m^2)
σ_{oct}	Octahedral normal stress (N/m^2)
σ_{ref}	Reference stress (N/m^2)
σ_{sb}, σ_{bs}, σ_{sg}, σ_{go}	Vertical stresses at the sleeper-ballast, ballast-subballast, subballast-subgrade interfaces and bottom of subgrade layer (N/m^2)
σ_v	Vertical stress (N/m^2)
σ'_x, σ'_y, σ'_z	Effective stresses along x, y and z directions (N/m^2)
τ_{cyc}	Cyclic shear stress amplitude (N/m^2)
τ_{oct}	Octahedral shear stress (N/m^2)
φ	Friction angle (°)
φ_c, φ_e	Critical state friction angles under triaxial compression and extension (°)
φ_d	Dynamic amplification factor
φ'_m	Mobilised friction angle (°)
χ_i, χ_{tc}	Dilatancy parameter corresponding to image state and triaxial compression
ψ	State parameter
ψ_d	Dilation angle (°)
ψ_i	Image state parameter
ψ_m	Mobilised dilation angle (°)

Abbreviations:

2D	Two-dimensional
2.5D	Two and a half dimensional
3D	Three-dimensional
ACR	Additional confinement ratio
AREA	American Railway Engineering Association
ARTC	Australian Rail Track Corporation
BEM	Boundary element method
BoEF	Beam on elastic foundation
CBM	Cement bound mixture
CBR	California Bearing Ratio
CG	Coir geotextile

CSL	Critical state line
CSSR	Cyclic shear stress ratio
CVSR	Cyclic vertical stress ratio
DEM	Discrete element method
FDM	Finite difference method
FEM	Finite element method
GB	Geocell reinforced ballast
GG	Geocell reinforced subgrade
GS	Geocell reinforced subballast
HDPE	High-density polyethylene
HMA	Hot-mix asphalt
LVDT	Linear variable displacement transformer
MDD	Multi-depth deflectometers
MGT	Million gross tonnes
MSD	Mass-spring-dashpot
NCL	Normal compression line
ORE	Office for Research and Experiments
PE	Polyethylene
PP	Polypropylene
PSR	Principal stress rotation
RAP	Recycled asphalt pavement
SS	Silica sand
UGM	Unbound granular material
UR	Unreinforced
US	United States
WMATA	Washington Metropolitan Area Transit Authority

CHAPTER 1
INTRODUCTION

1.1 Background

A rapid growth in population has substantially increased the transportation of passenger, resources, and goods throughout the world. Consequently, the demand for transportation facilities is escalating tremendously. To cater to such enormous demands, the existing modes of transportation are rapidly expanding their infrastructure. Therefore, the number of road vehicles, trains and aircrafts has significantly increased. However, a rise in the number of road vehicles and aircrafts has resulted in tremendous congestion and air pollution. On the other hand, rail transport is considered an environment-friendly mode of transportation for conveying a large volume of freight and a large number of passengers over long distances (Krylov 2001). Similar to its counterparts, railway transport has adopted modern technologies to increase the speed of passenger trains and improve the capacity of freight trains to meet the ever-growing demands. Consequently, the frequency and magnitude of the load on existing railway tracks have dramatically increased in recent years (Nimbalkar et al. 2012). Unfortunately, most of the existing tracks have not been designed to meet these additional load requirements. Therefore, the stability and geometry of the track may get compromised in most of the conventional tracks.

The stability of a railway track is inevitable for the smooth and safe operation of the railway traffic, whether it be a passenger train, a freight train or other rolling stock. This stability depends on the behaviour of the constituent track materials and subgrade soil subjected to train-induced loading. Throughout the service life, the track is subjected to repetitive loads due to the movement of the trains. With an increase in the frequency and magnitude of the load, the subgrade and the constituent track materials undergo a substantial amount of deformation and deterioration (Nimbalkar & Indraratna 2016). This degradation leads to unacceptable differential settlements, lateral instability and a loss of track geometry. Consequently, the operational efficiency (i.e., better utilization of existing assets) of rail tracks is hampered due to speed restrictions or costly maintenance and upgrade.

The problem of track instability due to an increase in frequency and magnitude of the load is the most challenging for critical zones. The critical zones are the discontinuities along a railway line that are often subjected to rapid degradation in track geometry due to an abrupt change in track stiffness, damping and foundation type. These zones include the transitions between ballasted and slab tracks, unreinforced and reinforced slab tracks, ballasted tracks with concrete and wooden sleepers, open track and stiff structures such as bridges, culverts, underpasses, and tunnels, special track works and level crossings. The track section on either side of these zones usually exhibits significantly different response. Therefore, these zones are susceptible to differential settlement, deterioration of track substructure layers, and wear and tear in the superstructure (Li & Davis 2005). Consequently, the critical zones require frequent maintenance, which is expensive, disrupts the traffic and reduces the efficiency of operations. This problem may get aggravated with an increase in train speed and axle load.

The frequency of maintenance in the critical zones is usually higher than that in the open tracks (tracks away from these zones). For example, in the Netherlands, the frequency of maintenance of the tracks in the critical zone is nearly four to eight times higher than the open tracks (Wang et al. 2018). Similarly, in the Spanish high-speed rail line, the deterioration rate of the railway track (consequently, the frequency of maintenance) in the critical zone is three times higher than that in the open track (López-Pita et al. 2007). Moreover, the maintenance operations in the critical zones are also costly. For instance, approximately US$ 110 million was being spent annually to maintain the critical zones in Europe till 1999, and this value is likely to have increased (Mishra et al. 2017). Similarly, in 2005, about US$ 200 million was spent for the maintenance of the critical zones in the USA (Stark et al. 2016). Additionally, the maintenance work requires track possession which causes train delays and decreases the track capacity and efficiency. The indirect costs related to these factors may be significant. Another challenge with critical zones is the speed restriction enforced by the railway operators to ensure passenger safety. This speed restriction may negatively impact the revenues generated from the high-speed trains, for which the travel time is of utmost importance.

A reduction in the frequency of maintenance operations by improving track performance using countermeasures and the prediction of maintenance cycles could lead to significant

cost savings, which will be beneficial to both the railway operators and users. This can only be achieved by developing a clear understanding of the behaviour of the tracks in the critical zones. Nonetheless, prior knowledge of the magnitude of differential settlements accumulated in the track is the key to the proper design of the critical zones. However, studies related to the prediction of the differential settlement accumulated in a critical zone over a specified period are somewhat scarce. In most studies, the plastic deformation in the soil layers is predicted using empirical expressions. However, uncertainties exist regarding the use of empirical models as they lack general applicability under different loading effects, boundary conditions and soil types. Moreover, such expressions are only applicable to the conditions on which they are based or derived. Clearly, more work is required to establish a theoretically consistent approach to predict the behaviour of the critical zones and analyse the efficacy of various mitigation strategies.

1.2 Research Significance

A tremendous amount of money is being spent annually on the maintenance of railway tracks worldwide, especially in critical zones. Recent demands for heavier axle load and high-speed trains will further exacerbate this situation. Although numerous mitigation techniques have been proposed elsewhere to solve the problem associated with the critical zones, these regions still exhibit poor performance. This is due to the site-specific nature of the track deterioration problem and limited understanding of the mechanism of applied countermeasures. Thus, a comprehensive evaluation of the behaviour of railway tracks in the critical zones and the effect of various remedial measures is essential to improve the design and optimise the performance. Notably, the problem of predicting the magnitude of track geometry degradation in these zones and the efficacy of various countermeasures still remains an intriguing challenge.

The present study seeks to develop a simple yet effective approach to predict the transient and long-term performance of the ballasted railway tracks (see **Figure 1.1**) under train-induced repeated loading. The proposed approach can also simulate the behaviour of the tracks with varied support conditions along the longitudinal track direction (i.e., in the direction of train movement), which is a characteristic of the track transitions (see **Figure 1.2**) and predict the magnitude of differential settlements, which are major concerns for

critical zones. The proposed methodology is a quick and straightforward technique that does not require any commercial FE-based software in contrast to existing approaches that rely on these software. It also serves as a convenient method to assess the performance of different remedial measures in mitigating the differential settlement at the critical zone.

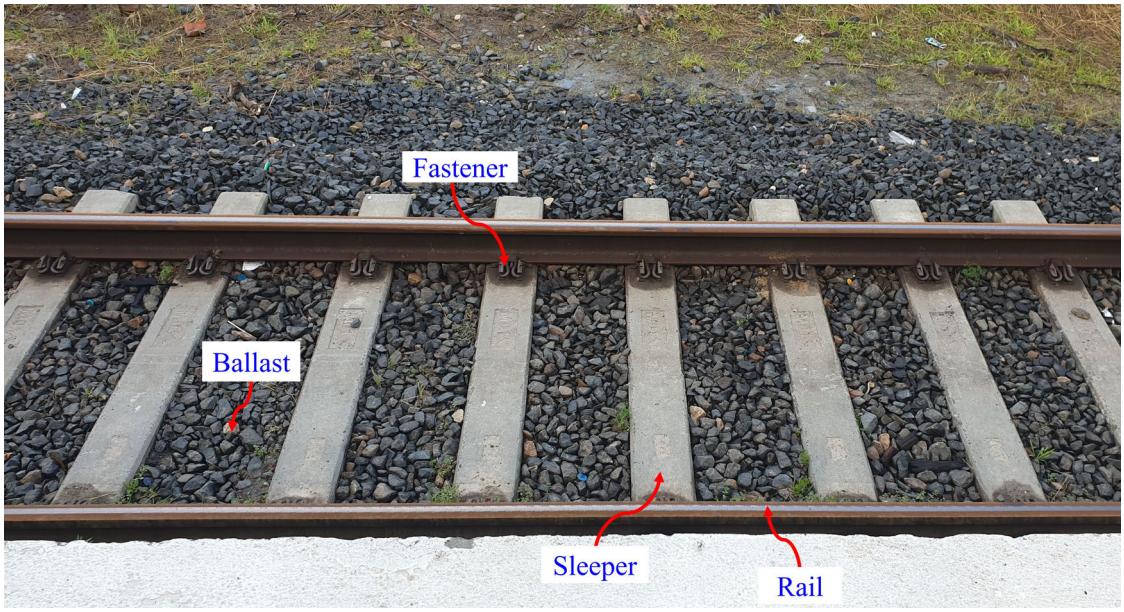

Figure 1.1 Ballasted railway track

Indeed, the railway industry has long been searching for a reliable method to predict the amount of vertical deformation accumulated in a railway track after multiple train passages. Prior information of this track behaviour is crucial to optimise its design, plan the maintenance operations, and improve the capacity of the track to allow heavier freight and high-speed passenger trains. The proposed methodology seeks to address this critical requirement of the railway industry. The methodology can potentially serve as a tool to assist the practising railway engineers to optimise the performance of the railway tracks, especially in the transition zones. The essential contribution of this study to the field of railway geotechnics is the more accurate simulation of the track response using a mechanistic approach compared to the existing methods that employ an empirical approach. Nonetheless, the developed method is available in the form of a MATLAB code (MathWorks Inc. 2021), which can be readily be converted into an application that can be used by the railway engineers.

Figure 1.2 Open track-bridge transition [Imagery © 2022 Google, Imagery © 2022 CNES / Airbus, Maxar Technologies, Map data © 2022; Image: © 2022 Google]

This study is also critical from a social perspective because railway tracks form an integral component of the transportation infrastructure and play a vital role in maintaining a healthy economy. A significant amount of funds are invested in the maintenance and rehabilitation of these tracks every year. Similar to its counterparts, railway transport needs to improve the capacity of the existing infrastructure in order to satisfy the ever-increasing demands. Such an upgradation would require a significant amount of financial investments, which may affect the economy. Therefore, railway engineers need reliable tools to assist them in deriving maximum performance from the railway tracks with optimum use of the available funding. The methodology developed in the thesis contributes to this requirement by furnishing a technique to evaluate track behaviour and investigate the adequacy of various alternatives to enhance its performance.

Nonetheless, the condition of the railway tracks determines the safety and comfort of the train passengers. A well-maintained track with proper geometry and alignment ensures a smooth train passage. Without appropriate maintenance, the track may lose its stability and lead to serious accidents, endangering the life of passengers. To prevent such incidents, the track geometry is regularly inspected using specialised vehicles, which adds to the operating cost of the railways. The methodology proposed in this project can be used to identify the problematic sections along a railway line without a physical examination, consequently reducing the number of maintenance inspections and minimising the operational costs.

1.3 Research Objectives

The present study attempts to address the challenges faced by the practising railway engineers in accurately predicting the short and long-term track performance, which is crucial for track design and planning of the maintenance operations. These challenges are as follows:

1. Lack of a suitable technique for a quick and accurate evaluation of the long-term performance of the railway tracks with a capability to incorporate heterogeneous support conditions along the track length.
2. Reliance on empirical methods for computing the cumulative irrecoverable deformation in the track, which lack general applicability under various loading conditions and soil types.
3. Uncertainty regarding the accuracy of the predictions from existing track models which simplify the ballasted railway track as a single or dual-layered structure instead of the actual multi-layered structure.
4. Inaccuracy associated with the computation of stiffness and vibrating mass of the substructure layers in existing track models, which ignore the overlapping of stress-distribution pyramids in the transverse direction (along the sleeper length).
5. Lack of an approach that considers the effect of principal stress rotation (PSR), which is experienced by the soil elements during a train passage, on the cumulated track deformation.
6. Lack of an adequate methodology for assessing the effectiveness of various countermeasures in improving the track performance and selecting the most appropriate strategy.

The aforementioned challenges have been identified based on an extensive literature review (see CHAPTER 2). Apparently, these challenges exist due to a gap in the state of knowledge pertaining to the prediction of short and long-term track performance. The present study aims to address these challenges or research gaps by:

1. Developing an innovative methodology for quick evaluation of the transient and long-term performance of the ballasted railway tracks with enhanced capability to incorporate varied support conditions along the longitudinal direction and predict the differential settlements associated with the critical zones.
2. Establishing a mechanistic approach to compute the cumulative irrecoverable deformation in the track by using plastic slider elements to capture material plasticity. To the author's knowledge, this study is the first attempt to incorporate the plastic sliders to simulate the inelastic behaviour of the materials constituting the railway tracks.
3. Considering more appropriate inclusion of three substructure layers (ballast, subballast, and subgrade) for simulating the behaviour of the ballasted rail tracks.
4. Incorporating the overlapping of the load-distribution pyramids along both transverse and longitudinal directions for a more accurate evaluation of track parameters.
5. Studying the effect of PSR on the track response using appropriate constitutive relationships for plastic slider elements.
6. Using the developed computational approach to compare the effectiveness of different mitigation strategies in improving the performance of critical zones, which will help in selecting the most appropriate strategy for a particular transition.
7. Developing a method for computing the magnitude of improvement provided by the three-dimensional (3D) cellular geoinclusions and assessing their adequacy in improving the track performance.

1.4 Thesis Organisation

This thesis is organised into eight chapters:

CHAPTER 1 introduces the research problem and describes the significance, objectives and scope of the present study.

CHAPTER 2 begins with an introduction to the basic concepts related to the ballasted railway track and its design. This is followed by a comprehensive discussion on the existing methods to evaluate the response of the ballasted railway tracks to train-induced loads. Subsequently, the problems associated with the transition zones are highlighted, and the remedial measures are discussed. Finally, the existing methods to predict the performance of the railway tracks in transition zones is discussed.

CHAPTER 3 describes the development of novel methods for predicting the behaviour of the substructure layers in the ballasted railway tracks. It is divided into two parts, in which the first part describes an integrated approach that combines the track loading, resiliency and empirical settlement models. The second part of the chapter discusses the evolution of a novel geotechnical rheological model to predict the transient and irrecoverable response of the ballasted railway track subjected to train-induced repeated loads. This model considers material plasticity through the use of slider elements, which are described by appropriate constitutive relationships.

CHAPTER 4 explains the development of a novel 3D mechanistic approach to evaluate the transient and long-term performance of the critical zones. The methodology is applied to an open track-bridge transition, and the adequacy of different countermeasures to mitigate the differential track settlements is examined. The importance of considering material plasticity in track transition models is also illustrated.

CHAPTER 5 deals with the effect of PSR on the response of the ballasted railway tracks. This effect is accounted for in the geotechnical rheological model by modifying the constitutive relationships used for the plastic slider elements. The importance of including PSR in predicting track response is elucidated by comparing the results with and without PSR inclusion.

CHAPTER 6 probes into the effectiveness of using 3D cellular inclusions to improve the performance of the railway tracks in the transition zones. Initially, a comprehensive review of existing literature related to the use of cellular geoinclusions in the railway tracks is provided. Subsequently, a novel semi-empirical model is developed to evaluate the additional confinement provided by the cellular geoinclusions under the 3D stress

state. Finally, the additional confinement model is incorporated into the geotechnical rheological model, and the adequacy of using 3D artificial inclusions in improving the performance of a transition zone is assessed.

CHAPTER 7 is devoted to the development of numerical models for simulating the behaviour of ballasted railway tracks under moving train loads. To this end, a 3D finite element (FE) model of a standard ballasted track is first established, which acts as a precursor to understand the behaviour of an open track or softer side of the transition zone. Subsequently, the numerical model for a typical open track-bridge transition is developed. The model is validated against the field data available in the literature. Further insights into the performance of transition zones reinforced with 3D cellular geoinclusions are attained using FE modelling.

CHAPTER 8 summarises the significant findings from the present research and highlights the future scope of work.

CHAPTER 2
LITERATURE REVIEW

2.1 Overview

The development of a technique to evaluate the behaviour of railway tracks requires a fundamental understanding of the track structure, properties of the geomaterials that constitute the track, nature of loading, interaction between various track components and the existing approaches available for predicting the track response. These fundamental concepts are treated at the beginning of this chapter. Subsequently, the problems associated with the critical zones in railway tracks are described. The major causes of the problems, factors affecting the track deterioration, insights from the field investigations and different mitigation strategies are also discussed. Finally, the existing methods available for evaluating the performance of critical zones are reviewed, and the research gaps are elucidated.

2.2 Railway Track: Basic Concepts

The railway track is the structure on which the trains and other rolling stocks move. The primary function of a railway track is to provide a stable and robust bed for the movement of the trains. The track must transfer the traffic-induced loads safely to the subgrade soil. Safety implies that the stresses transferred to the soil must be within the permissible limits, enabling a sufficient safety margin for various risks and uncertainties (Esveld 2001). The settlement of the track must also be within acceptable limits.

2.2.1 Structure of Ballasted Railway Tracks

The ballasted railway tracks employ multiple layers of granular material to transfer the train-induced loads safely to the subgrade. These tracks consist of two essential components: superstructure and substructure. The superstructure comprises rails, rail pads, sleepers (or ties), and the fasteners. Moreover, the substructure constitutes ballast, subballast, fill layers (structural and general), and soil subgrade (prepared and natural subgrade or formation). **Figure 2.1** shows the cross-section of a typical ballasted railway track.

The rail is a longitudinal steel member which is supported by sleepers at regular intervals. It provides a firm base for the movement of trains. It must possess adequate strength and stiffness to resist the loads exerted by the rolling stock without undergoing significant deformation. The rail primarily accommodates the wheel and transfers the load from the train to the sleepers. Moreover, it may also serve as an electric signal conductor in an electrified line (Remennikov & Kaewunruen 2008; Indraratna et al. 2011).

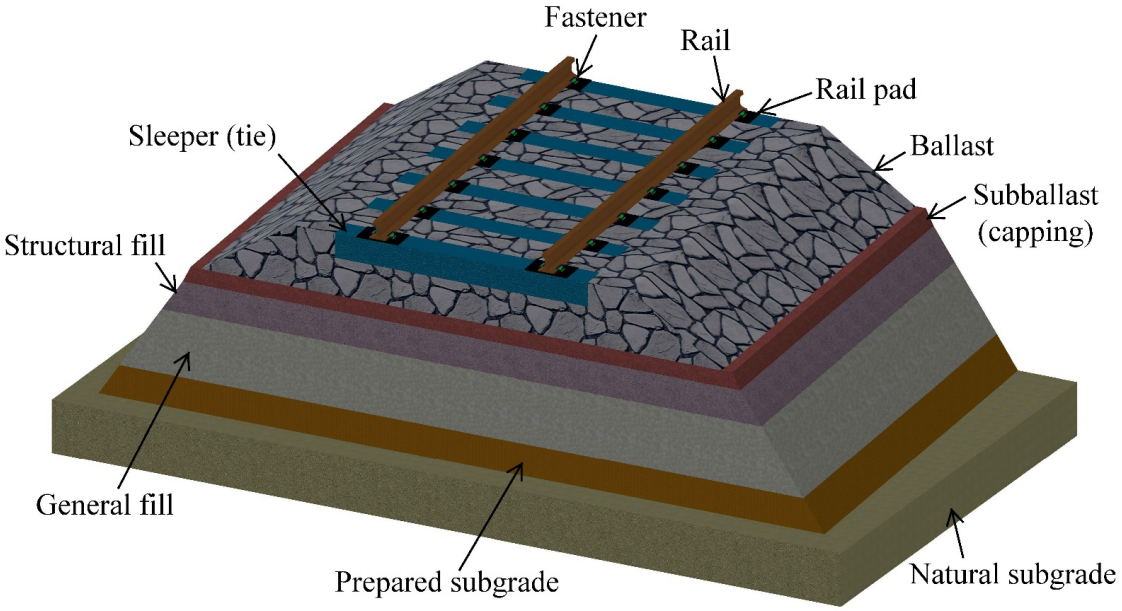

Figure 2.1 Ballasted railway track structure

The rail pads are often provided below the rail to filter out or dampen the dynamic forces generated from the movement of the high-speed rolling stock (Indraratna et al. 2011). Therefore, they reduce the amount of vibration transmitted to the sleeper and the substructure. The sleepers (or ties) are the transverse beams that support the rails and transfer the traffic-induced vertical, lateral, and longitudinal forces to the substructure (Doyle 1980). The sleepers can be manufactured using steel, concrete, or timber. However, the prestressed concrete sleepers are the most commonly used sleepers due to their high strength and durability (Remennikov & Kaewunruen 2008). The fasteners are used to maintain the position of the rail on the sleepers. They resist a combination of train-induced vertical, lateral, and longitudinal forces in addition to the overturning moments (Remennikov & Kaewunruen 2008).

The ballast bed is a layer of coarse aggregates that supports the sleepers. It comprises crushed stones and gravel with particle size ranging typically between 20 mm and 60 mm (Esveld 2001). The primary functions of the ballast bed are to provide a stiff bearing surface for the sleepers and to transfer the imposed superstructure loads safely to the underlying layers and the subgrade (Doyle 1980). Moreover, the ballast bed facilitates the drainage of water away from the track, reduces vibrations, and absorbs the noise (Selig & Waters 1994). The subballast bed (permeable capping) is a layer of granular material that acts as a filter to prevent the movement of fines from the underlying layers to the ballast. Moreover, it arrests the penetration of the ballast into the bottom layers and drains water away from the subgrade into the ditches. The subballast layer also distributes the traffic-induced stresses uniformly over a wide area of the subgrade or the embankment (Indraratna et al. 2011).

The railway tracks are laid on embankments to maintain the vertical alignment either in the case of low-lying areas or areas where deposits of soft or weak subgrade are encountered. The embankments usually comprise structural fill and general fill. The structural fill is a layer of compacted material lying below the subballast bed whose thickness depends on the strength of the underlying layers (Asset Standards Authority 2018). The general fill is a layer of compacted material that is provided between the structural fill and the subgrade. The general fill material usually possesses lower strength than the structural fill material (Asset Standards Authority 2018).

The subgrade is the lowermost part of the railway track that ultimately bears the weight of the track and the traffic-induced loads. The safety and long-term performance of a track primarily depend on the mechanical and hydraulic behaviour of the subgrade. Therefore, it must possess adequate strength (bearing capacity), stiffness, and drainage ability. However, some natural subgrades, such as soft compressible clays, possess poor engineering properties and require engineering treatment before the construction of the overlying track layers. The treated layer with enhanced engineering properties is known as the prepared subgrade.

2.2.2 Loads on a Railway Track

A railway track withstands a combination of loads in vertical, lateral, and longitudinal directions resulting from the traffic, track condition, and temperature. The vertical load is primarily due to the weight of the rolling stock. In addition to the weight, the vertical loads also emerge due to the movement of the vehicle on the track with geometrical irregularities. These loads are known as dynamic loads, and their magnitude and frequency depend on the amount of rail/wheel irregularities (Remennikov & Kaewunruen 2008). The lateral loading arises from the wind, the reaction of the train to geometric deviations in the track, centrifugal force in curves and buckling reaction force on the rail (at high rail temperatures) (Indraratna et al. 2011). The longitudinal loading originates from the traction and braking forces from the trains, thermal effects, and wave action of rail (Selig & Waters 1994).

2.2.2.1 Vertical Load

The vertical load is a combination of moving static and dynamic loads (Esveld 2001). The total vertical load on a railway track is given as:

$$Q_{\mathrm{tv}} = Q_{\mathrm{qs}} + Q_{\mathrm{dy}} \tag{2.1}$$

where Q_{tv} is the total vertical wheel load; Q_{qs} is the quasi-static wheel load, which is the sum of the static wheel load, wind load and non-compensated centrifugal force on the outer rail (in a curve); Q_{dy} is the dynamic component of load that depends on the train speed, quality of the track, and the wheel and vehicle parameters (such as wheel diameter and unsprung mass).

$$Q_{\mathrm{qs}} = \left(\frac{Q_{\mathrm{a}}}{2}\right) + \frac{H_{\mathrm{w}} l_{\mathrm{w}}}{b_{\mathrm{t}}} + \frac{Q_{\mathrm{a}} l_{\mathrm{c}}}{{b_{\mathrm{t}}}^2}\left(\frac{b_{\mathrm{t}} V^2}{g R_{\mathrm{c}}} - h_{\mathrm{se}}\right) \tag{2.2}$$

where Q_{a} is the static axle load; H_{w} is the crosswind force; l_{w} is the distance between the centre of rails and the resultant wind force; l_{c} is the distance between rail top and centre of gravity of the train; b_{t} is the track width; V is the train speed; g is the acceleration due to gravity; R_{c} is the radius of curvature of the track; h_{se} is the superelevation.

The dynamic component of the load is very complex as it depends on a large number of parameters such as track geometry, train configuration, and speed, among others. Consequently, the dynamic effect is represented in the form of a factor which is a

multiplier to the static wheel load (Equation 2.3) (Doyle 1980; Remennikov & Kaewunruen 2008). This factor is known as the dynamic amplification factor (φ_d) or the impact factor. The magnitude of φ_d depends on the parameters such as the train speed, quality (or condition) of the rail and wheel as well as the stiffness of subgrade (Sayeed & Shahin 2016). The total design vertical wheel load is calculated using the following equation:

$$Q_d = \varphi_d Q \tag{2.3}$$

where Q_d is the design wheel load; Q is the static wheel load. **Table 2.1** shows the different empirical equations to evaluate φ_d. More details of these methods can be found elsewhere (Prause et al. 1974; Doyle 1980; Indraratna et al. 2011; Van Dyk et al. 2016).

2.2.2.2 Lateral Load

The loads acting on the railhead in the lateral direction depend on the parameters such as the radius of curvature of the track, speed, and configuration of the train (Doyle 1980). Several empirical expressions have been developed based on the field investigations to evaluate the magnitude of the lateral load exerted by the wheel flange on the railhead while negotiating the curves. Some of these empirical expressions are discussed in the subsequent paragraphs:

Office for Research and Experiments (ORE) Formula.

The ORE conducted field investigations to evaluate the magnitude of the lateral load exerted by a wheel flange on the railhead for different train configurations, speed (up to 200 km/h), and curve radii. The results showed that the lateral force depends only on the radius of curvature of the track. The magnitude of the lateral load was calculated using the following equation (Doyle 1980):

$$H_L = 35 + \frac{7400}{R_c} \tag{2.4}$$

where H_L is the lateral load (kN).

Table 2.1 Empirical equations to calculate the impact factor

Method	Equation	Remarks
ORE (1968)†	$\varphi_{\mathrm{d}} = 1 + \alpha' + \beta' + \gamma'$ $\alpha' = 0.04\left(\frac{V}{100}\right)^3$ $\beta' = \frac{\mathrm{V}^2(2h + h_{\mathrm{se}})}{127 R_{\mathrm{c}} l_{\mathrm{g}}} - \frac{2 h_{\mathrm{se}} h}{l_{\mathrm{g}}^2}$ $\gamma' = \gamma_{\mathrm{o}} a_{\mathrm{o}} b_{\mathrm{o}}$ $\gamma_{\mathrm{o}} = 0.1 + 0.017\left(\frac{V}{100}\right)^3$	α' depends on track irregularities, train suspension, and speed; β' accounts for the movement of the train along a curve; γ' depends on the train speed, its configuration, and track condition; h_{se} = superelevation (m), l_{g} = gauge width (m), h = vertical distance from rail top to the centre of gravity of train (m), a_{o} and b_{o} = locomotive and track maintenance factors
Eisenmann (1972)	$\varphi_{\mathrm{d}} = 1 + \delta_{\mathrm{t}} \eta_{\mathrm{v}} t_{\mathrm{u}}$ $\eta_{\mathrm{v}} = 1$ for $V <$ 60 km/h $\eta_{\mathrm{v}} = \left(1 + \frac{V - 60}{140}\right)$ for $60 \leq V \leq 200$ km/h	δ_{t} = factor that depends on the track condition; η_{v} = factor that depends on vehicle speed; t_{u} = factor that depends on the upper confidence limit
WMATA‡ (Prause et al. 1974)	$\varphi_{\mathrm{d}} = (1 + 0.0001V^2)^{0.67}$	V = speed of train (miles/h)
AREA (1978)*	$\varphi_{\mathrm{d}} = 1 + \frac{0.00521V}{D_{\mathrm{w}}}$	V = train speed (km/h); D_{w} = diameter of the wheel (m)
British Railways (Doyle 1980)	$\varphi_{\mathrm{d}} = 1 + \frac{8.784(\theta_1 + \theta_2)V}{Q}\sqrt{\frac{K_{\mathrm{j}} W_{\mathrm{u}}}{g}}$	$(\theta_1 + \theta_2)$ = total dip angle of the rail joint (radians); Q = static wheel load (kN); K_{j} = track stiffness at joint (kN/mm); W_{u} = unsprung weight at one wheel (kN)
German formula (Doyle 1980)	$\varphi_{\mathrm{d}} = 1 + \frac{V^2}{3\times10^4}$ for $V \leq 100$ km/h $\varphi_{\mathrm{d}} = 1 + \frac{4.5\,V^2}{10^5} - \frac{1.5\,V^3}{10^7}$ for $V >$ 100 km/h	
Indian Railways (Doyle 1980)	$\varphi_{\mathrm{d}} = 1 + \frac{V}{58.14\sqrt{k}}$	k = track modulus (MPa)
South African formula (Doyle 1980)	$\varphi_{\mathrm{d}} = 1 + \frac{4.92V}{D_{\mathrm{w}}}$	D_{w} = diameter of wheel (mm)
Japanese standard (Shin et al. 2002)	$\varphi_{\mathrm{d}} = \left(1 + 0.3\frac{V}{100}\right)(1 + C)$	C = coefficient (value ≈ 0.3)
Sun et al. (2016)	$\varphi_{\mathrm{d}} = e^{\alpha^* V}$	α^* = empirical parameter (value = 0.003)
Nimbalkar & Indraratna (2016)	$\varphi_{\mathrm{d}} = 1 + i_1\left(\frac{V}{D_{\mathrm{w}}}\right)^{i_2}$	i_1, i_2 = empirical parameters

*AREA: American Railway Engineering Association; †ORE: Office for Research and Experiments; ‡WMATA: Washington Metropolitan Area Transit Authority

Swedish Railways Formula.

The Swedish Railways conducted similar field investigations to evaluate the magnitude of the lateral load exerted by a wheel flange on the railhead for different train configurations, speed, and a curve radius of 600 m. The following empirical expression was developed:

$$H_{\text{mean}} = 17 + \frac{V}{27.6} \tag{2.5}$$

where H_{mean} is the mean lateral load (kN).

British Railways Formula.

The British Railways recommend the evaluation of the lateral load using the following relationship (British Railways Board 1993).

$$H_{\text{L}} = Q_{\text{a}} A_{\text{d}} + A_{\text{y}} V_{\text{m}} \sqrt{\frac{M_{\text{u}}\left(K_{\text{y}} M_{\text{u}}\right)}{M_{\text{u}} + M_{\text{y}}}} \tag{2.6}$$

where A_{d} is the maximum normal operating cant deficiency angle (rad); A_{y} is the angle of lateral ramp discontinuity (0.0039 rad); V_{m} is the maximum normal operating speed (m/s); M_{u} is the effective lateral unsprung mass per axle (kg); M_{y} is the effective lateral rail mass per wheel (170 kg); K_{y} is the effective lateral rail stiffness per wheel (25×10^6 N/m). As per the British standards (British Railways Board 1993), the total lateral load per axle on the track must not exceed 71 kN when a rolling stock negotiates a curve with a lateral ramp discontinuity at maximum permissible speed and cant deficiency. The maximum permissible value of 71 kN corresponds to the lateral force theoretically induced by a Class 86/2 electric locomotive travelling at a speed of 180 km/h over a curve with a lateral ramp in outer rail and a cant deficiency of 5.8° (British Railways Board 1995). Moreover, the lateral load on the track per axle (sustained over a length ≥ 2 m) must never be greater than (Q_{a}/3 + 10) kN.

2.2.2.3 Longitudinal Loads

The longitudinal loads develop from the thermal expansion and contraction of the rails, wheel action, and the traction and braking forces from the wheel. The thermal effects can

lead to rail buckling and are much more pronounced in the continuously welded rails. Moreover, the traction and braking result in excessive wear and tear on both rails and wheels (Prause et al. 1974). The traction and braking forces from the wheel generate additional shear stresses and longitudinal displacement in soil elements below the railway track. Consequently, the track layers may undergo a significant amount of deformation at locations where the trains often accelerate or brake, thus requiring frequent maintenance (Yang et al. 2009).

2.2.2.4 Impact Loads

In addition to the quasi-static loads, the railway track is often subjected to impact loads due to inevitable track and train abnormalities. The impact loads are characterised by a high magnitude and short duration. Worn wheel/rail surface profile, wheel flats, bad welds, switches, dipped rails, joints, rail corrugation, turnouts, unsupported sleepers, an abrupt change in track stiffness are some of the inevitable causative factors of the impact loads in a railway track (Remennikov & Kaewunruen 2008; Nimbalkar et al. 2012).

The impact loads induce vibrations and oscillations in the train body and the various track components. Additionally, they generate a considerable amount of noise. The vibrations affect the performance of the track as well as passenger comfort. The magnitude and nature of the vibration depend on the characteristics of the geometric irregularity of the track and the wheel. A geometric irregularity with a large wavelength (e.g., due to differential settlement of the track) primarily causes train body vibrations that reduce passenger comfort. However, the irregularity with a small wavelength (wheel or rail corrugations) primarily generates the wheel vibration. The wheel vibration leads to the fluctuation in axle weight and results in the vibration in the track (Miura et al. 1998). Moreover, the vibrations produced due to the impact loads accelerate the deterioration of the ballast and subballast bed (especially for stiff subgrade) and consequently endanger the stability and operational efficiency of a track (Nimbalkar et al. 2012). The impact loads may also lead to the differential track settlement due to the localised compaction of the subgrade at the impact location (Sadri & Steenbergen 2018).

Figure 2.2 shows an example of the impact loads generated near the bridge approach. A railroad vehicle experiences an abrupt change in the track stiffness while approaching a

bridge. This change leads to an amplification of the dynamic forces induced by the train-track interaction and produces impact loads. The track substructure undergoes a considerable amount of deterioration due to these impact loads and ultimately results in undesirable differential settlements. The differential settlement further exacerbates the track stability and undermines the safety of the passengers (Kaewunruen et al. 2016). Therefore, frequent maintenance is required near the bridge approaches to keep the track in an operating condition. A possible solution to this problem is to gradually increase the vertical track stiffness in the transition zone between the open track and the bridge. The gradual increase in the track stiffness reduces the magnitude of impact loads and preserves the track geometry over an extended period.

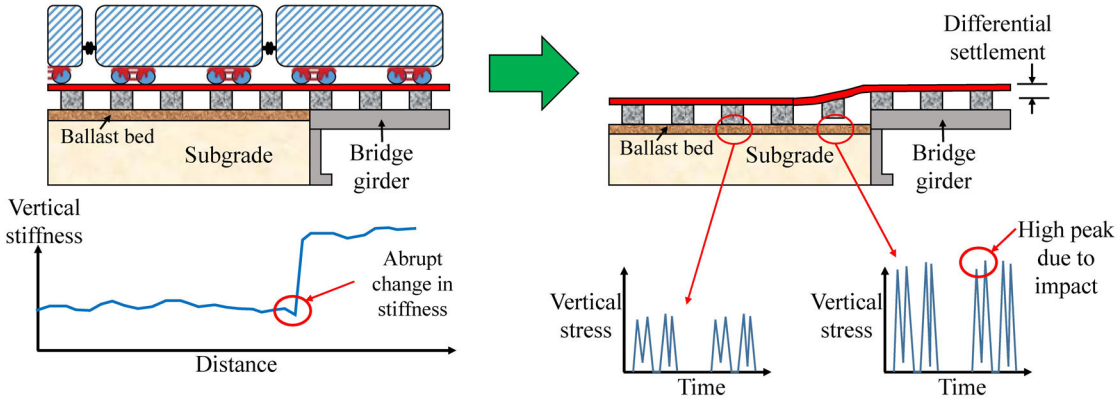

Figure 2.2 Impact loads generated near the bridge approach [modified from Wang & Markine (2018a)]

2.2.3 Behaviour of Track Materials under Repeated Loading

When a track material (ballast, subballast or subgrade soil) is subjected to repeated loading, the amount of deformation in each cycle includes a resilient component (recoverable) and a plastic component (irrecoverable or inelastic) (see **Figure 2.3**). The resilient (elastic) component for each cycle is calculated by subtracting the maximum strain under the peak load with the permanent strain after unloading.

Initially, the amount of plastic strain increment is much higher than the resilient strain. However, the magnitude of plastic strain increment decreases with an increase in the number of load cycles. Subsequently, a stage is reached (known as shakedown) when the plastic strain increment diminishes, and the elastic strain becomes virtually constant (Selig & Waters 1994). The corresponding ratio of the deviator stress to the recoverable

(elastic) strain at this stage is termed as the resilient modulus of the material. It must be noted that the variation of plastic strain with the number of cycles also depends on the stress levels. The plastic strain may increase continuously (at an increasing rate) with an increase in the number of cycles (known as ratcheting) at high deviator stress and low confining pressure (Lekarp et al. 2000). Moreover, the track material may also undergo cyclic creep wherein the plastic strain accumulates with an increasing number of load cycles but at an ever-decreasing rate (Powrie et al. 2019).

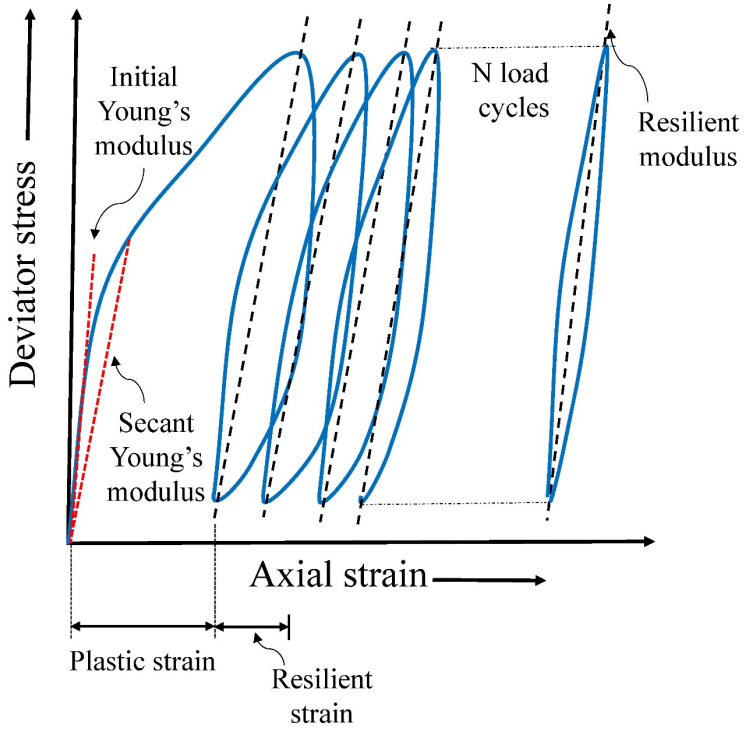

Figure 2.3 Young's modulus and resilient modulus for soil

2.2.3.1 Resilient Modulus

Definition.

The resilient modulus (E_R) is defined as the ratio of the cyclic deviator stress (σ_{cyc}) to the elastic vertical strain (resilient strain) during unloading (ε_1^e) (Elliott & Thornton 1988). It is expressed as:

$$E_R = \frac{\sigma_{cyc}}{\varepsilon_1{}^e} \tag{2.7}$$

E_R is most commonly determined using the cyclic triaxial tests with a constant value of confining pressure and a cyclic variation of the deviator stress (Li & Selig 1994). It is often very challenging to conduct laboratory testing on geomaterials prior to their use in

pavement or railway applications. Therefore, several empirical models (based on comprehensive experimental investigations) have been developed that can be used to directly evaluate the value of E_R at specific physical states, loading conditions, and stress states (Li & Selig 1994).

Empirical Models for Resilient Modulus.

Several empirical models have been developed for the prediction of E_R for soil (Li & Selig 1994). **Table 2.2** lists the various models. Here, σ_{di} is the deviator stress at which slope of E_R versus deviator stress (σ_d) curve changes; σ'_c is the effective confining pressure; σ_{oct} and τ_{oct} are the octahedral normal and shear stresses, respectively; P_a is the atmospheric pressure; θ is the bulk stress.

Table 2.2 Empirical models for the prediction of resilient modulus

Type	**Model**	**Reference**	**Fitting parameters**
Bilinear	$E_R = K_1 + K_2\sigma_d$, for $\sigma_d < \sigma_{di}$ $E_R = K_3 + K_4\sigma_d$, for $\sigma_d > \sigma_{di}$	Thompson & Robnett (1976)	K_1, K_2 K_3, K_4
Power	$E_R = k^*{\sigma_d}^n$	Moossazadeh & Witczak (1981)	k^*, n
Power†	$E_R = k^*\left(\frac{\sigma_d}{\sigma'_c}\right)^n$	Brown et al. (1975)	k^*, n
Semi-log	$E_R = 10^{(k^* - n\sigma_d)}$	Fredlund et al. (1975)	k^*, n
Semi-log	$\log(E_R) = k^* - n\left(\frac{\sigma_d}{\sigma_{d(failure)}}\right)$	Raymond et al. (1979)	k^*, n
Hyperbolic	$E_R = \frac{k^* + n\sigma_d}{\sigma_d}$	Drumm et al. (1990)	k^*, n
Octahedral	$E_R = k^*\left(\frac{\sigma_{oct}^n}{\tau_{oct}^m}\right)$	Shackel (1973)	k^*, m, n
Stress-dependent	$E_R = k_1^* P_a\left(\frac{\theta}{P_a}\right)^{k_2^*}\left(\frac{\tau_{oct}}{P_a} + 1\right)^{k_3^*}$	Uzan (1985, 1992)	k_1^*, k_2^*, k_3^* ($k_1^* > 0$, $k_2^* \geq 0$ and $k_3^* \leq 0$)

† for saturated over-consolidated soils.

The stress-dependent model given by Uzan (1985, 1992) is the most commonly used method to evaluate E_R (see **Table 2.2**). The bulk and octahedral shear stresses in this model can be evaluated by using the following equations:

$$\tau_{oct} = \frac{1}{3}\sqrt{(\sigma_1 - \sigma_2)^2 + (\sigma_1 - \sigma_3)^2 + (\sigma_2 - \sigma_3)^2} \quad 2.8$$

$$\theta = \sigma_1 + \sigma_2 + \sigma_3 \quad 2.9$$

where σ_1, σ_2, and σ_3 are the major, intermediate, and minor principal stresses, respectively. It is interesting to note that the stress-dependent model by Uzan (1985, 1992) applies to both coarse-grained and fine-grained soils (Christopher et al. 2006). The model includes both the increment of resilient modulus with bulk stress and the reduction with an increase in the deviator stress for the coarse-grained and fine-grained soils, respectively (Thompson & Robnett 1976; Mengelt et al. 2006).

The resilient modulus is a measure of the elastic stiffness of the geomaterials used for the construction of the track substructure (Li & Selig 1994). Therefore, it can be used to predict the track performance under repeated loads due to rail traffic. Consequently, its study is essential for the design of railway tracks. The resilient modulus of the soil depends on (Janardhanam & Desai 1983; Li & Selig 1994):

- Soil properties such as type, gradation, degree of compaction, and moisture content.
- Stress state such as the magnitude of confining pressure.
- Loading parameters such as magnitude, frequency, duration and the number of load cycles.

Resilient Modulus versus Young's Modulus.

E_R of a granular material is often confused with Young's modulus. Although both the terms measure the resistance against the elastic deformation, they distinctly differ in terms of evaluation and application. E_R is most commonly used to describe the behaviour of granular materials under repeated (cyclic) loading. It is an essential parameter for designing the pavements and the railway tracks (Christopher et al. 2006).

The Young's modulus of a material is the ratio of the stress to the strain under loading, within the elastic limits. It is generally employed to describe the behaviour of a material

under monotonic loading conditions, and its value is constant for an isotropic linear-elastic material. The Young's modulus is the slope of the linear (elastic) portion of the stress-strain curve of the material, usually obtained from axial compression or tension tests. However, the soil (or granular material) often exhibits non-linear elastic behaviour. Therefore, two Young's moduli are used to describe its response: initial Young's modulus (E_i) and secant Young's modulus (E_{sec}). The initial Young's modulus is the slope of the initial portion of the stress-strain curve, whereas the secant modulus is the slope of the line joining the origin to a particular level of stress (or strain) in the stress-strain curve (Budhu 2015).

E_R is usually determined after the completion of a certain number of load cycles (Selig & Waters 1994; Christopher et al. 2006). However, it may also be calculated for each load cycle for an accurate (or more realistic) prediction of the material behaviour under repeated loading. The magnitude of E_R (if calculated for each cycle) increases with an increase in the number of load cycles and becomes almost constant after a particular value. Moreover, the material becomes progressively stiffer with an increase in the number of load cycles (Lekarp et al. 2000). Consequently, the magnitude of E_R of a material may even exceed E_i or E_{sec}.

Resilient Modulus versus Track Modulus.

The track modulus (k) is defined as the force per unit deflection per unit length of the track (Doyle 1980). It is a measure of the resistance against deflection produced by the track when a static wheel load is applied on the rail. In other words, k is the static wheel load per unit length of the rail that is required to produce unit deflection in the track. The magnitude of k primarily depends on the properties of both the substructure and the superstructure, such as rail size, quality, dimensions and spacing of sleepers, quality, and degree of compaction of ballast, subballast, structural fill, general fill and the subgrade (Doyle 1980). Moreover, the train parameters such as V and Q_a also influence the magnitude of k (Nimbalkar & Indraratna 2016). k is a measure of the overall response of the railway track to a static wheel load, whereas E_R is a measure of the response of a particular material layer (ballast, subballast, or subgrade) to repeated loading. In other words, k is the property on a global level, whereas E_R is the property of individual components.

Young's Modulus versus Stiffness.

The Young's modulus of a material is the ratio of the stress to the strain within the elastic limit. It is a measure of the resistance offered by a material to the elastic deformation under loading. It is a material property and does not depend on the shape and size of the material under loading. The unit of Young's modulus is identical to the unit of stress, i.e., N/m^2. The stiffness of a material is the measure of the resistance offered by the material against deformation under loading. It depends on the shape and size of the material. The unit of stiffness is N/m.

2.2.3.2 Irrecoverable Deformations

The granular materials usually tend to densify under the application of cyclic or repeated loading (Indraratna et al. 2010; Indraratna & Nimbalkar 2013). This densification is due to the reorientation and rearrangement of the particles, and also due to the particle breakage in response to the repeated loading. This response leads to permanent deformation in the track, and consequently, the track geometry deteriorates. Nevertheless, the plastic response of the granular materials depends on a large number of factors such as (Lekarp et al. 2000; Sun et al. 2017; Li et al. 2018):

- Stress levels: plastic deformation is directly proportional to the deviator stress and inversely proportional to the confining pressure.
- Principal stress rotation: leads to larger inelastic strain than those predicted by cyclic triaxial tests.
- The number of load cycles.
- Moisture content: plastic deformation may increase due to excessive positive porewater pressure or lubrication.
- Density: deformation decreases with an increase in density.
- Stress history.
- Grading, type of aggregate and fine content.

The long-term performance of a railway track depends on the plastic deformations in its constituent materials. The excessive plastic deformation of the soil subgrade or the granular layers (ballast, subballast, structural fill, and general fill) under repeated traffic loads is detrimental to the track stability. It demands frequent maintenance cycles and also leads to poor riding quality, which decreases passenger comfort (Li & Selig 1996).

2.2.4 Track Design

The design of a ballasted railway track involves the determination of the stresses and settlements at crucial locations within the track such as the sleeper–ballast, ballast–subballast, subballast–fill, and fill–subgrade interfaces, among others. Subsequently, the magnitude of the induced stresses and settlements are compared with the permissible values to arrive at a suitable factor of safety (Doyle 1980). The dimensions of the sleepers and the thickness of the granular layers (viz. ballast, subballast, structural fill, and general fill) are then adjusted to control the magnitude of the stresses and settlements (Doyle 1980; Li & Selig 1998). **Figure 2.4** shows the flowchart for the design of a ballasted railway track.

The existing design techniques use semi-empirical equations that are based on experience with in-service tracks, augmented with extensive laboratory and field testing data to evaluate the load and deformations in the track (Heath et al. 1972; Li & Selig 1998; Li et al. 2016). The reliance on empirical expressions is primarily due to the complexity in the accurate prediction of the train-induced loads and the corresponding track response. The loads are complex combinations of moving static and dynamic components (as discussed in the previous sections). Moreover, the track structure increases this complexity manifolds since it comprises different layers with distinct properties.

Since the conventional design approaches are based on semi-empirical equations, they lack general applicability under different traffic loading and soil conditions. This severe limitation has become evident during the last few decades due to a rapid surge in transportation needs, which has amplified the geometry degradation of the existing tracks and incurred substantial maintenance costs (Nimbalkar & Indraratna 2016). Thus, there is an inevitable need for more reliable, practical and adaptable design methods to improve the performance of the railway tracks. Developing such an improved design technique requires a comprehensive analysis of the mechanical behaviour of track substructure layers and their mutual interaction. The subsequent section discusses the existing methods that can be employed to understand the behaviour of the ballasted railway tracks and investigate the influence of various factors that affect the track response.

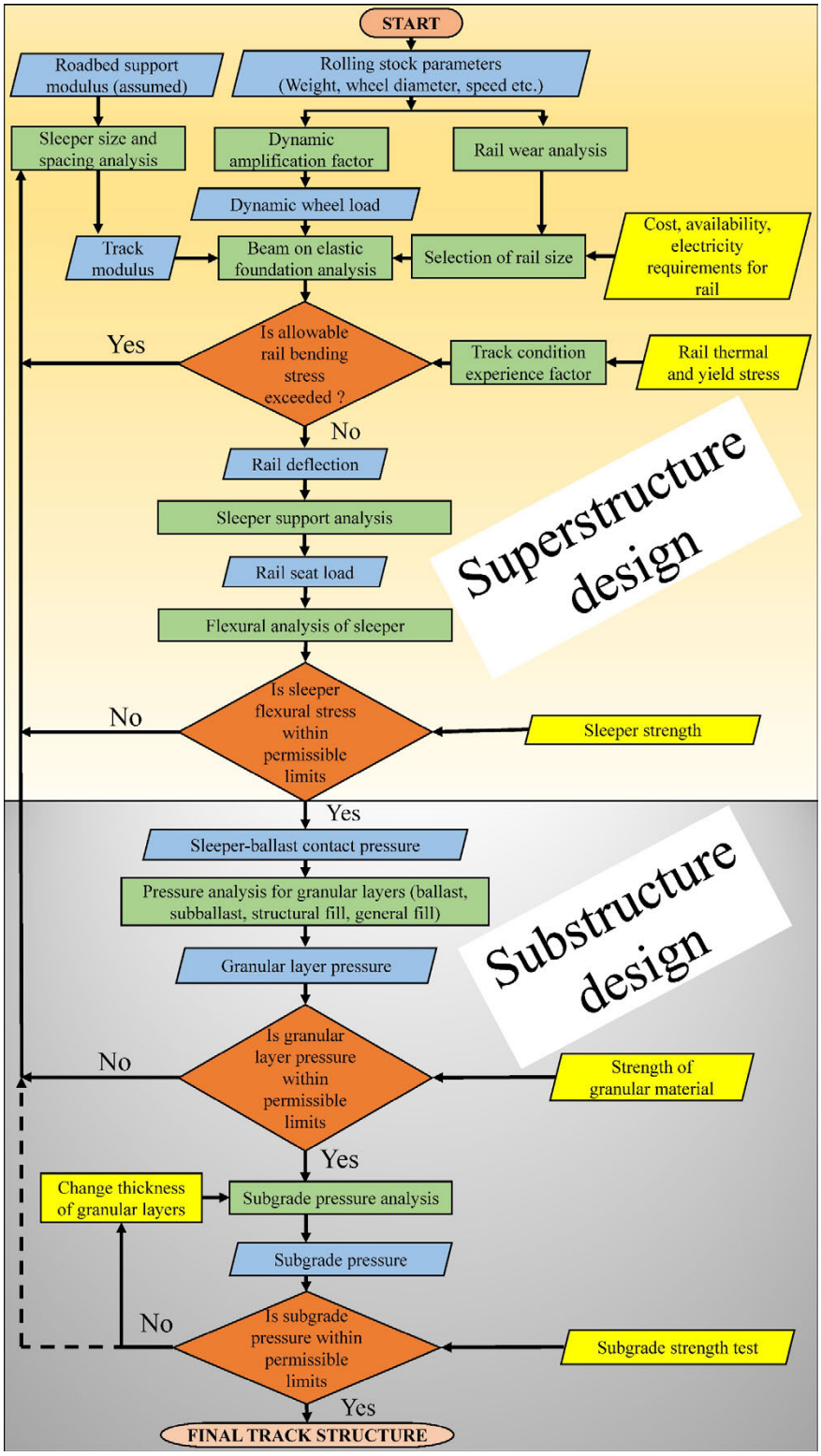

Figure 2.4 Flowchart for the design of conventional ballasted track [modified from Doyle (1980)]

2.3 Existing Approaches to Analyse Track Behaviour

2.3.1 Field Investigations

The field investigations are essential tools to understand the behaviour of individual substructure layers of a ballasted railway track and their mutual interaction. Consequently, several researchers have carried out field studies to measure the track response under train-induced loading (for e.g., Yoo & Selig 1979; Shahu et al. 1999; Kaynia et al. 2000; Degrande & Schillemans 2001; Gräbe et al. 2005; Chebli et al. 2008; Galvín & Domínguez 2009; Gräbe & Shaw 2010; Indraratna et al. 2010; Priest et al. 2010; Connolly et al. 2014; Nimbalkar & Indraratna 2016; Boler et al. 2018a). Usually, the displacements, acceleration and in-situ stresses are monitored at several positions within a track using advanced instrumentation methods. The instrumentation includes accelerometers, geophones, linear variable displacement transformers (LVDT), multi-depth deflectometers (MDD), pressure plates, remote video monitoring, settlement pegs and strain gauges.

Although field measurements provide invaluable insights into the response of ballasted railway tracks under train-induced repetitive loading, there are a few limitations associated with them. Firstly, a substantial amount of financial resources and time are required for long-term monitoring of the track behaviour. Consequently, only the transient response of the railway tracks during a train passage is recorded in most of the field studies. Secondly, the number of influencing factors in field investigations is too large for accurate parametric studies.

2.3.2 Numerical and Analytical Methods

The numerical and analytical approaches offer cost-effective alternatives to understand the behaviour of the substructure layers. The numerical methods such as boundary element method (BEM), discrete element method (DEM), finite difference method (FDM) and FE method are most commonly employed to simulate the dynamic response of the ballasted railway tracks.

The BEM can be used to study the propagation of waves generated due to the moving train loads in the soil. However, the modelling of irregular geometries and non-linear material behaviour in this method is problematic. To address this limitation, the BEM is

often coupled with FEM, wherein the track with complex geometry is modelled using FEM while the soil subgrade is simulated using BEM (e.g., O'Brien & Rizos 2005; Sheng et al. 2006; Galvín & Domínguez 2009; Galvín et al. 2014). Nonetheless, the prediction of track response (especially the evaluation of plastic deformation in the track substructure layers) using a coupled BE-FE approach is computationally expensive (Connolly et al. 2015).

Numerous researchers employed DEM to understand the geometry degradation mechanism in the ballasted railway tracks (e.g., Chen & McDowell 2016; Zhang et al. 2017; Bian et al. 2020). The DEM realistically captures the load distribution and particle level interactions in the substructure layers under the train-induced loading (Tutumluer et al. 2013; Gao et al. 2017). However, it can only be employed to study the behaviour of a small segment of a rail track due to the substantial amount of computational time required to perform DE analyses. In addition, the prediction of the long-term performance of a railway track (i.e., for load cycles in the order of millions) using DEM is impractical owing to the considerable computational effort associated with it.

The FDM has been used in the past to study the mechanism of ground vibrations and noise generated by the moving wheel loads (Thornely-Taylor 2004; Katou et al. 2008). This approach is much faster than the aforementioned techniques since a small track model is adequate for the analysis due to the use of high-performance absorbing boundary conditions. However, this method may perform poorly for problems involving complex geometries and free surfaces (Connolly et al. 2015). Furthermore, the prediction of track settlement using this method is quite challenging.

Several researchers have attempted to predict the track response using two-dimensional (2D) (e.g. Kuo & Huang 2009; Yang et al. 2009), two and a half dimensional (2.5 D) (e.g. Yang & Hung 2001; Costa et al. 2010; Hung et al. 2013; Galvín et al. 2018) and 3D FE analyses (e.g. Stewart & Selig 1982; Shahu et al. 1999; Hall 2003; Bian et al. 2010; Galvín et al. 2010; Banimahd et al. 2013; Connolly et al. 2013; Sayeed & Shahin 2016; Chen & Zhou 2018; Li et al. 2018). **Figure 2.5** shows the examples of 2D plane-strain, 2.5D and 3D FE models of the ballasted railway tracks. The 2D FE models are simple, require low computational effort and less time than the 2.5D or 3D FE models. The 2D models usually

involve a few input parameters and can be readily developed by practising engineers to solve complex problems. Although the 2D models may be appropriate for predicting the static response of the track, these models cannot accurately simulate the 3D loading due to train traffic, lateral spreading of the granular layers along the track transverse direction (for models simulating longitudinal track section) and complex geometries such as ballast profile, rail fasteners and three-dimensional geoinclusions (Powrie et al. 2007). To overcome these limitations, 3D FE models of the railway tracks can be used. However, the analyses involving 3D models may be computationally intensive and time-consuming. To reduce the computational demand of the 3D models, the 2.5D approach can be used. This method considers the 3D loading due to the train traffic while approximating the track structure using a 2D geometry [see **Figure 2.5(b)**]. This simplification in geometry is achieved by assuming the track structure as invariant along the longitudinal direction. The solution is then obtained in the frequency-wavenumber domain, requiring significantly less computational effort than the 3D approach. Nonetheless, the 2.5D approach ignores the discrete nature of the support in the ballasted railway tracks, which may affect the accuracy of the predictions. The prediction of inelastic deformations in the track layers using this method is also problematic.

In general, numerical modelling accurately simulates the dynamic behaviour of railway tracks and the wave propagation phenomenon. However, these models may require a relatively large amount of computational resources and time to accurately predict the accumulation of irrecoverable deformation in the substructure layers, especially when the number of load cycles is huge (in the order of millions) (Karlström & Boström 2006; Varandas et al. 2013). To reduce the computational time required, for e.g. in FE analyses, advanced explicit elastoplastic material models (Suiker & de Borst 2003; Indraratna & Nimbalkar 2013) can be used; however, these models typically require 10–15 input parameters to simulate the behaviour of granular layers accurately.

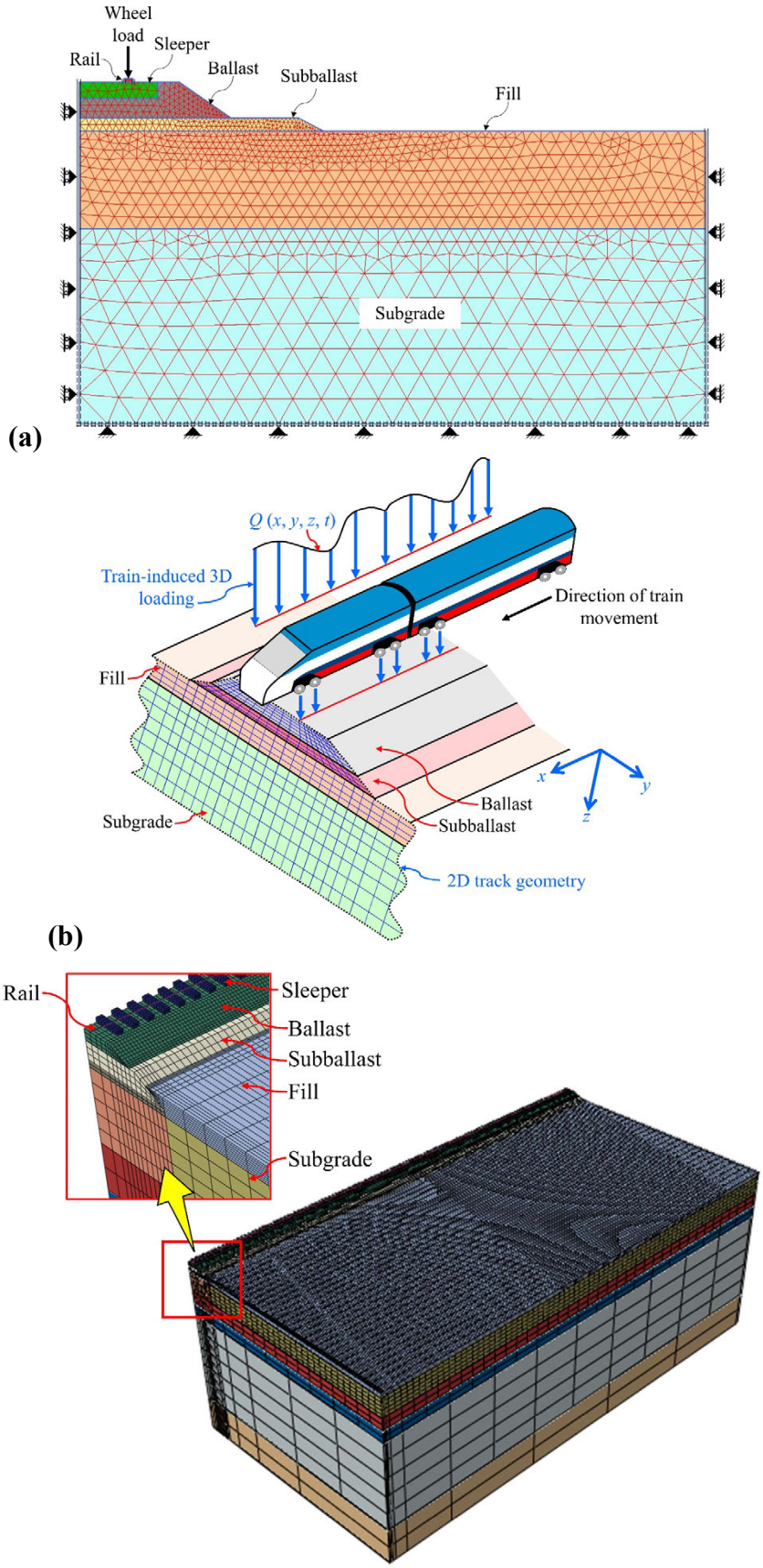

Figure 2.5 Examples of **(a)** 2D plane-strain; **(b)** 2.5D; **(c)** 3D FE model of ballasted railway tracks

In contrast to numerical modelling, analytical techniques are comparatively faster and may also facilitate the interpretation of results obtained from numerical analyses. Therefore, several analytical models have been developed to predict the behaviour of railway tracks under train-induced repeated loading. These models range from a simple beam on elastic foundation (BoEF) approach (Winkler 1867; Esveld 2001) to advanced 3D vehicle-track coupled models (e.g. Zhai et al. 2009; Guo & Zhai 2018) (see **Figure 2.6**). Usually, the substructure in analytical models is either represented using equivalent springs and/or dashpots (Chen & Huang 2000; Basu & Kameswara Rao 2013), as a homogenous or multi-layered half-space (Dieterman & Metrikine 1997; Metrikine & Popp 1999; Kaynia et al. 2000; Takemiya & Bian 2005) or a combination of multi-layered half-space, springs and/or dashpots (Sheng et al. 1999). The representation of substructure as an equivalent spring may predict the overall track response; however, it neglects the mutual interaction between the substructure layers. This negligence may negatively affect the accuracy of the predictions. Thus, the computational models for predicting the track response must consider the actual multi-layered structure of the railway track and include the mutual interaction between the various substructure layers. This research gap has been addressed in the present study by considering three substructure layers, viz. ballast, subballast and subgrade.

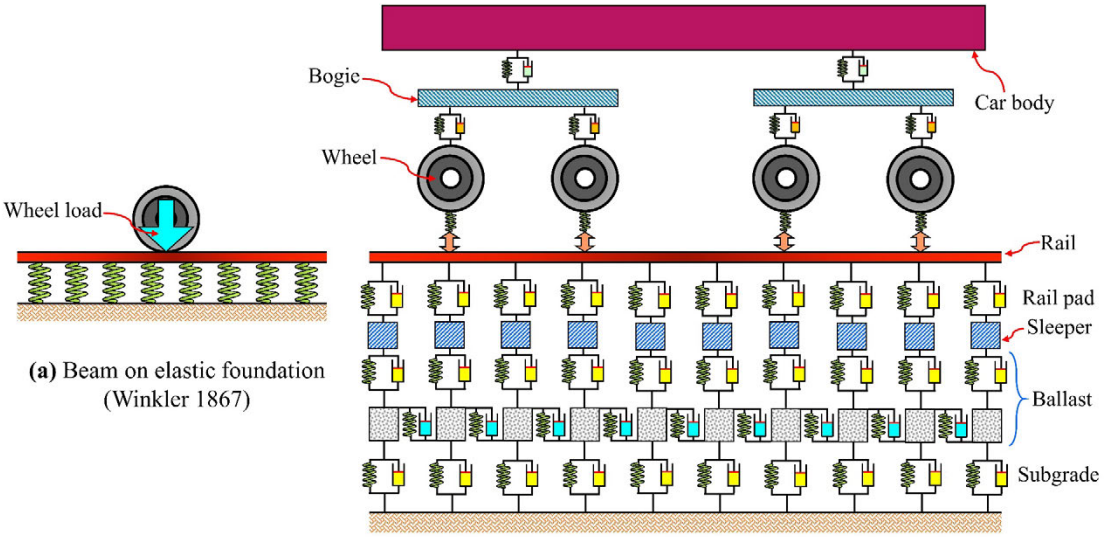

(a) Beam on elastic foundation (Winkler 1867)

(b) Vehicle-track coupled model (Zhai et al. 2009)

Figure 2.6 (a) Beam on elastic foundation model; **(b)** Vehicle-track coupled model

A few researchers represented the ballast and/or subballast layers as individual masses connected by springs and dashpots (Sun & Dhanasekar 2002; Zhai et al. 2004).

Choudhury et al. (2008) employed a two-degree of freedom mass-spring-dashpot model to study the response of different subgrade soils below a railway track under cyclic loading conditions. However, their approach neglected the role of subballast in the track response and also ignored the continuity of the substructure layers along the longitudinal direction. Nevertheless, a limited number of approaches have captured the irrecoverable deformation in the individual substructure layers under train-induced repeated loads. Thus, there is an inevitable need for a methodology that can provide an insight into the deformation of the individual substructure layers of a ballasted rail track, their mutual interaction and the influence of substructure layer properties on track response under train-induced repeated loads. CHAPTER 3 of this thesis addresses this research gap and describes the development of a novel methodology to predict the transient and long-term behaviour of a typical ballasted rail track.

The existing approaches predominantly rely on empirical models based on extensive field and laboratory investigations to predict the accumulation of irrecoverable deformation in the substructure layers (Lekarp et al. 2000; Dahlberg 2001; Indraratna & Nimbalkar 2013). However, these models lack a rational theoretical basis with a limited application domain. Nevertheless, laboratory tests are often restricted in size due to financial constraints. Meanwhile, the cost and the number of influencing factors in field investigations is too high for accurate parametric studies. Therefore, there is an immediate need for a mechanistic approach to predict the cumulative deformations occurring in the track substructure layers. CHAPTER 3 (Part-B) of this thesis addresses this research gap and illustrates the development of a mechanistic approach for predicting the deformations in the substructure layers under train-induced repeated loading.

The subsequent sections of this chapter discuss the critical zones in the railway tracks, the associated problems, potential causes, remedial measures and existing modelling techniques.

2.4 Critical Zones in Railway Tracks

As discussed in CHAPTER 1, the critical zones are the regions that are susceptible to differential settlement due to an abrupt change in stiffness, damping and support conditions. These zones exhibit a rapid degradation in track geometry, wear and tear in

the superstructure and vehicle components and poor ride quality (Li & Davis 2005; Stark & Wilk 2015; Wang et al. 2018). Consequently, these regions require frequent maintenance, which is costly and also reduces operational efficiency of rail tracks. The critical zones may also be subjected to speed restrictions to ensure the safety of operations (Boler et al. 2018b). **Figure 2.7** shows an example of a transition zone near the bridge or underpass approach. A railroad vehicle experiences an abrupt change in the track stiffness while approaching a bridge or underpass. This change leads to an amplification of the dynamic loads induced by the train-track interaction. This amplification in load causes differential settlement and damage to the track and wheel components.

Numerous techniques have been proposed to mitigate the problems associated with the critical zones. However, no unique solution exists due to the site-specific nature of the problem. Thus, it is essential to understand the behaviour of the critical zones before applying an adequate mitigation measure. To understand the phenomenon, several researchers have conducted field investigations and have identified the probable causes of the critical zone problems. Some of the causes are described in the subsequent section.

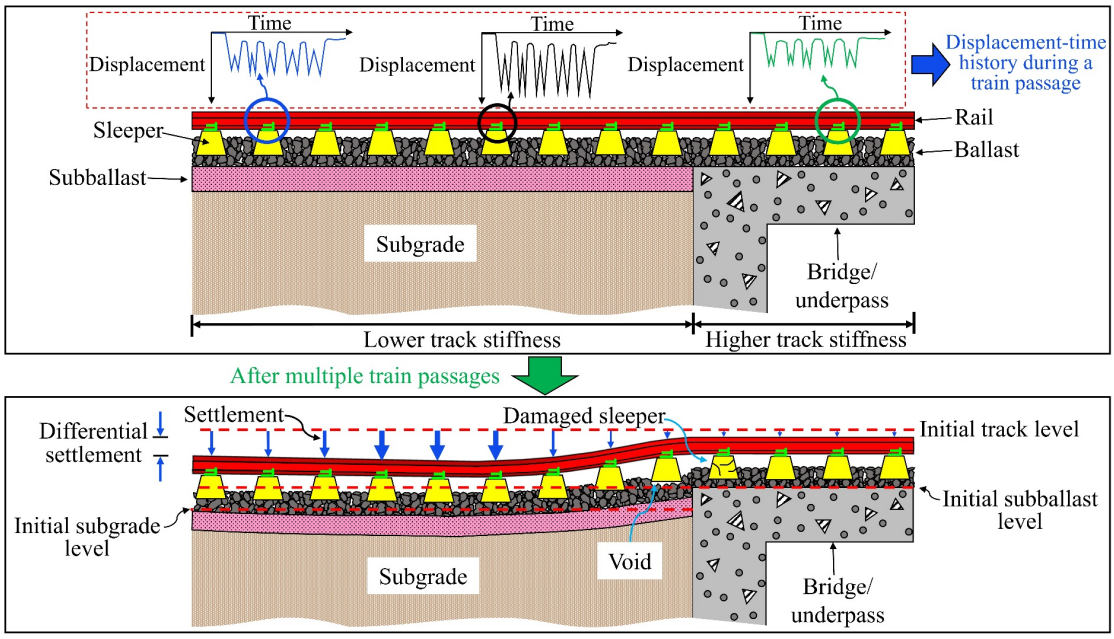

Figure 2.7 Transition zone between an open track and stiff structure such as a bridge or underpass

2.4.1 Major Causes of Transition Zone Problems

The problems associated with the transition zones are most commonly attributed to two main reasons:

- An abrupt change in the track stiffness that increases the vertical acceleration of the wheel and car body, thereby increasing the dynamic wheel load (Kerr & Moroney 1993; Boler et al. 2018b). The stiffness variation between the stiffer and softer side in a transition zone can be as high as two times (Ribeiro et al. 2017).
- The natural tendency of the track founded on the soft subgrade to undergo larger settlement than the track laid on stiff structure (such as bridge, tunnel or culvert), for the same magnitude of load. This phenomenon leads to differential settlement at the transition zone, which increases the dynamic loads on the track (Stark & Wilk 2015). The increased dynamic loads further enhance the differential settlement and accelerate the track geometry degradation. Thus, the initial differential settlement triggers the self-perpetuating cycle of increased dynamic loads and subsequent differential settlement. The magnitude of damage caused due to existing settlement in the track is often considered greater than that caused due to an amplification in the dynamic wheel load (Boler et al. 2018b).

In addition to these basic causes, the problems in the transition zones may also arise due to the following reasons:

- The presence of hanging sleepers in the transition zone. It has been observed that the quality of sleeper support affects the distribution of loads transmitted to the track substructure (Stark & Wilk 2015). The loads are uniformly distributed in the case of good sleeper support. However, in the case of poor sleeper support (i.e. for hanging sleepers), the sleepers adjacent to the poorly supported ones are subjected to a higher magnitude of the load. This load redistribution damages the track components and accelerates the track geometry degradation (Wang et al. 2018). Moreover, the presence of a hanging sleeper generates impact loads due to the momentum of the moving sleeper hitting the ballast (Stark & Wilk 2015).
- Geotechnical factors such as inadequate drainage of subgrade, use of inferior quality materials in the track, poor initial compaction and consolidation of embankment materials, lack of adequate confinement of granular materials, ballast fouling and

ballast penetration into the subgrade (Li & Davis 2005; Stark & Wilk 2015; Wang et al. 2018).

Thus, the problem associated with the transition zones may be caused due to a large number of factors. The success of a particular mitigation measure depends on the accurate identification of the causative factors.

2.4.2 Factors Affecting Track Deterioration

The track deterioration in the transition zone depends on a large number of factors. These factors include speed and direction of the train, the distance between adjacent axles and bogies, existing differential settlement in the track, presence of hanging sleepers, permanent rail deformation and irregularity in lateral alignment (Li & Davis 2005; Banimahd et al. 2012; Stark et al. 2016; Wang & Markine 2018b). The train speed and existing differential settlement in the track significantly influence the magnitude of dynamic wheel load. The dynamic wheel load usually increases with an increase in train speed and the magnitude of differential settlement (Wang & Markine 2018b). Therefore, the problem of transition zones may be more serious for high-speed rail where the train speed usually exceeds 200 km/h (López-Pita et al. 2007). In fact, the problem of differential settlement near the bridge-open track transition zone is gradually emerging in the Chinese high-speed rail lines (Shan et al. 2017).

The train direction may also play a significant role in the behaviour of the transition zone. The movement of a train from the softer to the stiffer side of the transition usually causes higher settlement than that caused by stiffer to softer side movement (Wang & Markine 2018b). However, few researchers reported that the problem of differential settlement is more significant when the train moves from the stiffer to the softer side of the transition, whereas the movement in the opposite direction causes wear and tear in the superstructure components (Mishra et al. 2012). When the train moves from the stiffer side to the softer side, the amplified dynamic wheel load is applied to the softer side that accelerates the settlement. In the opposite case (i.e. movement from softer to stiffer side), the dynamic load gets amplified in the stiffer side, causing an impact that leads to deterioration of superstructure components (Read & Li 2006). Furthermore, the deterioration in track geometry does not remain concentrated at a specific location, but it propagates away from the stiffer zones with time.

Thus, a large number of factors affect the degradation of track geometry at the transition zone. However, the quantification of the influence of each factor is necessary for the selection and design of an appropriate mitigation measure.

2.4.3 Field Investigations

The field investigations are essential tools for understanding the behaviour of the transition zones. These studies also provide valuable data which may be used for validating the numerical or analytical models. The field investigations related to transition zones are rather scarce. Li & Davis (2005) investigated four bridge-embankment transition zones and observed that an abrupt change in stiffness in the transition zone accelerated the track geometry degradation and caused cracking in concrete sleepers. Moreover, the ballast and subballast layers contributed significantly to the overall track geometry degradation. It was observed that the mitigation measures such as geocells, hot-mix asphalt (HMA) layer, and cement-stabilised backfill were ineffective in alleviating the problem. This behaviour was obvious because these techniques were used to improve the stiffness and bearing capacity of the subgrade, while the track geometry degradation problem was due to the ballast and subballast layers.

Coelho et al. (2011) investigated an embankment-culvert transition zone that employed a reinforced concrete approach slab to mitigate track geometry degradation. The study revealed that the track in the transition zone suffered significantly higher settlement than that on the culvert. The use of reinforced concrete approach slab further exacerbated the settlement problem in the transition zone rather than mitigating it. This observation was attributed to a significant contribution of the subgrade soil to the overall settlement of the track. Stark & Wilk (2015) investigated three bridge approaches that had experienced track geometry degradation in the past to identify the probable factors for the problem. They observed a significant contribution of the ballast layer to the overall settlement. Wang et al. (2018) measured the dynamic displacement of the railway track at multiple locations to give a profile of the track displacement, i.e. the extent of the zone for differential settlement (or ‘dip’). They observed that the length of ‘dip’ varies from one place to another depending on the subgrade properties, structure type (bridge, culvert, and tunnel), train configuration, among others.

It is apparent from the field investigations that the root cause of the problem must be identified before the application of an appropriate mitigation measure. Another important aspect is to quantify the relative contribution of each track layer (ballast, subballast or subgrade) to the overall settlement. This quantification is vital for selecting an adequate mitigation strategy since a mitigation measure that improves the subgrade strength and stiffness may not be successful if the problem exists with the ballast or vice versa.

2.4.4 Mitigation Techniques

Numerous techniques have been developed to mitigate the track geometry problems near the transition zones. It is essential to understand the root cause of the problem before applying a suitable countermeasure. The track geometry degradation in a transition zone may occur due to the presence of hanging sleepers, irrecoverable deformation in the ballast, subballast and subgrade. Thus, it may be possible that multiple design features need to be applied instead of a single technique. Ideally, the track-transition problem can be solved using the following four steps (Li & Davis 2005):

- Problem identification: it involves field investigations to obtain the severity of the damage, rate of deterioration of track geometry and costs associated with its maintenance.
- Mechanism: it involves understanding the cause of the degradation, i.e. identifying whether the degradation is due to an abrupt change in stiffness, geotechnical issues or other factors.
- Mitigation: identification or selection of a suitable mitigation technique from the available strategies including (but not limited to) the use of geosynthetics, hot-mix asphalt layer below the ballast, ground improvement techniques to improve the stiffness and strength of subgrade, approach slabs, polyurethane geocomposites, confinement walls and transition wedges.
- Implementation and monitoring: implementation of the mitigation measure and monitoring its effectiveness.

The degradation of track geometry in a transition zone primarily occurs due to an abrupt change in the vertical acceleration of wheels and cars, which may be caused due to an existing differential settlement or stiffness difference. Thus, the mitigation measures are designed to decrease the stiffness difference in the transition zone by either increasing the

stiffness of the softer side, reducing the stiffness of the stiffer side or providing a smooth transition of stiffness (Kerr & Moroney 1993). The stiffness on the softer side can be increased by using geocell, hot-mix asphalt layer, geocomposites, geogrids, cement grouting or other ground improvement techniques (Mishra et al. 2012). Similarly, the stiffness on the stiffer side can be reduced by employing rail pads, sleeper underpads, ballast mats, and plastic sleepers. The problem with this technique is that the stiffness of the stiffer side remains higher than the softer side. Consequently, the recurring problem of differential settlements starts once the substructure on the softer side begins to displace permanently. Nevertheless, a smooth transition in the stiffness can be provided by using geocells, reinforced concrete approach slabs and wedge-shaped transition zones in backfill (Paixão et al. 2015a). In high-speed railways, a technical block is provided between the open track and the structure (such as bridge abutment) to provide a smooth stiffness transition (Ribeiro et al. 2017). The technical block comprises two wedges, one made up of cement-treated aggregates, and the other is made up of compacted granular material. The wedge comprising cement-treated aggregates is provided next to the structure, while the second wedge is provided between the open track and the first wedge.

Recent studies have shown that the formation of the sleeper-ballast gap can also cause significant degradation in track geometry (Stark & Wilk 2015). Thus, its formation must be prevented through proper design of the transition zone. If the gap is formed, stone blowing may be employed to fill the gap and prevent subsequent damage (Boler et al. 2018b). However, it may not be a permanent solution as the small particles inserted below the sleepers may penetrate the voids of larger ballast particles.

2.4.5 Modelling of Transition Zones

Although field investigations help in understanding the behaviour of the transition zones, these are time-consuming and costly. An alternative to the field studies is the experimental investigation which involves the simulation of the real field problem at a small scale to understand the governing parameters and the mechanism involved. However, it is also time-consuming and costly. Numerical and analytical approaches offer cost-effective alternatives to understand and quantify the influence of each parameter on the overall response of the track in the transition zone.

As discussed in Section 2.3, several numerical and analytical models have been developed to study the behaviour of open or standard railway tracks. However, the models for studying the behaviour of the tracks in critical zones are rather scarce. **Table 2.3** provides a summary of the existing modelling approaches used for studying the behaviour of critical zones. Metrikine et al. (1998) studied the wave generation due to the movement of a constant load along the track in a critical zone. They modelled the track as a string resting on an inhomogeneous elastic foundation subjected to a moving vertical load. Dimitrovová & Varandas (2009) studied the vibrations generated in the track and ground due to the movement of high-speed trains over the critical zones. They considered the track as Euler-Bernoulli's beam on a viscoelastic foundation and developed an analytical solution for predicting the dynamic response of the track supported by inhomogeneous foundation subjected to a moving load.

Lundqvist & Dahlberg (2005) investigated the influence of unsupported sleepers on the behaviour of the railway tracks using the commercial FE program LS-DYNA. They observed that the presence of hanging/unsupported sleeper might increase the sleeper-ballast contact force below the adjacent sleeper by 70%. This effect is exacerbated with an increase in train speed. However, they modelled the ballast bed as an elastic continuum which may not represent the ballast accurately. Galvín et al. (2010) studied the behaviour of a transition zone between ballasted and slab track using 3D coupled FEM and BEM. They predicted the ground/track vibrations produced due to the passage of a train in the ballasted-slab track transition. However, they assumed the subgrade as an elastic half-space and neglected the irrecoverable deformations that may occur in the subgrade.

Mishra et al. (2014a) employed DEM to simulate the dynamic behaviour of the railway track transitions numerically. They predicted the distribution of acceleration within the ballast layer and concluded that the assignment of a single value of acceleration to the entire ballast layer might lead to incorrect predictions of dynamic track behaviour. However, they considered the boundary below the ballast layer to be rigid, which may significantly influence the results.

Table 2.3 Summary of the existing modelling techniques for critical zones

Reference	Model type	Findings	Limitations
Hunt (1997)	Winkler type model coupled with an empirical model	Settlement is primarily governed by the action of static axle loads while the dynamic component of load controls local effects	Material plasticity is captured using empirical equations
Metrikine et al. (1998)	Analytical model	Wave generation depends on the stiffness difference between softer and stiffer sides	Neglected inelastic deformations
Lei & Mao (2004)	2D FE model	Excessive settlement of the softer side is the primary cause of transition zone problems	Material behaviour is considered elastic
Li & Davis (2005)	3D FE model	Large stiffness change causes marginally higher (6%) dynamic load variation	Simplified track model
Lundqvist & Dahlberg (2005)	3D FE model	Hanging sleeper increases the contact pressure at adjacent sleeper by 70%	Material behaviour is considered elastic
Read & Li (2006)	2D FE model	Resilient pads effective only for stiff subgrades	Considered only a single wheel load
Namura & Suzuki (2007)	Analytical model	Hanging sleepers significantly increase differential settlement	Subgrade is assumed to be rigid
Dimitrovová & Varandas (2009)	Analytical model	Softer to stiffer zone movement generates more vibration than reverse movement	Vibration analysis
Galvín et al. (2010)	3D FE model	Soft rail pads on the softer side of the critical zone reduce excessive vibration	Material behaviour is considered elastic
Banimahd et al. (2012)	3D coupled FE model	An abrupt change in stiffness may not cause significant load amplification	Material behaviour is considered elastic
Mishra et al. (2014a)	Fully coupled 3D dynamic model	Characterisation of ballast layer as a continuum may lead to erroneous predictions	Subgrade is assumed to be rigid
Shahraki et al. (2015)	3D FE model	Subgrade properties significantly influence the dynamic behaviour	Ignored vehicle-track interaction
Wang & Markine (2018c)	3D FE model coupled with an empirical model	Track geometry degradation spreads from stiffer to softer zones	Neglected irrecoverable subgrade deformation
Shan et al. (2020)	3D FE model coupled with an empirical model	Increase in axle load accelerates the track geometry degradation	Material plasticity is captured using empirical equations

Shahraki et al. (2015) studied the dynamic behaviour of a ballasted-slab track transition zone (with mitigation measures) under the passage of a high-speed train using commercial FE software ANSYS. They observed that the use of auxiliary rails improves the behaviour

of the transition zone. However, they ignored the vehicle-track interaction. Wang & Markine (2018c) combined the FE method (to evaluate transient response) with an empirical model (to predict cumulative track settlement) to study the long-term behaviour of the transition zones. They observed that the vertical settlement in the transition zone does not concentrate at a specific location but spreads away from the stiffer side due to the redistribution of stresses. However, they only considered the irrecoverable deformation in the ballast and neglected the irrecoverable deformation in subballast and subgrade layers. Shan et al. (2020) used a similar procedure (combined FEM and empirical model) to predict the accumulation of irrecoverable deformation in a transition zone.

Thus, several analytical and numerical models have been developed to investigate the dynamic behaviour of transition zones. However, most of these studies dealt with the track and ground vibrations generated due to the movement of trains along the transition zones and neglected the material plasticity. Only a few studies dealt with the irrecoverable deformation of the track layers, the influence of speed on the track behaviour, lateral deformation in the track layers and long-term behaviour of the transition zones. Nonetheless, the irrecoverable deformation in the past studies was captured using empirical settlement equations, which lack general applicability under different loading conditions and soil types. Thus, there is an urgent need for an adequate computational methodology that can mechanistically predict the long-term behaviour of the transition zones and assess the adequacy of various strategies for improving the track performance. CHAPTER 4 of this thesis addresses this research gap and proposes a novel methodology for predicting the response of the transition zones in railway tracks under train-induced repeated loads.

2.5 Effect of Principal Stress Rotation

As a train passes a particular section of the railway track, a soil element within the substructure experiences complex stress paths that involve a rotation of the principal stress directions (Brown 1996). This PSR is linked with a shear stress reversal experienced by the soil elements during the train passage. The repetitive loading (due to multiple train wheels) along with PSR (due to wheel movement) can influence the accumulation of inelastic deformations in the track substructure layers. Several

researchers have investigated the effect of PSR on geomaterials using hollow cylinder torsional shear device (e.g., Hight et al. 1983; Symes et al. 1988; Wijewickreme & Vaid 2008; Gräbe & Clayton 2009; Guo et al. 2018), cyclic simple shear apparatus (Ansell & Brown 1978; McDonald & Raymond 1984) or directional shear cell (Wong & Arthur 1986). These studies found that PSR significantly influences the rate of accumulation of inelastic strain in geomaterials, with the rate being higher for some soils when subjected to repeated loading with PSR than when only repeated loading is applied. In addition, the reduced scale model test results revealed that the moving wheel load (with PSR) caused a much larger track settlement as compared to the case when the wheel load was applied only at a fixed point (i.e., without PSR) (Momoya et al. 2005; Ishikawa et al. 2011). Thus, it is apparent that PSR causes additional deformation in the geomaterials, which may contribute to the degradation of the track geometry. Therefore, the effects of PSR must be carefully considered while predicting the response of a track subjected to moving train loads.

As discussed in previous sections, the computational models are the most appropriate and economically viable tools to understand the behaviour of railway tracks under various soil types, loads, and boundary conditions. Several numerical and analytical methods with different levels of complexity are available to predict the behaviour of railway tracks subjected to repeated train loading (see Sections 2.3.2 and 2.4.5). However, most of the existing methodologies disregard the influence of PSR on track response, which may compromise the accuracy of the predictions. Therefore, substantial efforts are still required to incorporate this critical aspect of soil behaviour in the computational models. CHAPTER 5 of the thesis addresses this research gap by incorporating the effect of PSR on the track response in the novel computational method.

2.6 Discussion

The literature review reveals that the behaviour of a ballasted railway track results from a complex interaction of its superstructure and substructure components in response to the train-induced loads. These loads are exerted in the track in the vertical, longitudinal and lateral directions, with vertical loading being predominant in a straight track. The vertical load is a combination of moving static and dynamic components. The dynamic part is commonly represented as a factor, which is multiplied to the static wheel load. Due

to inherent complexity in the accurate prediction of the train-induced loads and the corresponding track response, the existing design approaches rely on empirical and simplified theoretical approaches that are based on experience with in-service tracks, augmented with extensive laboratory and field testing. To derive optimum performance from the railway tracks, there is an imminent need for more accurate and adaptable design techniques. The development of such a design technique requires a detailed analysis of the behaviour of track substructure layers.

Indeed, the response of a ballasted railway track to train-induced repeated loading depends on the behaviour of individual track layers and their mutual interaction. Several numerical and analytical approaches with varying degree of complexity have been developed to evaluate the behaviour of a railway track. However, a limited number of studies have captured the irrecoverable deformation in the individual substructure layers under train-induced repeated loads. Apparently, more work is required to develop a methodology that can quickly evaluate the transient as well as the long-term performance of the ballasted railway tracks.

It is also apparent that a clear understanding of the behaviour of railway tracks in transition zones is inevitable to reduce the track maintenance requirements or to plan the maintenance cycles. Numerous techniques have been developed to mitigate track degradation in the transition zones. However, these zones still exhibit poor performance. In some cases, the mitigation measures even exacerbated the track geometry degradation problem. The reason is a limited understanding of the behaviour of the tracks in the transition zones.

Field investigations in the transition zones have revealed several causative factors associated with the problem. However, the number of such investigations is rather scarce due to the high cost and time-consuming nature. Similarly, the number of laboratory investigations related to the transition zones are limited. Numerical and analytical approaches offer cost-effective alternatives to field and laboratory investigations to study the behaviour of the transition zones. However, the modelling of the railway tracks and the moving train load is very complex. This complexity is further enhanced by the non-linear behaviour of the geomaterials and the vehicle-track interaction. Thus, there is an

urgent need to develop simple yet accurate analytical and numerical models that can realistically capture the behaviour of the railway tracks in the transition zone. The models must be able to quantify the effect of all the contributing parameters on the overall track response and help in the selection and design of an appropriate mitigation measure. Moreover, the models must predict the long-term performance of the transition zone, which is essential for planning the maintenance cycle.

Thus, the following research gaps have been identified:

1. There is a lack of an apt computational methodology for a rapid and reliable prediction of the long-term performance of the ballasted railway tracks.
2. The existing approaches use empirical methods to evaluate the plastic deformation in the track layers. The empirical approaches lack a detailed rational theoretical basis, and their application is often limited to specific conditions on which they are based.
3. The actual multi-layered structure of the ballasted railway track and the mutual interaction between the various substructure layers is neglected in most of the existing analytical approaches, which may negatively affect the accuracy of the predictions.
4. An appropriate methodology that can predict the long-term performance of the critical zones with heterogeneous support conditions along the track length is relatively scarce. Prior knowledge of the magnitude of deformation anticipated in the track transitions could significantly assist the rail infrastructure managers in planning the maintenance operations and seeking appropriate techniques to minimise the problem.
5. The behaviour of soil subgrade is not properly addressed in the computational models for critical zones. The subgrade greatly influences the stability of the tracks in the transitions. The difficulty in identifying the problems associated with the subgrade by visual inspections makes the study inevitable. Moreover, the problems associated with the subgrade are more challenging to solve than those associated with the ballast, subballast or superstructure components.
6. The effect of principal stress rotation experienced by the soil elements due to moving wheel loads on the cumulative track deformation is disregarded in the existing computational models.
7. There is a lack of an adequate tool for quantifying the magnitude of improvement offered by different countermeasures. Such a tool may allow a rational comparison of

various strategies and assist the practising railway engineers in identifying the most appropriate alternative for improving the performance of a transition zone.

8. The influence of axle load, train speed and substructure properties on the performance of the transition zones are not entirely understood.
9. There is a lack of a proper guideline for selecting an adequate mitigation measure against a particular transition zone problem.

The subsequent chapters seek to address these research gaps and improve the accuracy of the existing computational models for evaluating the performance of ballasted rail tracks, especially at the transition zones (refer to section 1.3 for more details regarding the treatment of research gaps).

CHAPTER 3 (PART-A)
ANALYTICAL EVALUATION OF A BALLASTED RAILWAY TRACK RESPONSE UNDER REPEATED TRAIN LOADS

3.1 General

The ballasted railway track is a complex engineering structure that consists of two primary components: substructure and superstructure. The substructure comprises of ballast, subballast, structural fill, general fill and subgrade layers whose behaviour governs the track performance and maintenance requirements (Selig & Waters 1994). These substructure layers undergo resilient (elastic) as well as irrecoverable deformation under the application of train-induced repeated loads. The differential settlement produced due to non-uniform irrecoverable deformation in these layers is detrimental for track stability as it demands frequent maintenance cycles, increases the dynamic wheel-rail interactions and leads to poor riding quality (Esveld 2001). A hike in traffic volume, speed and axle loads on railway tracks has increased the stresses and deformations in the substructure layers (Priest et al. 2010; Nimbalkar & Indraratna 2016). Consequently, the frequency of maintenance cycles has increased to meet this ever-increasing demand. These maintenance operations require substantial financial investments due to the lack of proper planning and poor diagnosis of the track geometry degradation problems (Nguyen et al. 2016). Therefore, the accurate prediction of the behaviour of individual track layers is imperative to plan and reduce the frequency of maintenance operations.

This chapter presents a novel methodology to evaluate both the resilient and irrecoverable responses of the track substructure layers under train-induced repetitive loads. The resilient response is evaluated by modelling the substructure layers as lumped masses connected by springs and dashpots. The irrecoverable response is evaluated using the empirical settlement models for ballast, subballast and subgrade. The present model provides an insight into the deformation of the individual substructure layers, their mutual interaction and the influence of substructure layer properties on track response. The accuracy of the present method is validated by comparing the predicted results against the field investigation data reported in the literature. The present methodology is simple, computationally efficient and can readily be used to predict the cumulative track deformations. Consequently, the long-term performance of the tracks can be evaluated.

3.2 Methodology for Prediction of Track Settlement

The present study employs an integrated approach that combines three models as illustrated below:

- Track loading model: this model evaluates the train-induced repetitive loads that act on the top of the ballast layer.
- Track resiliency model: this model determines the resilient response of the track layers to the repeated train loading in terms of displacement, velocity and acceleration time histories.
- Track settlement model: this model evaluates the cumulative settlement in the substructure layers due to repeated passage of trains.

The main assumptions in the proposed method are:

- The distribution of vertical load from the sleeper to the substructure layers is pyramidal.
- No-slip condition exists for the ballast-subballast and subballast-subgrade interfaces.
- The track structure is symmetric with respect to the track centreline.
- The substructure layers overlay the bedrock.

3.2.1 Track Loading Model

In the ballasted railway tracks, the train-induced repetitive loads are transferred to the substructure layers through the sleeper-ballast contact. The sleeper-ballast contact force at each sleeper location varies with time during the train passage. This force can be evaluated by using the BoEF method. In this approach, the railway track is considered as an Euler-Bernoulli beam resting on an elastic foundation and the governing differential equation for the displacement of the beam is given by (Esveld 2001):

$$E_{\mathrm{r}}I_{\mathrm{r}}\frac{d^4w(x)}{dx^4} + kw(x) = 0 \qquad 3.1$$

where E_{r} and I_{r} are Young's modulus (N/m^2) and the moment of inertia of the rail (m^4), respectively; $w(x)$ is the vertical track deflection (m) at a distance 'x' (m) along the longitudinal direction as shown in **Figure 3.1**. The vertical deflection due to Q (located at $x = 0$) can be evaluated by solving Equation 3.1 under the boundary conditions $w(\infty) = 0$, $w'(0) = 0$ and $w'''(0) = Q/(2E_{\mathrm{r}}I_{\mathrm{r}})$ as:

$$w(x) = \frac{Q}{2kL} e^{-\left(\frac{x}{L}\right)} \left[\cos\left(\frac{x}{L}\right) + \sin\left(\frac{x}{L}\right)\right] \quad 3.2$$

where L is the characteristic length (m) [$L = (4E_rI_r/k)^{1/4}$]. The term $kw(x)$ in Equation 3.1 represents the reaction force per unit length provided by the track to the rail. Since the rail is supported at discrete locations by the sleepers, the reaction force provided by each rail seat (i.e., the rail seat load) can be calculated by multiplying $kw(x)$ with the sleeper spacing [S (m)].

As the BoEF approach (Equation 3.2) considers the downward deflection to occur within a distance of $-3\pi L/4$ to $3\pi L/4$ from the point of load application (Esveld 2001), the rail seat load at a particular time instant due to a single wheel can be calculated for all sleepers lying within this range. Subsequently, the variation of rail seat load [$Q_{r,n}(t)$] with time due to the cumulative train loading can be calculated using the superposition principle as:

$$Q_{r,n}(t) = Sk \sum_{j=1}^{a_t} w(x_{nj}, t) \quad 3.3$$

where $Q_{r,n}$ (t) is the total rail seat load (N) at n^{th} sleeper at time t (i.e. sleeper–ballast contact force); a_t denotes the total number of wheels under consideration; x_{nj} is the distance (m) between the n^{th} sleeper and j^{th} wheel. **Figure 3.1** illustrates an example to calculate the rail seat load-time history at a sleeper due to the passage of Thalys high-speed train travelling at a speed of 100 km/h. Thalys high-speed train operates on the European high-speed rail corridor with a maximum speed of 300 km/h. It is assumed that the rail and the wheels are free from defects, and the subgrade is stiff. A stiff subgrade is usually characterised by a high value of resilient modulus (69 MPa – 138 MPa) and high compressive strength (207 kPa – 345 kPa) (Li et al. 2016).

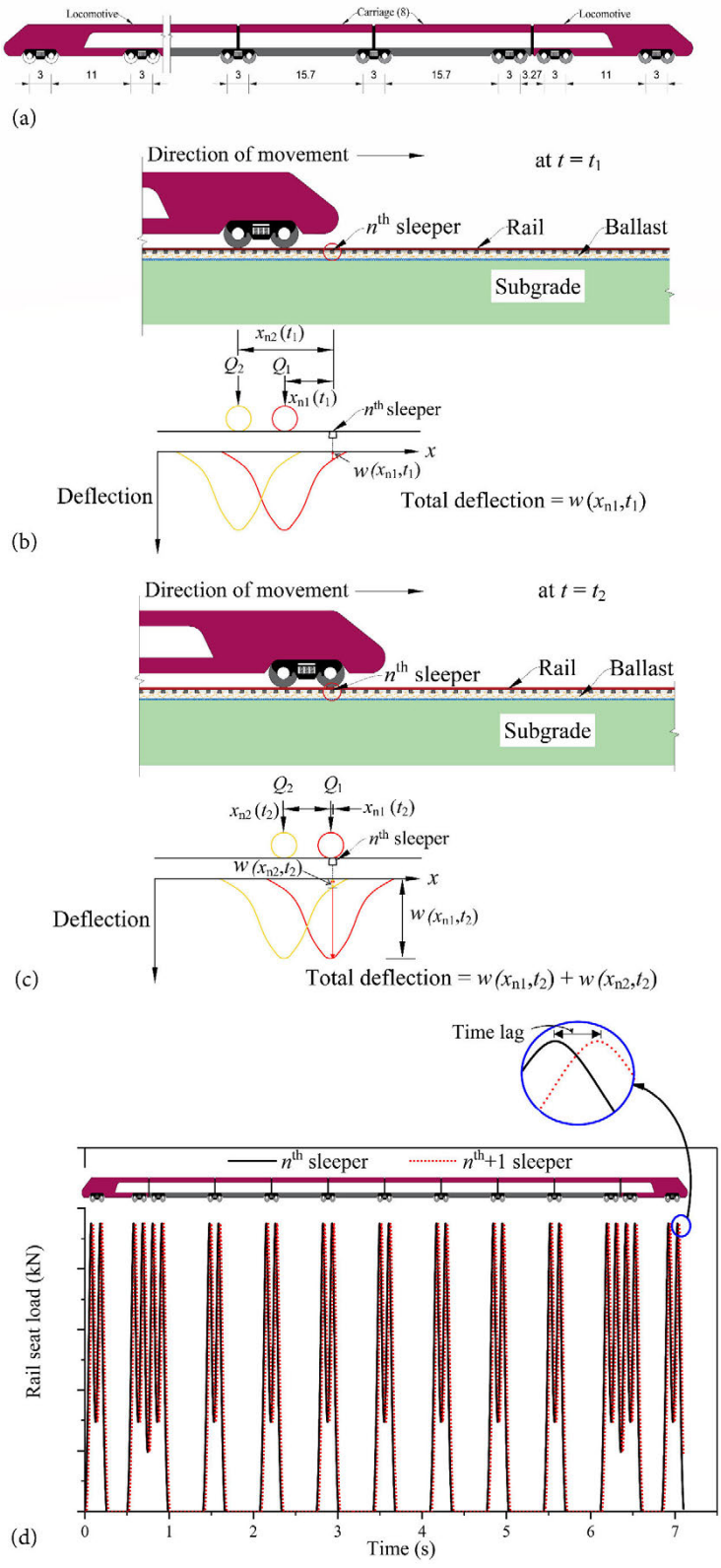

Figure 3.1 (a) Configuration of the Thalys high-speed train; **(b)** calculation of track deflection at time t_1; **(c)** calculation of track deflection at time t_2; **(d)** final rail seat load-time history

Figure 3.1(a) shows the configuration of the Thalys high-speed train. It comprises of two locomotives and eight carriages that are supported by two-axle bogies. The total number of axles on the train is 26. It is assumed that the train is moving in the positive x-direction. Referring to **Figure 3.1(b)**, at time instant t_1, the n^{th} sleeper is at a distance of x_{n1} (t_1) and x_{n2} (t_1) from the leading (Q_1) and trailing wheel (Q_2), respectively. The distribution of rail deflection due to each wheel load, calculated using Equation 3.2, is also shown in **Figure 3.1(b)**. It is apparent from the figure that the trailing wheel does not contribute to the deflection at the n^{th} sleeper at time t_1, since x_{n2} (t_1) is greater than $3\pi L/4$. As the train moves forward, the total deflection at the n^{th} sleeper at time t_2 is the sum of deflection due to both wheels [refer to **Figure 3.1(c)**]. Similarly, the deflection due to other wheel loads can be calculated at each time instant. Subsequently, the rail seat load-time history is calculated using Equation 3.3 at all the sleeper locations by applying a time shift (time lag) according to the axle spacing and train speed. **Figure 3.1(d)** shows the resulting rail seat load-time history at the n^{th} and n^{th}+1 sleeper (i.e. next to n^{th} sleeper) due to a single passage of Thalys train at a speed of 100 km/h. It can be observed that a time lag exists in the load-time history for the n^{th}+1 sleeper. This time lag is equal to S/V.

3.2.2 Track Resiliency Model

The dynamic response of the railway track to train-induced repetitive loads is simulated using a three-degree-of-freedom mass-spring-dashpot (3DoF MSD) model. **Figure 3.2** shows the MSD model for the dynamic analysis of the track. The ballast, subballast, and subgrade layers are represented as lumped masses that are connected by springs and dashpots. The motion of the track layers is considered only in the vertical direction. Zhai et al. (2004) used shear springs and dashpots between adjacent ballast masses to account for the continuity along the longitudinal direction. This approach of employing shear springs and dashpots has been extended to the subballast and subgrade masses in the present method.

3.2.2.1 Equations of Motion

Considering the dynamic equilibrium of the system below n^{th} sleeper (refer to **Figure 3.2**), the following system of equations can be derived using the D'Alembert's principle:

$$m_{\mathrm{g}}\ddot{z}_{\mathrm{g,n}}(t) + c_{\mathrm{g}}\dot{z}_{\mathrm{g,n}}(t) + c_{\mathrm{s}}\left[\dot{z}_{\mathrm{g,n}}(t) - \dot{z}_{\mathrm{s,n}}(t)\right] + k_{\mathrm{g}}z_{\mathrm{g,n}}(t) + k_{\mathrm{s}}\left[z_{\mathrm{g,n}}(t) - z_{\mathrm{s,n}}(t)\right] + k_{\mathrm{g}}^{s}\left[2z_{\mathrm{g,n}}(t) - z_{\mathrm{g,n+1}}(t) - z_{\mathrm{g,n-1}}(t)\right] + c_{\mathrm{g}}^{s}\left[2\dot{z}_{\mathrm{g,n}}(t) - \dot{z}_{\mathrm{g,n+1}}(t) - \dot{z}_{\mathrm{g,n-1}}(t)\right] = F_{\mathrm{g,n}}(t) \quad 3.4(a)$$

$$m_{\mathrm{s}}\ddot{z}_{\mathrm{s,n}}(t) + c_{\mathrm{s}}[\dot{z}_{\mathrm{s,n}}(t) - \dot{z}_{\mathrm{g,n}}(t)] + c_{\mathrm{b}}\left[\dot{z}_{\mathrm{s,n}}(t) - \dot{z}_{\mathrm{b,n}}(t)\right] + k_{\mathrm{s}}[z_{\mathrm{s,n}}(t) - z_{\mathrm{g,n}}(t)] + k_{\mathrm{b}}\left[z_{\mathrm{s,n}}(t) - z_{\mathrm{b,n}}(t)\right] + k_{\mathrm{s}}^{s}\left[2z_{\mathrm{s,n}}(t) - z_{\mathrm{s,n+1}}(t) - z_{\mathrm{s,n-1}}(t)\right] + c_{\mathrm{s}}^{s}\left[2\dot{z}_{\mathrm{s,n}}(t) - \dot{z}_{\mathrm{s,n+1}}(t) - \dot{z}_{\mathrm{s,n-1}}(t)\right] = F_{\mathrm{s,n}}(t) \quad 3.4(b)$$

$$m_{\mathrm{b}}\ddot{z}_{\mathrm{b,n}}(t) + c_{\mathrm{b}}\left[\dot{z}_{\mathrm{b,n}}(t) - \dot{z}_{\mathrm{s,n}}(t)\right] + k_{\mathrm{b}}\left[z_{\mathrm{b,n}}(t) - z_{\mathrm{s,n}}(t)\right] + k_{\mathrm{b}}^{s}\left[2z_{\mathrm{b,n}}(t) - z_{\mathrm{b,n+1}}(t) - z_{\mathrm{b,n-1}}(t)\right] + c_{\mathrm{b}}^{s}\left[2\dot{z}_{\mathrm{b,n}}(t) - \dot{z}_{\mathrm{b,n+1}}(t) - \dot{z}_{\mathrm{b,n-1}}(t)\right] = F_{\mathrm{b,n}}(t) \quad 3.4(c)$$

where the subscripts 'b', 's' and 'g' denote the ballast, subballast and subgrade layers, respectively; subscripts 'n', 'n-1' and 'n+1' represent the n^{th}, previous and next to n^{th} sleeper, respectively; m, c and k represent the vibrating mass (kg), damping coefficient (Ns/m) and stiffness (N/m), respectively; k^s and c^s are the shear stiffness (N/m), and shear damping coefficients (Ns/m), respectively; $F(t)$, $\ddot{z}(t)$, $\dot{z}(t)$ and $z(t)$ denote the external force (N), vertical acceleration (m/s^2), velocity (m/s) and displacement (m), respectively. Equations 3.4(a), 3.4(b) and 3.4(c) can be further simplified as:

$$\begin{bmatrix} m_{\mathrm{g}} & 0 & 0 \\ 0 & m_{\mathrm{s}} & 0 \\ 0 & 0 & m_{\mathrm{b}} \end{bmatrix} \begin{Bmatrix} \ddot{z}_{\mathrm{g,n}}(t) \\ \ddot{z}_{\mathrm{s,n}}(t) \\ \ddot{z}_{\mathrm{b,n}}(t) \end{Bmatrix} + \begin{bmatrix} c_{\mathrm{g}} + c_{\mathrm{s}} + 2c_{\mathrm{g}}^{s} & -c_{\mathrm{s}} & 0 \\ -c_{\mathrm{s}} & c_{\mathrm{s}} + c_{\mathrm{b}} + 2c_{\mathrm{s}}^{s} & -c_{\mathrm{b}} \\ 0 & -c_{\mathrm{b}} & c_{\mathrm{b}} + 2c_{\mathrm{b}}^{s} \end{bmatrix} \begin{Bmatrix} \dot{z}_{\mathrm{g,n}}(t) \\ \dot{z}_{\mathrm{s,n}}(t) \\ \dot{z}_{\mathrm{b,n}}(t) \end{Bmatrix} + \begin{bmatrix} k_{\mathrm{g}} + k_{\mathrm{s}} + 2k_{\mathrm{g}}^{s} & -k_{\mathrm{s}} & 0 \\ -k_{\mathrm{s}} & k_{\mathrm{s}} + k_{\mathrm{b}} + 2k_{\mathrm{s}}^{s} & -k_{\mathrm{b}} \\ 0 & -k_{\mathrm{b}} & k_{\mathrm{b}} + 2k_{\mathrm{b}}^{s} \end{bmatrix} \begin{Bmatrix} z_{\mathrm{g,n}}(t) \\ z_{\mathrm{s,n}}(t) \\ z_{\mathrm{b,n}}(t) \end{Bmatrix} = \begin{Bmatrix} F_{\mathrm{g,n}}(t) \\ F_{\mathrm{s,n}}(t) \\ F_{\mathrm{b,n}}(t) \end{Bmatrix}$$
$$+ \begin{bmatrix} c_{\mathrm{g}}^{s} & 0 & 0 \\ 0 & c_{\mathrm{s}}^{s} & 0 \\ 0 & 0 & c_{\mathrm{b}}^{s} \end{bmatrix} \begin{Bmatrix} \dot{z}_{\mathrm{g,n+1}}(t) + \dot{z}_{\mathrm{g,n-1}}(t) \\ \dot{z}_{\mathrm{s,n+1}}(t) + \dot{z}_{\mathrm{s,n-1}}(t) \\ \dot{z}_{\mathrm{b,n+1}}(t) + \dot{z}_{\mathrm{b,n-1}}(t) \end{Bmatrix} + \begin{bmatrix} k_{\mathrm{g}}^{s} & 0 & 0 \\ 0 & k_{\mathrm{s}}^{s} & 0 \\ 0 & 0 & k_{\mathrm{b}}^{s} \end{bmatrix} \begin{Bmatrix} z_{\mathrm{g,n+1}}(t) + z_{\mathrm{g,n-1}}(t) \\ z_{\mathrm{s,n+1}}(t) + z_{\mathrm{s,n-1}}(t) \\ z_{\mathrm{b,n+1}}(t) + z_{\mathrm{b,n-1}}(t) \end{Bmatrix} \quad 3.5$$

Equation 3.5 is solved using the Newmark's-β numerical integration scheme. The solution of the equation gives the transient displacement, velocity and acceleration response for the ballast, subballast and subgrade layers. The time step in the present study is chosen as 1×10^{-4} s based on the findings of the sensitivity analysis to achieve the desired accuracy.

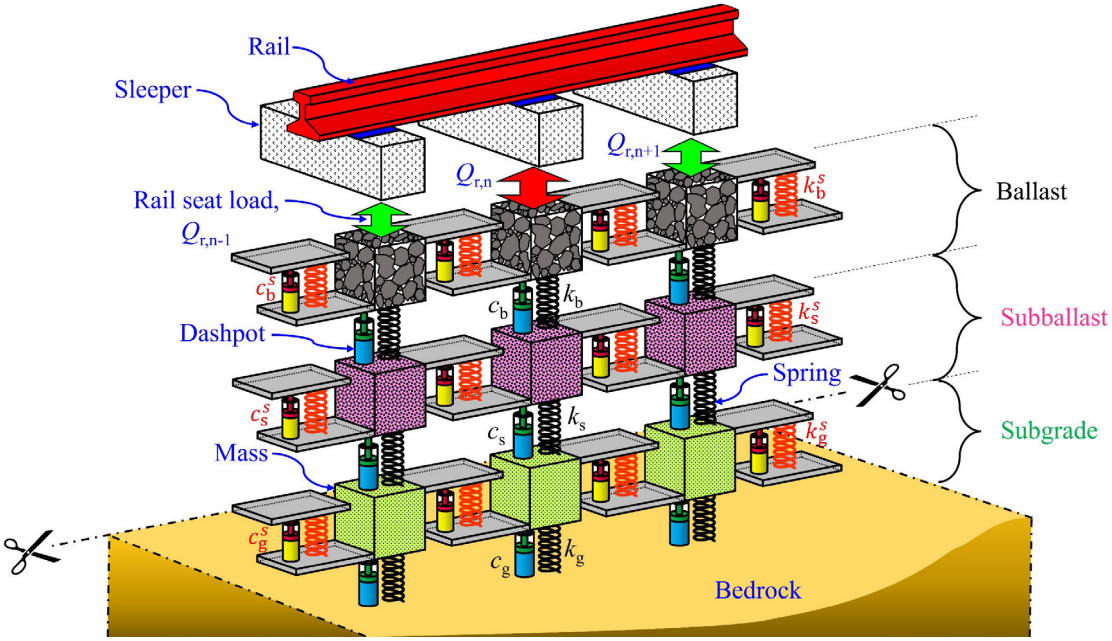

Figure 3.2 Three-degree-of-freedom mass-spring-dashpot (MSD) model of track

3.2.2.2 Determination of Model Parameters

The input parameters include the mass, stiffness and damping coefficient of the ballast, subballast and subgrade layers. To determine these parameters, a pyramidal distribution of vertical load from the sleeper to the substructure layers is assumed (Ahlbeck et al. 1978), which was found to be in close agreement with the field measurements (Zhang et al. 2016). In this model, the vertical stresses in the substructure layers are uniformly distributed within the pyramid and zero outside the pyramid. Thus, the portion inside the load distribution pyramid can be considered as the effective region of ballast, subballast and subgrade in the dynamic analysis. Consequently, the mass and stiffness of the effective regions of substructure layers below each sleeper can be determined using the geometry of the pyramid as:

$$m_{\mathrm{b}} = \rho_{\mathrm{b}} h_{\mathrm{b}} \left[l_{\mathrm{e}} b_{\mathrm{sl}} + (l_{\mathrm{e}} + b_{\mathrm{sl}}) h_{\mathrm{b}} \tan\alpha + \frac{4}{3} h_{\mathrm{b}}^2 \tan^2\alpha \right] \tag{3.6}$$

$$m_{\mathrm{s}} = \rho_{\mathrm{s}} h_{\mathrm{s}} \left[l_{\mathrm{e}} b_{\mathrm{sl}} + (l_{\mathrm{e}} + b_{\mathrm{sl}})(2h_{\mathrm{b}} \tan\alpha + h_{\mathrm{s}} \tan\beta) + 4h_{\mathrm{b}} \tan\alpha \, (h_{\mathrm{b}} \tan\alpha + h_{\mathrm{s}} \tan\beta) + \frac{4}{3} h_{\mathrm{s}}^2 \tan^2\beta \right] \tag{3.7}$$

$$m_g = \rho_g h_g \Big[l_e b_{sl} + (l_e + b_{sl})\big(2h_b \tan\alpha + 2h_s \tan\beta + h_g \tan\gamma\big) + 4(h_b \tan\alpha + h_s \tan\beta)(h_b \tan\alpha + h_s \tan\beta + h_g \tan\gamma) + \frac{4}{3} h_g^2 \tan^2\gamma \Big] \quad 3.8$$

$$k_b = \frac{2E_b(l_e - b_{sl})\tan\alpha}{\ln\left[\left(\frac{l_e}{b_{sl}}\right)\left(\frac{b_{sl} + 2h_b \tan\alpha}{l_e + 2h_b \tan\alpha}\right)\right]} \quad 3.9$$

$$k_s = \frac{2E_s(l_e - b_{sl})\tan\beta}{\ln\left[\left(\frac{l_e + 2h_b \tan\alpha}{b_{sl} + 2h_b \tan\alpha}\right)\left(\frac{b_{sl} + 2h_b \tan\alpha + 2h_s \tan\beta}{l_e + 2h_b \tan\alpha + 2h_s \tan\beta}\right)\right]} \quad 3.10$$

$$k_g = \frac{2E_g(l_e - b_{sl})\tan\gamma}{\ln\left[\left(\frac{l_e + 2h_b \tan\alpha + 2h_s \tan\beta}{b_{sl} + 2h_b \tan\alpha + 2h_s \tan\beta}\right)\left(\frac{b_{sl} + 2h_b \tan\alpha + 2h_s \tan\beta + 2h_g \tan\gamma}{l_e + 2h_b \tan\alpha + 2h_s \tan\beta + 2h_g \tan\gamma}\right)\right]} \quad 3.11$$

where the subscripts 'b', 's' and 'g' denote the ballast, subballast and subgrade layers, respectively; ρ, E and h represent the density (kg/m^3), resilient modulus (N/m^2) and thickness (m), respectively; l_e and b_{sl} are the effective length (m) and width (m) of sleeper, respectively (l_e=l_{sl}–g_t); l_{sl} is sleeper length (m); g_t is the centre-to-centre distance between the rails (m); α, β and γ are the stress distribution angles (°) of ballast, subballast and subgrade layers, respectively. The detailed derivation of Equations 3.6, 3.7, 3.8, 3.9, 3.10 and 3.11 is provided in APPENDIX A.

The stress distribution angle (i.e., the inclination angle of the pyramid with vertical) can be evaluated using Burmister's theory of stress distribution in layered soil (Burmister 1958; Giroud & Han 2004a):

$$\tan\alpha = \tan\alpha_0 \left[1 + 0.204\left(\frac{E_b}{E_s} - 1\right)\right];\ \tan\beta = \tan\beta_0 \left[1 + 0.204\left(\frac{E_s}{E_g} - 1\right)\right] \quad 3.12$$

where α_0 and β_0 are the reference stress distribution angles in uniform ballast (i.e., for E_b = E_s) and subballast (i.e., for E_s = E_g), respectively. The value of α_0 is 45° unless otherwise specified (Zhang et al. 2016). The value of β_0 is considered as 27° based on the assumed stress distribution of 2:1 (Han et al. 2013).

It is interesting to note that the load distribution pyramids below adjacent sleepers might overlap in the longitudinal direction in case of large thickness, small sleeper spacing and

high stress distribution angles (Zhai et al. 2004). **Figures 3.3(a)**, **3.3(b)** and **3.3(c)** show the overlapping in the pyramids along the longitudinal direction in the ballast, subballast and subgrade layers, respectively. The height of the overlapped regions can be evaluated as:

$$h_{\mathrm{bL}} = h_{\mathrm{b}} - \left(\frac{S - b_{\mathrm{sl}}}{2\tan\alpha}\right) \tag{3.13}$$

$$h_{\mathrm{sL}} = h_{\mathrm{s}} - \left(\frac{S - b_{\mathrm{sl}} - 2h_{\mathrm{b}}\tan\alpha}{2\tan\beta}\right) \tag{3.14}$$

$$h_{\mathrm{gL}} = h_{\mathrm{g}} - \left(\frac{S - b_{\mathrm{sl}} - 2h_{\mathrm{b}}\tan\alpha - 2h_{\mathrm{s}}\tan\beta}{2\tan\gamma}\right) \tag{3.15}$$

where h_{bL}, h_{sL} and h_{gL} are the overlap height (m) in ballast, subballast and subgrade along the longitudinal direction, respectively. The established pyramidal load distribution model only considers the overlapping along the longitudinal direction (Zhai et al. 2004). However, the load distribution pyramids may also overlap along the transverse direction if the layer thickness and stress-distribution angles are high and the sleeper length is small. **Figures 3.3(d)**, **3.3(e)** and **3.3(f)** show the overlapping along the transverse directions in ballast, subballast and subgrade, respectively. The overlap height in the ballast, subballast and subgrade along the transverse direction can be determined as:

$$h_{\mathrm{bt}} = h_{\mathrm{b}} - \left(\frac{l_{\mathrm{sl}} - 2l_{\mathrm{e}}}{2\tan\alpha}\right) \tag{3.16}$$

$$h_{\mathrm{st}} = h_{\mathrm{s}} - \left(\frac{l_{\mathrm{sl}} - 2l_{\mathrm{e}} - 2h_{\mathrm{b}}\tan\alpha}{2\tan\beta}\right) \tag{3.17}$$

$$h_{\mathrm{gt}} = h_{\mathrm{g}} - \left(\frac{l_{\mathrm{sl}} - 2l_{\mathrm{e}} - 2h_{\mathrm{b}}\tan\alpha - 2h_{\mathrm{s}}\tan\beta}{2\tan\gamma}\right) \tag{3.18}$$

where h_{bt}, h_{st} and h_{gt} are the overlap height (m) in ballast, subballast and subgrade along the transverse direction, respectively. **Figure 3.4** shows the effective portion of the substructure layers below each sleeper point considered in the analysis. The geometry of this effective portion (consequently, the vibrating mass and stiffness of substructure layers) varies depending on the overlapping within the substructure layers. It is apparent from **Figure 3.4** that the stiffness and vibrating mass of the substructure layers may be over-predicted if the overlapping along the transverse direction is neglected in the

analysis. Therefore, the mass and stiffness of the substructure layers can be determined more accurately if the overlapping is also considered along the transverse direction.

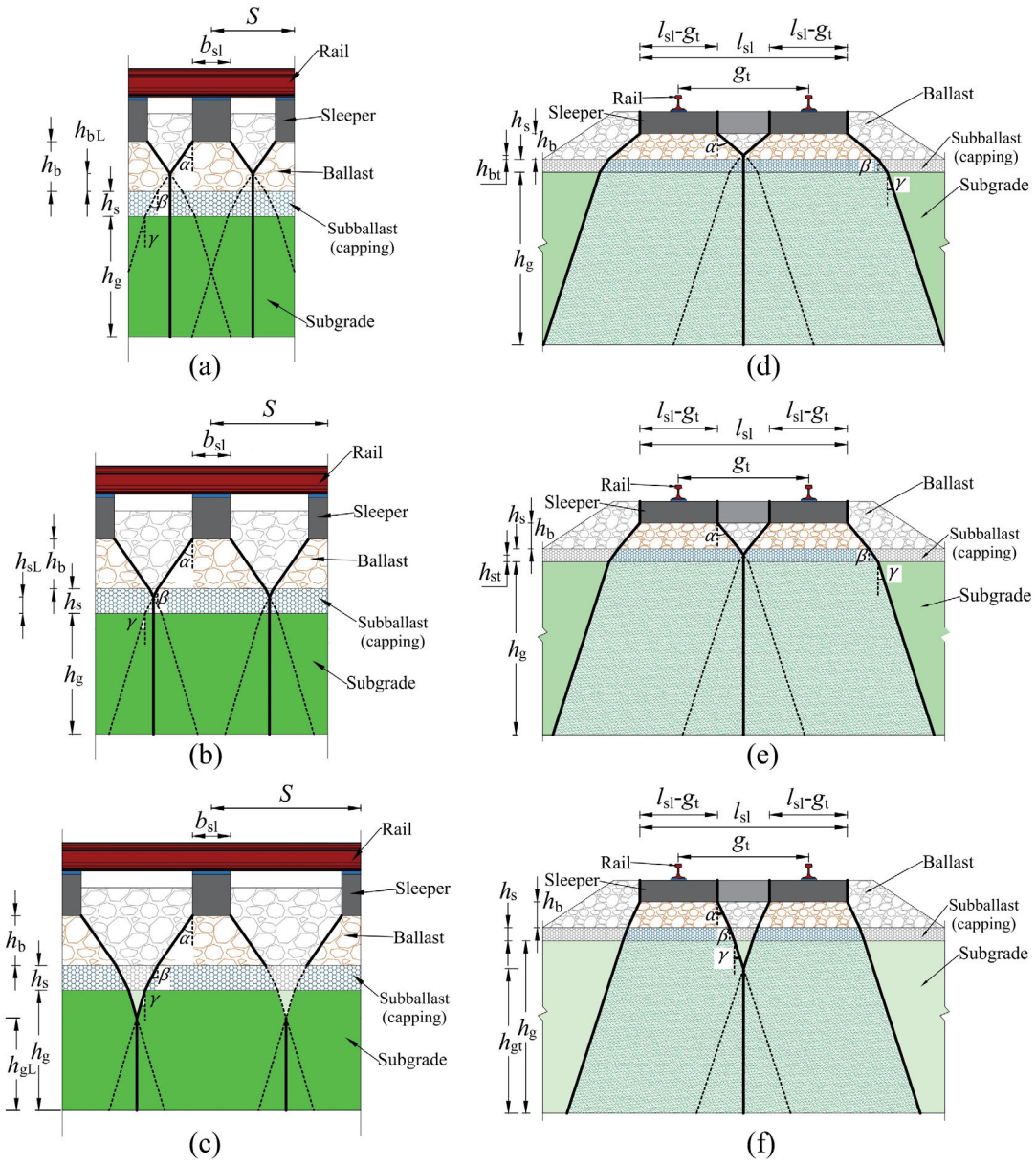

Figure 3.3 Overlapping along longitudinal direction in **(a)** ballast; **(b)** subballast; **(c)** subgrade; transverse direction in **(d)** ballast; **(e)** subballast; **(f)** subgrade

In summary, the overlap height is first calculated using Equations 3.13, 3.14, 3.15, 3.16, 3.17 and 3.18, and the resulting geometry of the load distribution pyramid is identified. Subsequently, the vibrating mass and stiffness of the substructure layers (effective region) are determined using a similar procedure as described in APPENDIX A. Thus, the effect of overlapping is accounted for in the analysis by modifying the vibrating mass and stiffness of the substructure layers. Nevertheless, a detailed description of the different

cases (or geometries) that may arise due to overlapping and the corresponding equations to evaluate the mass and stiffness of the substructure layers for each case will be provided by the author upon reasonable request.

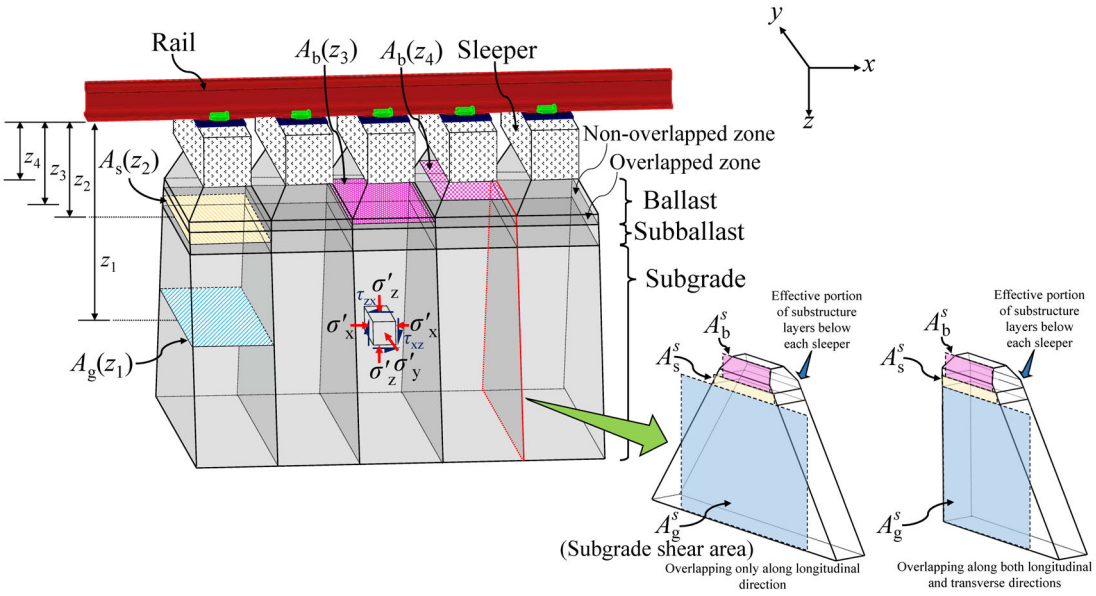

Figure 3.4 Effective portion of substructure layers considered in analysis

The equivalent damping coefficient of the substructure layers can be calculated as (Nimbalkar et al. 2012):

$$c_g = \sqrt{\frac{E_g \rho_g}{(1+\nu_g)(1-\nu_g)}} \qquad 3.19(a)$$

$$c_s = \sqrt{\frac{E_s \rho_s}{(1+\nu_s)(1-\nu_s)}} \qquad 3.19(b)$$

$$c_b = \sqrt{\frac{E_b \rho_b}{(1+\nu_b)(1-\nu_b)}} \qquad 3.19(c)$$

where ν_g, ν_s and ν_b are the Poisson's ratios of subgrade, subballast and ballast layers, respectively. The external force $F_{b,n}(t)$ in Equation 3.5 is equal to the load-time history calculated using the loading model, while the external forces $F_{g,n}(t)$ and $F_{s,n}(t)$ are considered as zero. The input parameters to evaluate the load-time history include E_r, I_r, S, Q and k. The parameters E_r, I_r and S are usually pre-defined. The wheel load is one half of Q_a. To account for the dynamic effects due to the wheel-rail irregularities, the wheel

load can also be multiplied by φ_d. In the present study, φ_d is evaluated using the method developed by Nimbalkar & Indraratna (2016):

$$\varphi_d = 1 + i_1 \left(\frac{V}{D_w}\right)^{i_2} \quad 3.20$$

where i_1 and i_2 are the empirical parameters that depend on Q_a and subgrade type. This method was derived from the field investigations, and it accounts for the variation in load amplification due to a change in subgrade type, Q_a and V. The value of parameters i_1 and i_2 may range between 0.0052 to 0.0065 and 0.75 to 1.02, respectively, depending on the subgrade type and Q_a (Nimbalkar & Indraratna 2016).

The track modulus is calculated by modifying the approach described in Doyle (1980):

$$\frac{1}{k} = S\left(\frac{1}{k_p} + \frac{1}{k_b} + \frac{1}{k_s} + \frac{1}{k_g}\right) \quad 3.21$$

where k_p is the stiffness of rail pad (N/m).

3.2.3 Track Settlement Model

The cumulative settlement (or irrecoverable deformation) in the substructure layers has been predicted using empirical models.

3.2.3.1 Settlement in Granular (Ballast and Subballast) Layers

The irrecoverable deformation in ballast and subballast has been calculated using a power model:

$$\varepsilon_b^p = k_1^b \left(\frac{\sigma_{oct}}{P_a}\right)^{k_2^b} \left(\frac{\tau_{oct}}{P_a}\right)^{k_3^b} N^{k_4^b} \quad 3.22$$

$$\varepsilon_s^p = k_1^s \left(\frac{\sigma_{oct}}{P_a}\right)^{k_2^s} \left(\frac{\tau_{oct}}{P_a}\right)^{k_3^s} N^{k_4^s} \quad 3.23$$

where the superscripts 'b' and 's' denote the ballast and subballast layer, respectively; k_1, k_2, k_3, and k_4 are the empirical parameters; ε_b^p and ε_s^p are the irrecoverable strains (%) in the vertical direction in ballast and subballast, respectively; N is the number of load cycles. The parameters k_1, k_2, and k_3 represent the influence of the infill type, octahedral normal, and shear stresses on the magnitude of ε_b^p (or ε_s^p) corresponding to the first load

cycle. The parameter k_4 governs the variation of ε_b^p (or ε_s^p) with N. The parameters k_1, k_2, k_3 and k_4 can be evaluated by fitting the experimental curves of ε_b^p or ε_s^p with N at different loading conditions. The total settlement can be evaluated by multiplying the strain with the thickness of the ballast and subballast layers.

3.2.3.2 Settlement in Subgrade Layer

The model developed by Li & Selig (1996) has been used to predict the irrecoverable deformation in the subgrade layer:

$$\varepsilon_g^p = a' \left(\frac{\sigma'_d}{\sigma_g} \right)^{m^*} N^{b_g} \tag{3.24}$$

where ε_g^p is the cumulative plastic strain in subgrade (%); σ'_d is the deviatoric stress (N/m^2); σ_g is the compressive strength of subgrade soil (N/m^2); a', m^* and b_g are the parameters that depend on the subgrade soil type. **Table 3.1** shows the values of these parameters for different subgrade soil type. The subgrade is assumed to be divided into ten layers, and the strain in each layer is evaluated using Equation 3.24. Subsequently, the total irrecoverable deformation (s_g) is calculated as:

$$s_g = \sum_{i=1}^{10} (\varepsilon_g^p)_i \, h_i \tag{3.25}$$

where h_i is the thickness of i^{th} subgrade layer (m); $(\varepsilon_g^p)_i$ is the cumulative plastic strain in the i^{th} subgrade layer. The irrecoverable deformation is calculated after the completion of an individual load cycle. The stresses in the substructure layers are calculated using the method described in APPENDIX B.

Table 3.1 Parameters a', b_g and m^* for different subgrade soils [adapted from Li & Selig (1996)]

Subgrade soil type	a'	b_g	m^*
ML (silt)	0.64	0.06 – 0.17	1.4 – 2.0
MH (silt of high plasticity)	0.84	0.08 – 0.19	1.3 – 4.2
CL (clay of low plasticity)	0.30 – 3.5	0.08 – 0.34	1.0 – 2.6
CH (clay of high plasticity)	0.82 – 1.5	0.12 – 0.27	1.3 – 3.9

3.3 Model Validation

The present method can be used to predict the resilient as well as the irrecoverable response of the ballasted railway tracks under train-induced repeated loading. The response includes the resilient displacement, velocity and acceleration, and irrecoverable displacement of the substructure layers. The substructure layer response predicted using the present method is compared with the field investigation data reported by Takemiya & Bian (2005), Gräbe et al. (2005), Gräbe & Shaw (2010), Priest et al. (2010) and Mishra et al. (2014a).

Takemiya & Bian (2005) reported the ground displacement and acceleration recorded during the passage of the Swedish X-2000 train at a speed of 70 km/h and 200 km/h. The track was located over very soft ground at the West Coast line in Sweden. **Table 3.2** shows the values of the parameters used in the analysis. The ballast layer is replaced by an equivalent top soil layer in the analysis to ensure consistency with the approach used by Takemiya & Bian (2005). The train is initially at a distance of $3\pi L/4$ from the first sleeper and is assumed to travel in the positive x-direction (i.e. from left to right). A total of 25 sleepers are considered in the analysis to ensure accurate prediction of deformations, and the results are reported for the central sleeper (i.e. 13^{th} sleeper).

Figure 3.5 compares the vertical displacement and vertical acceleration time histories computed using the present method with the data measured from field investigations. It can be observed that the ground displacement calculated using the present method is in good agreement with the field data at a train speed of 70 km/h. For 200 km/h, the vertical displacement in the downward direction is nearly identical to the field observation. However, a little discrepancy exists in the predictions corresponding to 200 km/h as the field data also showed vertical displacement in the upward direction, which is absent in the model predictions. The accelerations predicted using the present method show a similar trend as the field data for both 70 km/h and 200 km/h; however, the peak values are underestimated.

Table 3.2 Parameters used for evaluation of track response

Variable	Symbol	Unit	Takemiya & Bian (2005)	Gräbe et al. (2005); Gräbe & Shaw (2010)	Priest et al. (2010)	Mishra et al. (2014a)	Parametric study
Ballast (Top layer):							
Resilient modulus	E_b	MPa	23	100*	100*	69	138–551 (276)
Poisson's ratio	ν_b	–	0.45	0.3	0.3	0.3	0.3
Shear stiffness	k_b^s	MN/m	1	0.1	0.1	78.4	78.4
Shear damping	c_b^s	kNs/m	80	80	80	80	80
Density	ρ_b	kg/m^3	1,500	1,800	1,800	1,990	1,760
Thickness	h_b	m	1	0.3	0.3	0.305	0.15–0.6 (0.3)
Subballast (Middle layer):							
Resilient modulus	E_s	MPa	6	220†	220†	55	69–276 (138)
Poisson's ratio	ν_s	–	0.45	0.3	0.3	0.4	0.35
Shear stiffness	k_s^s	MN/m	250	476	476	1,600	476
Shear damping	c_s^s	kNs/m	800	80	80	80	80
Density	ρ_s	kg/m^3	1,260	2,175	2,175	2,092	1,920
Thickness	h_s	m	3	0.8	0.8	0.127	0.15–0.45 (0.15)
Subgrade:							
Resilient modulus	E_g	MPa	44	27,000‡	27,000‡	45	14–276 (14)
Poisson's ratio	ν_g	–	0.45	0.25	0.25	0.4	0.35
Shear stiffness	k_g^s	MN/m	3,000	1,600	1,600	1,600	1,600
Shear damping	c_g^s	kNs/m	800	80	80	80	80
Density	ρ_g	kg/m^3	1,475	2,300	2,300	2,092	1,920
Thickness	h_g	m	44	3.29	3.29	2	1– 10 (4.5)

Note: The values of shear stiffness and damping have been calculated using a trial and error procedure to obtain good agreement between the model predictions and corresponding literature data. The initial values for the trial and error procedure, and the parametric study were chosen according to those reported by Zhai et al. (2004) and Oscarsson & Dahlberg (1998); empirical parameters for irrecoverable deformation are taken from Sun et al. (2016) and Suiker et al. (2005) for ballast and subballast, respectively. The best agreement with the literature data is obtained at $^{*}E_b$ = 80 MPa, $^{\dagger}E_s$ = 140 MPa and $^{\ddagger}E_g$ = 600 MPa.

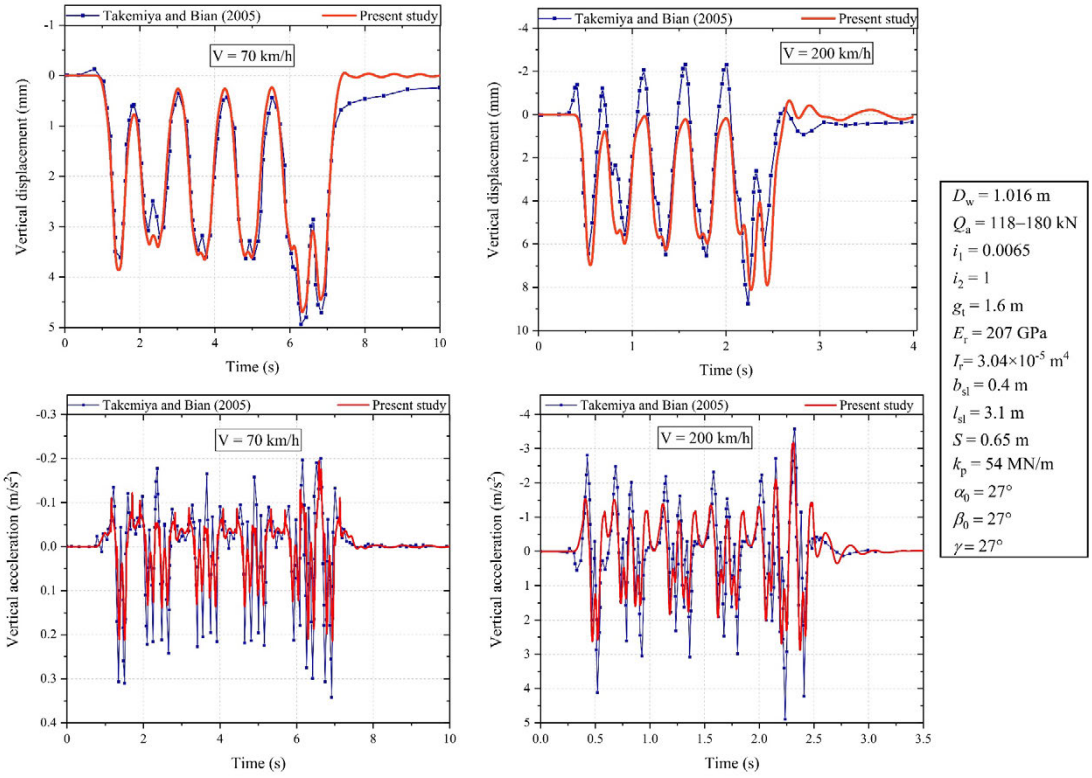

Figure 3.5 Comparison of vertical displacement and acceleration time histories predicted using the present method with field results reported by Takemiya & Bian (2005)

Gräbe et al. (2005) conducted field investigations in a heavy haul track at the Bloubank site in the Broodsnyersplaas–Richards Bay Coal Export Line, South Africa. The track comprises of a 300 mm thick ballast layer overlying the formation, which constitutes of four layers of selected high-quality material (each 200 mm thick) and the in-situ material (weathered tillite). The instrumentation included MDDs, pressure plates, LVDT, accelerometers and strain gauges. These instruments were used to monitor the layer

deformation (resilient and permanent), vertical stresses in substructure layers, rail and sleeper displacement, wheel load, lateral force, sleeper reaction and acceleration in rail, sleeper and ballast. **Table 3.2** shows the values of the parameters used in the model predictions. **Table 3.3** compares the resilient displacement and vertical stress (σ_v) calculated using the present method with field data. It can be observed that the model predictions are consistent with field investigations. The present method slightly underpredicts the magnitude of σ_v just below the ballast layer (0 mm below the foundation). Gräbe & Shaw (2010) reported the variation of irrecoverable/ permanent deformation of the substructure layers below the ballast with tonnage in million gross tonnes (MGT) at the same site. **Figure 3.6** compares the irrecoverable deformation calculated using the present method with that reported by Gräbe & Shaw (2010). It can be observed that the predicted results are in good agreement with the data measured from field investigations.

Table 3.3 Comparison of results reported by Gräbe et al. (2005) with model predictions

Depth below foundation (mm)	Displacement (mm)		Vertical stress (kPa)	
	Gräbe et al. (2005)	Present study	Gräbe et al. (2005)	Present study
0	0.54	0.51	110	84
400	–	–	76	75
800	0.23	0.18	59.6	53

Priest et al. (2010) also conducted field investigations at the Bloubank site in the Broodsnyersplaas–Richards Bay Coal Export Line, South Africa. The instrumentation included geophones to measure the velocity in substructure layers (which was used to back-calculate the displacement) and a combination of remote video monitoring and particle image velocimetry to measure the sleeper displacement. **Table 3.2** shows the parameters used to predict the response of the substructure layers. **Figure 3.7(a)** compares the variation of the resilient displacement with time due to the passage of 26 t axle load coal wagons, predicted using the present method with that recorded in the field experiments. It can be observed that the predicted response is in good agreement with the field data. **Figure 3.7(b)** shows the variation of resilient displacement with time at different depths below the sleeper due to the passage of two adjacent bogies (four axles).

It can be observed that the predicted results are consistent with the field data. The resilient displacement decreases with depth, and the influence of the individual axles in the response diminishes with depth.

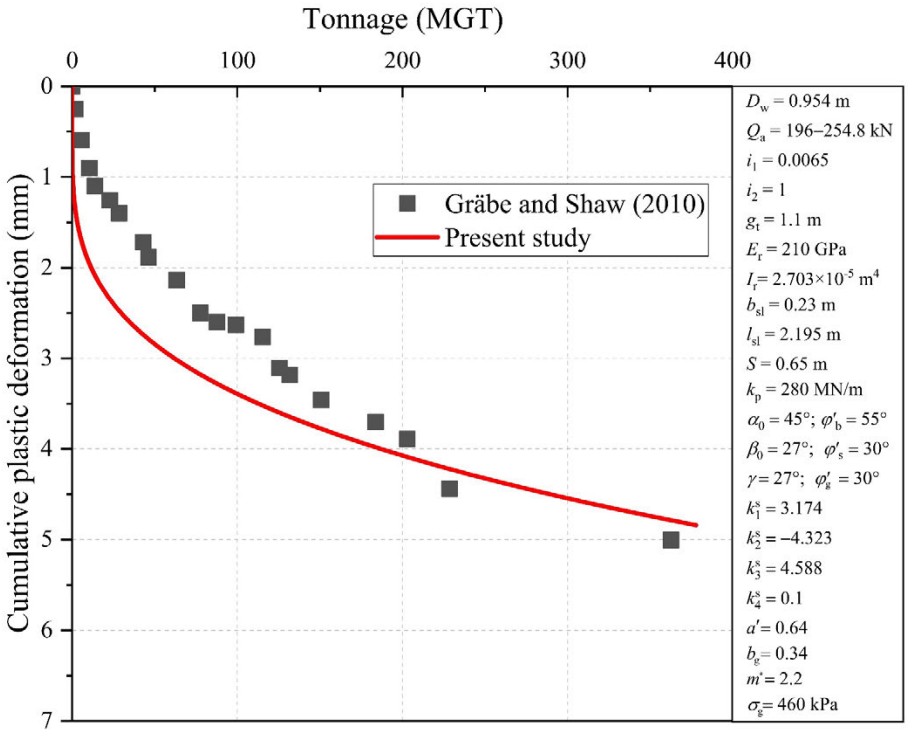

Figure 3.6 Comparison of model predictions with the field results reported by Gräbe & Shaw (2010)

The four 200 mm thick layers of selected high-quality material were replaced by a single subballast layer (800 mm thick) with equivalent resilient modulus in the analysis. Therefore, the results are only available for the top of the ballast layer (0 m), the bottom of the ballast layer (0.3 m) and the bottom of the subballast layer (1.1 m). **Figure 3.7(c)** compares the variation of the resilient displacement with time due to the passage of 20 t axle load coal wagons, predicted using the present method with the field data. It can be observed that the predicted results are in good agreement with the field observations. **Figure 3.7(d)** shows the increase in σ_v at 800 mm below the bottom of the sleeper predicted using the present method and that using the FE analysis by Priest et al. (2010). It can be observed that the predictions using the present method are consistent with that reported by Priest et al. (2010).

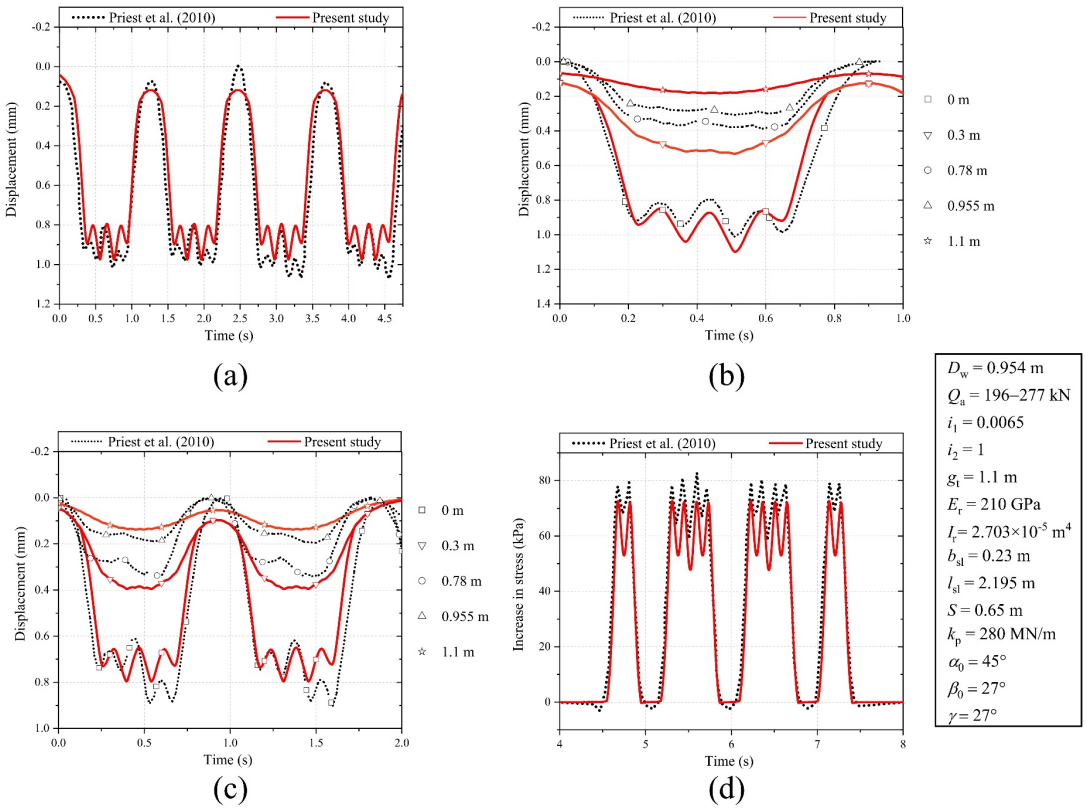

Figure 3.7 Comparison of model predictions with results reported by Priest et al. (2010): **(a)** resilient displacement for 26 t axle load coal wagons; **(b)** resilient displacement at different depth below the sleeper; **(c)** resilient displacement for 20 t axle load coal wagons **(d)** vertical stress at 800 mm below sleeper bottom

Mishra et al. (2014a) conducted field investigations near several bridge approaches along Amtrak's North East Corridor in the USA. The instrumentation included MDDs to monitor the deformation of the substructure layers and strain gauges to monitor the wheel load and sleeper reactions. **Table 3.2** shows the parameters used for the prediction of the track response. **Figure 3.8** compares the resilient deformation in the ballast layer due to the passage of the Acela express train predicted using the present method with the field measurements. It can be observed that the predicted trend is consistent with the field data. The small discrepancy in the peak values is likely due to a slight difference in the actual and the predicted load-time history.

Thus, the proposed method in this study can predict the stresses, resilient and irrecoverable response of the track substructure layers with adequate accuracy. The method is simple and computationally efficient. It can serve as a tool to optimise the track

performance by selecting the best possible combination of geomaterials in the substructure layers. The method can capture the irrecoverable deformation of the substructure layers and hence, predict the long-term performance of the track, which can be used to design and optimise the maintenance cycles.

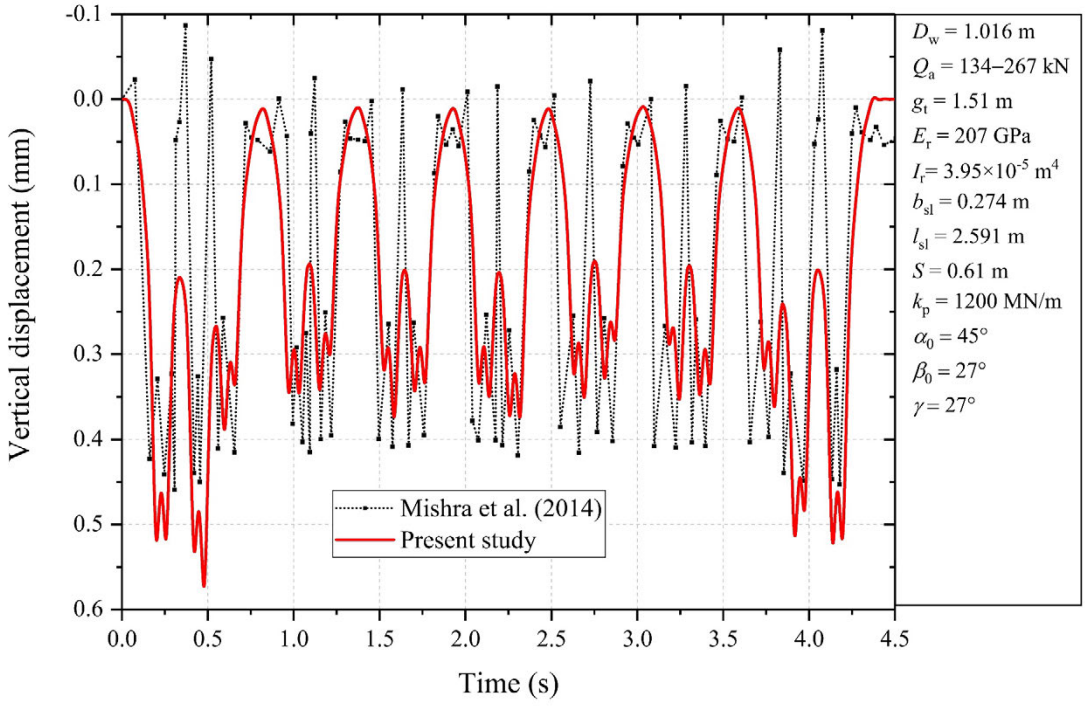

Figure 3.8 Comparison of model predictions with field results reported by Mishra et al. (2014a)

3.4 Results and Discussion

A parametric study is conducted to investigate the influence of thickness and resilient modulus of the substructure layers on the track performance. **Table 3.2** provides the range of the substructure parameters considered in the analysis. The nominal values of the parameters are shown in the parenthesis. The results are calculated for the passage of the Thalys high-speed train at a speed of 100 km/h. In each analysis, the value of one parameter is varied at a time while the other parameters are assigned the nominal values.

3.4.1 Influence of Layer Thickness

Figure 3.9(a) illustrates the influence of thickness on the average irrecoverable strain accumulated in the substructure layers when the track is subjected to a tonnage of 100 MGT. The average irrecoverable strain is the ratio of irrecoverable vertical deformation

in a layer to its initial thickness. It can be observed from the figure that the average irrecoverable strain in the ballast, subballast and subgrade layers decreases by 22%, 47% and 31%, respectively, with an increase in ballast thickness (h_b) from 0.15 m to 0.6 m. It is interesting to note that a 31% reduction in the subgrade strain, in this case, represents a decrease in the permanent subgrade settlement by 10 mm. This decrease in strain results from a combination of two counteracting effects. First, an increase in granular layer thickness increases the track modulus (and consequently, the rail seat load), which increases the stresses in substructure layers (Li et al. 2016). Second, an increase in h_b enhances the stress spreading ability of ballast and increases the depth of substructure layers from sleeper bottom, which decreases the stress (Li & Selig 1998). It is apparent that the second effect is dominant in this case, as there is an overall reduction in strain.

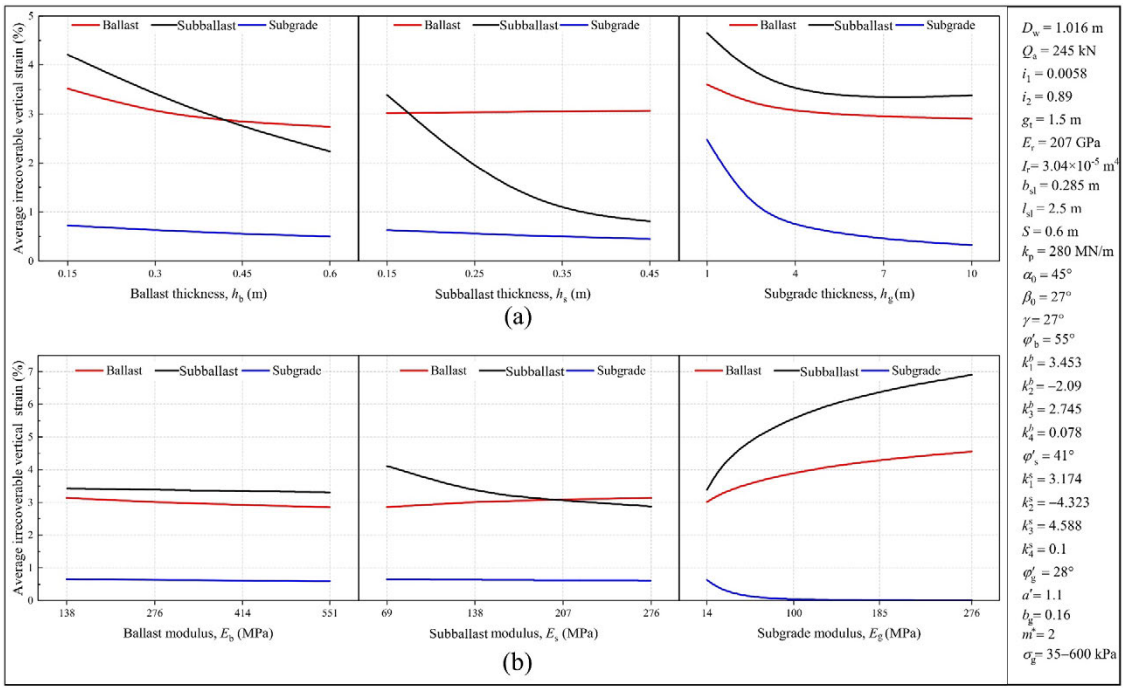

Figure 3.9 Variation of average irrecoverable strain in substructure layers with **(a)** thickness; **(b)** resilient modulus

The average irrecoverable strain in subballast and subgrade decreases by 76% and 29%, respectively, with an increase in subballast thickness (h_s) from 0.15 m to 0.45 m. However, the ballast strain increases by 1.6% with an increase in h_s. This increment is due to a rise in ballast stress with an increase in h_s for a fixed value of h_b. The increase in stress is reasonable since the second effect mentioned above is negligible for this case.

The subgrade thickness (h_g) also influences the strain in the substructure layers. The average irrecoverable strain in ballast, subballast and subgrade decreases by 19%, 27% and 87%, respectively, with an increase in h_g from 1 m to 10 m. This strain reduction in ballast and subballast is due to a decrease in the stresses in the granular layers with an increase in h_g. Since the track modulus decreases with an increase in h_g (Li et al. 2016), the rail seat load decreases and consequently, the stresses in the track layers reduce. The average subgrade strain also decreases with an increase in h_g. This is reasonable since the contribution of the deep subgrade layers to the total subgrade settlement is minimal. Thus, it is apparent that the thickness of the substructure layers significantly influences the irrecoverable deformation response of the track substructure.

3.4.2 Influence of Resilient Modulus

Figure 3.9(b) shows the variation of average irrecoverable strain accumulated in the substructure layers with the resilient modulus when the track is subjected to a tonnage of 100 MGT. It can be observed that the average irrecoverable strain in ballast, subballast and subgrade decreases by 9.3%, 2.3% and 9%, respectively, with an increase in ballast modulus (E_b) from 138 MPa to 551 MPa. The increase in E_b leads to an increment in the track modulus, which increases the rail seat load (Selig & Waters 1994). Consequently, the stress in the substructure layers must increase with an increase in E_b. However, a stiff ballast layer (with large E_b) distributes the load to a wider area of subballast as compared to a less stiff ballast layer. Therefore, the actual magnitude of the stress depends on the degree of increment of both rail seat load and the load distribution zone/area. In this case, the strain decreases, which implies that the increment in load distribution area dominates the response.

The average irrecoverable strain in subballast and subgrade decreases by 30% and 3.5%, with an increase in subballast modulus (E_s) from 69 MPa to 276 MPa. However, the ballast strain increases by 9.8% with an increase in E_s. The increase in ballast strain may be ascribed to a reduction in the load spread area with an increase in E_s. Burmister (1958) showed that the σ_v at the interface of a two-layer medium increases with a reduction in the ratio of modulus of upper to lower layer materials. In the present study, this increase in σ_v (due to a reduction in E_b/E_s ratio) is manifested by a corresponding decrease in α.

Consequently, the stress and the associated strain in the ballast layer increases with an increase in E_s. Nevertheless, β increases with an increase in E_s and therefore, the stress and the associated strain in the subballast and subgrade layers decreases.

It is apparent from **Figure 3.9(b)** that E_g plays a significant role in the irrecoverable response of the substructure. The average irrecoverable strain in the ballast and subballast layers increases by 51% and 104%, with an increase in E_g from 14 MPa to 276 MPa, respectively. However, the subgrade strain decreases by 99% with an increase in E_g. An increment in E_g increases the track modulus and the rail seat load (Li et al. 2016). Thus, the stresses in the substructure layers increase with an increase in E_g. Consequently, the ballast and subballast strain increases. However, in the subgrade, the increase in stress is compensated by a corresponding increase in strength with an increment in E_g (Li et al. 2016). Therefore, the subgrade settlement decreases with an increase in E_g.

Thus, the present method can accurately predict the variation in the irrecoverable deformation of the track layers in response to the track parameters. This method may help the practising engineers to evaluate the magnitude of track substructure settlement after the completion of a fixed number of load cycles (or tonnage). This may aid in the adequate planning of the maintenance cycles by predicting the time when the substructure settlement exceeds a permissible/safe limit. Moreover, using the present approach, the track performance can be enhanced by optimising the substructure layer parameters.

3.5 Advantages, Limitations and Future Scope

The advantages of the proposed method are as follows:

- Track response is evaluated by solving the equations in a step-by-step manner, which can be carried out by developing MATLAB codes (MathWorks Inc. 2021) or programs in other programming languages.
- There is no need to generate the model geometry and only the values of input parameters are required.
- Present approach is computationally more efficient as compared to the FE based methods.

- Conducting parametric analyses using the present approach is much easier as compared to FE based methods.
- Interpretation of predicted response is easy.

The limitations of the present approach are as follows:

- Principal stress rotation: The present approach neglects the influence of principal stress rotation on the track response. The rotation of principal stress can affect the irrecoverable deformations of the geomaterials (Gräbe & Clayton 2009).
- Vehicle-track interaction: In the present study, a dynamic amplification factor has been employed to account for the additional loads applied on the track due to vehicle-track interaction, which is a simplified approach.
- Loading direction: The present approach considers loading only along the vertical direction. However, in reality, the track is subjected to a combination of loads along the vertical, lateral and longitudinal directions (Esveld 2001).
- Empirical approach: The present method employs empirical models to predict the irrecoverable deformations, which lack general applicability under various loading conditions and soil types.

The empirical approach is replaced with a mechanistic approach in CHAPTER 3 (PART-B) and the effect of principal stress rotation is treated in CHAPTER 5, while other limitations shall be addressed in future investigations to improve the accuracy of the present approach.

3.6 Concluding Remarks

This section of the chapter presents an integrated approach to evaluate the recoverable and irrecoverable responses of the substructure layers in ballasted railway tracks. The track substructure layers have been represented as lumped masses connected by springs and dashpots, which accounts for the discrete sleeper support. The key features of the present approach include:

- Consideration of more appropriate inclusion of three substructure layers (ballast, subballast and subgrade), compared to the existing models simplifying track substructure as single or dual layers.

- Incorporation of overlapping of the load distribution pyramids along both transverse and longitudinal directions, which is an improvement over the existing models.
- Prediction of irrecoverable deformation in ballast, subballast and subgrade layers using empirical settlement models for individual layers.

A good agreement between the responses predicted using the present method and the field investigations reported in the literature clearly indicates that the model can accurately predict the behaviour of track substructure layers. The parametric investigation reveals that the irrecoverable deformation in the substructure layers is sensitive to the resilient modulus and thickness of individual layers. The response of each track layer is affected by the adjacent layers, and the incorporation of a multi-layered track structure enables a more accurate prediction of track behaviour. The proposed method is simple, computationally efficient and can be used readily as a tool by practising engineers to optimise the track performance.

CHAPTER 3 (PART-B)
REPLACING THE EMPIRICAL APPROACH WITH A MECHANISTIC APPROACH TO EVALUATE TRACK RESPONSE

3.7 General

The previous part of this chapter elucidated the development of an innovative approach for predicting the transient and long-term performance of the ballasted railway tracks. However, the irrecoverable deformation in the substructure layers was predicted using empirical settlement equations, which lack general applicability under various loading conditions and soil types. This part of the chapter attempts to replace the empirical approach with a mechanistic approach for predicting the irrecoverable deformations in the track layers.

3.8 Background

The ballasted railway track is the most commonly used track system, which employs multiple layers of geomaterials to safely transmit the train-induced load into the subgrade soil. These layers are conventionally designed using empirical and simplified theoretical approaches that are based on experience with in-service tracks, augmented with extensive laboratory and field testing data (Heath et al. 1972; Li & Selig 1998; Li et al. 2016). Usually, these conventional design approaches lack general applicability in different traffic loading and soil conditions. This serious limitation has recently become more apparent due to a dramatic hike in transportation needs, which has accelerated the deterioration of the existing tracks and incurred significant maintenance costs (Nimbalkar & Indraratna 2016). Thus, to derive optimum performance from the railway tracks, there is an inevitable need for a more reliable, practical and adaptable design method. The development of such a design technique requires a detailed analysis of the mechanical behaviour of track substructure layers and their mutual interaction.

The prediction of accumulative permanent deformation in the substructure layers has attracted a great deal of attention in the last few decades. Several researchers have developed empirical models based on extensive field and laboratory investigations to predict the accumulation of irrecoverable deformation in the substructure layers (Lekarp et al. 2000; Dahlberg 2001; Indraratna & Nimbalkar 2013). However, these models lack

a detailed rational theoretical basis, and their applications are often limited to specific conditions on which they are based. Nevertheless, laboratory tests are often restricted in size due to financial constraints. Meanwhile, the cost and the number of influencing factors in field investigations is too large for accurate parametric studies.

The numerical modelling provides an alternative approach to simulate the track response under the repetitive wheel loads and understand the role of each layer on the overall track response. The behaviour of the ballasted track has been studied in the past using 2D, 2.5D and 3D FE analyses. The FE modelling accurately simulates the dynamic behaviour of the railway tracks and the wave propagation phenomenon. However, these models may require an extensive amount of computational resources and time to accurately predict the inelastic deformation in the substructure layers accumulated over a large number of load cycles.

The analytical modelling technique offers a relatively faster and computationally more efficient alternative to FE analyses for the accurate prediction of track response. Consequently, numerous analytical models with varying degree of complexity have been established to predict the response of the railway track and the surrounding area during train passage (Knothe & Grassie 1993; Esveld 2001; Connolly et al. 2015). A few studies have also considered the substructure layers as an assemblage of discrete particles. Suiker et al. (2001a) modelled the ballast as a layer of discrete particles that are mutually connected by elastic longitudinal and shear springs, and studied the propagation of body waves through this layer. In a similar study, Suiker et al. (2001b) investigated the steady-state response of the ballast layer composed of discrete particles to a moving, harmonically vibrating load. Most of these studies investigated the transient response of the tracks during train passage, and research regarding the prediction of settlement accumulated in the substructure layers over a specified period or tonnage is still very limited.

This section of the chapter attempts to evaluate the mechanical response of the ballasted track substructure layers using a novel simplified geotechnical rheological model. The proposed model can predict both the transient response during a train passage and the irrecoverable deformations accumulated over a specified period or tonnage. The elastic

response is represented using elastic springs, while the viscous response is captured through dashpots (or dampers). The plastic (or irrecoverable) response is simulated using the slider elements. The first part of the section describes the viscoelasto-plastic model formulation, and the second part illustrates its validation against published field investigation data. Subsequently, a parametric investigation is carried out to study the influence of train and track parameters on the cumulative deformation. The purpose of this study is to provide a simple geotechnical rheological technique that can be used for a quick evaluation of the track substructure response under repeated traffic loadings.

3.9 Model Description

The evaluation of track response in the present approach is carried out in two parts. Firstly, the train-induced load transmitted to the substructure layers is calculated using the procedure outlined in Section 3.2.1. As an improvement to the method described in APPENDIX B, the stress state in this computational model is evaluated using the modified Boussinesq approach. In the second part, the transient and irrecoverable response of the track layers is predicted using a viscoelasto-plastic geotechnical rheological model.

3.9.1 Determination of Load

The rail seat load-time history is determined using the track loading model discussed in Section 3.2.1 for all the sleepers considered in the analysis. **Figure 3.10** shows the deflection profile below the train wheels, calculated using Equation 3.2, at time instant t_1. The total deflection below each sleeper due to multiple wheels, at each time instant, can be calculated using the superposition principle. The resultant deflection profile is represented using dashed lines in **Figure 3.10**. After evaluating the total deflection, the vertical rail seat load (or sleeper reaction) at each time instant can be determined by employing Equation 3.3 for all the sleepers under consideration (25 in the present study). Similarly, the entire load-time history during the passage of all the wheels of a train can be calculated for all the sleepers.

To assess the suitability of this approach, the predicted rail seat load-time history is compared with the data recorded in the field measurements. **Figure 3.11** depicts a comparison of the rail seat load predicted using the present method with the field data

reported by Mishra et al. (2017) during the passage of the Acela Express passenger train. The rail seat load or sleeper reaction, in the field, was calculated by subtracting the wheel load measured at sleeper location [see **Figure 3.11(b)**] from that measured between adjacent sleepers [see **Figure 3.11(a)**] (Mishra et al. 2014b). It can be observed that the rail seat load-time history predicted using the present method is in an acceptable agreement with the in-situ measurements [see **Figure 3.11(c)**]. Therefore, this method can accurately predict the load transmitted to the track substructure layers during the train passage.

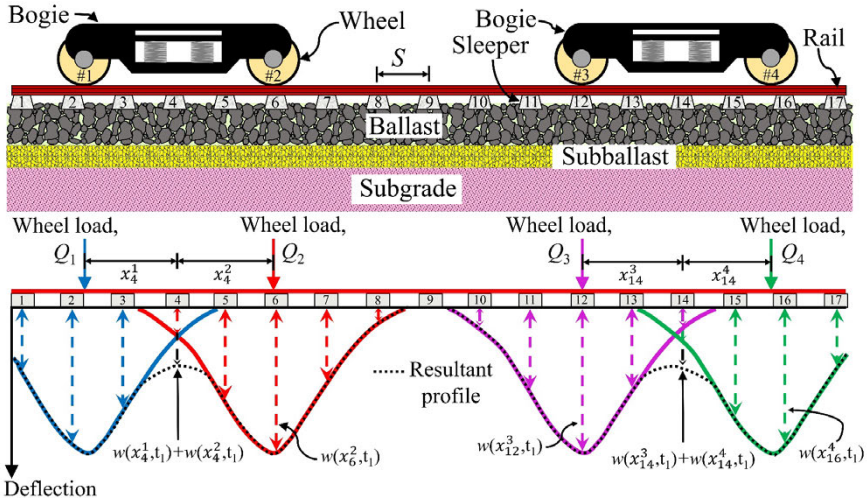

Figure 3.10 Deflection profile during the passage of train wheels

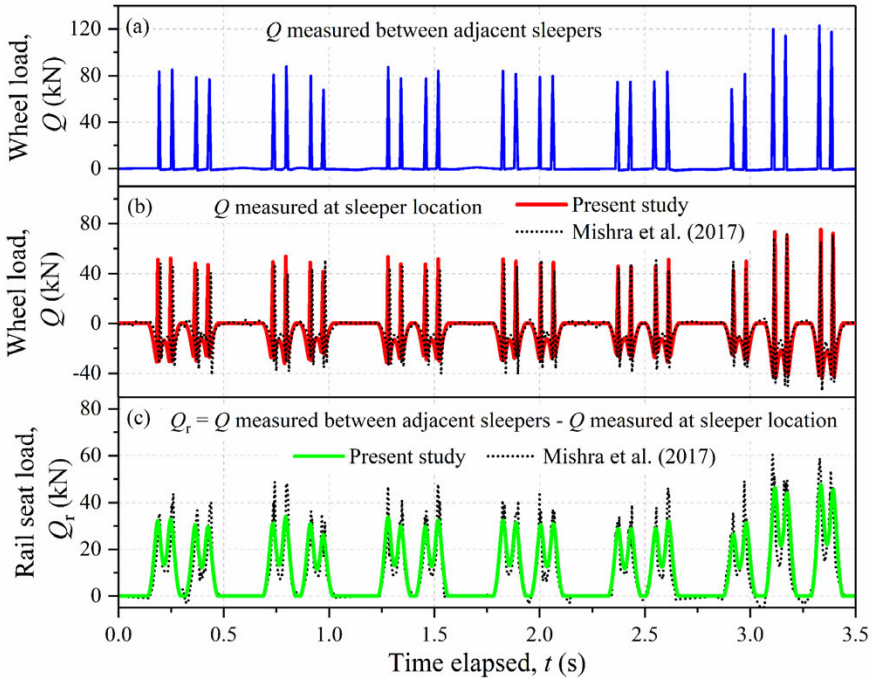

Figure 3.11 (a) Wheel load measured between adjacent sleepers (Mishra et al. 2017); **(b)** wheel load measured at sleeper location; **(c)** sleeper reaction force or rail seat load

3.9.1.1 Stress Distribution

The stress distribution below a sleeper is calculated using the Boussinesq solutions for a uniformly loaded circular footing (Waterways Experiment Station 1954; Ahlvin & Ulery 1962; Poulos & Davis 1974). However, the Boussinesq approach considers the substructure as an isotropic elastic homogenous medium in contrast to the actual layered structure. An approximate solution to this problem is the theory of equivalent thickness proposed by Palmer & Barber (1941) and Odemark (1949), which transforms the multiple layers of soil, such as ballast and subballast, into an equivalent thickness of single layer material. Using this theory, the equivalent thickness of the ballast (h_{eb}) and subballast (h_{es}) layers can be determined by (Hirai 2008):

$$h_{\mathrm{eb}} = \begin{cases} h_{\mathrm{b}} \left[\dfrac{E_{\mathrm{b}}\left(1-\nu_{\mathrm{g}}^2\right)}{E_{\mathrm{g}}\left(1-\nu_{\mathrm{b}}^2\right)}\right]^{\frac{1}{3}}, & E_{\mathrm{b}} > E_{\mathrm{g}} \\ h_{\mathrm{b}}\langle 0.75 + 0.25 \left[\dfrac{E_{\mathrm{b}}\left(1-\nu_{\mathrm{g}}^2\right)}{E_{\mathrm{g}}\left(1-\nu_{\mathrm{b}}^2\right)}\right]^{\frac{1}{3}} \rangle, & E_{\mathrm{b}} < E_{\mathrm{g}} \end{cases} \quad 3.26$$

$$h_{\mathrm{es}} = \begin{cases} h_{\mathrm{s}} \left[\dfrac{E_{\mathrm{s}}\left(1-\nu_{\mathrm{g}}^2\right)}{E_{\mathrm{g}}\left(1-\nu_{\mathrm{s}}^2\right)}\right]^{\frac{1}{3}}, & E_{\mathrm{s}} > E_{\mathrm{g}} \\ h_{\mathrm{s}}\langle 0.75 + 0.25 \left[\dfrac{E_{\mathrm{s}}\left(1-\nu_{\mathrm{g}}^2\right)}{E_{\mathrm{g}}\left(1-\nu_{\mathrm{s}}^2\right)}\right]^{\frac{1}{3}} \rangle, & E_{\mathrm{s}} < E_{\mathrm{g}} \end{cases} \quad 3.27$$

Thus, the stress distribution is determined by assuming the sleeper-ballast contact pressure below each rail seat to be uniformly distributed over a circular area whose size is related to the sleeper dimensions [as shown in APPENDIX C (**Figure C.1**)]. A similar assumption has been used in past studies for the sleeper-ballast contact pressure [e.g., Love's equation (Selig & Waters 1994)].

3.9.2 Prediction of the Track Response

The substructure of the ballasted railway tracks comprises of multiple layers of granular materials that undergo both recoverable and irrecoverable deformations under the application of repeated traffic loadings. In this section of the chapter, the recoverable and irrecoverable response of the substructure layers is predicted using a novel geotechnical rheological model. Three substructure layers have been considered: ballast, subballast and subgrade. The model employs elastic and viscous elements, such as springs and

dashpots, to represent the viscoelastic response while the slider elements capture the irrecoverable response of the substructure layers.

Figure 3.12 presents the geotechnical rheological model of the track used in this study. One half of the track is modelled due to the symmetry with respect to the track's centreline. The interfaces between the substructure layers (ballast-subballast and subballast-subgrade interfaces) are considered rigid, i.e., no slippage is allowed between the layers. The track substructure layers are represented as discrete masses that are connected using elastic springs, viscous dampers (or dashpots) and plastic slider elements, as shown in **Figure 3.12**.

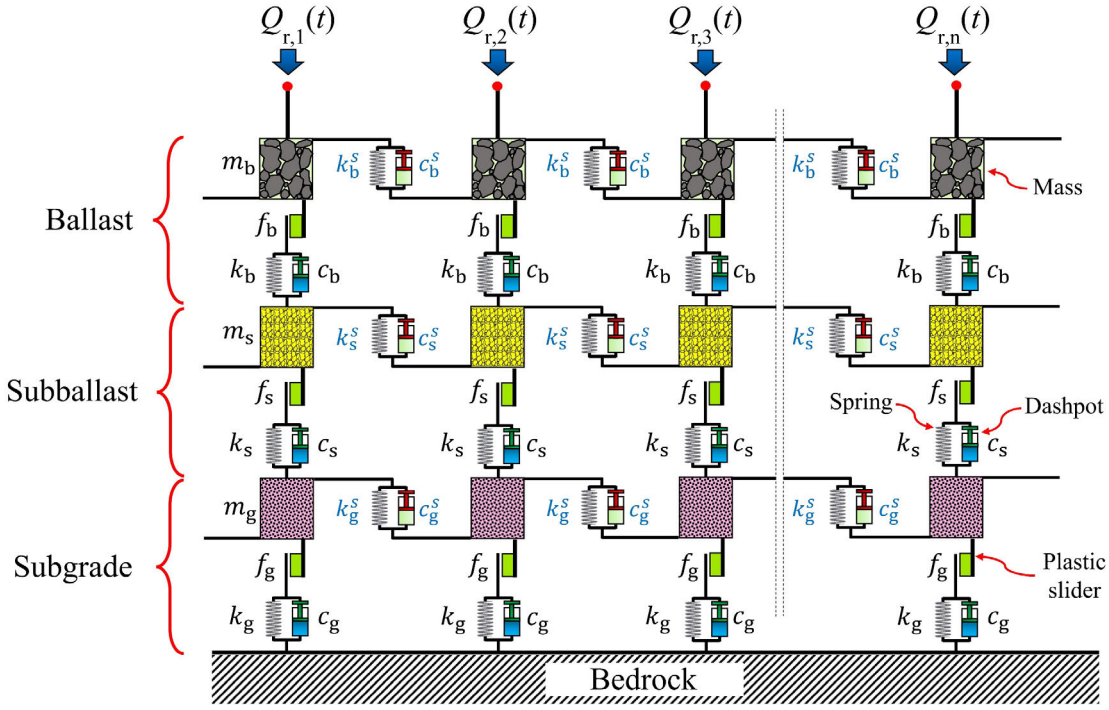

Figure 3.12 Simplified geotechnical rheological model of the ballasted railway track

As the loading commences, the springs and dampers deform viscoelastically while the plastic slider elements remain fixed. Once the stress state in the substructure layers reaches the yield surface (defined by f_b, f_s and f_g for ballast, subballast and subgrade, respectively), the slider elements start moving. During unloading, the springs and dampers deform, however, the plastic slider element does not move. When the track is reloaded, the springs and dampers deform, whereas the slider element moves only if the stress state reaches the yield surface. Thus, the movement of the slider element is irrecoverable, and it accumulates with an increase in the number of load repetitions. The

amount by which the slider element moves during a loading stage can be described by using an appropriate constitutive relationship, which is discussed later in section 3.9.2.2. Thus, the total displacement in each substructure layer of the track can be decomposed into a recoverable part (viscoelastic) and an irrecoverable part (plastic) as:

$$z_{\mathrm{g}}(t) = z_{\mathrm{g}}^{ve}(t) + z_{\mathrm{g}}^{p}(t);\ z_{\mathrm{s}}(t) = z_{\mathrm{g}}(t) + z_{\mathrm{s}}^{ve}(t) + z_{\mathrm{s}}^{p}(t);$$

$$z_{\mathrm{b}}(t) = z_{\mathrm{s}}(t) + z_{\mathrm{b}}^{ve}(t) + z_{\mathrm{b}}^{p}(t) \qquad 3.28$$

where the superscript *ve* and *p* represent the viscoelastic and plastic components of the response, respectively. In this equation, the initiation and evolution of the plastic displacement in the substructure layers can be described by using an appropriate constitutive relationship, which is discussed later in section 3.9.2.2.

3.9.2.1 Equations of Motion for the Track Layers

On applying the dynamic equilibrium condition in the rheological model shown in **Figure 3.12**, the following system of equations in the incremental form can be derived:

$$\begin{bmatrix} m_{\mathrm{g}} & 0 & 0 \\ 0 & m_{\mathrm{s}} & 0 \\ 0 & 0 & m_{\mathrm{b}} \end{bmatrix} \begin{Bmatrix} d\ddot{z}_{\mathrm{g,n}} \\ d\ddot{z}_{\mathrm{s,n}} \\ d\ddot{z}_{\mathrm{b,n}} \end{Bmatrix} + \begin{bmatrix} c_{\mathrm{g}} + c_{\mathrm{s}} + 2c_{\mathrm{g}}^{s} & -c_{\mathrm{s}} & 0 \\ -c_{\mathrm{s}} & c_{\mathrm{s}} + c_{\mathrm{b}} + 2c_{\mathrm{s}}^{s} & -c_{\mathrm{b}} \\ 0 & -c_{\mathrm{b}} & c_{\mathrm{b}} + 2c_{\mathrm{b}}^{s} \end{bmatrix} \begin{Bmatrix} d\dot{z}_{\mathrm{g,n}} \\ d\dot{z}_{\mathrm{s,n}} \\ d\dot{z}_{\mathrm{b,n}} \end{Bmatrix}$$
$$+ \begin{bmatrix} k_{\mathrm{g}} + k_{\mathrm{s}} + 2k_{\mathrm{g}}^{s} & -k_{\mathrm{s}} & 0 \\ -k_{\mathrm{s}} & k_{\mathrm{s}} + k_{\mathrm{b}} + 2k_{\mathrm{s}}^{s} & -k_{\mathrm{b}} \\ 0 & -k_{\mathrm{b}} & k_{\mathrm{b}} + 2k_{\mathrm{b}}^{s} \end{bmatrix} \begin{Bmatrix} dz_{\mathrm{g,n}} \\ dz_{\mathrm{s,n}} \\ dz_{\mathrm{b,n}} \end{Bmatrix}$$
$$+ \begin{bmatrix} -k_{\mathrm{g}} - 2k_{\mathrm{g}}^{s} & k_{\mathrm{s}} & 0 \\ -2k_{\mathrm{s}}^{s} & -k_{\mathrm{s}} - 2k_{\mathrm{s}}^{s} & k_{\mathrm{b}} \\ -2k_{\mathrm{b}}^{s} & -2k_{\mathrm{b}}^{s} & -k_{\mathrm{b}} - 2k_{\mathrm{b}}^{s} \end{bmatrix} \begin{Bmatrix} dz_{\mathrm{g,n}}^{p} \\ dz_{\mathrm{s,n}}^{p} \\ dz_{\mathrm{b,n}}^{p} \end{Bmatrix}$$
$$+ \begin{bmatrix} -c_{\mathrm{g}} - 2c_{\mathrm{g}}^{s} & c_{\mathrm{s}} & 0 \\ -2c_{\mathrm{s}}^{s} & -c_{\mathrm{s}} - 2c_{\mathrm{s}}^{s} & c_{\mathrm{b}} \\ -2c_{\mathrm{b}}^{s} & -2c_{\mathrm{b}}^{s} & -c_{\mathrm{b}} - 2c_{\mathrm{b}}^{s} \end{bmatrix} \begin{Bmatrix} d\dot{z}_{\mathrm{g,n}}^{p} \\ d\dot{z}_{\mathrm{s,n}}^{p} \\ d\dot{z}_{\mathrm{b,n}}^{p} \end{Bmatrix}$$
$$= \begin{Bmatrix} dF_{\mathrm{g,n}} \\ dF_{\mathrm{s,n}} \\ dF_{\mathrm{b,n}} \end{Bmatrix} + \begin{bmatrix} c_{\mathrm{g}}^{s} & 0 & 0 \\ 0 & c_{\mathrm{s}}^{s} & 0 \\ 0 & 0 & c_{\mathrm{b}}^{s} \end{bmatrix} \begin{Bmatrix} d\dot{z}_{\mathrm{g,n+1}} + d\dot{z}_{\mathrm{g,n-1}} \\ d\dot{z}_{\mathrm{s,n+1}} + d\dot{z}_{\mathrm{s,n-1}} \\ d\dot{z}_{\mathrm{b,n+1}} + d\dot{z}_{\mathrm{b,n-1}} \end{Bmatrix} + \begin{bmatrix} k_{\mathrm{g}}^{s} & 0 & 0 \\ 0 & k_{\mathrm{s}}^{s} & 0 \\ 0 & 0 & k_{\mathrm{b}}^{s} \end{bmatrix} \begin{Bmatrix} dz_{\mathrm{g,n+1}} + dz_{\mathrm{g,n-1}} \\ dz_{\mathrm{s,n+1}} + dz_{\mathrm{s,n-1}} \\ dz_{\mathrm{b,n+1}} + dz_{\mathrm{b,n-1}} \end{Bmatrix}$$
$$- \begin{bmatrix} c_{\mathrm{g}}^{s} & 0 & 0 \\ c_{\mathrm{s}}^{s} & c_{\mathrm{s}}^{s} & 0 \\ c_{\mathrm{b}}^{s} & c_{\mathrm{b}}^{s} & c_{\mathrm{b}}^{s} \end{bmatrix} \begin{Bmatrix} d\dot{z}_{\mathrm{g,n+1}}^{p} + d\dot{z}_{\mathrm{g,n-1}}^{p} \\ d\dot{z}_{\mathrm{s,n+1}}^{p} + d\dot{z}_{\mathrm{s,n-1}}^{p} \\ d\dot{z}_{\mathrm{b,n+1}}^{p} + d\dot{z}_{\mathrm{b,n-1}}^{p} \end{Bmatrix} - \begin{bmatrix} k_{\mathrm{g}}^{s} & 0 & 0 \\ k_{\mathrm{s}}^{s} & k_{\mathrm{s}}^{s} & 0 \\ k_{\mathrm{b}}^{s} & k_{\mathrm{b}}^{s} & k_{\mathrm{b}}^{s} \end{bmatrix} \begin{Bmatrix} dz_{\mathrm{g,n+1}}^{p} + dz_{\mathrm{g,n-1}}^{p} \\ dz_{\mathrm{s,n+1}}^{p} + dz_{\mathrm{s,n-1}}^{p} \\ dz_{\mathrm{b,n+1}}^{p} + dz_{\mathrm{b,n-1}}^{p} \end{Bmatrix} \qquad 3.29$$

where the superscript *p* represents the irrecoverable component of the response. The force increment $dF_{\mathrm{b,n}}$ is equal to the increment in the rail seat load calculated using Equation 3.3 for the n^{th} sleeper, whereas the force increments $dF_{\mathrm{g,n}}$ and $dF_{\mathrm{s,n}}$ are considered as zero.

Equation 3.29 can be rearranged into a general force-displacement relationship form as follows:

$$d\bar{\boldsymbol{F}} = \boldsymbol{K}d\boldsymbol{z} \qquad 3.30$$

where $\boldsymbol{K}$ is the stiffness matrix; $d\bar{\boldsymbol{F}}$ and $d\boldsymbol{z}$ are the incremental equivalent force and displacement vectors, respectively (see APPENDIX D). This equation can be solved using the Newmark's–β numerical integration scheme at each time instant to evaluate the complete track response.

The damping coefficients for the three substructure layers are evaluated using Equation 3.19. To evaluate the vibrating mass and stiffness of the substructure layers, pyramidal distribution of vertical load from the sleeper bottom to the track substructure layers is assumed, which incorporates the overlapping of the load distribution pyramids along both longitudinal and transverse directions (see Section 3.2.2.2). **Figure 3.13** illustrates the effective region of the load distribution pyramids beneath each sleeper position. The geometry of the load distribution pyramids is first identified based on the thickness of the substructure layers, the stress distribution angles, the effective length and the width of sleeper. Subsequently, the vibrating mass and stiffness for each track layer are determined (see section 3.2.2.2).

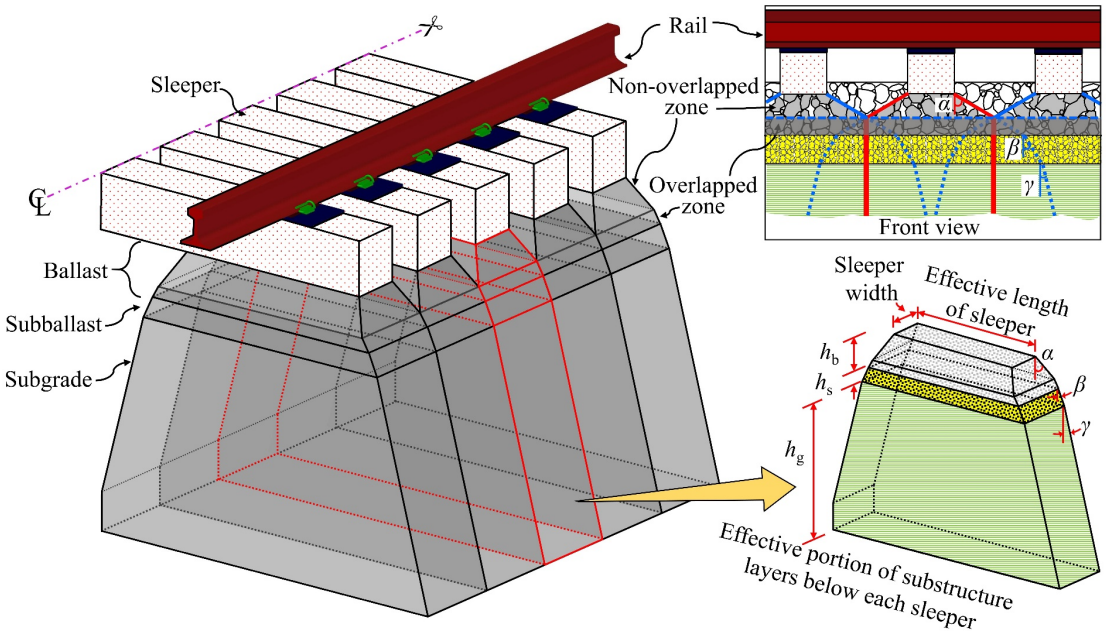

Figure 3.13 Effective region of the track substructure layers considered in the analysis

The stress distribution angles in this method are determined by extending the approach used by Han et al. (2011) to the track substructure layers:

$$\alpha = \tan^{-1}\left\{\frac{a}{h_{\mathrm{b}}}\left[\sqrt{\frac{\sigma_{\mathrm{sb}}}{\sigma_{\mathrm{bs}}}}-1\right]\right\} \quad 3.31$$

$$\beta = \tan^{-1}\left\{\frac{(a+h_{\mathrm{b}}\tan\alpha)}{h_{\mathrm{s}}}\left[\sqrt{\frac{\sigma_{\mathrm{bs}}}{\sigma_{\mathrm{sg}}}}-1\right]\right\} \quad 3.32$$

$$\gamma = \tan^{-1}\left\{\frac{(a+h_{\mathrm{b}}\tan\alpha+h_{\mathrm{s}}\tan\beta)}{h_{\mathrm{g}}}\left[\sqrt{\frac{\sigma_{\mathrm{sg}}}{\sigma_{\mathrm{go}}}}-1\right]\right\} \quad 3.33$$

where σ_{sb}, σ_{bs} and σ_{sg} are the vertical stresses (N/m^2) at the sleeper-ballast, ballast-subballast, and subballast-subgrade interfaces, respectively; a is an equivalent radius of the sleeper-ballast contact area (m); σ_{go} is the vertical stress (N/m^2) at the bottom of the subgrade layer.

3.9.2.2 Slider Elements

The following sections describe the constitutive relationships used for the plastic slider elements in the case of granular layers (ballast and subballast) and subgrade.

Granular Layers.

The constitutive relationship introduced here for the granular materials is based on the Nor-sand model developed by Jefferies (1993) and Jefferies & Shuttle (2002) for triaxial and 3D loading condition, respectively. It is a state parameter based model, which has been derived from the fundamental axioms of the critical state theory. This approach allows the simulation of the response of granular materials under general stress conditions over a wide range of density and stress states, using the same set of model parameters. The technique is based on isotropic hardening plasticity and employs an associated flow rule. The maximum dilatancy in this model is controlled by applying a limit on the hardening of the yield surface. The present relationship for the slider element employs all the parameters associated with the original Nor-sand model with one additional parameter that characterises the behaviour under repeated loading conditions.

Yield Surface.

The yield surface (f) for the slider element in the case of granular materials (ballast and subballast) is defined as (Jefferies & Been 2015):

$$f = \frac{\eta}{M_{\mathrm{i}}} + \ln\left(\frac{p}{p_{\mathrm{i}}}\right) - 1 \qquad 3.34$$

where the subscript i represents the image state condition; M is the critical stress ratio; η is the stress ratio; $\eta = q/p$, where q and p are deviatoric and mean effective stresses, respectively; $p = \boldsymbol{\sigma}_{\mathrm{kk}}/3$; $q = \sqrt{\frac{3}{2}\boldsymbol{s}_{\mathrm{ij}}\boldsymbol{s}_{\mathrm{ij}}}$, where $\boldsymbol{s}_{\mathrm{ij}}$ is the deviatoric stress tensor ($\boldsymbol{s}_{\mathrm{ij}} = \boldsymbol{\sigma}_{\mathrm{ij}} - p\delta_{\mathrm{ij}}$, where $\boldsymbol{\sigma}_{\mathrm{ij}}$ and δ_{ij} are the stress tensor and Kronecker delta, respectively). The stress state for the slider element is determined using the modified Boussinesq approach discussed in section 3.9.1.1. This technique of translating the boundary force into the continuum stress variables for the slider elements is consistent with the approach used by Di Prisco & Vecchiotti (2006).

The image state corresponds to the condition where zero dilatancy (D) exists (i.e., $D = d\varepsilon_{\mathrm{v}}/d\varepsilon_{\mathrm{q}} = 0$, where $d\varepsilon_{\mathrm{v}}$ and $d\varepsilon_{\mathrm{q}}$ are the volumetric and deviatoric strain increments, respectively). The image mean effective stress (p_{i}) controls the size of the yield surface. The critical stress ratio corresponding to the image state is calculated as (Jefferies & Been 2015):

$$M_{\mathrm{i}} = M\left[1 - \frac{N_{\mathrm{v}}\chi_{\mathrm{i}}|\psi_{\mathrm{i}}|}{M_{\mathrm{tc}}}\right] \qquad 3.35$$

where the subscripts i and tc represent the image state and triaxial compression condition, respectively; N_{v} is the volumetric coupling coefficient suggested by Nova (1982); ψ_{i} is the image state parameter [$\psi_{\mathrm{i}} = \psi + \lambda \ln(p_{\mathrm{i}}/p)$]; ψ is the state parameter ($\psi = e - e_{\mathrm{c}}$); e is the current void ratio; e_{c} is the void ratio on the critical state line at the current mean effective stress ($e_{\mathrm{c}} = \Gamma - \lambda \ln p$); Γ is the critical void ratio at p = 1 kPa; λ is the slope of the critical state line in e–ln p space; χ relates maximum dilatancy to the state parameter [$\chi_{\mathrm{i}} = \chi_{\mathrm{tc}}/(1-\lambda\chi_{\mathrm{tc}}/M_{\mathrm{itc}})$]; M_{itc} is the critical stress ratio corresponding to the image of the critical state for triaxial compression condition. The stress-dilatancy relationship for this model is given as (Jefferies & Been 2015):

$$D_{\mathrm{p}} = \frac{d\varepsilon_{\mathrm{v}}^{p}}{d\varepsilon_{\mathrm{q}}^{p}} = M_{\mathrm{i}} - \eta \tag{3.36}$$

where D_{p} is the plastic dilatancy; $d\varepsilon_{\mathrm{v}}^{p}$ and $d\varepsilon_{\mathrm{q}}^{p}$ are the plastic volumetric and deviatoric strain increments, respectively. The plastic strain increments are determined using:

$$d\boldsymbol{\varepsilon}_{\mathrm{ij}}^{p} = \Lambda_{\mathrm{g}} \frac{\partial f(q, p, M_{\mathrm{i}}, p_{\mathrm{i}})}{\partial \boldsymbol{\sigma}_{\mathrm{ij}}} \tag{3.37}$$

where $d\boldsymbol{\varepsilon}_{\mathrm{ij}}^{p}$ is the plastic strain increment; Λ_{g} is a scalar expressed as:

$$\Lambda_{\mathrm{g}} = \frac{\mathcal{I}(d\boldsymbol{\varepsilon}_{\mathrm{ij}}^{p})}{\partial f(q, p, M_{\mathrm{i}}, p_{\mathrm{i}}) / \partial \mathcal{I}(\boldsymbol{\sigma}_{\mathrm{ij}})} = d\varepsilon_{\mathrm{q}}^{p} \tag{3.38}$$

where $\mathcal{I}$ is the tensorial invariant. The displacement increment of the slider element is then calculated by multiplying the granular layer thickness with the plastic strain increment ($d\varepsilon_{\mathrm{z}}^{p}$) in the vertical direction (determined using Equation 3.37). The plastic displacement rate of the slider element is computed by differentiating the plastic displacement in the vertical direction with respect to time. These values are used as an input in Equation 3.29 to determine the total track response.

Hardening Rule.

The hardening rule formulation follows the Nor-sand model (Jefferies & Been 2015), but it has been modified in this study to realistically simulate the response of granular soil under repeated loading condition:

$$\frac{dp_{\mathrm{i}}}{p_{\mathrm{i}}} = \frac{H}{R_{\mathrm{i}}} \frac{M_{\mathrm{i}}}{M_{\mathrm{itc}}} \left(\frac{p}{p_{\mathrm{i}}}\right)^{2} \left[e^{\left(\frac{-\chi_{\mathrm{i}}\psi_{\mathrm{i}}}{M_{\mathrm{itc}}}\right)} - \left(\frac{p_{\mathrm{i}}}{p}\right) \right] d\varepsilon_{\mathrm{q}}^{p} \tag{3.39}$$

where dp_{i} is the increment in mean effective stress at the image state; H is the hardening parameter. The modification from the original Nor-sand model is the introduction of the parameter R_{i}, which controls the magnitude of plastic strain accumulated during repeated loading condition. This parameter is calculated as:

$$R_{\mathrm{i}} = e^{-\frac{1}{a_{\mathrm{h}}}\left(1-\frac{p_{\mathrm{i}}}{p_{\mathrm{ic}}}\right)} \sqrt{\frac{p_{\mathrm{i}} - p_{\mathrm{im}}}{p_{\mathrm{ic}} - p_{\mathrm{im}}}} \tag{3.40}$$

where a_{h} is a cyclic hardening parameter that can be determined by calibration of the model against the experimental data; p_{im} is the minimum value of p_{i} observed; p_{ic} is a

parameter that accumulates with the activation (or reactivation) of the slider element and is calculated as p_{ic} (t+dt) = p_{ic} (t) + dp_i when the slider element is activated and p_{ic} (t+dt) = p_{ic} (t), when the slider element is deactivated. As the number of activation-deactivation cycles of the slider element increases, p_{ic} increases and the magnitude of R_i decreases. Consequently, the magnitude of $d\varepsilon_q^p$ decreases with an increase in the number of activation-deactivation cycles. The conditions for activation and deactivation of the slider element are discussed in the next section.

Loading/unloading Condition.

In order to distinguish between the loading (activation) and unloading (deactivation) of the slider element during repeated loading conditions, the Kuhn-Tucker relations must be met (Simo & Hughes 1998; Suiker & de Borst 2003):

$$\Lambda_g \geq 0; f(q, p, M_i, p_i) \leq 0; \Lambda_g f(q, p, M_i, p_i) = 0 \qquad 3.41$$

Equation 3.41 suggests that for the activation or loading of the slider element, Λ_g must be greater than zero, the stresses must be admissible and the yield condition remains satisfied. The unloading of the slider element occurs when the stresses are admissible, and the yield conditions are not satisfied. The unloading may also occur if the yield condition is satisfied, but Λ_g is zero.

Figure 3.14 shows an example of the generation of irrecoverable deformations during train-induced repeated loading. The dashed vertical lines in the figure correspond to the time of passage of individual axle. For each axle pass, the slider element remains inactive until the plastic loading condition (Equation 3.41) is satisfied. During the active state of the slider element (represented by bold lines in deviatoric stress-time history in **Figure 3.14**), the magnitude of irrecoverable deformation increment ($d\varepsilon_q^p$) for each time instant is calculated using Equation 3.39. Subsequently, the cumulative plastic strain at any instant is determined as $\varepsilon_q^p(t + dt) = \varepsilon_q^p(t) + d\varepsilon_q^p$, where dt is the time step.

During the inactive state of the slider element, no irrecoverable deformation is generated ($d\varepsilon_q^p = 0$), and the magnitude of R_i is considered as 0. For the first active state of the slider element, the magnitude of R_i remains at unity since p_{ic} and p_i are equal. With an increase in the number of axle passes, the magnitude of R_i decreases since p_{ic} accumulates

with the activation (or reactivation) of the slider element between consecutive axle passes (see Equation 3.40). Since the plastic strain increment depends on the magnitude of R_i, it decreases with an increase in the number of axle passes.

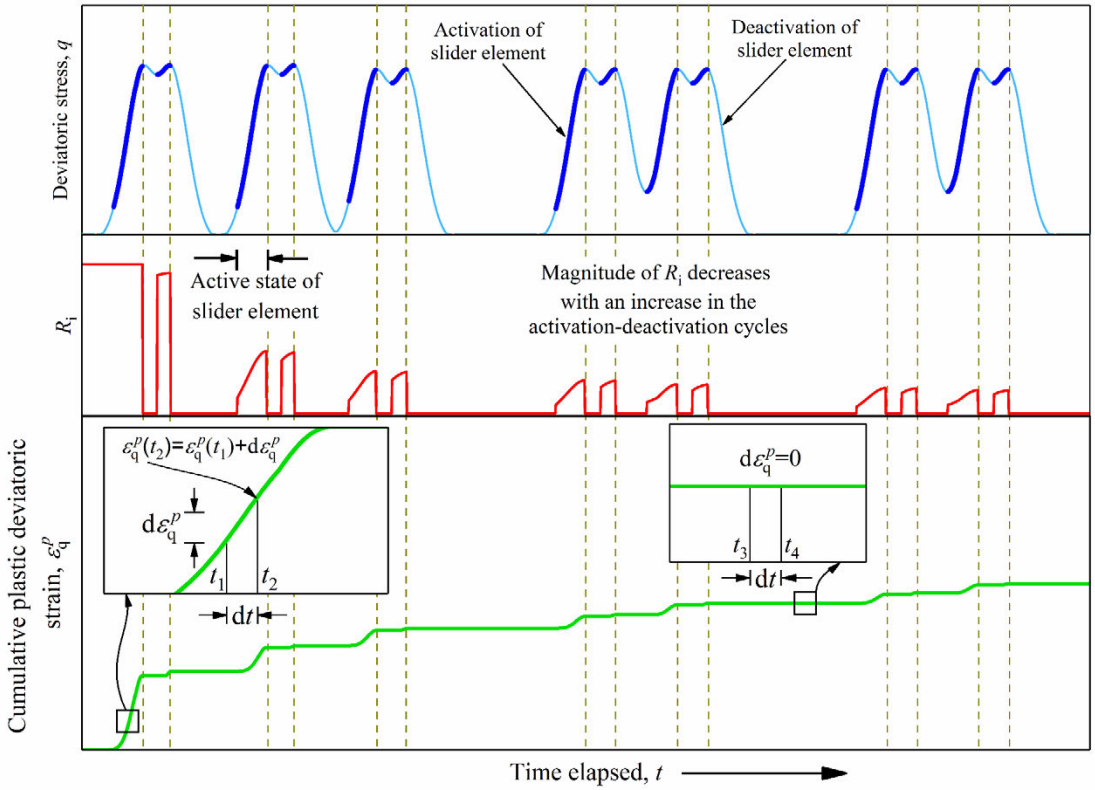

Figure 3.14 Generation of irrecoverable deformations during train-induced repeated loading

Calibration of Constitutive Parameters for Ballast and Subballast Slider Elements. The input parameters for the slider element for the granular layers (ballast and subballast) are obtained from the results of the cyclic loading triaxial tests conducted by Suiker et al. (2005). The ballast used in their study was crushed basalt, which is classified as uniformly graded gravel, while the subballast comprised of well-graded sand with gravel. The cyclic triaxial tests were carried out in a load-controlled mode at two different confining pressures (σ_c): 41.3 kPa and 68.9 kPa. At both the confining pressures, the amplitude of the cyclic stress ratio $(q/p)_{cyc}$ was taken as a specific fraction (n) of the static failure stress ratio $(q/p)_{stat,max}$.

Figure 3.15 illustrates a comparison between the experimental data and the results predicted using the constitutive relationship for the slider element for ballast. The symbols show the data obtained from the experiments, and the solid lines show the

predicted results. The model parameters used for the simulation are provided in **Table 3.4**. The critical state parameters Γ and λ can be derived using the data from multiple undrained and drained triaxial compression tests on loose to dense samples (Jefferies & Shuttle 2002). However, due to the lack of adequate test data, these parameters were selected based on engineering judgement. The parameters M_{tc} and N_v are derived by plotting the data from triaxial tests in the stress-dilatancy form, i.e., peak stress ratio (η_{max}) versus maximum dilatancy ($D_{p,max}$). A linear best-fit curve is then drawn through the data whose slope and intercept yields ($1 - N_v$) and M_{tc}, respectively. The parameter χ_{tc} is derived by plotting the data from triaxial tests in the state-dilatancy form, i.e., $D_{p,max}$ versus ψ at maximum dilatancy. A linear best-fit curve, passing along the origin, is then drawn through the data whose slope yields the value of χ_{tc} (Jefferies & Been 2015). The value of the hardening parameters H and a_h were selected based on engineering judgement.

It is apparent from **Figures 3.15(a)** and **3.15(b)** that the predicted results are in good agreement with the experimental data at both the confining pressures. The model is able to simulate the rapid accumulation of strain during the initial stages of the repeated loading followed by a reduction in the rate of strain accumulation at the later stages of repeated loading. Thus, the present constitutive relationship can accurately capture the response of the ballast under repeated loading conditions.

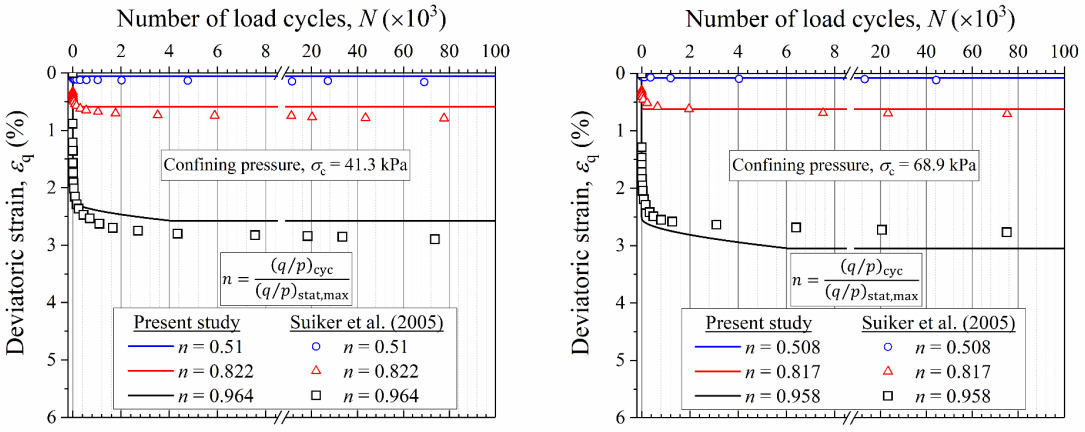

Figure 3.15 Comparison of the model predictions with the experimental results reported by Suiker et al. (2005) for cyclic load tests on ballast: variation of deviatoric strain with the number of load cycles at confining pressure of **(a)** 41.3 kPa; **(b)** 68.9 kPa

Table 3.4 Constitutive parameters for the plastic slider element for granular layers

Parameter	Suiker et al. (2005)		Gräbe & Shaw (2010)
	Ballast	**Subballast**	**Engineered fill**
Γ	1.4	0.9	0.9
λ	0.1	0.05	0.05
M_{tc}	1.25	1.15	1.25
N_v	0.2	0.3	0.3
χ_{tc}	3	4.2	4.5
a_h	0.143	0.185	0.175
H	$50–250\psi$	$160–260\psi$	$7{,}600–1{,}000\psi$

Note: ψ is the state parameter

Figure 3.16 shows a comparison of the experimental data with the results predicted using the constitutive relationship for the slider element for subballast. The experimental data and the predicted results are represented using symbols and solid lines, respectively. The model parameters used for the simulation are listed in **Table 3.4**. It is evident from **Figures 3.16(a)** and **3.16(b)** that the present constitutive relationship predicts the accumulation of strain under repeated loading quite well in relation to the strain accumulation observed during the laboratory experiments. Thus, the present constitutive relationship can accurately simulate the behaviour of subballast under repeated loading conditions. The calibrated constitutive parameters for both the ballast and subballast, thus obtained, are used later in the parametric analyses.

Subgrade.

The constitutive relationship for the plastic slider element in the case of subgrade is based on the 3D elastoplastic model conceived by Ma et al. (2017) to predict the mechanical behaviour of geomaterials under general stress conditions. The advantage of using this relationship is that it requires a limited number of parameters (seven parameters) to provide reasonably accurate predictions under 3D repeated loading conditions. This relationship builds on the Modified Cam-clay model, but in the characteristic stress space, which is formed by transforming the principal stress space using a parameter ξ (Lu et al. 2017):

$$\hat{\sigma}_j = \sigma_{ref}\left(\frac{\sigma_j}{\sigma_{ref}}\right)^{\xi}; j = 1,2,3 \qquad 3.42$$

where $\hat{\sigma}_j$ is the characteristic stress (N/m^2); σ_{ref} is the reference stress (assumed to be 1 kPa in this study); σ_j is the principal stress (N/m^2); ξ is a dimensionless material parameter, which can be obtained by solving the following equation (Lu et al. 2017):

$$\frac{(1+\sin\varphi_c)^{\xi}-(1-\sin\varphi_c)^{\xi}}{(1+\sin\varphi_c)^{\xi}+2(1-\sin\varphi_c)^{\xi}} = \frac{(1+\sin\varphi_e)^{\xi}-(1-\sin\varphi_e)^{\xi}}{(1-\sin\varphi_e)^{\xi}+2(1+\sin\varphi_e)^{\xi}} \qquad 3.43$$

where φ_c and φ_e are the critical state friction angles (°) under triaxial compression and extension tests, respectively. The model is based on isotropic hardening plasticity and employs a non-associated flow rule.

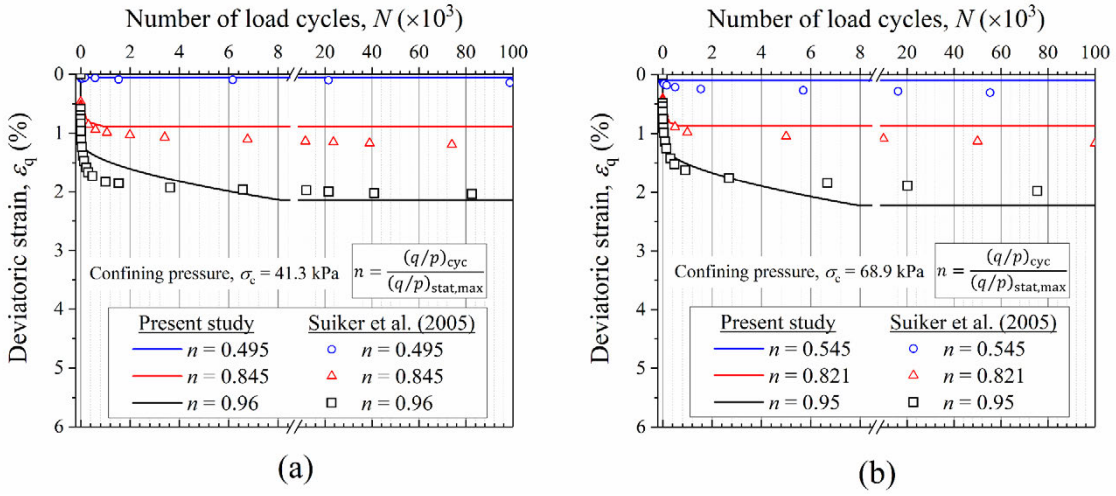

Figure 3.16 Comparison of the model predictions with the experimental results reported by Suiker et al. (2005) for cyclic load tests on subballast: variation of deviatoric strain with the number of load cycles at confining pressure of **(a)** 41.3 kPa; **(b)** 68.9 kPa

Yield and Plastic Potential Function.

The yield function for the slider element is based on the Modified Cam-clay model in the characteristic stress space with plastic volumetric strain as a hardening parameter (Lu et al. 2019):

$$f = \frac{(\lambda-\kappa)}{\xi(1+e_0)}\left[A\ln\left(\frac{\hat{M}^2+\hat{\eta}^2}{\hat{M}^2+\hat{\eta}_0^2}\right)+\ln\frac{\hat{p}}{\hat{p}_0}\right]-\int\frac{d\varepsilon_v^p}{R} \qquad 3.44$$

where the symbol ($\hat{}$) represents the component in the characteristic stress space; subscript '0' refers to the initial value; κ is the slope of swelling line (Roscoe & Burland 1968); $\hat{\eta}$ is the stress ratio ($\hat{\eta} = \hat{q}/\hat{p}$, where $\hat{q}$ and $\hat{p}$ are the deviatoric and hydrostatic stress invariants, respectively); $\varepsilon_{\mathrm{v}}^{p}$ is the plastic volumetric strain; R is a parameter that controls the magnitude of plastic volumetric strain increment. $\widehat{M}$ is the critical stress ratio expressed as (Lu et al. 2017):

$$\widehat{M} = 3\frac{(1+\sin\varphi_{\mathrm{c}})^{\xi} - (1-\sin\varphi_{\mathrm{c}})^{\xi}}{(1+\sin\varphi_{\mathrm{c}})^{\xi} + 2(1-\sin\varphi_{\mathrm{c}})^{\xi}} \tag{3.45}$$

Furthermore, A denotes a dimensionless constitutive parameter that describes the distance between normal compression line (NCL) and the critical state line (CSL), i.e.,

$$A = \frac{\xi(\widehat{N} - \widehat{\Gamma})}{(\lambda - \kappa)\ln 2} \tag{3.46}$$

where $\widehat{N}$ and $\widehat{\Gamma}$ are the void ratio of the NCL and CSL at $\hat{p}$ =1 kPa, respectively.

To simulate the accumulation of plastic strain with an increase in the number of load repetitions, the model employs the concept of sub-loading surfaces (Hashiguchi 1989) with isotropic hardening. Three surfaces: transitional (f_{t}), current (f_{c}) and reference surfaces (f_{r}) are used, which are defined as follows (Lu et al. 2019):

$$f_{\mathrm{t}} = A\ln\left(1 + \frac{\hat{\eta}^2}{\widehat{M}^2}\right) + \ln\frac{\hat{p}}{\hat{p}_{\mathrm{xt}}} = 0 \tag{3.47}$$

$$f_{\mathrm{c}} = A\ln\left(1 + \frac{\hat{\eta}^2}{\widehat{M}^2}\right) + \ln\frac{\hat{p}}{\hat{p}_{\mathrm{xc}}} = 0 \tag{3.48}$$

$$f_{\mathrm{r}} = A\ln\left(1 + \frac{\hat{\eta}^2}{\widehat{M}^2}\right) + \ln\frac{\hat{p}}{\hat{p}_{\mathrm{xr}}} = 0 \tag{3.49}$$

where $\hat{p}_{\mathrm{xt}}$, $\hat{p}_{\mathrm{xc}}$ and $\hat{p}_{\mathrm{xr}}$ are the intersections of the transitional, current and reference surfaces with the $\hat{p}$ axis, respectively. The parameter R is determined using the following Equation 3.50:

$$R = e^{-\frac{1}{a_{\mathrm{h}}}\left(1-\frac{\hat{p}_{\mathrm{xc}}}{\hat{p}_{\mathrm{xr}}}\right)}\sqrt{\frac{\hat{p}_{\mathrm{xc}} - \hat{p}_{\mathrm{xt}}}{\hat{p}_{\mathrm{xr}} - \hat{p}_{\mathrm{xt}}}} \tag{3.50}$$

where a_{h} is the cyclic hardening parameter, that can be determined by calibrating the model against the experimental data.

The sub-loading surface f_c always passes through the current stress state during both the activation and deactivation phases of the slider element. Whereas, the surface f_r expands because of the accumulated plastic strains according to the isotropic hardening rule and f_t evolves depending on the current state, i.e., activation or deactivation. Nevertheless, f_r and f_t retain geometrical similarity to the sub-loading surface f_c.

At the beginning of the activation phase, all the three surfaces are coincident, i.e., $\hat{p}_{xt} = \hat{p}_{xc} = \hat{p}_{xr}$ and $R = 1$. During the active state of the slider element, the surfaces f_c and f_r expand simultaneously, whereas f_t retains its initial position. The plastic strain, thus generated, is calculated using the plastic potential function as follows:

$$d\boldsymbol{\varepsilon}_{ij}^{p} = \Lambda_s \frac{\partial g_p}{\partial \widehat{\boldsymbol{\sigma}}_{ij}} \tag{3.51}$$

where Λ_s is a scalar; $\widehat{\boldsymbol{\sigma}}_{ij}$ is the characteristic stress tensor; g_p is the potential function defined by (Ma et al. 2017):

$$g_p = \ln\left[\frac{\widehat{M}^2 + (2\xi - 1)\hat{\eta}^2}{\widehat{M}^2}\right] + \frac{(2\xi - 1)}{\xi}\ln\left(\frac{\hat{p}}{\hat{p}_{xg}}\right) = 0 \tag{3.52}$$

where $\hat{p}_{xg}$ is the intersection of the potential function with the $\hat{p}$ axis. The scalar Λ_s is calculated from (Lu et al. 2019):

$$\Lambda_s = \frac{-\left(\frac{\partial f}{\partial \hat{q}} d\hat{q} + \frac{\partial f}{\partial \hat{p}} d\hat{p}\right)}{\left(\frac{\partial g_p}{\partial \hat{p}}\right)\left(\frac{\partial f}{\partial \varepsilon_v^p}\right)} \tag{3.53}$$

Substituting the value of g_p and Λ_s in Equation 3.51, the following relationship is obtained (Lu et al. 2019):

$$d\boldsymbol{\varepsilon}_{ij}^{p} = \frac{R(\lambda - \kappa)}{\xi(1 + e_0)}\left[\frac{\widehat{M}^2\hat{p}^2 + (1 - 2A)\hat{q}^2}{\hat{p}\left(\widehat{M}^2\hat{p}^2 + \hat{q}^2\right)} d\hat{p} + \frac{2A\hat{q}d\hat{q}}{\widehat{M}^2\hat{p}^2 + \hat{q}^2}\right]\left[\frac{3\xi\hat{p}\left(\widehat{\boldsymbol{\sigma}}_{ij} - \hat{p}\delta_{ij}\right)}{\widehat{M}^2\hat{p}^2 - \hat{q}^2} + \frac{\delta_{ij}}{3}\right] \tag{3.54}$$

where $d\hat{p}$ and $d\hat{q}$ are the hydrostatic and deviatoric stress increments in the characteristic stress space, respectively. The displacement increment of the slider element is then calculated by multiplying the subgrade thickness with the plastic strain increment ($d\varepsilon_z^p$) in the vertical direction (determined using Equation 3.54). The plastic displacement rate

of the slider element is computed by differentiating the plastic displacement of subgrade in the vertical direction with respect to time. These values are used as an input in Equation 3.29 to determine the total track response.

It can be noted that the parameter R controls the magnitude of plastic strain increment. During the first active state of the slider element, the surfaces f_c and f_r remain coincident, therefore, the value of R remains equal to 1. As soon as the slider is deactivated, the surface f_t expands and become coincident with f_c, i.e., $\hat{p}_{xt} = \hat{p}_{xc}$ and $R = 0$, whereas f_r remains in the position acquired at the end of the active state. As the deactivation phase proceeds, both f_c and f_t shrink simultaneously (keeping $R = 0$) while f_r retains its position. Since the magnitude of R is equal to 0, no plastic strain is generated during the deactivation stage.

As the reactivation of the slider element starts, both f_c and f_r expand simultaneously while the surface f_t remains in the position acquired at the end of the deactivation stage. However, the surfaces f_c and f_r are not coincident during reactivation, and the value of R varies between 0 and 1. The plastic strain generated during reactivation can be calculated using Equation 3.54. Since the magnitude of R remains below 1 during reactivation, the magnitude of plastic strain is less than that in the first active stage. Thus, the model can simulate the reduction in the plastic strain increment with an increase in the number of load repetitions or activation-deactivation cycles of the slider element. The conditions for activation and deactivation of the slider element are discussed in the next section.

Loading/unloading Condition.

To distinguish between the loading (activation) and unloading (deactivation) of the slider element during repeated loading conditions, the Kuhn-Tucker relations must be met (Simo & Hughes 1998; Suiker & de Borst 2003):

$$\Lambda_s \geq 0; f(\hat{q}, \hat{p}, \varepsilon_v^p) \leq 0; \Lambda_s f(\hat{q}, \hat{p}, \varepsilon_v^p) = 0 \qquad 3.55$$

Equation 3.55 indicates that for the activation or loading of the slider element for the subgrade, Λ_s must be greater than zero, the stresses must be admissible, and the yield criterion remains satisfied. The unloading of the slider element occurs when the stresses

are admissible and the yield conditions are not satisfied. The unloading may also occur if the yield condition is satisfied, but Λ_s is zero.

Calibration of Parameters for the Subgrade Slider Element.

In this study, the model parameters for the subgrade slider element are obtained from the results of the laboratory cyclic triaxial tests conducted by Wichtmann (2005). In **Figure 3.17**, the predicted results are compared with the data obtained from the laboratory cyclic triaxial tests. **Table 3.5** provides the details of the input parameters used for the simulation. The parameters λ and κ are derived using the data from multiple isotropic compression and swelling tests on soil specimens. The parameter φ_c is the critical state friction angle under triaxial compression. The value of ξ and parameter A are determined using Equations 3.43 and 3.46, respectively. The hardening parameter a_h is derived by calibrating the model against the experimental data.

Referring to **Figure 3.17(a)**, it can be observed that the predicted stress-strain behaviour is in an acceptable agreement with the experimental results at a deviatoric stress amplitude (q^{ampl}) and mean stress (p^{av}) of 80 kPa and 200 kPa, respectively. The irrecoverable component of the axial strain in each load cycle is high during the initial stages of loading and then decreases with an increase in the number of load cycles. In **Figure 3.17(b)**, the variation of accumulated axial strain with the number of load cycles predicted using the present constitutive relationship is compared with the experimental results, at different deviatoric stress amplitude (q^{ampl}). It can be observed that the predicted results are in an acceptable agreement with the laboratory data. The predicted results vary by 1% – 15% from the experimental results at 10,000 load cycles. The accuracy of the predictions can be increased further by using a more advanced calibration procedure (Luenberger 1973; Suiker & de Borst 2003).

Table 3.5 Model parameters for the plastic slider element for subgrade soil

Reference	e_0	λ	κ	φ_c (°)	ξ	A	a_h
Wichtmann (2005)	0.7	0.0046	0.0009	31.2	0.1	0.31	0.0135
Gräbe & Shaw (2010)	0.3	0.0022	0.002	51	0.45	0.02	0.075

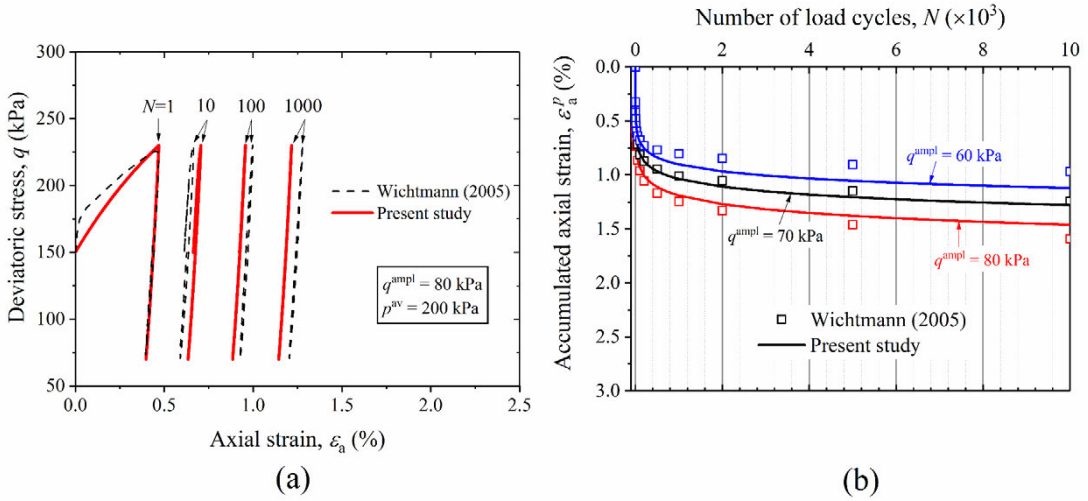

Figure 3.17 Comparison of the experimental results for soil reported by Wichtmann (2005) with the model predictions: **(a)** stress-strain curve; **(b)** variation of axial strain with the number of load cycles (solid lines and symbols represent model predictions and experimental data, respectively)

It can be noted that the accumulated axial strain increases rapidly during the initial phase, followed by a reduction in the rate of axial strain accumulation. The predicted results can also capture the increase in the magnitude of accumulated axial strain with an increase in the deviatoric stress amplitude. Thus, it is evident that the present approach can accurately capture the response of the soil under repeated loading conditions.

3.10 Model Validation

The dynamic equilibrium equation (Equation 3.29) is solved using the Newmark's–β numerical integration scheme at each time instant. The solution of the equation yields the variation of total displacement, velocity and acceleration of the three substructure layers with time. **Figure 3.18** presents the flowchart used to evaluate the total viscoelasto-plastic response of the substructure layers subjected to the repeated traffic loadings. The input data required in the analysis include the train properties; track properties, such as sleeper spacing, density, resilient modulus, Poisson's ratio, shear stiffness, shear damping and thickness of the substructure layers; and the constitutive parameters for the slider elements. Once the input parameters are derived, the effective region of the substructure layers below each sleeper is identified, and the vibrating mass, damping coefficient and stiffness of the track layers are calculated. Subsequently, the rail seat load-time history is derived at each sleeper location. For the slider elements, the continuum stress type

parameters (such as p, q) are required as input for the constitutive model. Therefore, the stress distribution in the track layers is estimated for each time instant using the method described in Section 3.9.1.1. If the stress state in a substructure layer at any instant reaches the yield surface (and the plastic loading conditions are satisfied), the irrecoverable strain is calculated using the constitutive relationship of the slider element. Since the method is an implicit step-by-step approach, the plastic strain is evaluated at each time instant. Once the irrecoverable strain is calculated, it is multiplied by the thickness of the individual layer to yield the plastic displacement. The plastic velocity is then calculated by differentiating the plastic displacement with respect to time. Finally, the total track response is evaluated by solving the dynamic equilibrium equation (Equation 3.29) at each time instant. The analysis is continued till the desired number of axles have passed the sleeper location (i.e., when the time elapsed, $t = t_f$, where t_f is the final time for analysis). A MATLAB code has been developed to perform all the calculations in the proposed computational method (MathWorks Inc. 2021). It must be noted that the track response in the present method is evaluated at individual sleeper locations. The deformation profile of the track between the sleeper locations can be determined by means of an interpolation technique.

To validate the reliability of the model, the results calculated using the present approach are compared with the in-situ measurements reported by Gräbe et al. (2005), Gräbe & Shaw (2010) and Priest et al. (2010). Gräbe et al. (2005) reported the vertical deformation and the stress distribution in the substructure layers in a heavy haul track in South Africa. The track comprised of a 300 mm thick ballast layer overlying the formation, which constitutes of four 200 mm thick layers of engineered fill (Layer 2) and the natural ground (comprising of weathered tillite). **Table 3.2** lists the input parameters used in the model predictions. **Figure 3.19(a)** illustrates the variation of σ_v with time at different depth below the formation level (i.e., below the ballast-engineered fill interface) during the passage of a coal wagon. It is evident that the predicted results are in good agreement with the in-situ measurements. The model overpredicts the vertical stress at the formation level (0 mm). However, the stress distribution with depth is the same as that observed in the field. At the formation level (0 mm), multiple peaks are visible, which correspond to the passage of individual axles. However, the influence of individual axles diminishes with depth.

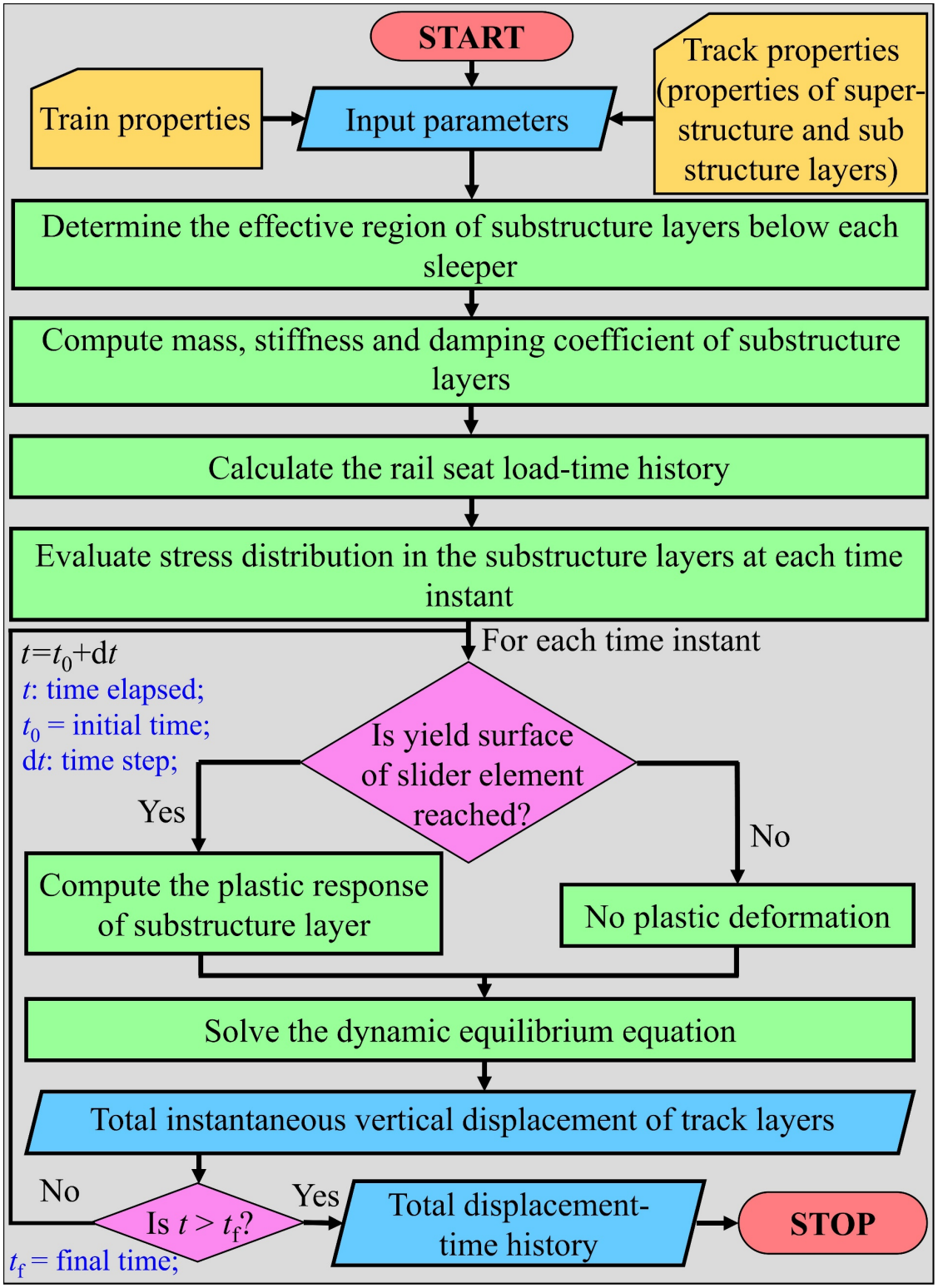

Figure 3.18 Flowchart to predict the track response under train-induced repeated loads

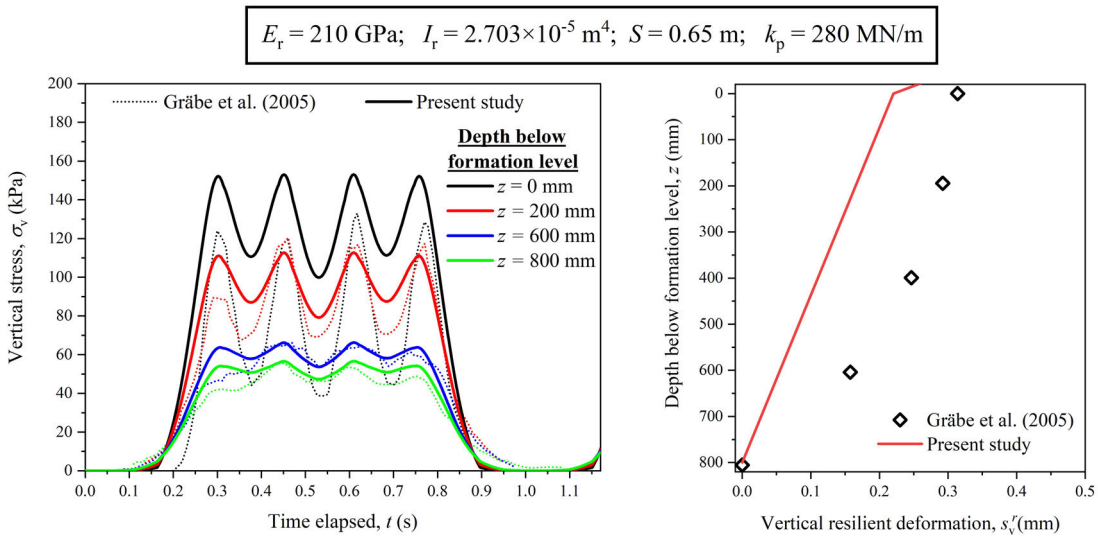

(a) (b)

Figure 3.19 Comparison of data reported by Gräbe et al. (2005) with predicted results: **(a)** variation of vertical stress with time (solid and dotted lines represent model predictions and in-situ measurements, respectively); **(b)** variation of vertical resilient deformation with depth

The variation of transient (or resilient) deformation with depth in the formation (engineered fill) layer computed using the present approach is compared with the in-situ measurements recorded by Gräbe et al. (2005) in **Figure 3.19(b)**. It can be seen that the predicted results are in an acceptable agreement with the in-situ measurements. The deformation decreases with an increase in depth from the ballast-engineered fill interface.

The variation of resilient vertical sleeper displacement with time during the passage of a 26 t axle load coal wagon predicted using the present approach is compared with the in-situ measurements recorded by Priest et al. (2010) in **Figure 3.20(a)**. **Table 3.2** lists the input parameters used in the model predictions. It is evident that the predicted results are in reasonable agreement with the field data. **Figure 3.20(b)** shows the increase in vertical and horizontal stresses at a depth of 800 mm beneath the sleeper bottom, predicted using the present approach and that using FE analysis by Priest et al. (2010). It can be observed that the results predicted using the present technique are in good agreement with the data reported by Priest et al. (2010).

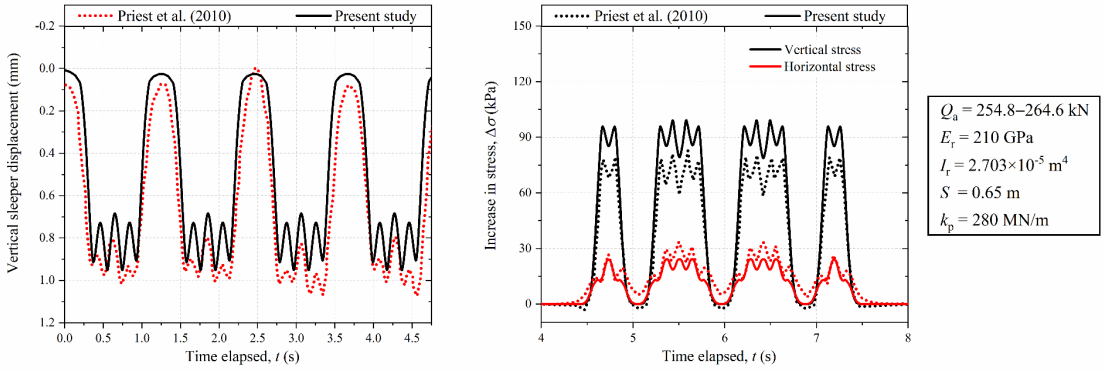

Figure 3.20 Comparison of data reported by Priest et al. (2010) with predicted results: **(a)** variation of vertical displacement of sleeper with time; **(b)** variation of the increase in vertical and horizontal stresses at 800 mm below sleeper bottom with time

The accumulation of irrecoverable deformation with tonnage (in MGT) predicted using the present technique is compared with the in-situ measurements reported by Gräbe & Shaw (2010) in **Figure 3.21**. **Tables 3.2, 3.4** and **3.5** list the input parameters used in the model predictions. It can be seen that the predicted results are in reasonable agreement with the field data. An overestimation of the cumulative deformation in the initial stages of loading may be attributed to the fact that the present method predicts a high rate of settlement during the initial loading stage followed by a reduction in the settlement rate with an increase in tonnage. However, the rate of settlement in the field measurements fluctuates due to the uncertainties associated with the train loading and temporal variation in the subgrade properties due to seasonal fluctuations in the temperature, as mentioned by Gräbe & Shaw (2010). Nevertheless, the magnitude of predicted cumulative deformation is similar to the in-situ measurements when the track is subjected to a tonnage of about 350 MGT (which may be more commonly associated with track deterioration in comparison to initial stages of loading). Therefore, the present approach can accurately capture the irrecoverable response of the rail track substructure layers over a period of time.

Thus, the present technique can accurately predict the transient and irrecoverable track response under the train traffic-induced repeated loads. The constitutive parameters for the slider elements can be calculated using the data from laboratory triaxial tests (both static and cyclic) on track materials (preferably under true triaxial conditions). The proposed approach is simple, computationally efficient and can predict the long-term

performance of the ballasted railway tracks. This method can also serve as a tool for practising engineers to optimise the track performance.

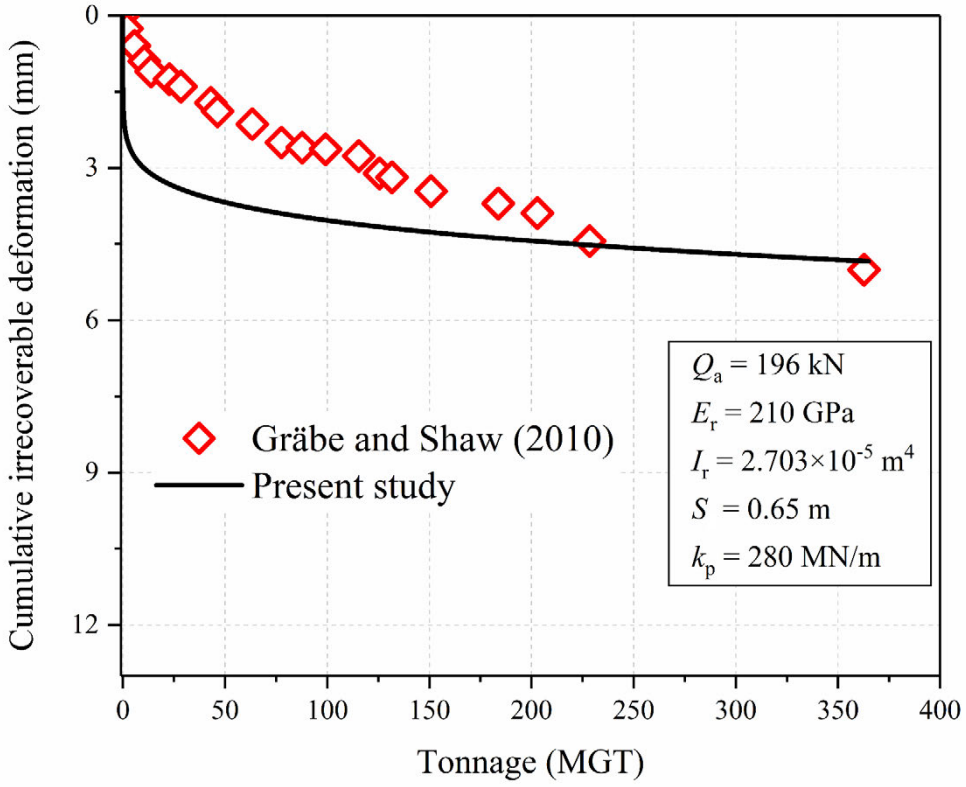

Figure 3.21 Comparison of cumulative irrecoverable deformation recorded by Gräbe & Shaw (2010) with model predictions

3.11 Results and Discussion

A parametric analysis is carried out to investigate the influence of Q_a, V and thickness of granular layers (h_{gl}) on the stress distribution and cumulative track settlement. The values of the parameters used in the analysis are listed in **Table 3.6**. The model parameters that were previously calibrated using the experimental data reported by Suiker et al. (2005) and Wichtmann (2005) are used for the slider element for granular layers and subgrade, respectively (see **Tables 3.4** and **3.5**). The values of shear stiffness, shear damping and density of the substructure layers are provided in **Table 3.2**. The results are calculated for the passage of a train consisting of 32 axles, with an axle configuration similar to the Acela express train. In each analysis, only one parameter is varied at a time, while nominal values are assigned to other parameters. The nominal value of Q_a is 25 t, while the nominal values of h_b and h_s are provided within the parenthesis in **Table 3.6**.

Table 3.6 Parameters for the simulation of viscoelasto-plastic track response

Layer	Variable	Symbol	Unit	Value
Ballast	Resilient modulus	E_b	MPa	276
	Poisson's ratio	ν_b	–	0.3
	Thickness	h_b	m	0.3 – 0.75 (0.3)
Subballast	Resilient modulus	E_s	MPa	115
	Poisson's ratio	ν_s	–	0.4
	Thickness	h_s	m	0.15 – 0.6 (0.15)
Subgrade	Resilient modulus	E_g	MPa	20
	Poisson's ratio	ν_g	–	0.45
	Thickness	h_g	m	10

3.11.1 Influence of Axle Load

The magnitude of Q_a is varied between 20 t and 30 t to study its influence on the response of the railway track. V for this analysis is considered as 150 km/h. **Figure 3.22** shows the variation of σ_v with depth (z) calculated using the present method at three different axle loads. It can be observed that σ_v decreases with an increase in depth. For each case, the traffic-induced σ_v at the subgrade top is about 36% of that at the ballast top. This finding highlights the critical function served by the granular layers, i.e., to reduce the magnitude of traffic-induced stresses transferred to the subgrade soil to a safe level (Selig & Waters 1994). It can also be noted that the peaks in σ_v versus time plots corresponding to the passage of individual axles are visible at the ballast top (0 mm). However, the effect of individual axles diminishes with depth. This finding is similar to that observed in the 3D FE analyses conducted by Powrie et al. (2007). As Q_a increases, the traffic-induced σ_v in the three substructure layers increases. Interestingly, the effect of Q_a increment is visible only in the top portion of the subgrade soil, and this effect diminishes with depth. At a depth of 3,000 mm, there is an insignificant change in the σ_v with an increase in Q_a.

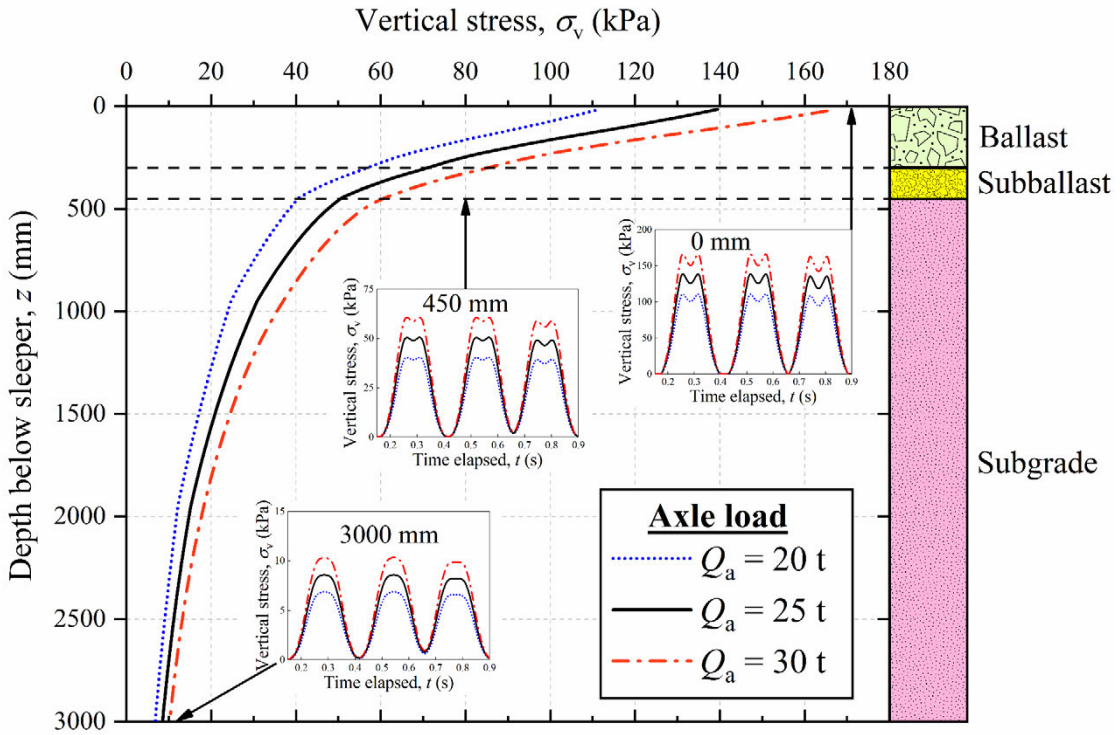

Figure 3.22 Vertical stress distribution with depth under different axle loads

Figure 3.23 shows the distribution of accumulated settlement with depth after a cumulative tonnage of 20 MGT for three different axle loads. It is evident that the settlement increases with an increase in Q_a. The overall track settlement increases by 41%, with an increase in Q_a from 20 t to 25 t. The increment rises to 73% when the Q_a increases from 25 t to 30 t. The settlement of the granular layers (s_{gl}) also increases from 3.6 mm to 5.9 mm, with an increase in Q_a from 20 t to 30 t, respectively. Thus, it is apparent that an increase in the Q_a may significantly increase the cumulative deformation in the existing tracks, resulting in a degradation of track geometry.

3.11.2 Influence of Train Speed

V is varied between 100 km/h and 200 km/h to investigate its influence on the magnitude of cumulative deformation in the track layers. **Figure 3.24** shows the distribution of settlement with depth after a cumulative tonnage of 25 MGT at three different train speeds. It can be observed that the magnitude of settlement accumulated in the track increases with an increase in V. The overall track settlement increases by 19% as V increases from 100 km/h to 150 km/h. The increment rises to 26% when V increases from 150 km/h to 200 km/h.

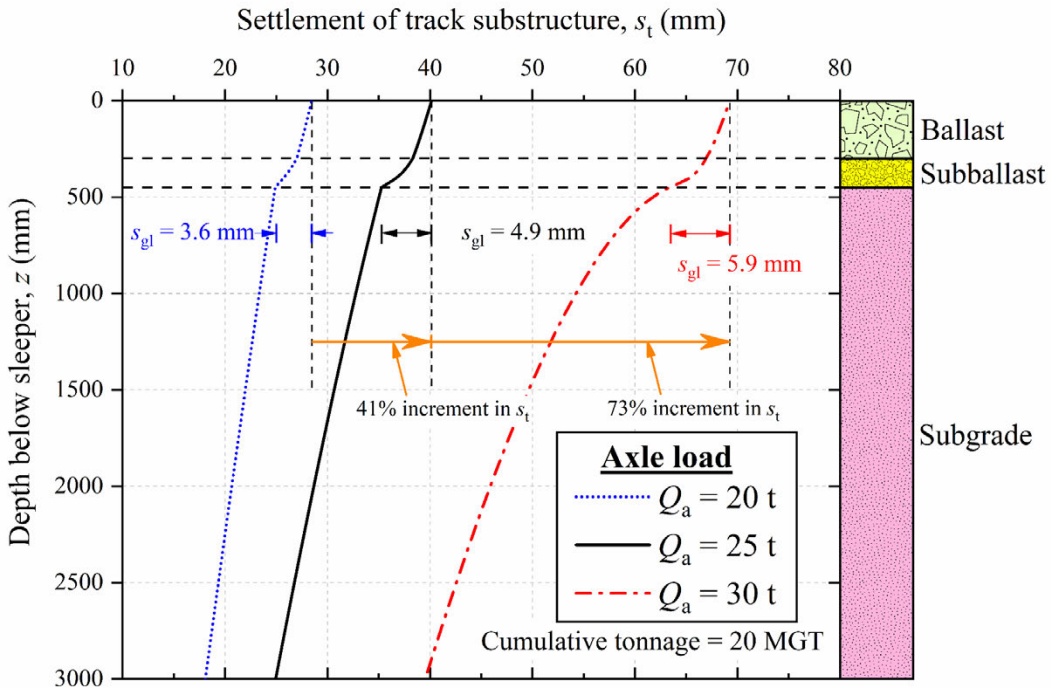

Figure 3.23 Distribution of settlement accumulated after a cumulative tonnage of 20 MGT with depth under different axle loads

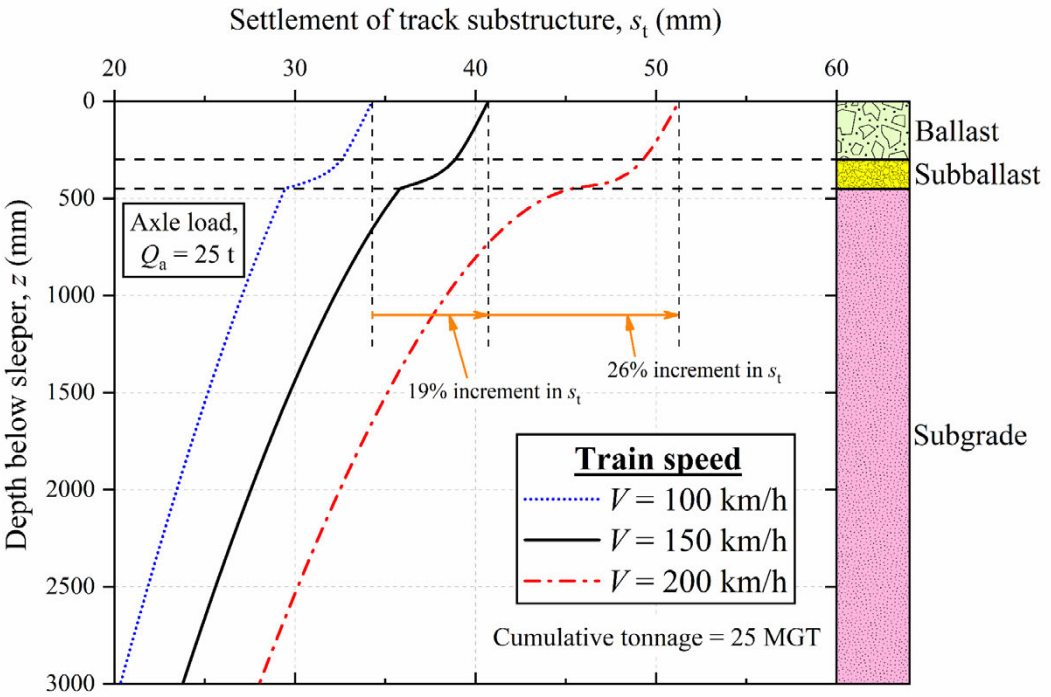

Figure 3.24 Distribution of settlement accumulated after a cumulative tonnage of 25 MGT with depth under different train speeds

It must be noted that the effect of V in this study is considered by employing φ_d, which is a multiplier to the axle load. φ_d increases with an increase in V, and consequently, the magnitude of stress and deformation accumulated in the track increases with V. φ_d

accounts for the increment in track response due to various effects such as the dynamic vehicle-track interaction (Doyle 1980; Knothe & Grassie 1993; Metrikine & Verichev 2001), the relative velocity of the vehicle with respect to the critical wave propagation velocity of the track-ground system (Dieterman & Metrikine 1996; Suiker et al. 1998; Metrikine & Verichev 2001; Suiker et al. 2001b, 2001a; Vostroukhov & Metrikine 2003) and the sleeper passing frequency (Metrikine & Popp 1999; Esveld 2001; Suiker et al. 2001b; Vostroukhov & Metrikine 2003).

In this study, φ_d is calculated using the empirical expression proposed by Nimbalkar & Indraratna (2016) (see Equation 3.20). This expression was developed using the field data, and it considers the influence of the subgrade properties (which affects the natural frequency and critical wave propagation velocity of the track-ground system) on the load amplification. The present study essentially captures the increment in track response due to the effects discussed above with minor contribution from the dynamic vehicle-track interaction as the track is assumed to be straight and free from inhomogeneities.

3.11.3 Influence of Granular Layer Thickness

The granular layer thickness, or the combined thickness of ballast and subballast layers, is a crucial parameter that influences the overall track stiffness and stress transfer. In this study, the thickness of the granular layer is varied between 0.45 m and 0.9 m using two approaches. In the first approach, h_b is assigned a nominal value, and h_s is varied. Whereas, in the second approach, h_s is kept constant while h_b is varied. V for this analysis is considered as 100 km/h.

Figure 3.25 shows the variation of settlement accumulated in the subgrade layer (s_g) with tonnage at different granular layer thicknesses. It can be observed that s_g decreases with an increase in h_{gl}. The s_g decreases by almost 56%, with an increase in h_{gl} from 0.45 m to 0.9 m. This reduction in the settlement is due to a decrease in subgrade stress owing to an increase in the distance between subgrade top and sleeper bottom, and higher stress spreading ability of the thicker granular layers (Li & Selig 1998).

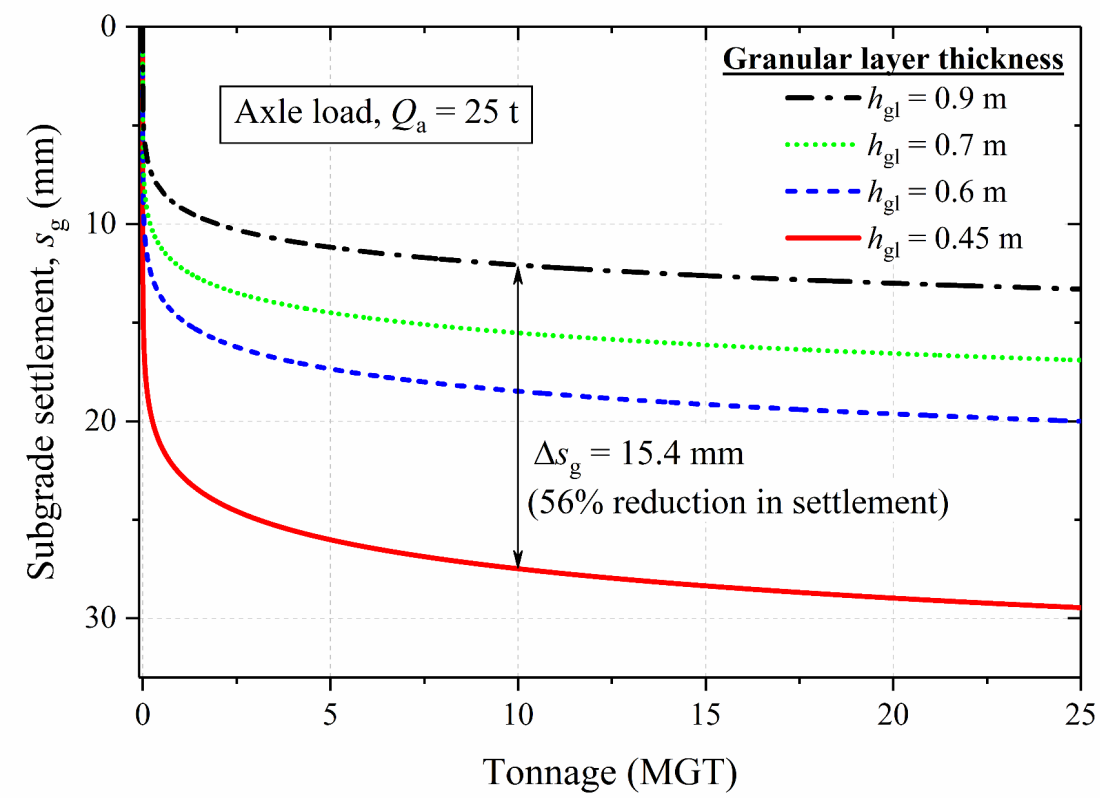

Figure 3.25 Variation of subgrade settlement with tonnage at different granular layer thickness

Figure 3.26 shows the variation of settlement accumulated in the track substructure layers with h_{gl}, after a cumulative tonnage of 25 MGT. It can be observed from **Figure 3.26(a)** that s_g decreases rapidly with an increase in h_{gl} from 0.45 to 0.7 m (13.3 mm). However, the magnitude of settlement reduction decreases as h_{gl} increases further (a reduction of 3 mm with an increase in h_{gl} from 0.7 to 0.9 m). It can be noted that s_g is almost identical for both the approaches used in this study. This observation is ascribed to similar stress distribution in the subgrade layer for the two approaches, which is a consequence of a large difference between resilient modulus of subgrade and granular layers used in this study. Referring to **Figure 3.26(b)**, it can be observed that the settlement in the granular layers increases with an increase in h_{gl}. The increment is higher for the case when h_s is increased and h_b is kept constant. However, this difference is negligible in comparison with the total track settlement.

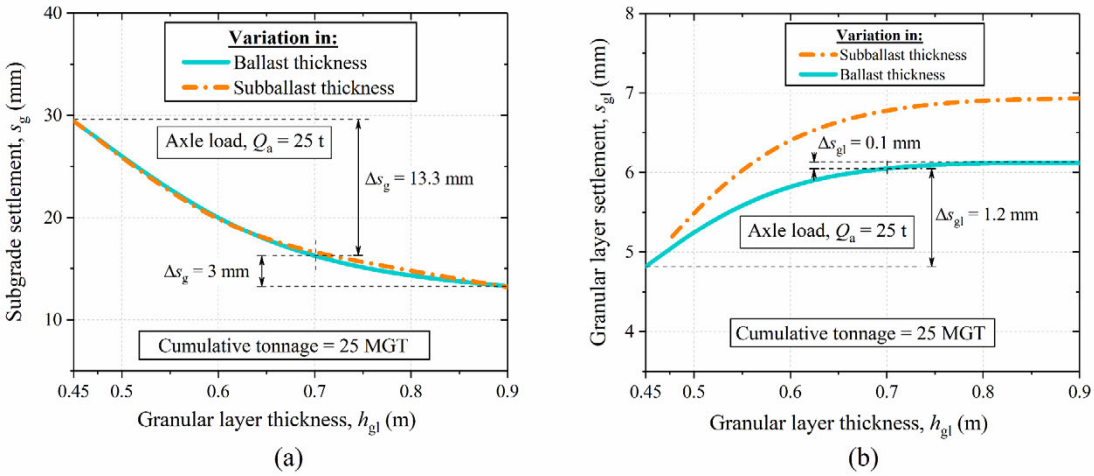

Figure 3.26 Variation of settlement accumulated after a cumulative tonnage of 25 MGT, with granular layer thickness, for **(a)** subgrade; **(b)** granular layers

3.12 Advantages, Limitations and Future Scope

The advantages of the novel rheological approach are as follows:

- Simple method that does not require any commercial FE based software to predict the transient and long-term performance of track substructure layers.
- Track response is evaluated by solving the governing equations in a step-by-step approach, which can be carried out by developing MATLAB codes (MathWorks Inc. 2021).
- Material plasticity is captured using plastic slider elements, which are described by accurate constitutive relationships.
- The proposed method is computationally efficient.
- The physical laws responsible for the predicted response are known therefore, the interpretation of predicted results is easier as compared to FE based methods.
- Conducting parametric analysis using this method is straightforward.

The limitations of the present approach are as follows:

- The train-induced loading is considered only along the vertical direction.
- The effects of vehicle-track interaction, relative velocity of the vehicle with respect to the critical wave propagation velocity of the track-ground system and sleeper passing frequency has been considered by employing a dynamic amplification factor, which is a simplified approach.

- The effect of seasonal fluctuations in the water content in the form of wetting and drying cycles, frost heave, mud pumping, unsaturated track materials, and consolidation on the response of ballasted railway tracks is neglected.
- The shear stress reversal or PSR, that the substructure experiences when a moving load is passing at a specific location, has been neglected.

CHAPTER 5 of this thesis deals with the effect of PSR on track response while other limitations shall be addressed in future investigations.

3.13 Concluding Remarks

In this section of the chapter, a new rheological approach, combining plastic slider, elastic springs and viscous dampers, is developed to predict the transient and long-term response of the track substructure layers under train traffic-induced repeated loading. The novel feature of the proposed approach is the use of plastic slider elements to capture the irrecoverable response of the substructure layers. To validate the methodology, the predicted results have been compared with the in-situ measurements reported in the literature. A good agreement between the predicted results and the field data has verified the accuracy of the model. The parametric investigation highlights the significant influence of Q_a, V and h_{gl}, on the accumulated settlement in the track layers. An increment in h_{gl} significantly reduces the cumulative settlement in the subgrade layer. The proposed methodology is simple yet comprehensive and can be used to predict the design life of the track. It may also assist the practising engineers to plan the maintenance and rehabilitation of the existing railway tracks.

CHAPTER 4
PREDICTION OF THE BEHAVIOUR OF TRANSITION ZONES IN RAILWAY TRACKS USING A GEOTECHNICAL RHEOLOGICAL MODEL

4.1 General

The previous chapter discussed the development of a novel computational approach for predicting the behaviour of a typical ballasted railway track under train-induced repeated loading. Initially, an empirical approach was used to predict the cumulative deformation in the track layers. This approach was replaced by a mechanistic approach involving plastic slider elements to simulate the material plasticity. The accuracy of the approach was validated by comparing the predicted results with the field data reported in the literature, and a parametric analysis was conducted to investigate the effect of train and substructure characteristics on the track response. In this chapter, the novel computational approach is applied to an open track-bridge transition with varied support conditions along the track length.

4.2 Background

A rapid increase in the demand for heavier freight and high-speed passenger trains has increased concerns regarding the safety and serviceability of the existing railway tracks (Priest et al. 2010; Nimbalkar & Indraratna 2016). The problem is crucial for zones such as transitions between open track and stiff structures (e.g., bridges, culverts or tunnels). These zones experience a rapid degradation in track geometry due to inconsistent response on either side of the transition. Consequently, frequent maintenance is required to maintain adequate levels of passenger safety and comfort.

Figure 4.1(a) illustrates a transition zone between an embankment and a bridge. The track is founded on multiple soil layers on one side of a critical zone and a concrete slab on the other. Thus, two distinct regions can be identified on each side of the bridge approach, one with a higher track stiffness and the other with a lower track stiffness. When a train passes this transition, the track supported by soil layers inherently deforms more than the track on the bridge. Consequently, differential deformation occurs, which accumulates with multiple train passages and produces an uneven track profile near the bridge

approach [see **Figure 4.1(b)**]. This differential track settlement jeopardises the operational safety of the trains and demands expensive maintenance activities to restore the track geometry (Powrie et al. 2019).

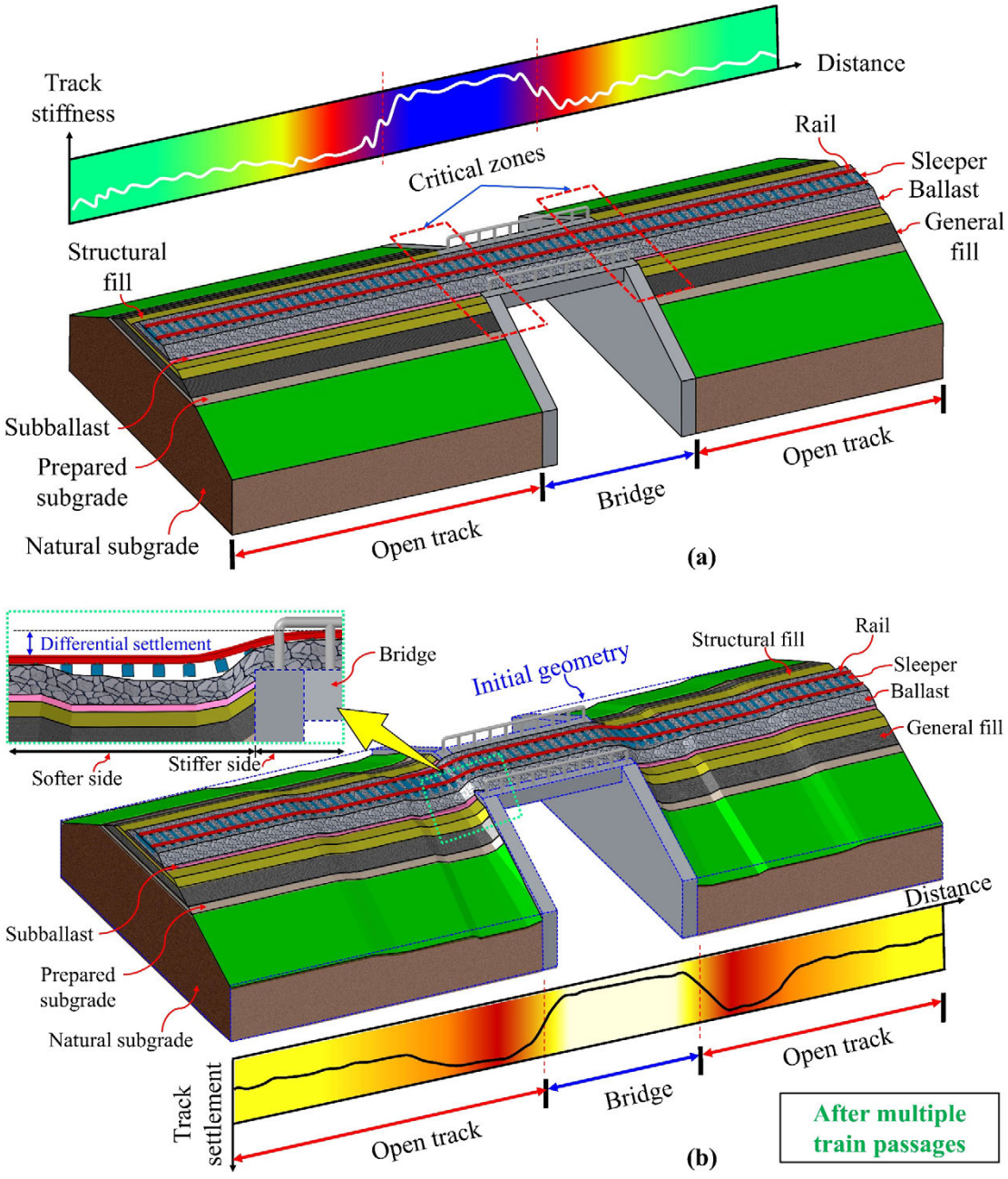

Figure 4.1 (a) Open track-bridge transition zone; **(b)** transition zone after multiple train passages

Several countermeasures have been proposed to mitigate the track geometry degradation in the critical zones. These techniques employ:

- Soft rail pads or resilient mats to reduce the stiffness of the stiffer side (Kerr & Moroney 1993; Sol-Sánchez et al. 2016).
- Cellular geoinclusions or ground improvement methods to increase the stiffness of the softer side (Briaud et al. 1997).
- Approach slabs or transition wedges to provide a gradual change in track stiffness (Coelho et al. 2011; Sañudo et al. 2016).
- Confinement walls or polyurethane geocomposites to reduce track settlements in the softer side (Kennedy et al. 2013; Stark et al. 2016).

Although previous studies have shown the viability of these countermeasures, the transition zones at several locations still exhibit poor performance (Wang et al. 2018). This is due to the site-specific nature of the track deterioration problem and limited understanding of the mechanism of applied countermeasures. An increase in axle load and train speed will exacerbate the problem of differential settlement in these track sections. Thus, a comprehensive evaluation of the behaviour of a transition zone and the effect of various remedial measures is essential to improve the design and optimise the performance. Notably, the problem of predicting the magnitude of track geometry degradation in these zones and the efficacy of various countermeasures still remains an intriguing challenge.

Prior knowledge of the magnitude of differential settlements accumulated in the substructure layers is the key to the proper design of the transition zones. However, the studies related to the prediction of the differential settlement accumulated in a transition zone over a specified period are somewhat scarce (e.g., Hunt 1997; Varandas et al. 2013; Nielsen & Li 2018; Wang & Markine 2018c; Shan et al. 2020). In most studies, the plastic deformation in the soil layers is predicted using empirical expressions. However, uncertainties exist regarding the use of empirical models as they lack general applicability under different loading effects, boundary conditions and soil types. Moreover, such expressions are only applicable to the conditions on which they are based or derived. Clearly, more work is required to establish a theoretically consistent approach to predict the behaviour of the transition zones and analyse the efficacy of various mitigation strategies.

This chapter explains the development of a 3D mechanistic approach to evaluate the transient and long-term performance of the transition zones. The proposed method employs a simple yet effective geotechnical rheological model to simulate the viscoelastic-plastic behaviour of the substructure layers on both sides of the transition. The technique is validated against the field measurements reported in the literature and 3D FE predictions. Subsequently, the methodology is applied to an open track-bridge transition zone, and the adequacy of different countermeasures to mitigate the differential track settlements is examined. The essential contribution of this chapter is the more accurate simulation of the plastic response of geomaterials using slider elements, which are described by appropriate constitutive relationships compared to the existing methods that employ empirical models. The main contribution of practical value is the capability to quickly evaluate the magnitude of the potential problem and assess the suitability of different countermeasures to improve the performance of the transition zones.

4.3 Methodology

The proposed approach involves two key components:

- A geotechnical rheological track model that considers varied support conditions along the direction of train movement.
- Slider elements described by accurate constitutive relations for geomaterials to capture their plastic response, and consequently, predict the differential track settlement in the transition zone.

4.3.1 Geotechnical Rheological Track Model

A typical open track-bridge transition zone is considered in which the track substructure on the softer side consists of three layers, i.e., ballast, subballast and subgrade, while it comprises a single ballast layer on the stiffer side (see **Figure 4.2**). Because of symmetry along the centreline, only one half of the track is considered. Each substructure layer on both sides of the transition is represented as an array of discrete masses connected via springs, dashpots and slider elements. The bridge and its abutment are simulated as fixed supports due to their negligible deformation compared to the soil layers. The continuity of the track layers along the *x*-direction (i.e. along the rail length) is represented using shear springs and shear dashpots. The origin of the coordinate system is assumed at the starting point of the stiffer side.

The track substructure layers on either side of a transition undergo recoverable and irrecoverable deformation when subjected to train-induced loading (Mamou et al. 2017). The total vertical displacement of these layers on softer and stiffer sides, at a given time instant, t, can be partitioned into viscoelastic and plastic components, as follows:

$$\boldsymbol{z_{\mathrm{m}}} = \begin{Bmatrix} z_{\mathrm{g,m}} \\ z_{\mathrm{s,m}} \\ z_{\mathrm{b,m}} \end{Bmatrix} = \begin{Bmatrix} z_{\mathrm{g,m}}^{ve} + z_{\mathrm{g,m}}^{p} \\ z_{\mathrm{g,m}} + z_{\mathrm{s,m}}^{ve} + z_{\mathrm{s,m}}^{p} \\ z_{\mathrm{s,m}} + z_{\mathrm{b,m}}^{ve} + z_{\mathrm{b,m}}^{p} \end{Bmatrix} \tag{4.1(a)}$$

$$z_{\mathrm{n}} = z_{\mathrm{b,n}}^{ve} + z_{\mathrm{b,n}}^{p} \tag{4.1(b)}$$

where subscripts m and n represent the m^{th} and the n^{th} sleeper in the softer and stiffer side of the transition, respectively.

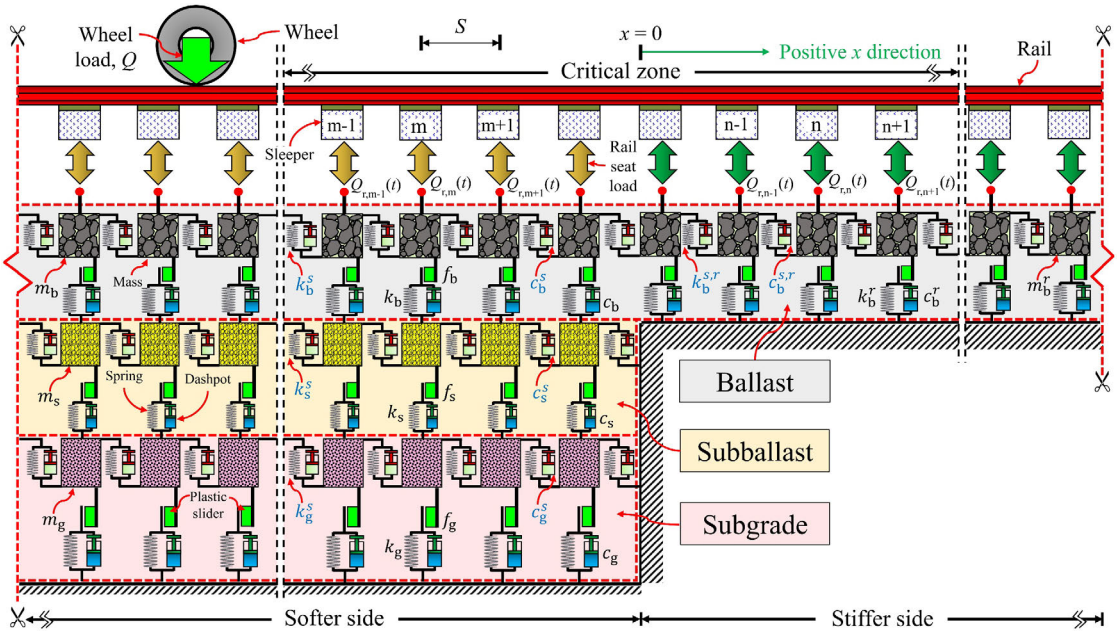

Figure 4.2 Rheological model of an open track-bridge transition zone

In the present geotechnical rheological model, the viscoelastic component of the response is simulated using spring and dashpots, while a slider element represents the plastic component. As explained in CHAPTER 3 (PART-B), three stages of track response can be identified under train-induced repetitive loading. The first phase is the initial loading stage, when the stress state in a track layer is within the yield surface (described by f_{g}, f_{s} or f_{b} for subgrade, subballast and ballast, respectively). In this phase, the springs and

dashpots deform, whereas slider elements remain inactive; thus, the track layer behaves in a purely viscoelastic manner. In the second phase, the stress state satisfies the yield criterion, thus, activating the slider elements and consequently, the total response is viscoelastic-plastic. The third phase is the unloading phase, in which the springs and dashpots deform, whereas the slider elements get deactivated, leading to a viscoelastic response.

The displacement of the slider element is essentially irreversible, and its magnitude is determined by employing appropriate constitutive relationships (see Section 3.9.2.2). The plastic response component, represented by the slip/movement in the slider element, accumulates with repeated train axle passages at a diminishing rate. The softer side usually accumulates greater plastic deformation as compared to the stiffer side, which results in an uneven track profile in the transition zone.

4.3.1.1 Equations of Motion for Track Substructure

The overall response of the substructure layers is determined by utilising the equations below, which are derived from the dynamic equilibrium condition in the track model (see **Figure 4.2**):

$$
\begin{bmatrix} m_{\mathrm{g}} & 0 & 0 \\ 0 & m_{\mathrm{s}} & 0 \\ 0 & 0 & m_{\mathrm{b}} \end{bmatrix} \begin{Bmatrix} d\ddot{z}_{\mathrm{g,m}}(t) \\ d\ddot{z}_{\mathrm{s,m}}(t) \\ d\ddot{z}_{\mathrm{b,m}}(t) \end{Bmatrix} + \begin{bmatrix} k_{\mathrm{g}} + k_{\mathrm{s}} + 2k_{\mathrm{g}}^{s} & -k_{\mathrm{s}} & 0 \\ -k_{\mathrm{s}} & k_{\mathrm{s}} + k_{\mathrm{b}} + 2k_{\mathrm{s}}^{s} & -k_{\mathrm{b}} \\ 0 & -k_{\mathrm{b}} & k_{\mathrm{b}} + 2k_{\mathrm{b}}^{s} \end{bmatrix} \begin{Bmatrix} dz_{\mathrm{g,m}}(t) \\ dz_{\mathrm{s,m}}(t) \\ dz_{\mathrm{b,m}}(t) \end{Bmatrix}
$$

$$
+ \begin{bmatrix} c_{\mathrm{g}} + c_{\mathrm{s}} + 2c_{\mathrm{g}}^{s} & -c_{\mathrm{s}} & 0 \\ -c_{\mathrm{s}} & c_{\mathrm{s}} + c_{\mathrm{b}} + 2c_{\mathrm{s}}^{s} & -c_{\mathrm{b}} \\ 0 & -c_{\mathrm{b}} & c_{\mathrm{b}} + 2c_{\mathrm{b}}^{s} \end{bmatrix} \begin{Bmatrix} d\dot{z}_{\mathrm{g,m}}(t) \\ d\dot{z}_{\mathrm{s,m}}(t) \\ d\dot{z}_{\mathrm{b,m}}(t) \end{Bmatrix}
$$

$$
- \begin{bmatrix} c_{\mathrm{g}} + 2c_{\mathrm{g}}^{s} & -c_{\mathrm{s}} & 0 \\ 2c_{\mathrm{s}}^{s} & c_{\mathrm{s}} + 2c_{\mathrm{s}}^{s} & -c_{\mathrm{b}} \\ 2c_{\mathrm{b}}^{s} & 2c_{\mathrm{b}}^{s} & c_{\mathrm{b}} + 2c_{\mathrm{b}}^{s} \end{bmatrix} \begin{Bmatrix} d\dot{z}_{\mathrm{g,m}}^{p}(t) \\ d\dot{z}_{\mathrm{s,m}}^{p}(t) \\ d\dot{z}_{\mathrm{b,m}}^{p}(t) \end{Bmatrix} - \begin{bmatrix} k_{\mathrm{g}} + 2k_{\mathrm{g}}^{s} & -k_{\mathrm{s}} & 0 \\ 2k_{\mathrm{s}}^{s} & k_{\mathrm{s}} + 2k_{\mathrm{s}}^{s} & -k_{\mathrm{b}} \\ 2k_{\mathrm{b}}^{s} & 2k_{\mathrm{b}}^{s} & k_{\mathrm{b}} + 2k_{\mathrm{b}}^{s} \end{bmatrix} \begin{Bmatrix} dz_{\mathrm{g,m}}^{p}(t) \\ dz_{\mathrm{s,m}}^{p}(t) \\ dz_{\mathrm{b,m}}^{p}(t) \end{Bmatrix}
$$

$$
- \begin{bmatrix} c_{\mathrm{g}}^{s} & 0 & 0 \\ 0 & c_{\mathrm{s}}^{s} & 0 \\ 0 & 0 & c_{\mathrm{b}}^{s} \end{bmatrix} \begin{Bmatrix} d\dot{z}_{\mathrm{g,m-1}}(t) \\ d\dot{z}_{\mathrm{s,m-1}}(t) \\ d\dot{z}_{\mathrm{b,m-1}}(t) \end{Bmatrix} - \begin{bmatrix} c_{\mathrm{g}}^{s} & 0 & 0 \\ 0 & c_{\mathrm{s}}^{s} & 0 \\ 0 & 0 & c_{\mathrm{b}}^{s} \end{bmatrix} \begin{Bmatrix} d\dot{z}_{\mathrm{g,m+1}}(t) \\ d\dot{z}_{\mathrm{s,m+1}}(t) \\ d\dot{z}_{\mathrm{b,m+1}}(t) \end{Bmatrix} - \begin{bmatrix} k_{\mathrm{g}}^{s} & 0 & 0 \\ 0 & k_{\mathrm{s}}^{s} & 0 \\ 0 & 0 & k_{\mathrm{b}}^{s} \end{bmatrix} \begin{Bmatrix} dz_{\mathrm{g,m-1}}(t) \\ dz_{\mathrm{s,m-1}}(t) \\ dz_{\mathrm{b,m-1}}(t) \end{Bmatrix}
$$

$$
- \begin{bmatrix} k_{\mathrm{g}}^{s} & 0 & 0 \\ 0 & k_{\mathrm{s}}^{s} & 0 \\ 0 & 0 & k_{\mathrm{b}}^{s} \end{bmatrix} \begin{Bmatrix} dz_{\mathrm{g,m+1}}(t) \\ dz_{\mathrm{s,m+1}}(t) \\ dz_{\mathrm{b,m+1}}(t) \end{Bmatrix} + \begin{bmatrix} c_{\mathrm{g}}^{s} & 0 & 0 \\ c_{\mathrm{s}}^{s} & c_{\mathrm{s}}^{s} & 0 \\ c_{\mathrm{b}}^{s} & c_{\mathrm{b}}^{s} & c_{\mathrm{b}}^{s} \end{bmatrix} \begin{Bmatrix} d\dot{z}_{\mathrm{g,m-1}}^{p}(t) \\ d\dot{z}_{\mathrm{s,m-1}}^{p}(t) \\ d\dot{z}_{\mathrm{b,m-1}}^{p}(t) \end{Bmatrix} + \begin{bmatrix} c_{\mathrm{g}}^{s} & 0 & 0 \\ c_{\mathrm{s}}^{s} & c_{\mathrm{s}}^{s} & 0 \\ c_{\mathrm{b}}^{s} & c_{\mathrm{b}}^{s} & c_{\mathrm{b}}^{s} \end{bmatrix} \begin{Bmatrix} d\dot{z}_{\mathrm{g,m+1}}^{p}(t) \\ d\dot{z}_{\mathrm{s,m+1}}^{p}(t) \\ d\dot{z}_{\mathrm{b,m+1}}^{p}(t) \end{Bmatrix}
$$

$$
+ \begin{bmatrix} k_{\mathrm{g}}^{s} & 0 & 0 \\ k_{\mathrm{s}}^{s} & k_{\mathrm{s}}^{s} & 0 \\ k_{\mathrm{b}}^{s} & k_{\mathrm{b}}^{s} & k_{\mathrm{b}}^{s} \end{bmatrix} \begin{Bmatrix} dz_{\mathrm{g,m-1}}^{p}(t) \\ dz_{\mathrm{s,m-1}}^{p}(t) \\ dz_{\mathrm{b,m-1}}^{p}(t) \end{Bmatrix} + \begin{bmatrix} k_{\mathrm{g}}^{s} & 0 & 0 \\ k_{\mathrm{s}}^{s} & k_{\mathrm{s}}^{s} & 0 \\ k_{\mathrm{b}}^{s} & k_{\mathrm{b}}^{s} & k_{\mathrm{b}}^{s} \end{bmatrix} \begin{Bmatrix} dz_{\mathrm{g,m+1}}^{p}(t) \\ dz_{\mathrm{s,m+1}}^{p}(t) \\ dz_{\mathrm{b,m+1}}^{p}(t) \end{Bmatrix} = \begin{Bmatrix} dF_{\mathrm{g,m}}(t) \\ dF_{\mathrm{s,m}}(t) \\ dF_{\mathrm{b,m}}(t) \end{Bmatrix} \qquad 4.2(a)
$$

$$m_{\mathrm{b}}^{r} d\ddot{z}_{\mathrm{b,n}}(\mathrm{t}) + k_{\mathrm{b}}^{r}\left[dz_{\mathrm{b,n}}(t) - dz_{\mathrm{b,n}}^{p}(t)\right] + c_{\mathrm{b}}^{r}\left[d\dot{z}_{\mathrm{b,n}}(t) - d\dot{z}_{\mathrm{b,n}}^{p}(t)\right]$$
$$+ c_{\mathrm{b}}^{s,r}\langle 2\left[d\dot{z}_{\mathrm{b,n}}(t) - d\dot{z}_{\mathrm{b,n}}^{p}(t)\right] - \left[d\dot{z}_{\mathrm{b,n-1}}(t) - d\dot{z}_{\mathrm{b,n-1}}^{p}(t)\right]$$
$$- \left[d\dot{z}_{\mathrm{b,n+1}}(t) - d\dot{z}_{\mathrm{b,n+1}}^{p}(t)\right]\rangle$$
$$+ k_{\mathrm{b}}^{s,r}\langle 2\left[dz_{\mathrm{b,n}}(t) - dz_{\mathrm{b,n}}^{p}(t)\right] - \left[dz_{\mathrm{b,n-1}}(t) - dz_{\mathrm{b,n-1}}^{p}(t)\right]$$
$$- \left[dz_{\mathrm{b,n+1}}(t) - dz_{\mathrm{b,n+1}}^{p}(t)\right]\rangle = dF_{\mathrm{b,n}}^{r}(t) \qquad 4.2(\mathrm{b})$$

where superscript '*r*' represents the stiffer zone.

Equations 4.2(a) and 4.2(b) represent the response of the track layers in the softer and stiffer side of the transition zone, respectively. These equations are solved using Newmark's beta numerical integration method at each time instant, *t*, to calculate the overall response of the track substructure layers below each sleeper location.

4.3.1.2 Vibrating Mass, Springs and Dashpots

To solve Equations 4.2(a) and 4.2(b), the parameters such as vibrating mass, spring stiffness and damping coefficient for the ballast, subballast and subgrade layers are required. The mass and spring stiffness for the track layers can be determined analytically based on the geometry of their effective acting region, which is assumed to coincide with a pyramidal-shaped load distribution zone within these layers (Ahlbeck et al. 1978; Zhai et al. 2004; Zhang et al. 2016). **Figures 4.3(a)** and **4.3(b)** show the effective acting region of the track layers below individual sleeper locations in the softer and stiffer side of the transition zone, respectively. The effective region is a truncated pyramid whose geometry varies depending on the extent of overlapping within the track layers. The procedure to determine the vibrating mass, spring stiffness and damping coefficients is described in Section 3.2.2.2 and APPENDIX E.

4.3.2 Determination of Train-Induced Load and Stress State

As shown in **Figure 4.2**, the train-induced vertical rail seat load excites the geotechnical rheological model at each sleeper position. This load is transmitted from the superstructure (comprising rail, rail pads, fasteners and sleepers) to the substructure layers through the sleeper-ballast contact. Its magnitude is determined using a similar procedure as described in Section 3.2.1 and APPENDIX F. The stress state is computed using the modified Boussinesq approach as discussed in Section 3.9.1.1.

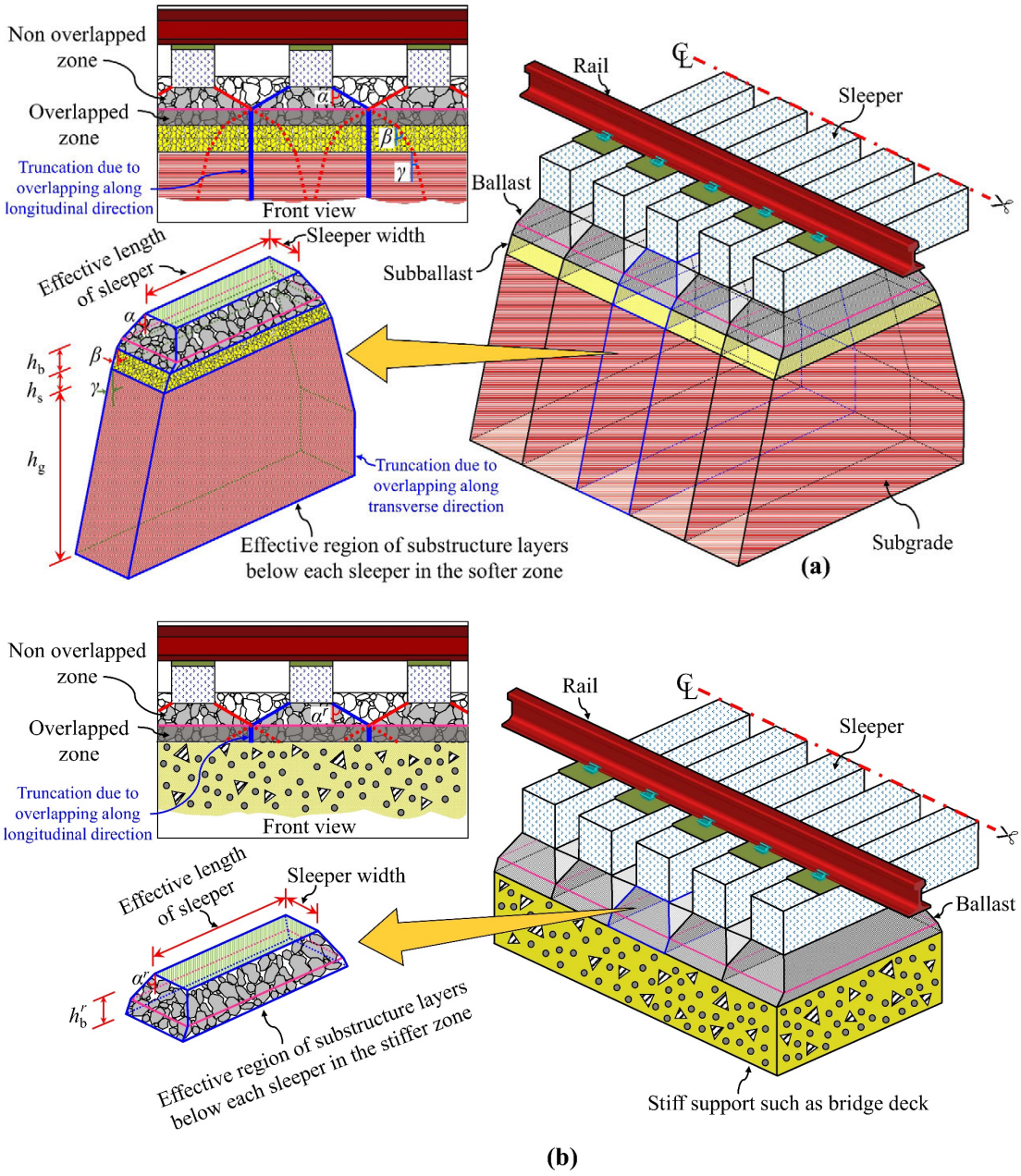

Figure 4.3 Effective acting region of track layers considered in the analysis at **(a)** softer side; **(b)** stiffer side

4.3.3 Application of the Methodology

The proposed approach can be employed in the following sequence: first, the varied track structure composition along the longitudinal direction is identified. Then, the effective portion of the substructure layers below individual sleeper location is determined, and the model parameters such as vibrating mass, spring stiffness and damping coefficients are computed. Subsequently, the magnitude of load transferred from the superstructure to the substructure layers is determined for each zone (stiffer and softer), and the stress state for

the plastic slider elements is derived using the modified Boussinesq solutions. For each time step, the loading-unloading conditions for the slider elements are inspected (see Section 3.9.2.2). If the slider is active, the magnitude of plastic displacement in the slider element is calculated. Finally, Equations 4.2(a) and 4.2(b) are solved to determine the total response of the track transition zone.

4.4 Model Validation

4.4.1 Comparison with 3D FE Model Results

4.4.1.1 Model Development

Figure 4.4 shows the 3D FE model of an open track-bridge transition zone developed using ABAQUS (Dassault Systèmes 2018). The transition zone geometry is based on a section of railway track along the Amtrak's North East Corridor in the United States (US), which comprises three regions: open track, near bridge (approach zone) and the bridge (Boler et al. 2018a). The track consists of 67.5 kg/m rails supported by sleepers placed at a spacing of 0.61 m. A 0.305 m thick ballast layer is provided below the sleepers along the entire length of the track. A multi-layered system underlies the ballast layer at the open track and the near bridge zones (see **Figure 4.4**). The ballast layer at the bridge is supported by the concrete deck slab, which is simulated by restricting the vertical displacement of the bottom nodes of the ballast layer.

The total thickness of the substructure at the open track and near bridge region is 20 m. The model dimension along the track transverse direction (i.e., y-direction) is taken as 20 m to ensure sufficient distance between the analysis segment and model boundaries. The vertical boundaries at the sides are connected to dashpots in horizontal and vertical directions to prevent the spurious reflection of stress waves. The nodes at the bottom boundary are assumed to be fixed, i.e., their movement is restricted in both vertical and horizontal directions. Only one half of the track is modelled owing to symmetry along the track centre-line.

The superstructure and the substructure layers are discretised using eight-noded 3D brick elements of type C3D8R, and the entire FE model comprises 301,176 elements. A fine mesh is used near the track region, and its coarseness is increased progressively with an

increase in distance from the track (Shih et al. 2016). Other details are provided in CHAPTER 7 and APPENDIX G.

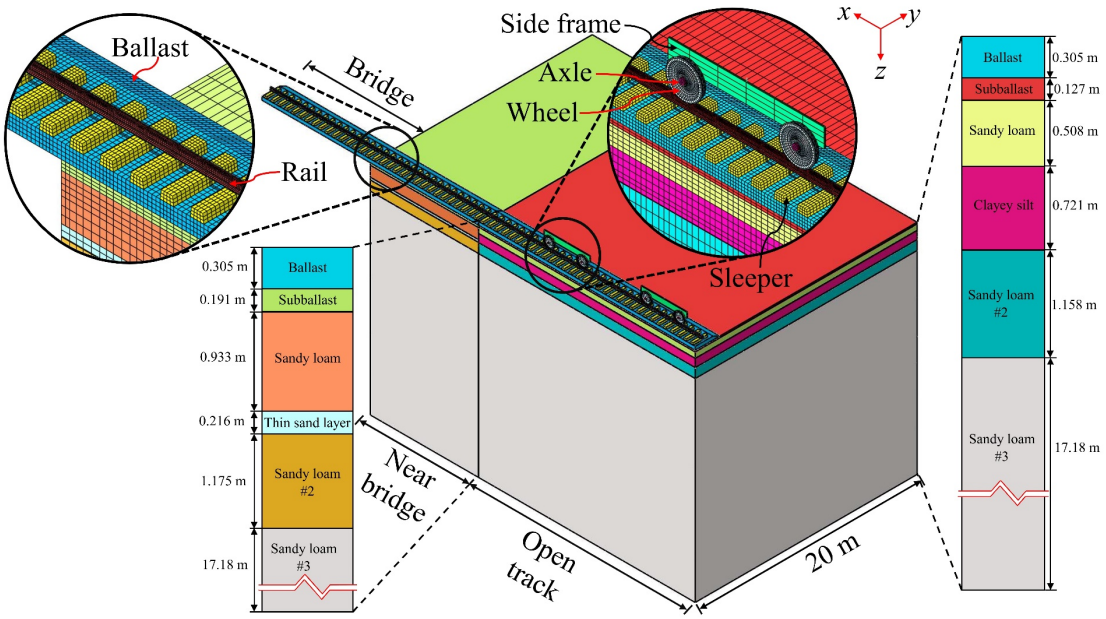

Figure 4.4 3D FE model of the open track-bridge transition zone

4.4.1.2 Comparison of Track Response

Table 4.1 lists the material properties used in the model predictions for both open track and near bridge locations [adopted from Boler et al. (2018a)]. The rheological model considers the soil layers beneath the subballast layer as a single equivalent layer. **Figure 4.5(a)** shows the variation of vertical displacement at the ballast top along the length of the track predicted using the proposed method and the FE analysis. **Figure 4.5(b)** shows the variation of transient vertical deformation in the track substructure layers with time during the passage of two bogies from adjacent wagons. A good agreement between the results predicted using the present method and that obtained from FEM can be observed. The main advantage of the proposed technique is its significantly higher computational efficiency over the FE analysis. For the present case, the proposed approach took 1,080 s, and FEM took about 355,615 s on a high-performance computing facility using thirty 2.5 GHz processors running in parallel.

Table 4.1 Model parameters for evaluation of track response

Variable	Symbol	Unit	Mishra et al. (2017); Boler et al. (2018a)		Paixão et al. (2014a)		Parametric study
			Open track	Near bridge	Section S3	Section S4	
Ballast (Layer 1)							
Resilient modulus	$E_b(=E_b^r)$	MPa	184	153	130	130	200
Poisson's ratio	$v_b\,(=v_b^r)$	–	0.3	0.3	0.2	0.2	0.3
Shear stiffness	$k_b^s\,(=k_b^{s,r})$	MN/m	2	2	78.4	78.4	78.4
Shear damping	$c_b^s\,(=c_b^{s,r})$	kNs/m	5	5	80	80	80
Density	$\rho_b\,(=\rho_b^r)$	kg/m^3	1,990	1,990	1,530	1,530	1,760
Thickness	$h_b\,(=h_b^r)$	m	0.305	0.305	0.3	0.3	0.3
Subballast (Layer 2)							
Resilient modulus	E_s	MPa	19	80	200	200	115
Poisson's ratio	v_s	–	0.4	0.4	0.3	0.3	0.4
Shear stiffness	k_s^s	MN/m	1	1	476	476	476
Shear damping	c_s^s	kNs/m	1	1	80	80	80
Density	ρ_s	kg/m^3	2,092	2,092	1,935	1,935	1,920
Thickness	h_s	m	0.127	0.191	0.3	0.3	0.15
Subgrade							
Resilient modulus	E_g	MPa	49	72	1,142	10,000	45
Poisson's ratio	v_g	–	0.4	0.4	0.3	0.3	0.45
Shear stiffness	k_g^s	MN/m	50	10	500	1,600	1,600
Shear damping	c_g^s	kNs/m	40	40	80	80	80
Density	ρ_g	kg/m^3	2,092	2,092	1,935	2,200	1,920
Thickness	h_g	m	2.082	2.019	3.2	3.2	10

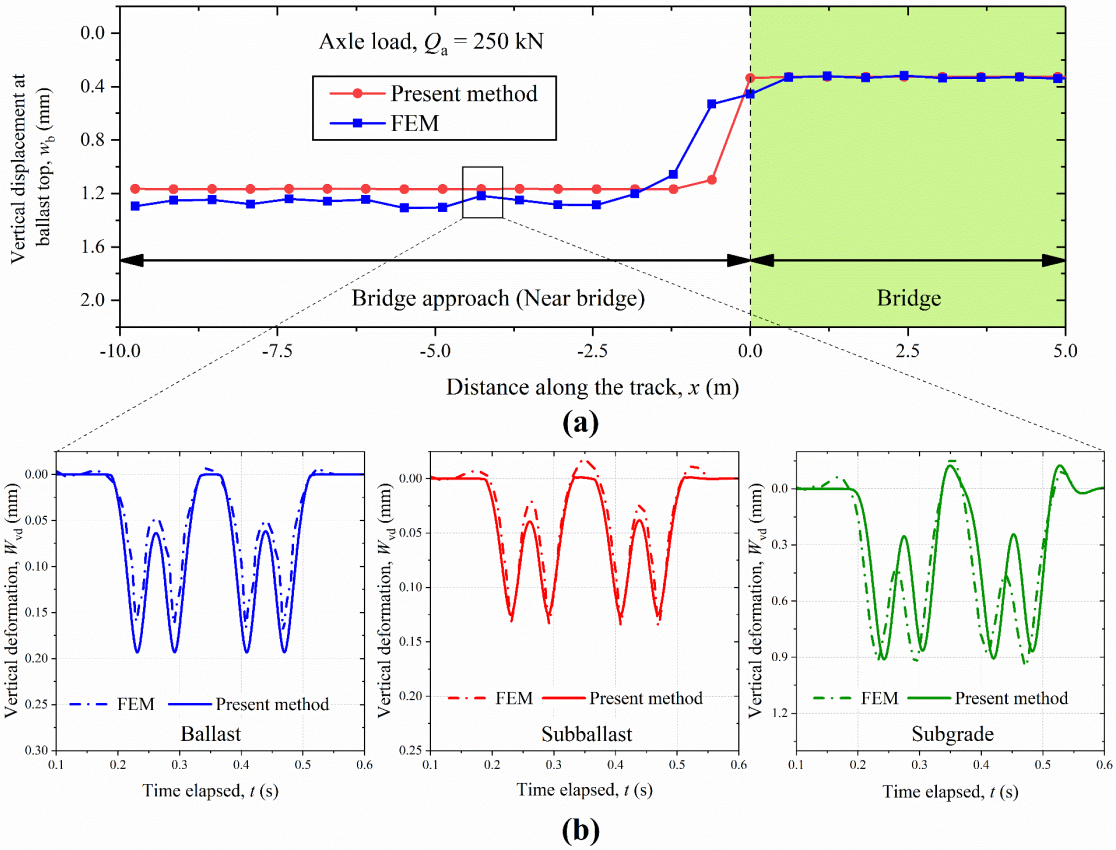

Figure 4.5 Comparison of results predicted using the proposed method and FEM: **(a)** variation of vertical displacement at ballast top with distance along the track; **(b)** variation of vertical deformation with time for ballast, subballast and subgrade

4.4.2 Comparison of Results with Data from Field Tests

The accuracy of the proposed methodology is investigated by comparing the predicted results with the field data reported by Paixão et al. (2014a) for an underpass-embankment transition zone in Portugal. The transition zone comprised of two wedge-shaped engineered fills between the underpass and the embankment that were constructed using unbound granular material (UGM) and cement bound mixtures (CBM). **Table 4.1** lists the parameters employed in the analysis. **Figure 4.6** presents a comparison of the vertical track displacement predicted using the present method with the field data recorded during one passage of the Portuguese Alfa pendular passenger tilting train at sections S3 and S4 (located at 8.4 m and 1.8 m from the underpass, respectively). It can be observed that the predicted results are in an acceptable agreement with the field measurements. The predicted results somewhat underestimate the vertical displacement at both the sections; however, the predicted average value of the peaks in the displacement-time history varies by 18% and 12 % from the corresponding field values at sections S3 and S4, respectively.

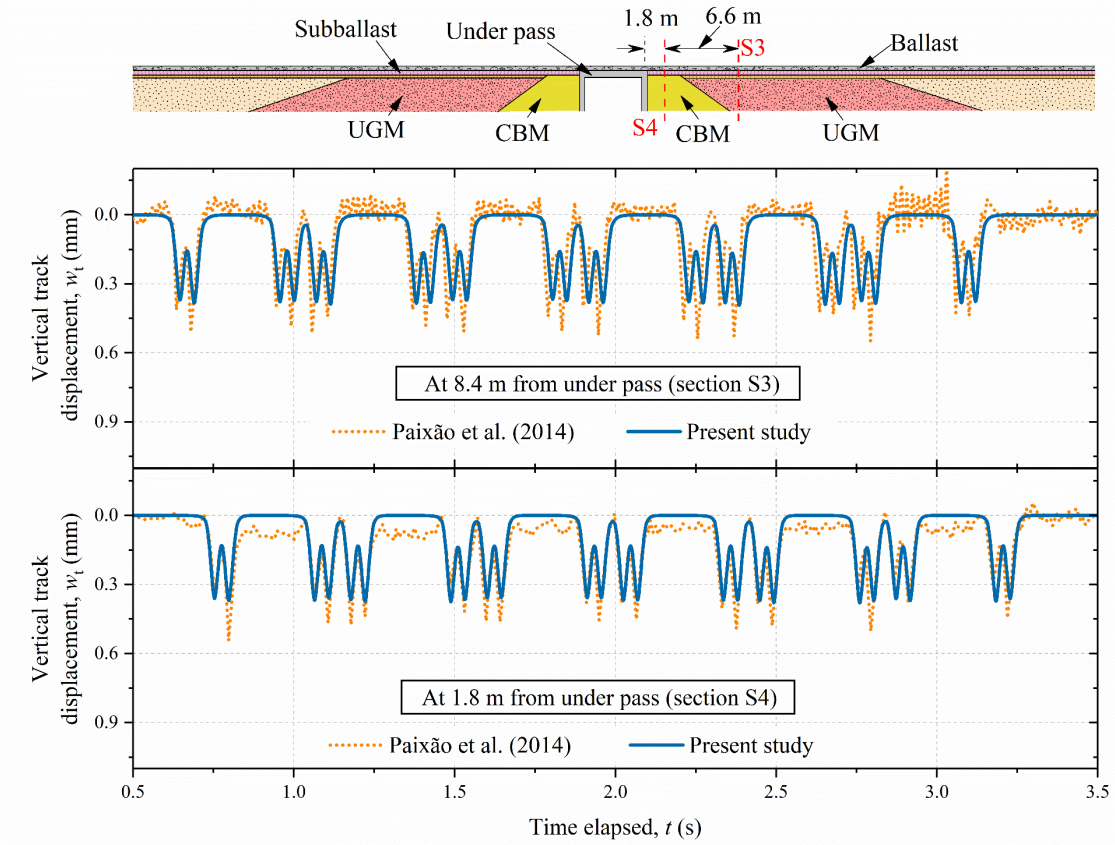

Figure 4.6 Comparison of predicted transient vertical displacement at sections S3 and S4 with the field data reported by Paixão et al. (2014a)

Mishra et al. (2017) recorded the vertical deformation in the track substructure layers near three bridge approaches along Amtrak's North East Corridor in the US. **Figure 4.7** presents a comparison of the accumulation of irrecoverable deformation in the ballast (layer 1), subballast (layer 2), and subgrade layers (layers 3–5 approximated to a single equivalent layer) predicted using the present method with the field data. **Tables 4.1**, **4.2** and **4.3** list the parameters used in the model predictions. It can be observed that the predicted results are in an acceptable agreement with the field data. The model can accurately predict the accumulation of settlement in the substructure layers under train-induced repeated loading at a diminishing rate.

Thus, it is apparent that the proposed methodology can accurately simulate the behaviour of the railway tracks in the transition zones. The technique can reproduce the observed transient behaviour in addition to the accumulation of settlement in the substructure layers at a diminishing rate with reasonable accuracy.

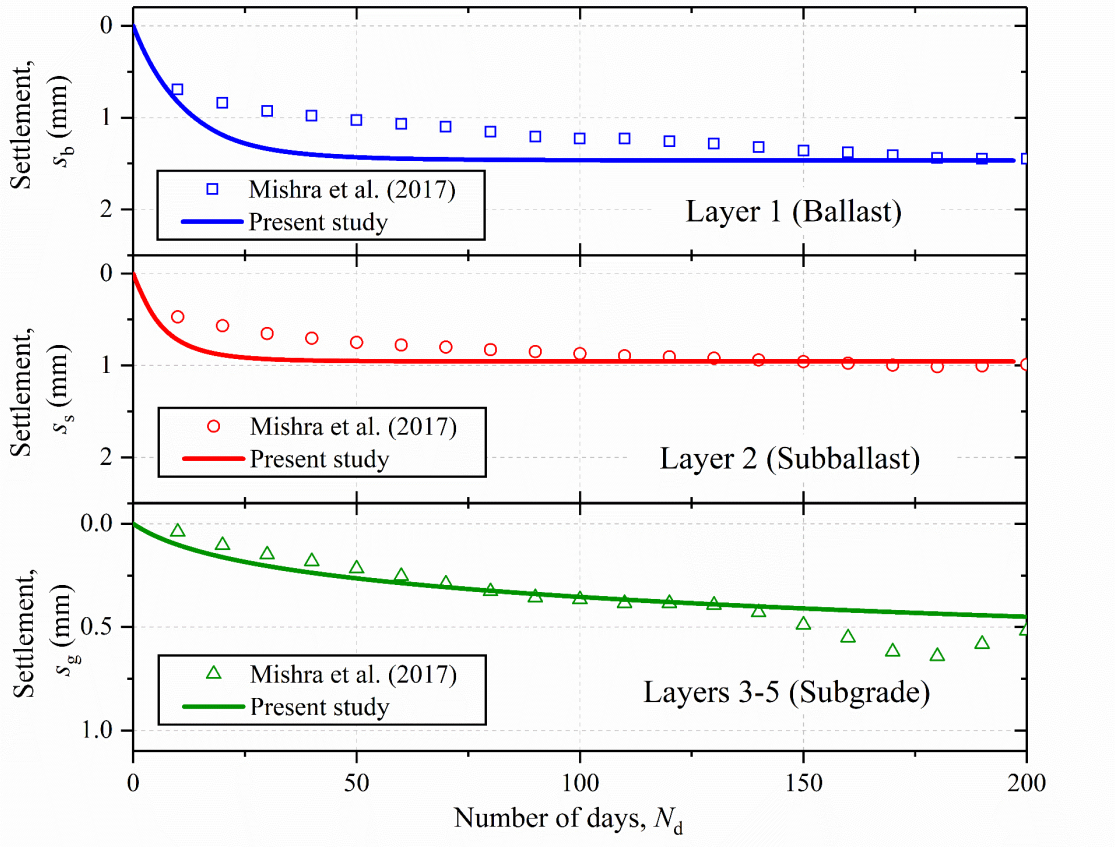

Figure 4.7 Comparison of predicted settlement in substructure layers with the field data reported by Mishra et al. (2017)

Table 4.2 Constitutive parameters for granular layers

Parameter	**Symbol**	**Mishra et al. (2017)**	
		Ballast	**Layer 2 (Subballast)**
Reference void ratio on CSL	Γ	1.4	0.9
Slope of CSL	λ	0.1	0.05
Critical stress ratio	M_{tc}	1.25	1.15
Volumetric coupling parameter	N_v	0.2	0.3
State-dilatancy parameter	χ_{tc}	3	4.2
Cyclic hardening parameter	a_h	0.3	0.222
Plastic hardening parameter	H	$50–250\psi$	$160–260\psi$

Table 4.3 Constitutive parameters for subgrade

Parameter	Symbol	Value
Initial void ratio	e_0	0.5
Slope of CSL	λ	0.0046
Slope of swelling line	κ	0.0009
Critical state friction angle (°)	φ_c	40
Characteristic stress parameter	ξ	0.1
Spacing parameter	A	0.31
Cyclic hardening parameter	a_h	0.0025

4.5 Results and Discussion

4.5.1 Performance under Increased Axle Load

The validated methodology is used to investigate the performance of an open track-bridge transition zone (shown in **Figure 4.2**) subjected to an increase in Q_a. **Tables 3.4, 3.5 and 4.1** list the parameters employed in the analysis. The values of the constitutive parameters for granular layers and subgrade have been derived from the cyclic triaxial tests conducted by Suiker et al. (2005) and Wichtmann (2005), respectively. The Q_a is varied between 20 t – 30 t to investigate its influence on the behaviour of the transition zone. The differential settlement is computed as the maximum difference between the cumulative settlement in the softer (or improved zone, if present) and stiffer sides.

Figure 4.8(a) shows the variation of cumulative settlement along the track length for three different axle loads. It can be observed that the differential settlement between the softer and stiffer side of the transition increases with an increase in Q_a. It increases by 25% and 26 % as Q_a increases from 20 t to 25 t and from 25 t to 30 t, respectively, after a cumulative tonnage of 25 MGT. The differential settlement also increases with an increase in tonnage. For 25 t axle load, the differential settlement increases from 16.2 mm at 0.1 MGT to 27 mm at 25 MGT.

Figure 4.8(b) shows the variation of settlement of the track substructure with tonnage for the three axle loads at three different locations. The substructure settlement is much higher at 7 m than at 0.3 m from the bridge. The settlement at 7 m from the bridge increases by 25% and 58%, with an increase in Q_a from 20 t to 25 t and 30 t, respectively.

Similarly, the settlement at 0.3 m from the bridge and 4 m on the bridge increases by 51% and 47%, respectively, with an increase in Q_a from 20 t – 30 t.

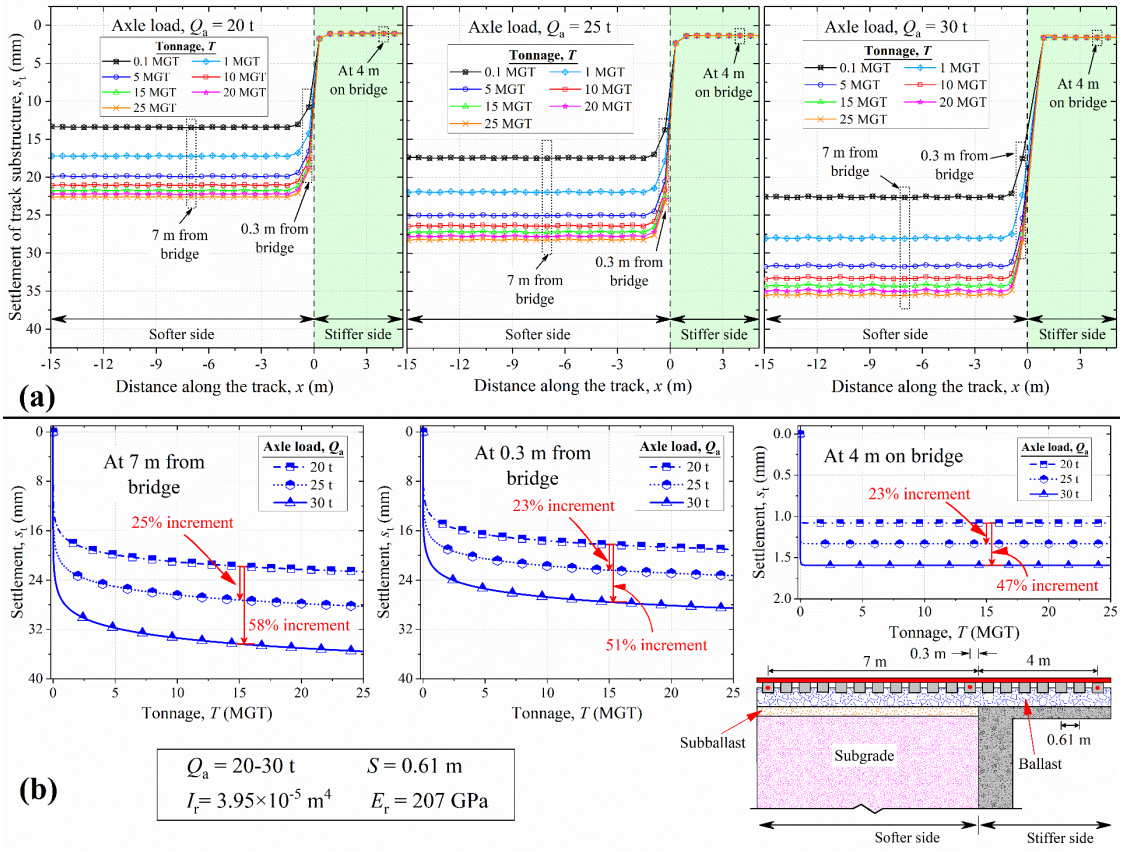

Figure 4.8 Variation of settlement at different axle loads with **(a)** distance; **(b)** tonnage at different locations

Thus, an increase in Q_a increases the differential settlement in the transition zone, exacerbating the track geometry degradation problem. Therefore, the application of remedial measures becomes more necessary with an increase in the axle loads.

4.5.2 Performance under Increased Granular Layer Thickness

In the previous section, Q_a increased the differential settlement in the transition zone. A plausible technique for reducing this differential settlement is to increase h_{gl}. This section investigates the efficacy of increased h_{gl} in decreasing the differential settlement. Two cases are studied: in the first case, h_b is increased from 0.3 m to 0.9 m, while h_s is kept constant at 0.15 m. In the second case, h_s is increased from 0.15 m to 0.6 m, while h_b is assigned a constant value of 0.3 m. Q_a of 25 t is considered in both cases.

4.5.2.1 Influence of Ballast Thickness

Figure 4.9 shows the variation of settlement with distance along the track and depth at different ballast layer thickness. The depth has been normalised with respect to h_b to allow efficient comparison of the response at different h_b. It can be observed that the differential settlement decreases with an increase in h_b. The possible reason for such behaviour is that the subgrade soil is the weakest material involved in this critical zone, and its contribution towards the total settlement is maximum (about 90% for $h_b = 0.3$ m). On increasing h_b, the stress transferred to the subgrade soil decreases. This happens due to a higher stress spreading ability of the thicker ballast layer. The validity of this conjecture is investigated by comparing the stress distribution in the subballast and subgrade layers with depth for different h_b (shown in **Figure 4.10**). It is observed that the stress decreases with an increase in h_b. At the subgrade top, σ_v decreases by 23.7%, 20.4%, 18.5% and 16% on increasing h_b from 0.3 m to 0.45 m, 0.6 m, 0.75 m and 0.9 m, respectively. This stress reduction leads to a decrease in the settlement on the softer side (a reduction of 48% with an increase in h_b from 0.3 to 0.9 m). Consequently, the differential settlement between the stiffer and softer side of the transition decreases with an increase in h_b.

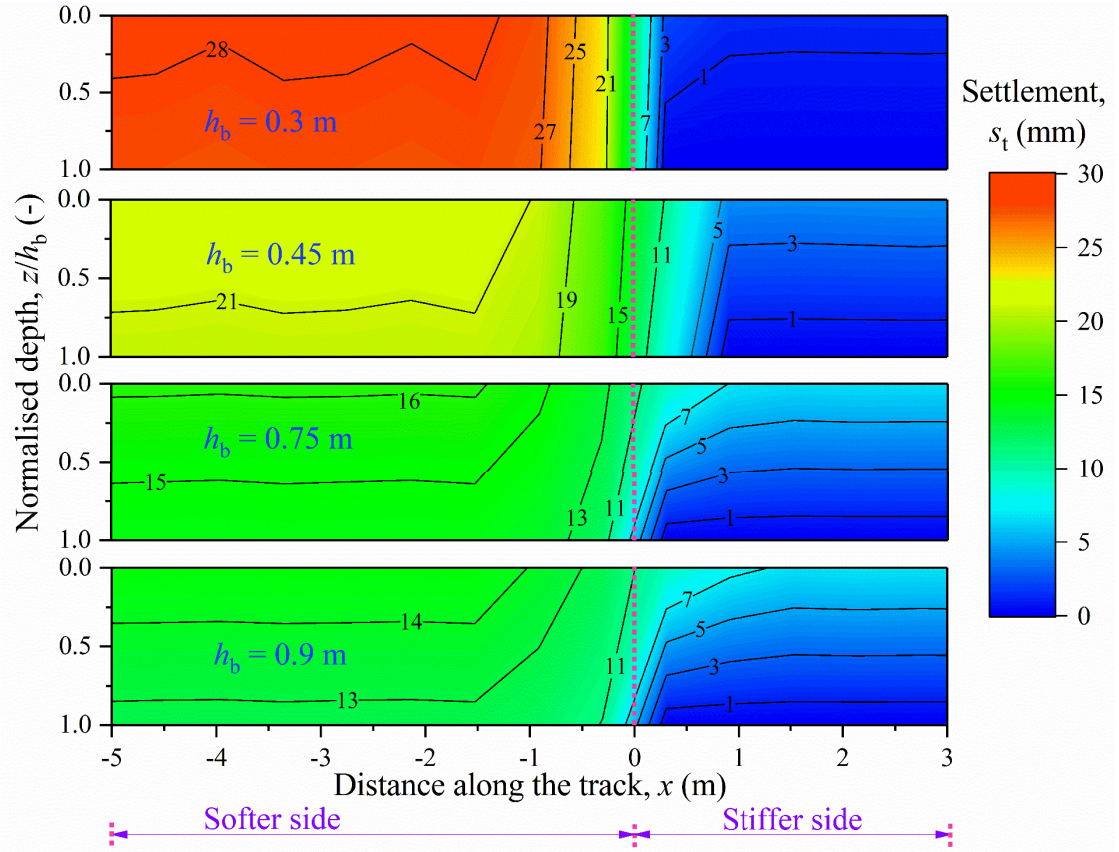

Figure 4.9 Variation of settlement with distance at different ballast layer thickness

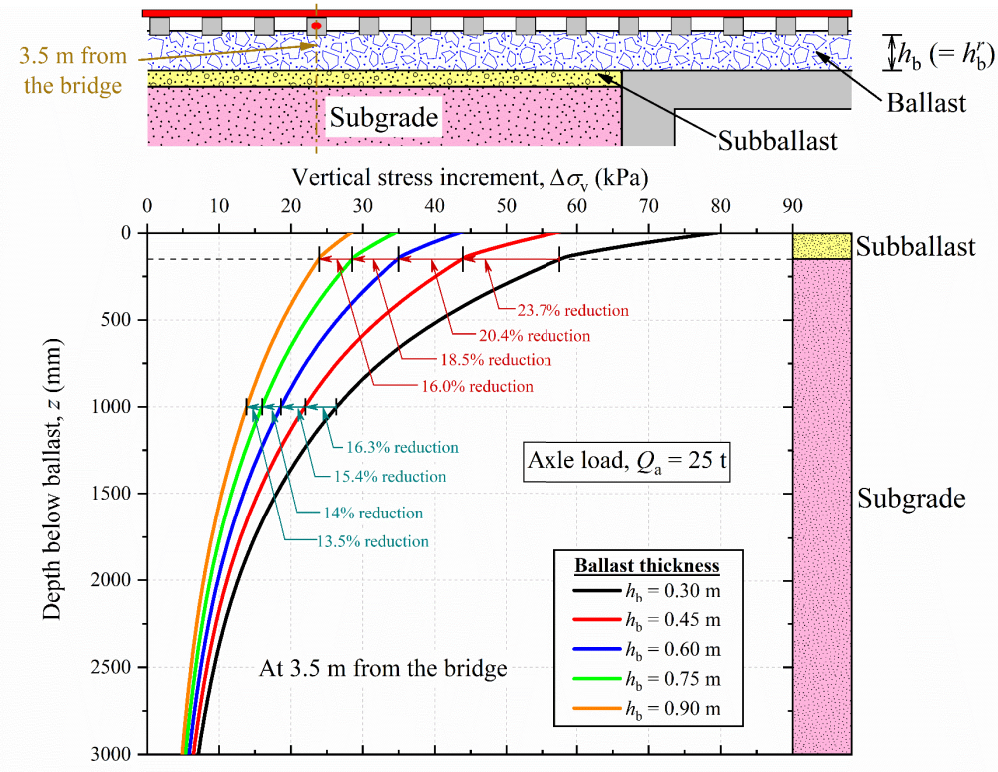

Figure 4.10 Distribution of vertical stress with depth at 3.5 m from the bridge for different ballast layer thickness

4.5.2.2 Influence of Subballast Thickness

Figure 4.11 shows the variation of settlement with distance along the track and depth (normalised with respect to h_b) at different subballast layer thickness. It can be observed that the differential settlement decreases with an increase in h_s. The reason being the reduction in the subgrade stress on increasing h_s. As shown in **Figure 4.12**, the stress at the subgrade top decreases by 23.1%, 20.2% and 17.5% on increasing h_s from 0.15 m to 0.3 m, 0.45 m and 0.6 m, respectively. Therefore, the settlement on the softer side and, consequently, the differential settlement decreases with an increase in h_s.

It is apparent that increasing the thickness of the granular layers can improve the performance of the railway track transition zone. Because the differential settlement, in this case, was primarily caused by the subgrade soil on the softer side, this technique worked rather effectively. Thus, it is crucial to correctly identify the root cause of the track geometry degradation problem in the transition zone before selecting an appropriate remedial measure.

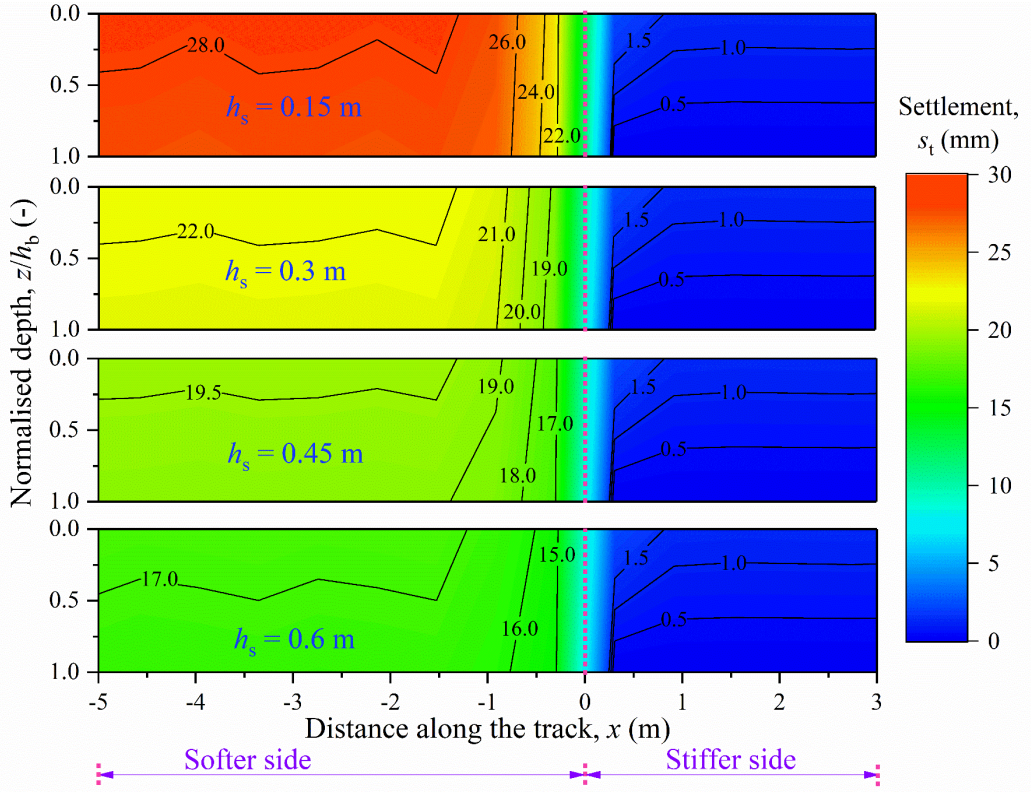

Figure 4.11 Variation of settlement with distance at different subballast layer thickness

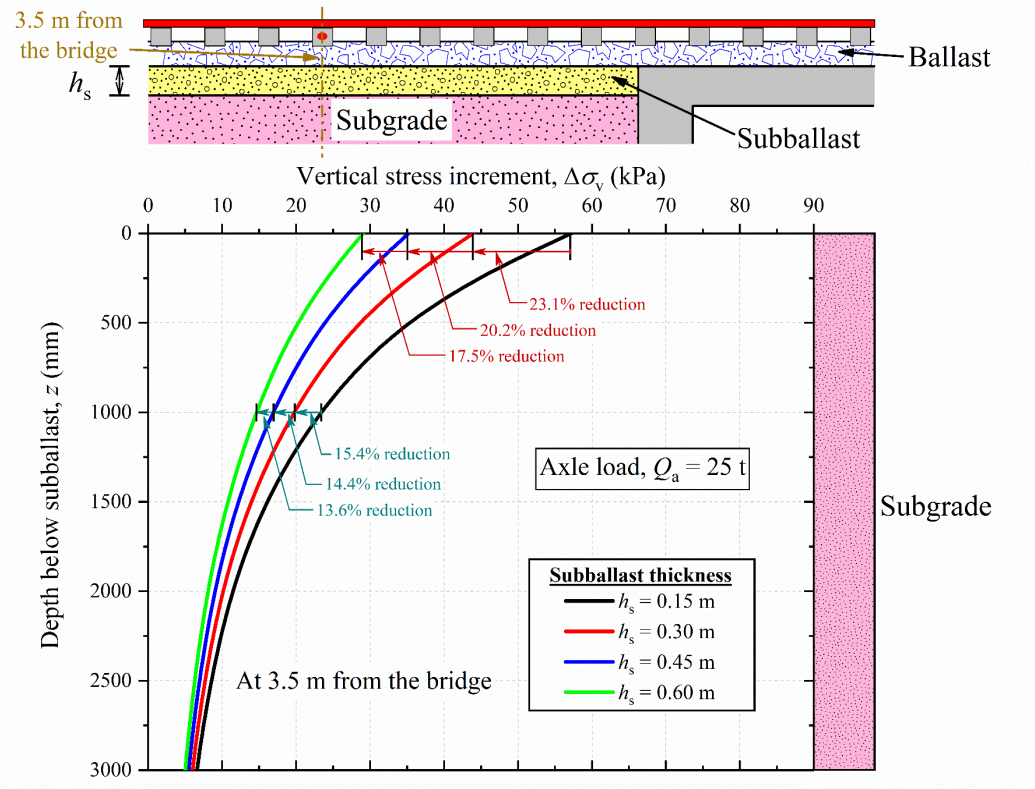

Figure 4.12 Distribution of vertical stress with depth at 3.5 m from the bridge for different subballast layer thickness

4.6 Importance of Considering Material Plasticity in Track Transition Models

Often, the behaviour of the soil layers in the railway track models is simulated using elastic constitutive relationships. Although the magnitude of plastic deformation in the substructure layers (after initial settlement) is very small for an individual axle passage, the cumulative effect over a large number of axle passages may be substantial. Therefore, the assumption of elastic material behaviour for the substructure layers may lead to an underestimation of the irrecoverable deformation in the railway track, especially after thousands or millions of axle passages. This assumption may be very critical for the analyses involving transition zones, in which differential settlement is one of the most severe problems.

In order to illustrate the importance of considering the material plasticity in predicting the behaviour of the transition zones, the results of two cases are compared: a) without slider elements (viscoelastic case); b) with slider elements (viscoelastic-plastic case). **Figure 4.13** presents a comparison of the behaviour of transition zones predicted with and without the slider elements. It can be observed that the displacement of the substructure layers is highly underestimated if the material plasticity is ignored. The difference in displacement between the softer and stiffer side of the track is very small for the case without the slider elements. The differential displacement increases significantly after incorporating the slider elements. Moreover, the differential displacement increases with an increase in tonnage due to the accumulation of plastic deformation with an increase in load repetitions.

At 7.6 m from the bridge, the subgrade displacement is underestimated by 16.2 mm after a cumulative tonnage of 0.1 MGT if the behaviour of the substructure layers is assumed as viscoelastic. The underestimation further increases with an increase in tonnage. Similar results can be observed at 0.3 m from the bridge. The total substructure displacement is underestimated by 23.3 mm after a cumulative tonnage of 25 MGT if the slider elements are not employed. Therefore, it is essential to capture the irrecoverable deformations occurring in the substructure layers under the train-induced repetitive loads, especially for the transition zones.

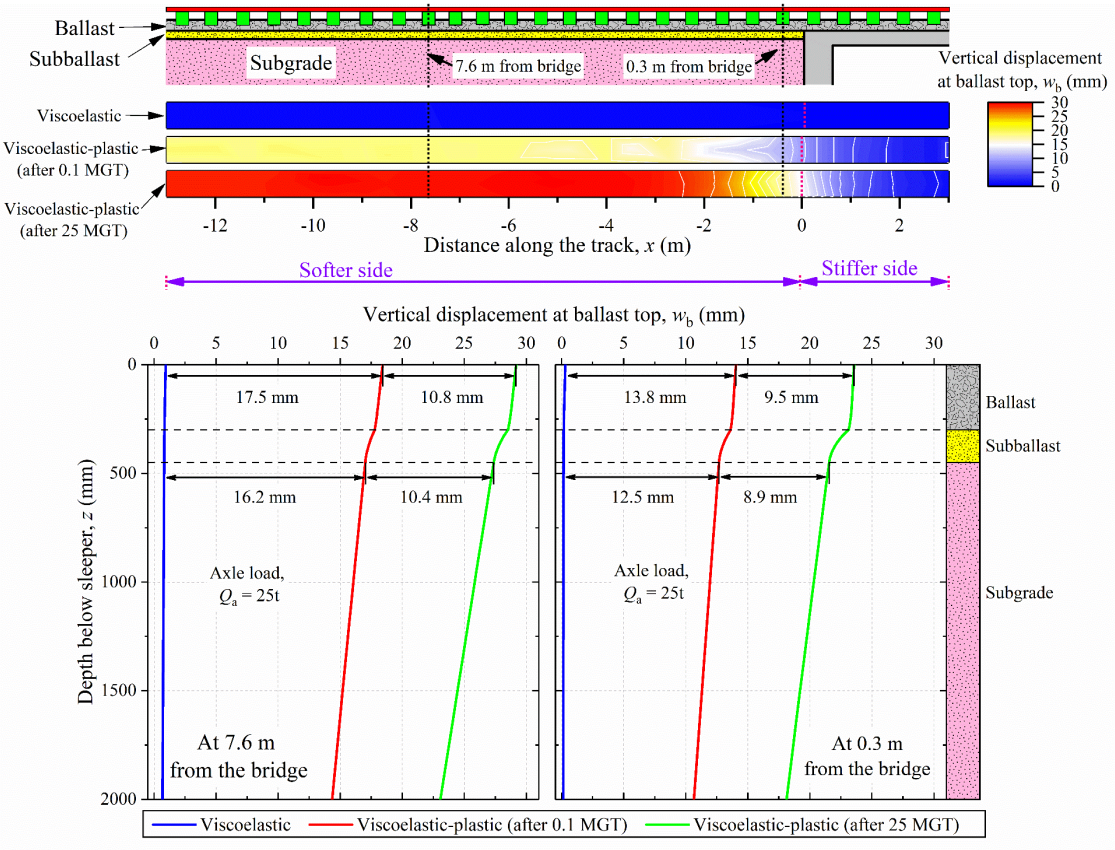

Figure 4.13 Variation of vertical displacement at ballast top with distance along the track and depth for the two cases: when slider elements are considered (viscoelastic-plastic) and when slider elements are ignored (viscoelastic)

4.7 Practical Relevance and Potential Applications

The proposed methodology provides a convenient means to assess the performance of different countermeasures in mitigating the differential settlement at the transition zone. To demonstrate this capability, the performance of two different mitigation strategies is compared. The results of the analyses are expressed in terms of settlement variation along the length and depth (normalised with respect to h_b) of the track. As discussed in Section 4.5, large plastic deformation in the subgrade is the primary cause of differential settlement in this study. Therefore, two different remedial strategies are employed: a) decreasing the stress transferred to the subgrade; b) strengthening the subgrade. The magnitude of subgrade stress can be reduced by either increasing the thickness (discussed in Sections 4.5.2.1 and 4.5.2.2) or stiffness of the granular layers (e.g., by using cellular geoinclusions) (Li et al. 2016). The subgrade soil can be strengthened by using ground improvement techniques.

Figure 4.14 shows the influence of increasing the ballast stiffness near the bridge approach (improved zone) on the differential settlement. The resilient modulus of the ballast layer in the improved zone is increased by 1.5–3 times the nominal value to represent the improvement. It can be observed that the performance of the transition zones can be improved by increasing the stiffness of the ballast layer. The differential settlement between the track on the stiffer and the softer side is reduced by 13% on increasing E_b from 200 MPa to 600 MPa.

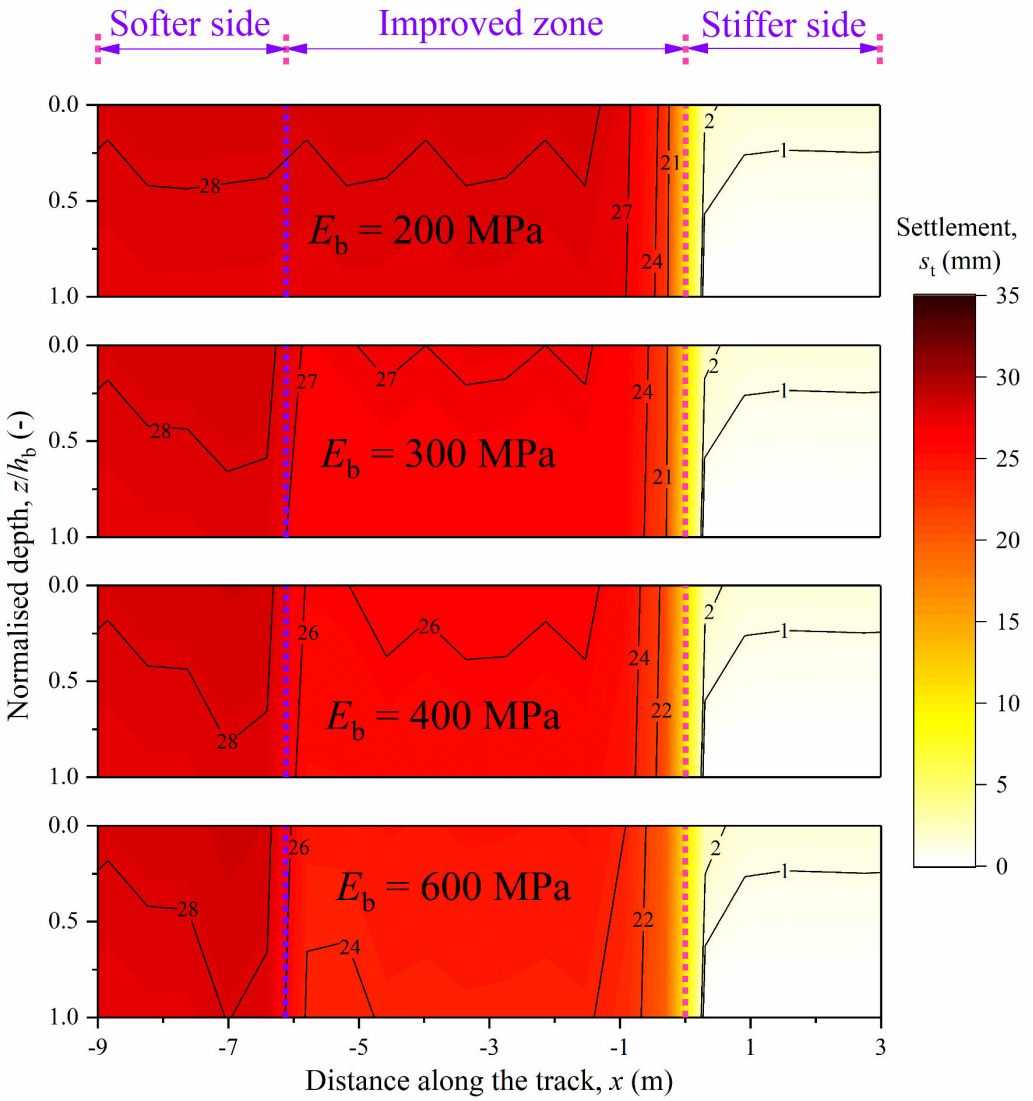

Figure 4.14 Variation of settlement with distance when ballast modulus in the improved zone is increased from 200 MPa – 600 MPa

Figure 4.15 shows the influence of increasing the subballast stiffness near the bridge approach on the differential settlement. The resilient modulus of the subballast layer in the improved zone is increased by 1.5–3 times the nominal value to represent the stiffness

increase provided by the remedial measure. It can be observed that the performance of the transition zone can be slightly improved by increasing the subballast layer stiffness. The differential settlement between the track on the stiffer and the softer side, accumulated after a tonnage of 25 MGT, decreases by 5% on increasing E_s from 115 MPa to 345 MPa. Although the differential settlement decreases with an increase in the stiffness of the granular layers, the reduction is very small.

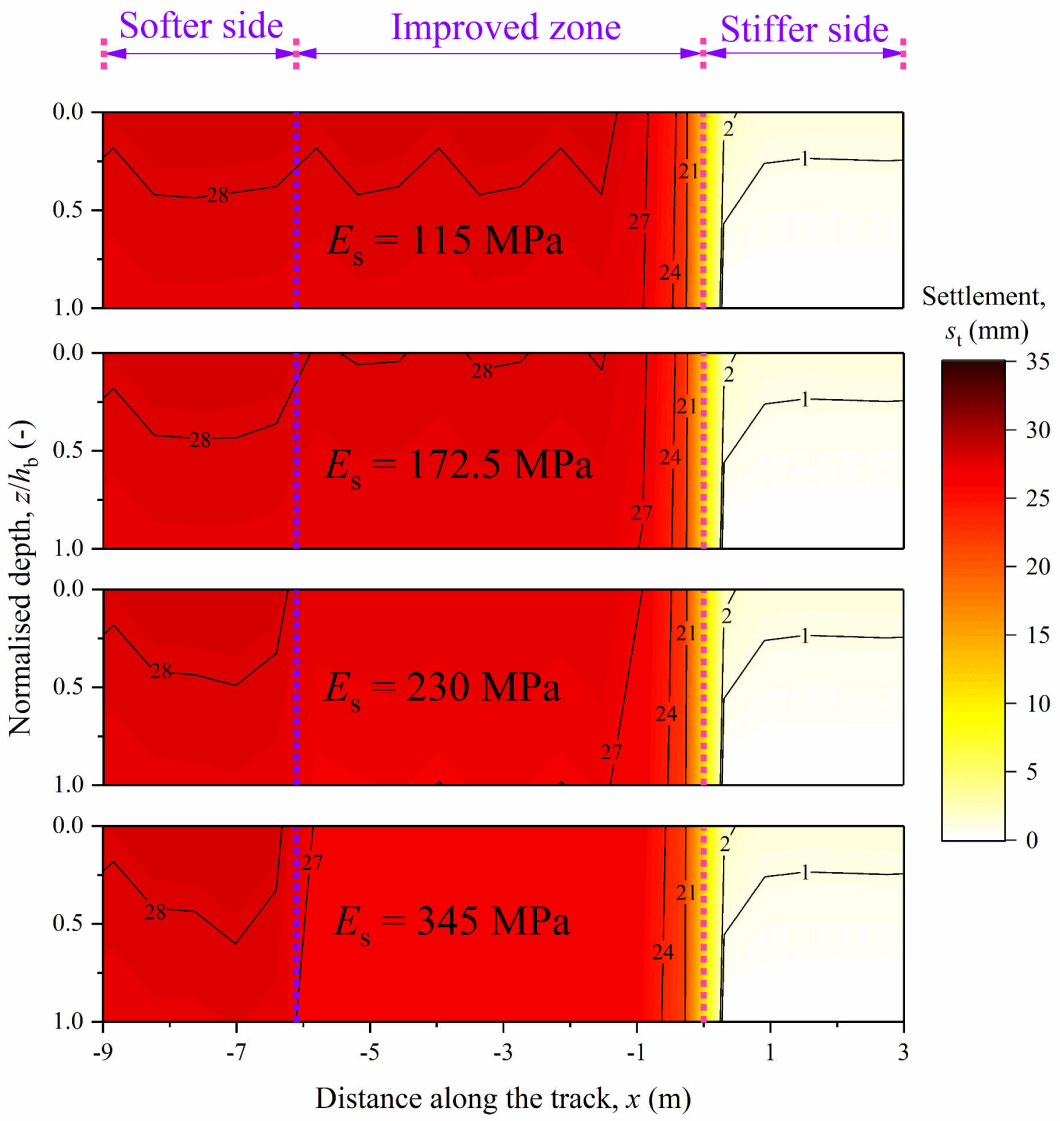

Figure 4.15 Variation of settlement with distance when subballast modulus in the improved zone is increased from 115 MPa – 345 MPa

Figure 4.16 shows the influence of improving the subgrade strength near the bridge approach on the track response. The friction angle of the subgrade layer in the improved

zone is increased to represent the strength increment provided by the countermeasures. It can be observed that the performance of the transition zone is significantly improved by increasing the subgrade strength. The differential settlement between the track on the stiffer and the softer side decreases by 39% on increasing the subgrade friction angle from 31° to 40°. Thus, it is evident that the remedies intended to strengthen the subgrade soil are more effective in mitigating the track geometry degradation in this study than those intended to increase the stiffness of the granular layers.

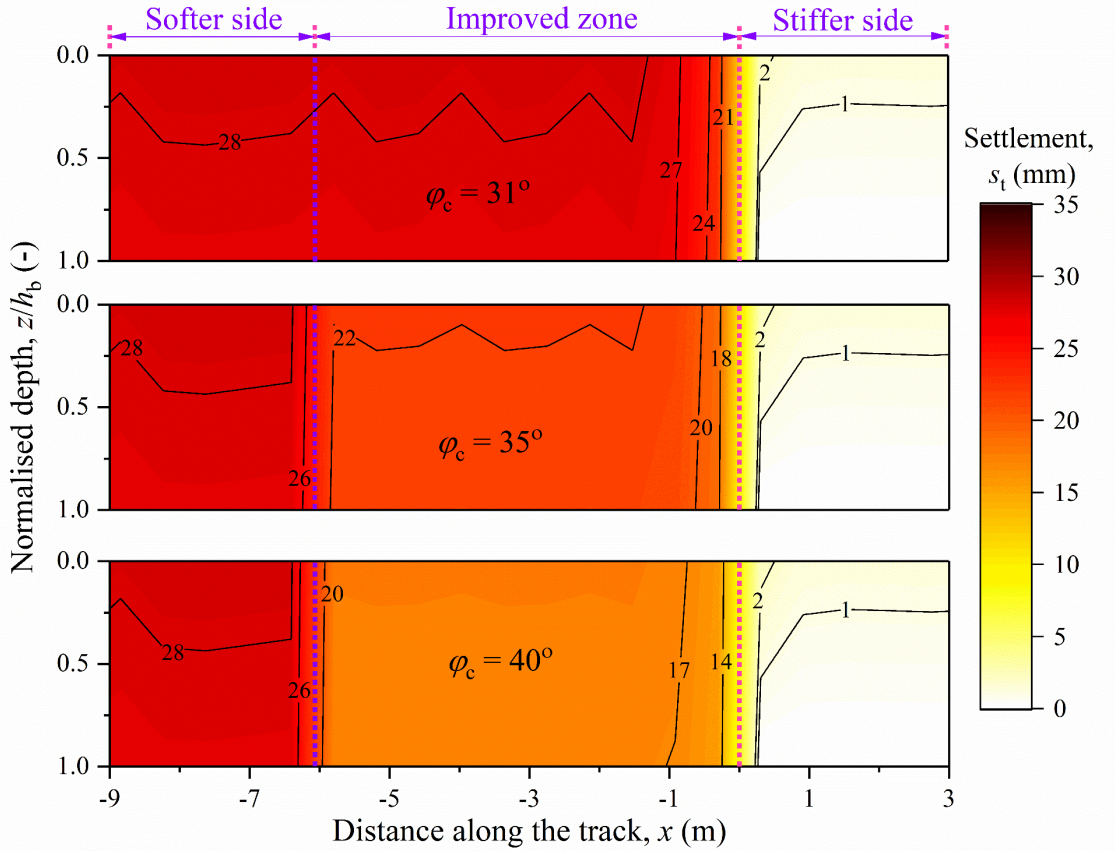

Figure 4.16 Variation of settlement with distance when subgrade friction angle in the improved zone is increased from 31° – 40°

4.8 Advantages, Limitations and Future Scope

The advantages of the novel methodology for predicting the behaviour of ballasted railway tracks in the transition zones are as follows:

- Track response is evaluated through step-by-step solution of the governing equations, which can be carried out by developing MATLAB codes (MathWorks Inc. 2021).

- The proposed methodology allows accurate prediction of differential settlement in the transition zones.
- Generation of complex model geometry is not required and only the values of input parameters is needed.
- Higher computational efficiency over FE based methods.
- Conducting parametric analyses using this methodology is easier than the FE based methods.
- Interpretation of results predicted using this methodology is relatively easier than those obtained using FE analyses.

The limitations of the novel methodology are as follows:

- Effects of vehicle-track interaction has been incorporated by using a simplified approach that employs a dynamic amplification factor.
- Effect of PSR on the behaviour of track materials has been neglected.
- Influence of water content fluctuations on the response of geomaterials is ignored.
- Ballast degradation due to impact loads generated in the transition zone because of hanging sleepers has been neglected.

The effect of PSR on track response has been treated in CHAPTER 5 of this thesis, while other limitations shall be addressed in future investigations.

4.9 Concluding Remarks

This chapter introduces a novel methodology for predicting the transient and long-term behaviour of the ballasted railway tracks in the transition zones. The main features of the proposed technique include:

- Simplified yet effective approach to simulate the behaviour of the tracks with varied support conditions along the longitudinal direction, including the enhanced capability to predict the differential settlements, which are major concerns for transition zones.
- Rational method that considers material plasticity through the use of slider elements, which are described by accurate constitutive relationships as opposed to existing methods employing empirical settlement models to capture material plasticity.
- Quick and straightforward technique that does not require any commercial FE based software in contrast to existing approaches that rely on these software.

- Convenient method to assess the performance of different remedial measures in mitigating the differential settlement at the transition zone.

A good agreement of the predicted results with those recorded in the field and computed using FE simulations prove that the novel approach can accurately predict the response of the critical track zones. The validated approach is then applied to an open track-bridge transition, and the main findings are as follows:

- An increase in axle load exacerbates the track geometry degradation problem. Therefore, it is essential to provide remedial strategies in the transition zones on which heavier trains are expected in future.
- The use of thicker granular layers reduced the differential settlement at the transition zone considered in this study. This technique worked well because the subgrade layer was the major contributor to the differential settlement, and a thicker granular layer reduced the subgrade settlement.
- The techniques intended to increase the strength of the subgrade may be more effective than the strategies aimed at improving the stiffness of granular layers for transition zones with weak/soft subgrade. However, this strategy (subgrade strength increment) may be inappropriate for the transitions where the granular layers are primary contributors to the differential settlement (see for e.g., Li & Davis 2005).

Thus, it is crucial to correctly identify the primary cause of the differential settlement problem before selecting an appropriate countermeasure. The outcomes of this study have huge potential to influence the real-world design implications of track critical zones. The approach is original, simple yet elegant, and it can enhance, if not fully replace, present complex track modelling procedures for anticipating the behaviour of transition zones and adopting appropriate mitigation strategies.

CHAPTER 5
IMPACT OF PRINCIPAL STRESS ROTATION ON BALLASTED RAILWAY TRACK RESPONSE

5.1 General

In the previous chapter, the novel computational approach was applied to the transition zones by simulating the heterogeneous support conditions encountered in these regions. This chapter attempts to improve the accuracy of the computational approach by incorporating the effect of PSR experienced by the soil elements in a track due to moving train loads. First, the methodology to include the effects of PSR in the geotechnical rheological model is discussed. Subsequently, the track response with and without PSR inclusion is compared, and the importance of considering the PSR effect is highlighted.

5.2 Background

A soil element in the track substructure experiences a complex change in the vertical, horizontal, and shear stresses during a train passage, which results in a rotation of the principal stress direction (McDonald & Raymond 1984; Powrie et al. 2007). Previous investigations have revealed that PSR significantly influences the accumulation of irrecoverable deformations in the tracks layers (Momoya et al. 2005; Wijewickreme & Vaid 2008; Gräbe & Clayton 2009; Ishikawa et al. 2011; Guo et al. 2018; Bian et al. 2020; Mamou et al. 2021). The additional deformation caused due to PSR contributes to the loss of stability and geometry of railway tracks. Therefore, the effects of PSR must be carefully addressed while evaluating the track response under moving wheel loads.

A comprehensive understanding of the track response under a large number of repeated train passages is crucial for its design and maintenance planning. The computational models are the most appropriate and economically viable tools to understand the behaviour of railway tracks under various soil types, loads, and boundary conditions (Varandas et al. 2020). A multitude of numerical and analytical methods with varying levels of complexity have been developed in the past to predict the behaviour of railway tracks under repeated train passages (e.g., Mauer 1995; Suiker & de Borst 2003; Indraratna & Nimbalkar 2013; Li et al. 2018; Shih et al. 2019; Varandas et al. 2020; Grossoni et al. 2021). However, the predictive models that can incorporate the effect of

PSR on track response are still scarce. Notwithstanding their practical value, the existing computational methodologies disregard the influence of PSR, which may limit the accuracy of the predicted response.

The accurate prediction of the track response is paramount for the transition zones in railway tracks that are highly susceptible to rapid degradation in track geometry (Li & Davis 2005). To improve the performance of the transition zones, prior information of the magnitude of differential settlement accumulated in the substructure layers is indispensable. Consequently, several researchers resorted to numerical and analytical modelling techniques to investigate the behaviour of these crucial regions and quantify the extent of the potential problem (e.g., Hunt 1997; Varandas et al. 2013; Paixão et al. 2015b; Nielsen & Li 2018; Wang & Markine 2018c; Shan et al. 2020). However, most of the existing methods neglect the additional deformation that is caused due to the PSR. Considerable efforts are still required to account for this critical aspect of soil behaviour in the predictive models.

This chapter is aimed to provide a computational approach that incorporates the influence of PSR due to train-induced repeated loads on the response of the ballasted railway tracks. To this end, a novel geotechnical rheological model is employed in which the behaviour of track layers is simulated using springs, dashpots, and slider elements. The effect of PSR is accounted for by modifying the constitutive relationships used for the plastic slider elements, which are validated against the experimental data available in the literature. The importance of including PSR in predicting track response is elucidated by comparing the results with and without PSR inclusion. Subsequently, the computational approach is applied to an open track-bridge transition by incorporating the inhomogeneous support conditions associated with the critical zone, and the influence of PSR on its behaviour is investigated. The practical utility of the present approach is demonstrated by examining the suitability of different countermeasures in improving the performance of the transition zone. The present study provides a valuable tool with enhanced capability of including the PSR effects for the practising railway engineers to accurately predict the track response, especially in the transition zones.

5.3 Geotechnical Rheological Track Model

In this study, the geotechnical rheological model developed in CHAPTER 3 is employed to predict the response of a track substructure, comprising three layers: ballast, subballast, and subgrade, under repeated train loads. The geotechnical rheological model of a ballasted railway track is illustrated in **Figure 3.12**. To account for the effect of PSR, the constitutive relationships of the plastic slider elements in the rheological model have been modified, as described in the subsequent sections.

5.3.1 Constitutive Relationships for Plastic Slider Elements

5.3.1.1 Ballast and Subballast

For granular layers such as ballast and subballast, the constitutive relationship is based on an extended version of the Nor-sand model, which incorporates the effect of PSR by rendering the hardening of the yield surface as a function of the PSR angle (Jefferies et al. 2015). The formulation of this model is within the framework of critical state soil mechanics, and it employs an associated flow rule with isotropic hardening plasticity.

The plastic deformation behaviour of the slider element for granular layers follows from Equation 3.36. The plastic deformation occurs in the slider element if the yield criterion, f, defined in Equation 3.34 is met and remains satisfied. The hardening of the yield surface is governed by the following equation:

$$\frac{dp_{\mathrm{i}}}{p_{\mathrm{i}}} = \frac{H}{R_{\mathrm{i}}}\frac{M_{\mathrm{i}}}{M_{\mathrm{itc}}}\left(\frac{p_{\mathrm{i}}}{p}\right)_{\alpha}^{-2}\left[e^{\left(\frac{-\chi_{\mathrm{i}}\psi_{\mathrm{i}}}{M_{\mathrm{itc}}}\right)} - \left(\frac{p_{\mathrm{i}}}{p}\right)_{\alpha}\right] d\varepsilon_{\mathrm{q}}^{p} \qquad 5.1$$

It is assumed that the size of the yield surface shrinks isotropically during the unloading stage (see APPENDIX H). This method of reducing the size of yield surface during unloading was originally proposed by Carter et al. (1982). The term $\left(\frac{p_{\mathrm{i}}}{p}\right)_{\alpha}$ in Equation 5.1 accounts for the effect of PSR and is determined using the following equation (Jefferies et al. 2015):

$$\left(\frac{p_{\mathrm{i}}}{p}\right)_{\alpha} = \left(\frac{p_{\mathrm{i}}}{p} - \frac{1}{r}\right)\left[1 - Z\left(\frac{|d\alpha_{\mathrm{v}}|}{180}\right)|\psi|\right] + \frac{1}{r} \qquad 5.2$$

where α_{v} is the angle between major principal stress direction and vertical (°); r is a constant known as the spacing ratio [taken as 2.71 (see Jefferies et al. 2015)]; Z is the plastic softening parameter. The parameter Z controls the size of the yield surface during

the rotation of the principal stress direction. It can be calibrated against the data obtained from hollow cylinder torsional or cyclic simple shear tests using the iterative forward modeling approach, wherein initial values of Z are assumed and subsequently updated based on simulation results (see Jefferies et al. 2015).

5.3.1.2 Subgrade

The constitutive relationship adopted for the plastic slider element for subgrade is based on the elastoplastic model proposed by Ma et al. (2017), which has been extended in this study to consider the deformation induced by the PSR. The effect of PSR is accounted for by rendering the yield surface, potential surface, and hardening rule as a function of α_v. Sassa & Sekiguchi (2001) have used a similar approach to incorporate the effect of PSR in the generalised plasticity model.

The plastic deformation behaviour of the slider element for the subgrade follows from Equation 3.51. The potential function in Equation 3.52 has been modified to account for the effect of PSR:

$$g_p = \ln\left[1 + \frac{(2\xi - Z_\alpha)}{Z_\alpha}\frac{\hat{\eta}^2}{\widehat{M}_\alpha^2}\right] + \frac{(2\xi - Z_\alpha)}{\xi}\ln\left(\frac{\hat{p}}{\hat{p}_{xg}}\right) \tag{5.3}$$

where $\widehat{M}_\alpha$ and Z_α are expressed as:

$$\widehat{M}_\alpha = \widehat{M}(1 - s_{1\alpha}U_\alpha) \tag{5.4(a)}$$

$$Z_\alpha = 1 + s_{2\alpha}U_\alpha \tag{5.4(b)}$$

$$U_\alpha = \begin{cases} 1 - \cos(2\alpha_v), \text{ for } 0 \le \alpha_v \le 45° \\ 1 - \cos(2|\alpha_v| - \pi), \text{ for } 45° \le |\alpha_v| \le 90° \end{cases} \tag{5.4(c)}$$

where $s_{1\alpha}$ and $s_{2\alpha}$ are the constitutive parameters to account for the effects of PSR. The parameters $s_{1\alpha}$ and $s_{2\alpha}$ control the reduction in M and variation in the slope of the stress-dilatancy plot, respectively, due to a rotation in principal stress direction, as revealed by the experimental findings (Symes et al. 1988).

The modified yield criterion, f, for the plastic slider element for subgrade is defined by:

$$f = \frac{(\lambda - \kappa)}{\xi(1 + e_0)}\left\{\frac{\bar{A}}{(2 - Z_\alpha)}\ln\left[\frac{(\hat{\eta}^2 + \widehat{M}_\alpha^2) + (1 - Z_\alpha)(\hat{\eta}^2 - \widehat{M}_\alpha^2)}{(\hat{\eta}_0^2 + \widehat{M}_\alpha^2) + (1 - Z_\alpha)(\hat{\eta}_0^2 - \widehat{M}_\alpha^2)}\right] + \ln\left(\frac{\hat{p}}{\hat{p}_0}\right)\right\} - \int \frac{d\varepsilon_v^p}{R} \tag{5.5}$$

where $\bar{A}$ is a parameter expressed as:

$$\bar{A} = A\frac{(2 - Z_\alpha)\ln 2}{\ln\left(\frac{2}{Z_\alpha}\right)} \tag{5.6}$$

The yield surface defined in Equation 5.5 is smooth and convex in the characteristic stress space (see **Figure 5.1**). The accumulation of irrecoverable deformation under repeated loading conditions is simulated using the concept of subloading surfaces with isotropic hardening (Hashiguchi 1989). Three subloading surfaces have been used, which are defined as follows:

$$f_\mathrm{t} = \frac{\bar{A}}{(2 - Z_\alpha)}\ln\left[\frac{\left(\hat{\eta}^2 + \hat{M}_\alpha^2\right) + (1 - Z_\alpha)(\hat{\eta}^2 - \hat{M}_\alpha^2)}{Z_\alpha \hat{M}_\alpha^2}\right] + \ln\left(\frac{\hat{p}}{\hat{p}_\mathrm{xt}}\right) = 0 \tag{5.7(a)}$$

$$f_\mathrm{c} = \frac{\bar{A}}{(2 - Z_\alpha)}\ln\left[\frac{\left(\hat{\eta}^2 + \hat{M}_\alpha^2\right) + (1 - Z_\alpha)(\hat{\eta}^2 - \hat{M}_\alpha^2)}{Z_\alpha \hat{M}_\alpha^2}\right] + \ln\left(\frac{\hat{p}}{\hat{p}_\mathrm{xc}}\right) = 0 \tag{5.7(b)}$$

$$f_\mathrm{r} = \frac{\bar{A}}{(2 - Z_\alpha)}\ln\left[\frac{\left(\hat{\eta}^2 + \hat{M}_\alpha^2\right) + (1 - Z_\alpha)(\hat{\eta}^2 - \hat{M}_\alpha^2)}{Z_\alpha \hat{M}_\alpha^2}\right] + \ln\left(\frac{\hat{p}}{\hat{p}_\mathrm{xr}}\right) = 0 \tag{5.7(c)}$$

The hardening parameter, R, is expressed as:

$$R = e^{-\frac{1}{a_\mathrm{h}(1+2U_\alpha)}\left(1-\frac{\hat{p}_\mathrm{xc}}{\hat{p}_\mathrm{xr}}\right)}\sqrt{\frac{\hat{p}_\mathrm{xc} - \hat{p}_\mathrm{xt}}{\hat{p}_\mathrm{xr} - \hat{p}_\mathrm{xt}}} \tag{5.8}$$

Substituting the value of g_p from Equation 5.3 to Equation 3.51, the following relationship is obtained:

$$d\boldsymbol{\varepsilon}_\mathrm{ij}^p = \frac{R(\lambda - \kappa)}{\xi(1 + e_0)}\left[\frac{\left\{(1 - 2\bar{A})\hat{q}^2 + \hat{M}_\alpha^2\hat{p}^2 + (1 - Z_\alpha)\left(\hat{q}^2 - \hat{M}_\alpha^2\hat{p}^2\right)\right\}d\hat{p}}{\hat{p}\left\{(\hat{q}^2 + \hat{M}_\alpha^2\hat{p}^2) + (1 - Z_\alpha)(\hat{q}^2 - \hat{M}_\alpha^2\hat{p}^2)\right\}} + \frac{2\bar{A}\hat{q}d\hat{q}}{\left\{\left(\hat{q}^2 + \hat{M}_\alpha^2\hat{p}^2\right) + (1 - Z_\alpha)\left(\hat{q}^2 - \hat{M}_\alpha^2\hat{p}^2\right)\right\}}\right]\left[\frac{3\xi\hat{p}\left(\hat{\boldsymbol{\sigma}}_\mathrm{ij} - \hat{p}\delta_\mathrm{ij}\right)}{Z_\alpha(\hat{M}_\alpha^2\hat{p}^2 - \hat{q}^2)} + \frac{\delta_\mathrm{ij}}{3}\right] \tag{5.9}$$

It must be noted that in this study, all the stresses are considered effective stresses.

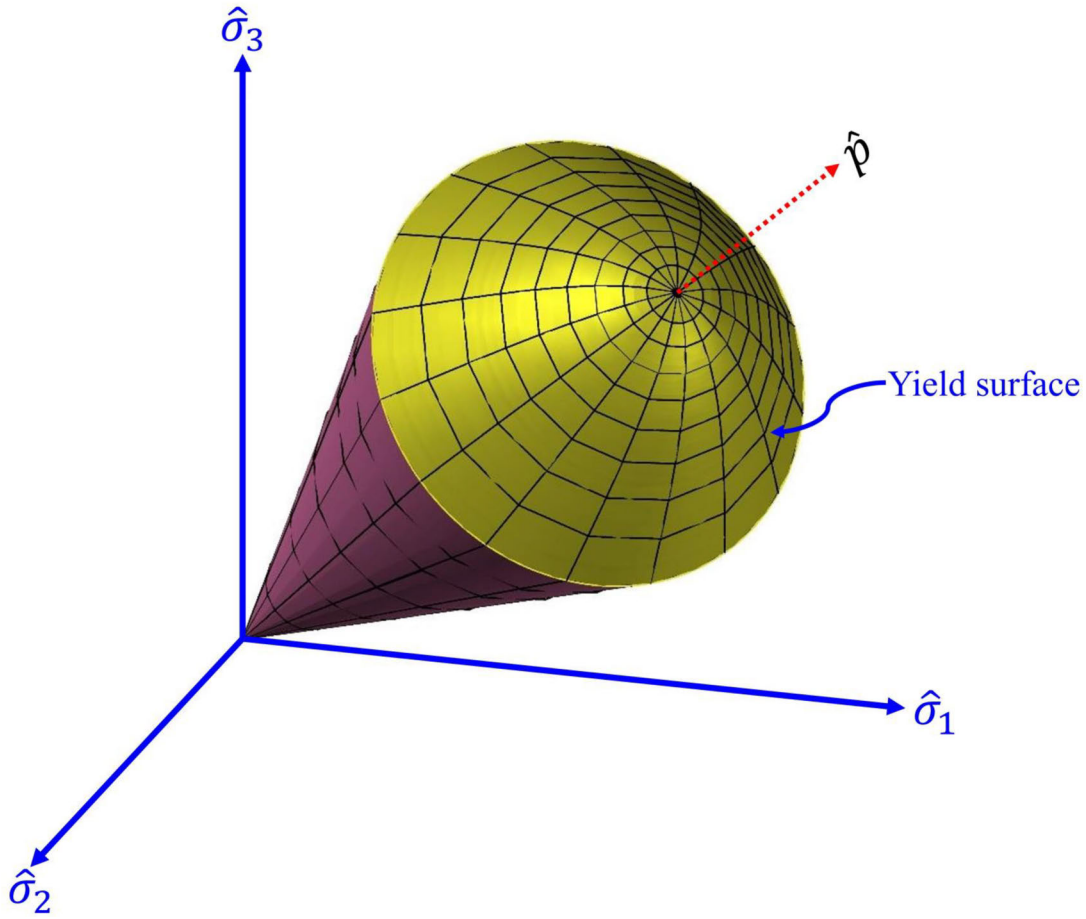

Figure 5.1 Yield surface in the characteristic stress space

The aforementioned model can be used to describe the compressive behavior of the soil. To simulate the dilative behavior, the yield criterion is revised as:

$$f = \frac{(\lambda-\kappa)}{\xi(1+e_0)}\left\{\frac{\bar{A}}{(2-Z_\alpha)}\ln\left[\frac{(\hat{\eta}^2+\hat{M}_{\alpha p}^2)+(1-Z_\alpha)(\hat{\eta}^2-\hat{M}_{\alpha p}^2)}{(\hat{\eta}_0^2+\hat{M}_{\alpha p}^2)+(1-Z_\alpha)(\hat{\eta}_0^2-\hat{M}_{\alpha p}^2)}\right]+\ln\left(\frac{\hat{p}}{\hat{p}_0}\right)\right\}-\int\frac{d\varepsilon_v^p}{R^*}=0 \qquad 5.10$$

where $\hat{M}_{\alpha p}=\hat{M}_p(1-s_{1\alpha}U_\alpha)$; M_p is the peak stress ratio; R^* is a hardening parameter given by:

$$R^* = R\left(\frac{\hat{M}_{\alpha p}}{\hat{M}_\alpha}\right)^2\left(\frac{\hat{M}_\alpha^2\hat{p}^2-\hat{q}^2}{\hat{M}_{\alpha p}^2\hat{p}^2-\hat{q}^2}\right) \qquad 5.11$$

The plastic strain increment can be obtained as:

$$d\boldsymbol{\varepsilon}_{ij}^p = \frac{R^*(\lambda-\kappa)}{\xi(1+e_0)}\left[\frac{\{(1-2\bar{A})\hat{q}^2+\hat{M}_{\alpha p}^2\hat{p}^2+(1-Z_\alpha)(\hat{q}^2-\hat{M}_{\alpha p}^2\hat{p}^2)\}d\hat{p}}{\hat{p}\{(\hat{q}^2+\hat{M}_{\alpha p}^2\hat{p}^2)+(1-Z_\alpha)(\hat{q}^2-\hat{M}_{\alpha p}^2\hat{p}^2)\}}+\frac{2\bar{A}\hat{q}d\hat{q}}{\{(\hat{q}^2+\hat{M}_{\alpha p}^2\hat{p}^2)+(1-Z_\alpha)(\hat{q}^2-\hat{M}_{\alpha p}^2\hat{p}^2)\}}\right]\left[\frac{3\xi\hat{p}(\hat{\boldsymbol{\sigma}}_{ij}-\hat{p}\delta_{ij})}{Z_\alpha(\hat{M}_\alpha^2\hat{p}^2-\hat{q}^2)}+\frac{\delta_{ij}}{3}\right] \qquad 5.12$$

The PSR parameter $s_{1\alpha}$ can be obtained using the stress-dilatancy plots derived from the hollow cylindrical torsional test data (with constant α_v). A trend-line is fitted through the plot whose intercept gives the values of $\widehat{M}_\alpha$ at different values of α_v. Subsequently, the values of $\widehat{M}_\alpha$ are plotted against U_α [derived using Equation 5.4(c)] and the parameter $s_{1\alpha}$ is derived using Equation 5.4(a). The value of PSR parameter $s_{2\alpha}$ is determined using the data derived from hollow cylindrical torsional tests conducted at various α_v values. First, a trend line is fitted through the $2\xi\hat{\eta}D_p$ versus $\hat{\eta}^2$ plot for different values of α_v. The slope of this line gives the value of $-Z_\alpha$. Next, the values of Z_α are plotted against U_α and the parameter $s_{2\alpha}$ is derived using Equation 5.4(b).

5.3.2 Model Validation

The extended model for the slider element for subgrade is validated against the results of experimental investigations conducted by Cai et al. (2015), Wijewickreme & Vaid (2008), Yang (2013), and Wu et al. (2020). **Table 5.1** lists the constitutive parameters used in the predictions.

Table 5.1 Constitutive parameters for plastic slider element for subgrade

	λ	κ	φ_c (°)	ξ	M_p	A	a_h	$s_{1\alpha}$	$s_{2\alpha}$
Cai et al. (2015)	0.004	0.002	36[a]	0.1	1.46[a]	0.1	0.03	0.7	0.05
Wijewickreme & Vaid (2008)	0.009	0.002	30	0.1	1.24	0.1	–	0.31	0.05
Yang (2013)	0.025[b]	0.005[b]	27[c]	0.1	1.64	0.12	–	0.1	0.05
Wu et al. (2020)	0.03[d]	0.003	32.6[e]	0.27	1.31[e]	0.45	0.0175	0.7	0.05
Parametric study	0.004	0.002	36 – 40	0.1	1.46 – 1.64	0.1	0.03	0.7	0.05

Note: values taken from [a]Kong et al. (2019); [b]Altaee et al. (1992); [c]Wang et al. (2019); [d]Altuhafi et al. (2018); [e]Sim et al. (2013).

Cai et al. (2015) studied the effect of principal stress rotation on the behavior of fine sand (relative density = 70%) using hollow cylinder torsional shear device under repeated loading conditions. **Figure 5.2(a)** shows the cyclic stress waveforms used in the experimental investigation conducted by Cai et al. (2015). **Figure 5.2(b)** shows the strain accumulation in the vertical direction with an increase in N at different cyclic vertical

stress ratios (CVSR), which is the ratio of vertical stress amplitude (σ_z^{ampl}) to two times of initial mean effective stress (p_0) [see **Figure 5.2(a)**]. These results are for the tests without PSR as the value of cyclic shear stress ratio (CSSR) is 0, which is the ratio of shear stress amplitude ($\tau_{z\theta}^{ampl}$) to σ_z^{ampl}. It is observed from **Figure 5.2(b)** that the predicted results are in close agreement with the experimental data. The model can satisfactorily reproduce the accumulation of vertical strain with an increase in N for different vertical stress amplitudes. **Figures 5.2(c)** and **5.2(d)** show the accumulation of vertical strain with an increase in the number of load cycles at CVSR of 0.15 and 0.25, respectively, for various CSSR values (i.e., for tests involving continuous PSR). It is apparent that the present model predicts the accumulation of vertical strain quite well in relation to the observed behaviour in the laboratory investigations.

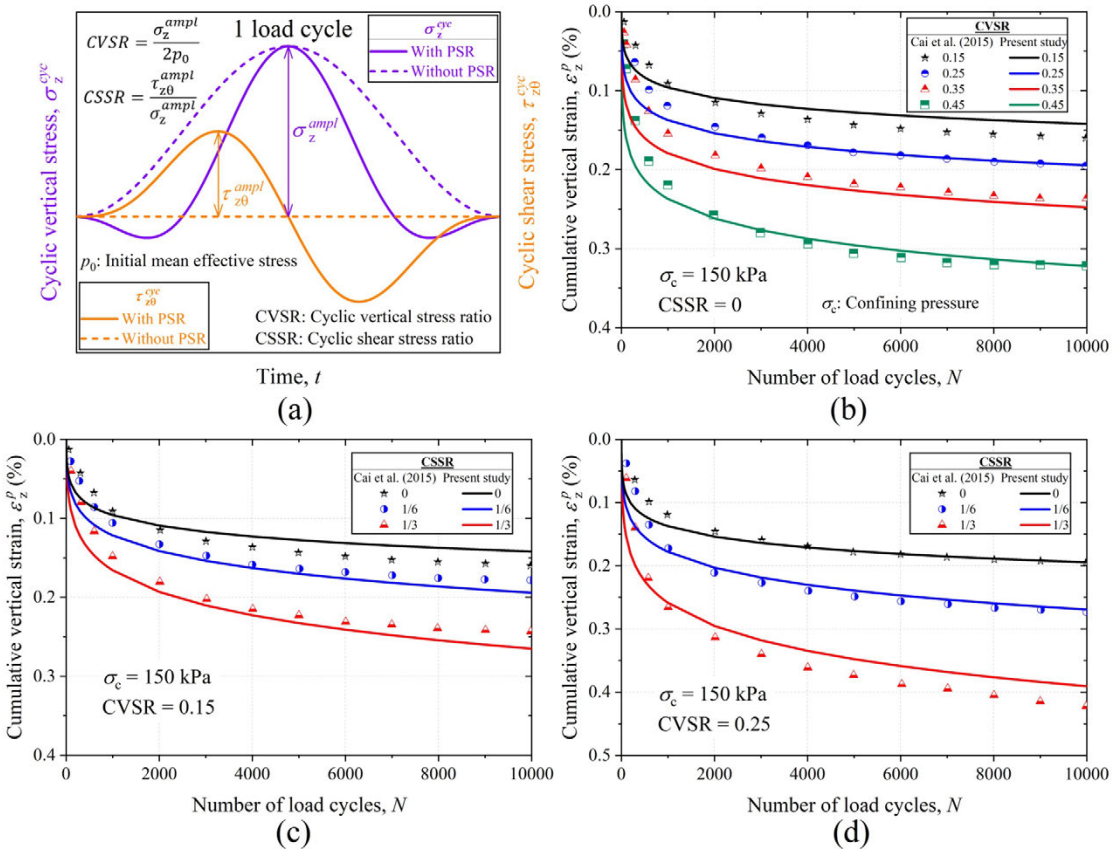

Figure 5.2 Comparison of response predicted using the present model with the experimental data reported by Cai et al. (2015) for subgrade soil under repeated loading conditions: **(a)** cyclic stress waveforms corresponding to one load cycle; accumulation of vertical strain with number of load cycles for **(b)** various CVSR at CSSR = 0; different CSSR at **(c)** CVSR = 0.15; **(d)** CVSR = 0.25

The model is also validated against the results of experimental investigations conducted by Wijewickreme & Vaid (2008) on loose Ottawa sand (relative density = 30%) using hollow cylinder torsional shear device under monotonic loading condition. **Figures 5.3(a)** and **5.3(b)** show the variation of stress ratio and volumetric strain with deviatoric strain, respectively, for three different cases: A3002R, M3451, and A0451. The major principal stress is oriented (and held constant) at 0° and 45° with the vertical direction for cases A3002R and A0451, respectively. For M3451, α_v is increased from 0 to 45° with an increase in stress ratio, R_s, from 1 to 2. It can be observed from **Figure 5.3** that the predicted results match reasonably well with the experimental data reported by Wijewickreme & Vaid (2008). The present model can predict the increase in strain generated due to the PSR for the cases when α_v is held constant and varied continuously.

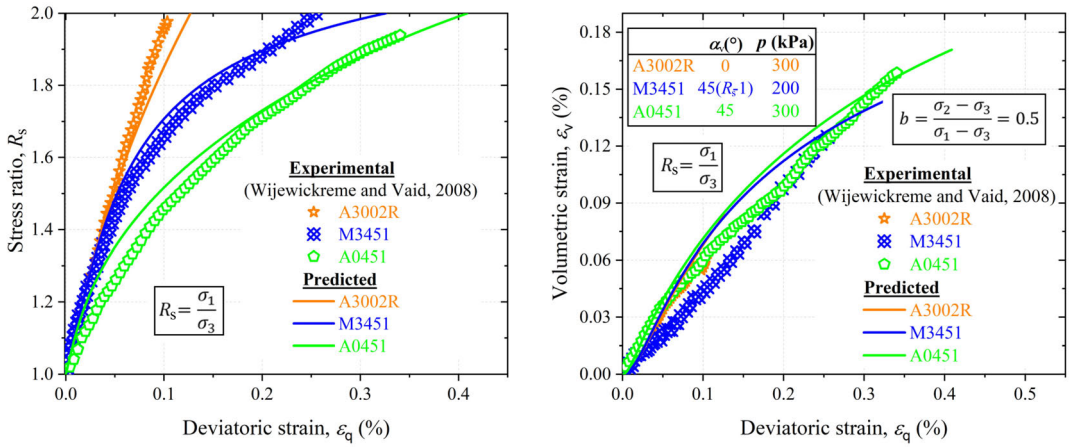

Figure 5.3 Comparison of the response predicted using the present model with the experimental data reported by Wijewickreme & Vaid (2008): (a) variation of stress ratio with deviatoric strain; (b) variation of volumetric strain with deviatoric strain

Figure 5.4 shows a comparison of the model predictions with the data reported by Yang (2013) for tests conducted on dense Leighton Buzzard sand (relative density = 75% – 77%) using small-strain hollow cylinder apparatus. It can be observed that the predicted results are in an acceptable agreement with the experimental data. The model can predict the dilative response (negative volumetric strain) of the dense sand and the reduction in stress ratio with an increase in α_v.

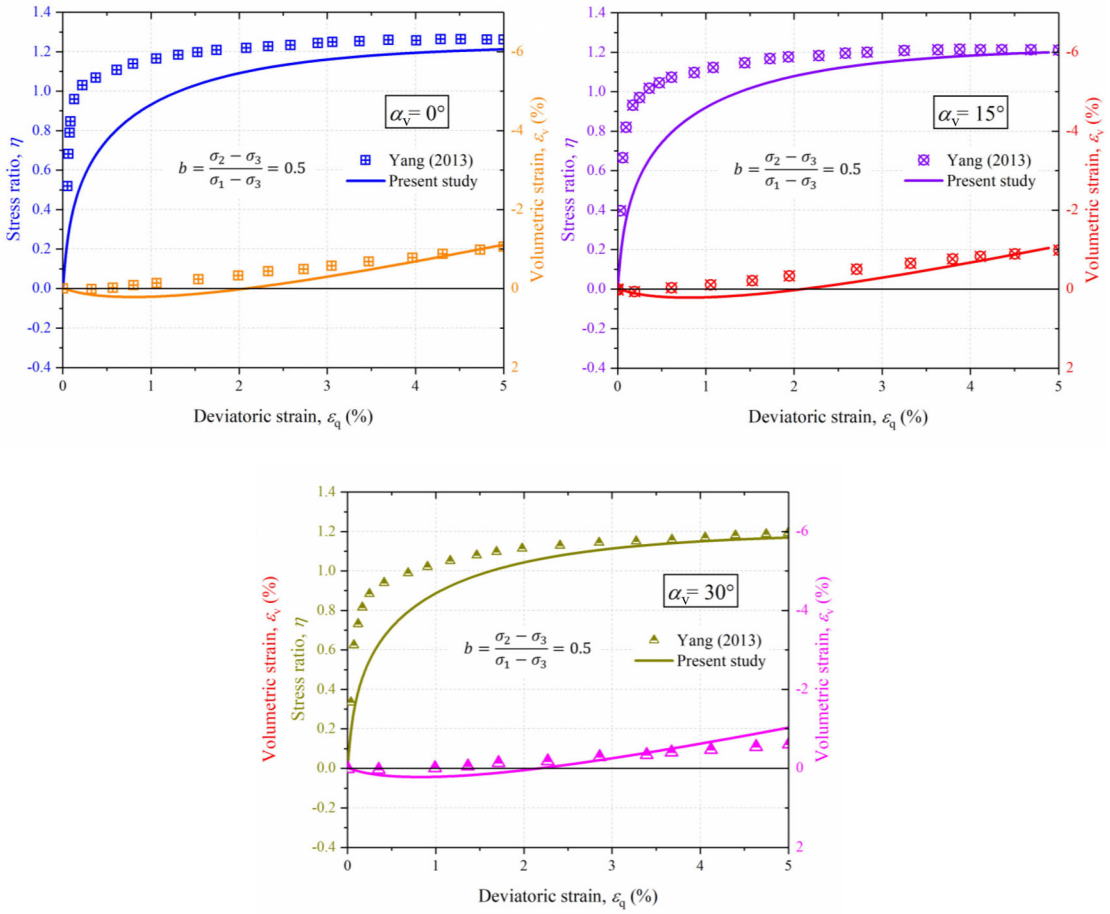

Figure 5.4 Comparison of the response predicted using the present model with the experimental data reported by Yang (2013)

Figure 5.5 compares the model predictions with the data reported by Wu et al. (2020) for tests conducted on Fontainebleau sand (relative density = 74%) using simple shear apparatus. It is observed that the model simulates the accumulation of volumetric strain with an increase in the number of load cycles reasonably well in comparison to the experimental data. It also simulates the increase in cumulative volumetric strain associated with an increase in the amplitude of cyclic shear stress. The predicted volumetric strain values after 5,000 load cycles vary by 3% to 14% from the experimental results.

Thus, the present model can successfully predict the behaviour of geomaterials under a rotation of principal stress directions. This model requires only two additional parameters ($s_{1\alpha}$ and $s_{2\alpha}$) than the existing model to describe the effect of PSR in a simple yet effective manner. A parametric analysis is conducted to understand the influence of constitutive

parameters $s_{1\alpha}$ and $s_{2\alpha}$ on the response of the geomaterials. The nominal values of the constitutive parameters used in this study are the same as that previously calibrated using the experimental data reported by Cai et al. (2015) (see **Table 5.1**). The input loading for this analysis is shown in **Figure 5.2(a)**. The values of σ_c, CVSR, and CSSR are taken as 150 kPa, 0.25, and 1/6, respectively. The values of parameters $s_{1\alpha}$ and $s_{2\alpha}$ are varied between 0 and 0.9. Only one parameter is changed at a time, while nominal values are assigned to other parameters.

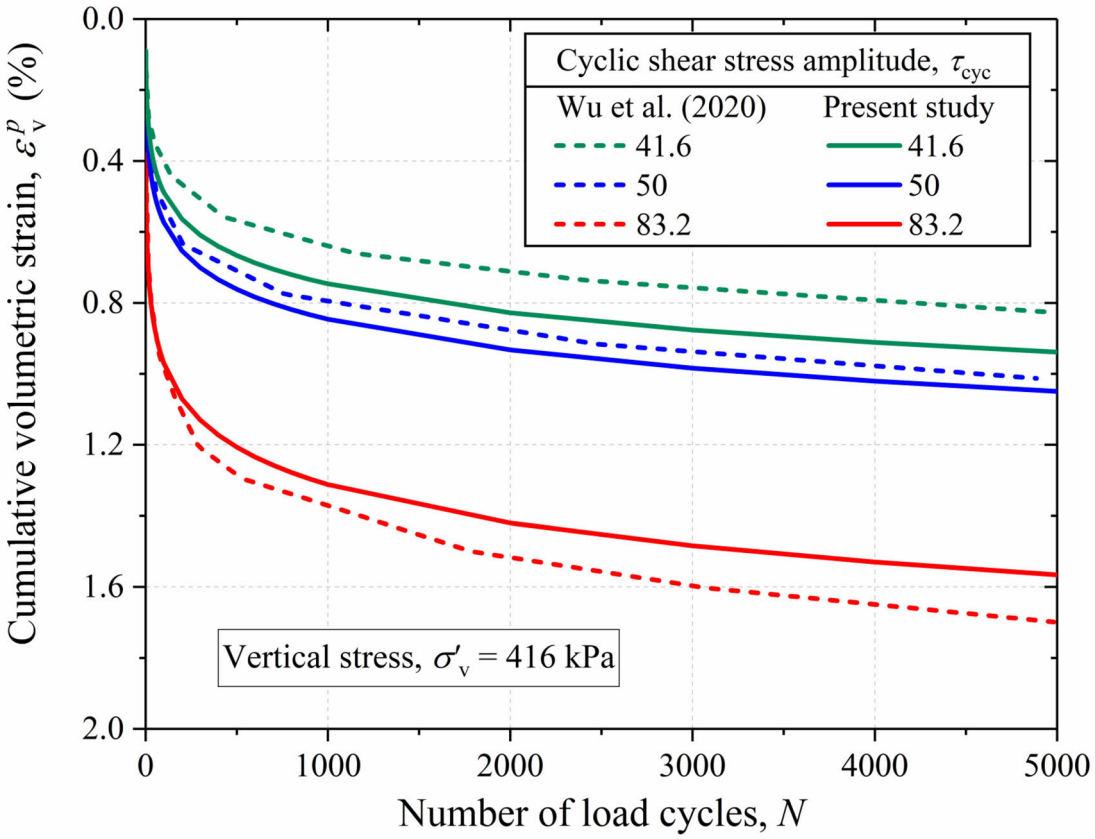

Figure 5.5 Comparison of the response predicted using the present model with the experimental data reported by Wu et al. (2020)

Figure 5.6(a) shows the influence of parameter $s_{1\alpha}$ on the accumulation of vertical strain. It can be observed that the cumulative vertical strain increases with an increase in $s_{1\alpha}$. This observation is reasonable as the value of $\widehat{M}_\alpha$ decreases with an increase in $s_{1\alpha}$ [see Equation 5.4(a)]. This leads to an increment in the magnitude of vertical strain (see Equation 5.9). **Figure 5.6(b)** shows the effect of parameter $s_{2\alpha}$ on the accumulation of vertical strain. It can be observed that the cumulative vertical strain decreases with an increase in $s_{2\alpha}$. This reduction is due to an increase in Z_α with increasing $s_{2\alpha}$ [see Equation

5.4(b)]. This increment in Z_α leads to a reduction in the magnitude of vertical strain (see Equation 5.9).

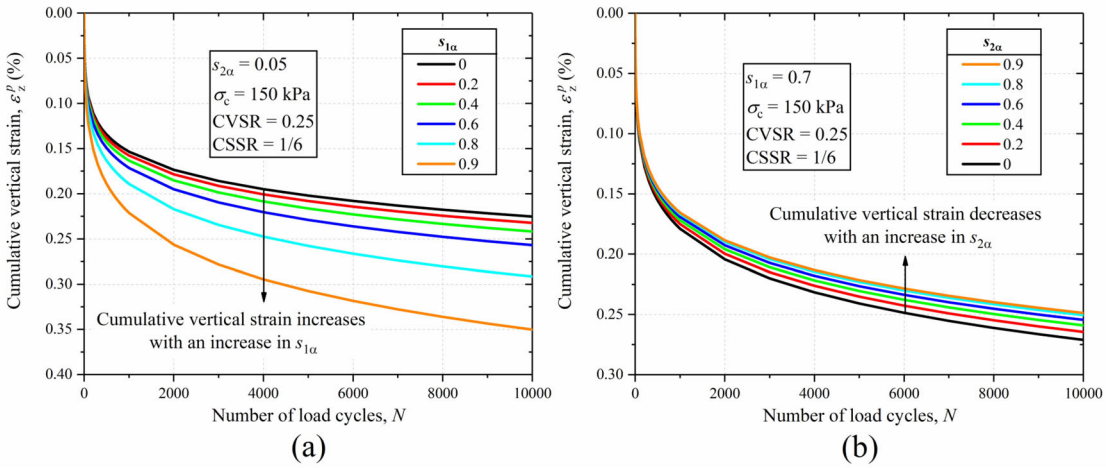

Figure 5.6 Influence of constitutive parameters on the accumulation of vertical strain: (a) effect of $s_{1\alpha}$; (b) effect of $s_{2\alpha}$

5.4 Results and Discussion

This section discusses the influence of PSR in the track response and elucidates the importance of considering this phenomenon for more accurate predictions. **Tables 3.4, 5.1** and **5.2** show the values of the input parameters used in the predictions. The values of the constitutive parameters for the granular layers have been derived from the cyclic triaxial tests conducted by Suiker et al. (2005) except for Z, which is considered as 10 and 20 for ballast and subballast, respectively. Note that the nominal value of Q_a is considered as 25 t unless otherwise specified. Firstly, the predicted stresses and settlement are discussed to describe the effect of PSR on a standard track. Subsequently, the effect of PSR under various axle loads and granular layer thickness is investigated.

5.4.1 Stress Variation due to Moving Load

Figure 5.7 illustrates the stress variation experienced by the substructure layers below a sleeper due to a moving wheel load. The stresses have been normalised with respect to maximum σ_{sb}, similar to the approach by Yang et al. (2009). At time instant t_1, the wheel is to the left of the sleeper under consideration, generating positive shear stress in the soil elements below the desired sleeper. As the wheel approaches the sleeper under consideration, the shear stress decreases and becomes equal to 0 at time instant t_2. At instant t_2, the wheel is exactly above the considered sleeper; consequently, the soil

elements experience only normal stresses. A reversal in shear stress direction occurs as soon as the wheel moves away from the sleeper under consideration (see **Figure 5.7**). This variation of the shear stresses, as the wheel passes a sleeper location, leads to the rotation in the direction of the principal stresses.

Table 5.2 Input parameters for geotechnical rheological model (Zhai et al. 2004; Paixão et al. 2014b; Li et al. 2016; Li et al. 2018).

Layer	Variable	Symbol	Unit	Parametric study	Paixão et al. (2014b)	
					Section 2	Section 4
Ballast	Resilient modulus	$E_b\,(=E_b^r)$	MPa	200	130	130
	Poisson's ratio	$\nu_b\,(=\nu_b^r)$	–	0.3	0.2	0.2
	Shear damping	$c_b{}^s\,(=c_b^{s,r})$	kNs/m	80	80	80
	Shear stiffness	$k_b{}^s\,(=k_b^{s,r})$	MN/m	78.4	78.4	78.4
	Density	$\rho_b\,(=\rho_b^r)$	kg/m^3	1,760	1,530	1,530
	Thickness	$h_b\,(=h_b^r)$	m	0.3	0.3	0.3
Subballast	Resilient modulus	E_s	MPa	115	200	200
	Poisson's ratio	ν_s	–	0.4	0.3	0.3
	Shear damping	c_s^s	kNs/m	80	80	80
	Shear stiffness	k_s^s	MN/m	476	476	476
	Density	ρ_s	kg/m^3	1,920	1,935	1,935
	Thickness	h_s	m	0.15	0.3	0.3
Subgrade	Resilient modulus	E_g	MPa	41	1,073	10,000
	Poisson's ratio	ν_g	–	0.35	0.3	0.3
	Shear damping	c_g^s	kNs/m	80	80	80
	Shear stiffness	k_g^s	MN/m	1,600	500	1,600
	Density	ρ_g	kg/m^3	1,920	1,935	2,200
	Thickness	h_g	m	5	9.2	9.2

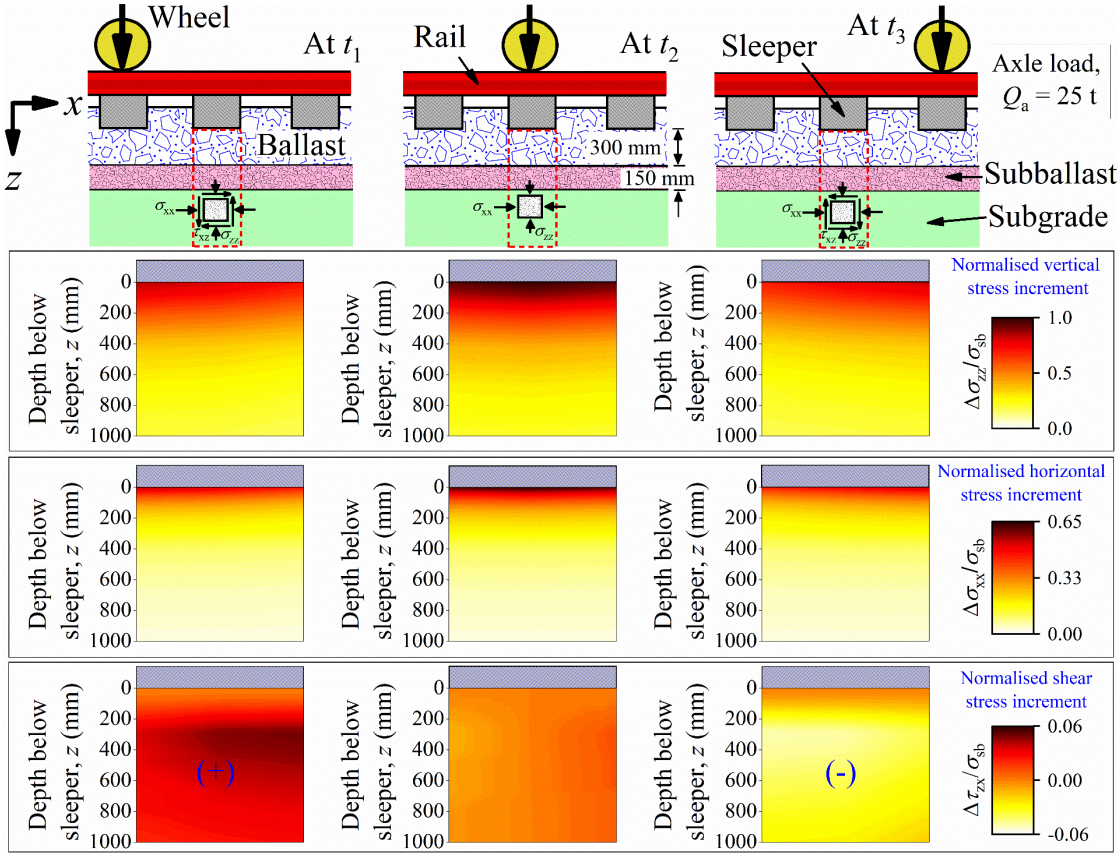

Figure 5.7 Stress variation experienced by the substructure layers below a sleeper due to a moving wheel load

Figure 5.8(a) shows the variation of vertical, horizontal, and shear stresses with time for a soil element located 1,200 mm below the sleeper bottom during a train passage. It is apparent that the shear stress direction reverses as the wheel passes a sleeper location, leading to PSR. **Figure 5.8(b)** shows that the magnitude of PSR varies with depth below a sleeper. During a train passage, the peak value of α_v initially increases with depth from sleeper bottom up to a maximum value and then decreases with a further increase in depth. Thus, the rotation of principal stresses is much higher for the subballast layer and the top portion of the subgrade layer than the ballast layer. This observation becomes evident in **Figures 5.8(c)**, **5.8(d)** and **5.8(e)**, which show the variation of q with α_v during a train passage at a depth of 100 mm (within ballast), 350 mm (within subballast) and 1,200 mm (within subgrade) from the sleeper bottom, respectively. The magnitude of α_v is minimal at a depth of 100 mm compared to that at 350 mm and 1,200 mm from the sleeper bottom. Nonetheless, q is the highest in the ballast layer and decreases with an increase in depth [see **Figures 5.8(c)**, **5.8(d)** and **5.8(e)**].

5.4.2 Effect of Principal Stress Rotation on Track Deformation

Figure 5.9 shows the accumulation of settlement with tonnage, with and without the inclusion of the PSR. It can be observed that the settlement is much higher when PSR is considered as compared to the case in which it is neglected. After a tonnage of 1 MGT, the cumulative settlement is 4.1 mm higher if PSR is considered than when neglected. Moreover, after a cumulative tonnage of 20 MGT, the total settlement increases by 19.3% if PSR is included in the analysis. Thus, it is essential to consider the effect of PSR for accurate prediction of the track response. These results also reveal that PSR accelerates the track geometry degradation. In the absence of PSR, 20 mm settlement is accumulated after a tonnage of 2.9 MGT; however, this tonnage reduces to 0.45 MGT with PSR inclusion. These findings reflect the need to consider this critical aspect of soil behaviour while computing the track response.

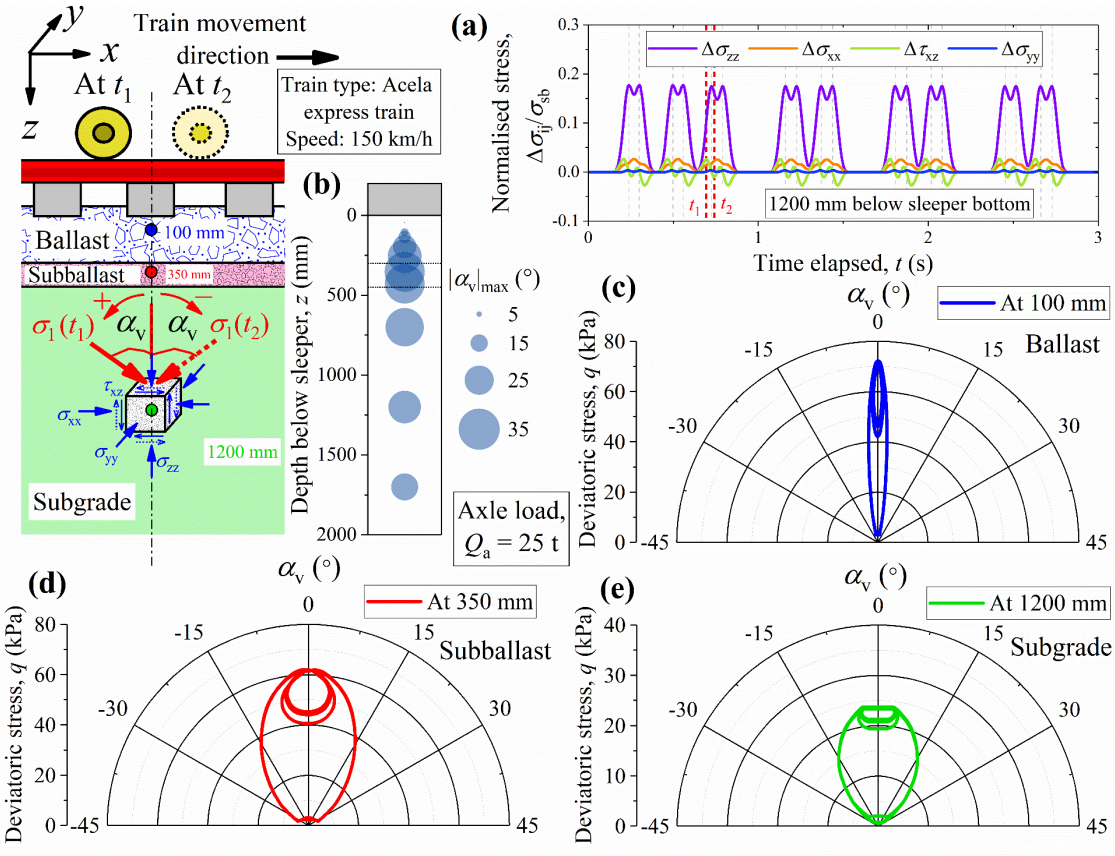

Figure 5.8 (a) Stress-time history for a soil element located 1,200 mm below the sleeper bottom during a train passage; **(b)** variation of PSR angle with depth; variation of deviatoric stress with PSR angle at **(c)** 100 mm; **(d)** 350 mm; **(e)** 1,200 mm below sleeper bottom

5.4.3 Influence of Axle Load

The rising trend of railways towards heavier axle loads to cater to the ever-increasing demands may lead to excessive deformation in the track substructure layers (Nimbalkar & Indraratna 2016). Therefore, the influence of Q_a on the track response is investigated using the present approach by varying Q_a from 20 t – 25 t. **Figure 5.10** shows the accumulation of settlement in the track substructure with tonnage at different axle loads. It is apparent that the cumulative settlement rises continuously with increasing Q_a. A higher Q_a generates larger stresses in the substructure layers, leading to increased settlement. The settlement at a cumulative tonnage of 20 MGT increases by 28.8 % on increasing Q_a from 20 t – 25 t. It is also apparent from **Figure 5.10** that the settlement is underestimated if the phenomenon of PSR is disregarded. For 25 t Q_a, the settlement predicted without PSR at a cumulative tonnage of 20 MGT is 16% less than when PSR is considered.

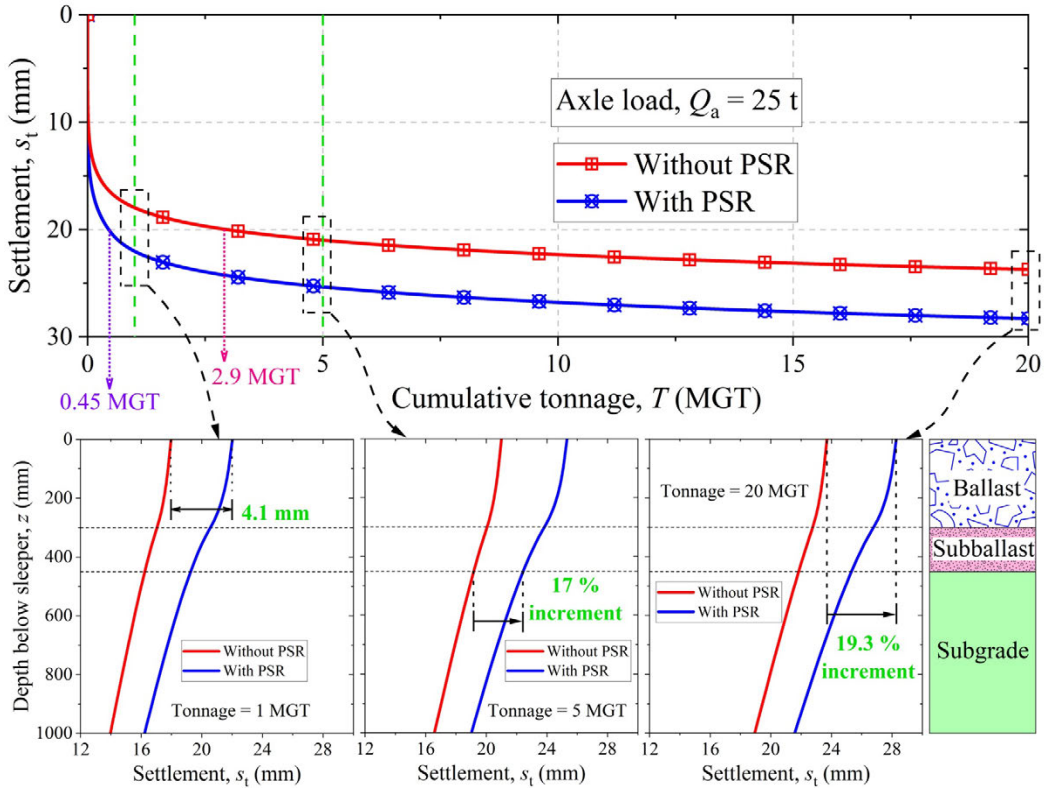

Figure 5.9 Effect of principal stress rotation on cumulative settlement

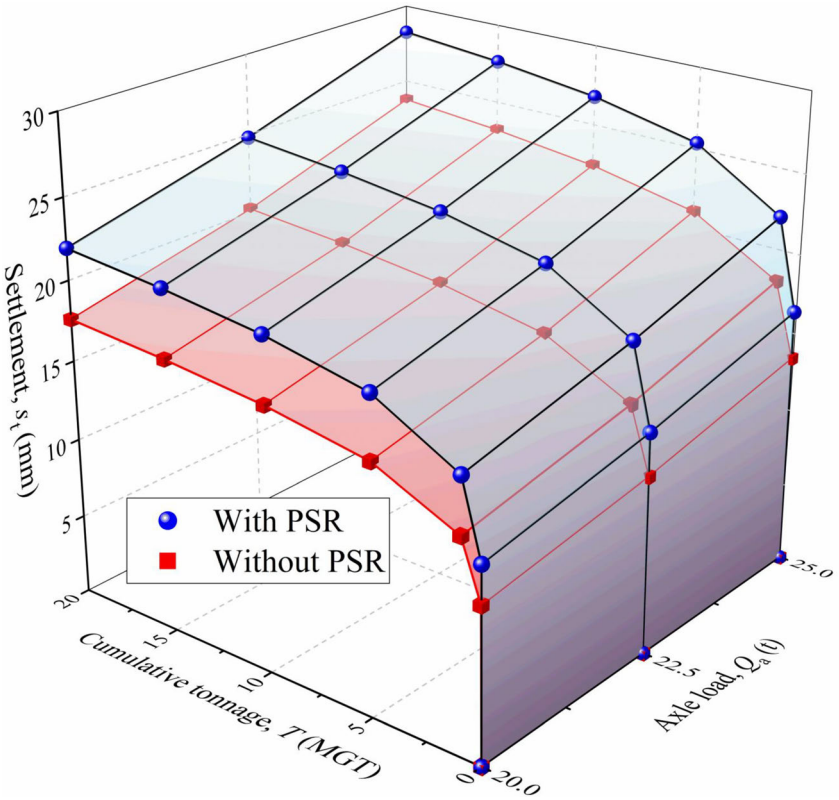

Figure 5.10 Influence of axle load on the cumulative settlement with and without the inclusion of PSR

5.4.4 Influence of Granular Layer Thickness

Increasing h_{gl} is one of the most economical and practical techniques to reduce the substructure layer deformations and improve track performance (Li & Selig 1998). For the tracks in which heavier axle loads are expected in the future, increasing h_{gl} may be a viable alternative for improving the track performance. Therefore, h_{gl} is varied between 450 mm – 900 mm to investigate its influence on the track behaviour. The thickness is varied through two approaches: i) changing h_b from 300 mm – 750 mm at h_s of 150 mm [**Figure 5.11(a)**], and ii) changing h_s from 150 mm – 600 mm at fixed h_b of 300 mm [**Figure 5.11(b)**]. Q_a for this analysis is taken as 25 t, which caused significant deformation in the track layers, as seen in the previous section.

Figure 5.11 illustrates the accumulation of settlement with tonnage at different granular layer thicknesses. It can be observed that the cumulative settlement decreases with an increase in h_{gl}. This occurs due to a reduction in stress transferred to the subgrade (which is the primary contributor to total settlement in this study) since the distance between the subgrade and sleeper bottom increases with granular layer thickness. Secondly, a thicker

granular layer has a higher stress spreading ability, which causes subgrade stress reduction (Li & Selig 1998). On comparing **Figures 5.11(a)** and **5.11(b)**, it is apparent that the settlement reduces by a significant amount when h_b is increased compared to the case when h_s is increased. For instance, at a cumulative tonnage of 20 MGT, the settlement decreases by 52% with an increase in h_b. However, this reduction reduces to 39.7% with an increase in h_s. This behaviour can be attributed to the higher strength of the ballast material than the subballast material.

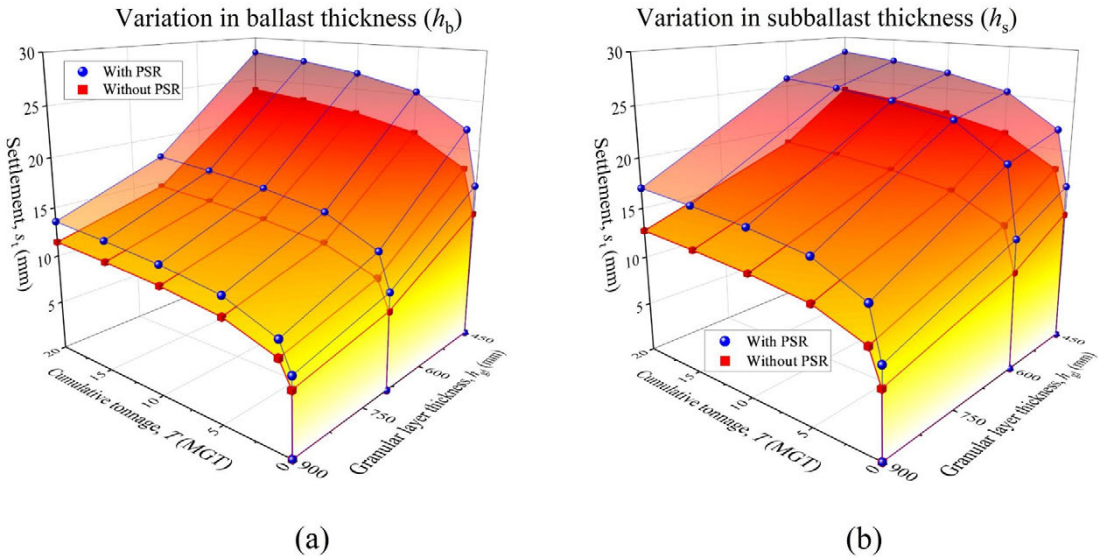

(a) (b)

Figure 5.11 Influence of granular layer thickness on the cumulative settlement with and without the inclusion of PSR: **(a)** for variation in ballast thickness; **(b)** for variation in subballast thickness

Figures 5.11(a) and **5.11(b)** also show that the response is underestimated if the phenomenon of PSR is disregarded. This underestimation can seriously affect the selection of adequate h_{gl} for a railway track, which is illustrated in **Figure 5.12**. Assuming that the allowable settlement of the track substructure is 25 mm after a cumulative tonnage of 20 MGT. If the contribution of PSR is ignored, h_{gl} of 450 mm will suffice (h_b = 300 mm and h_s = 150 mm) (see **Figure 5.12**). However, when PSR is considered, the required thickness rises to 525 mm (h_b = 375 mm and h_s = 150 mm). Thus, the selected thickness of the granular layer may be inadequate if the influence of PSR is disregarded during the response prediction.

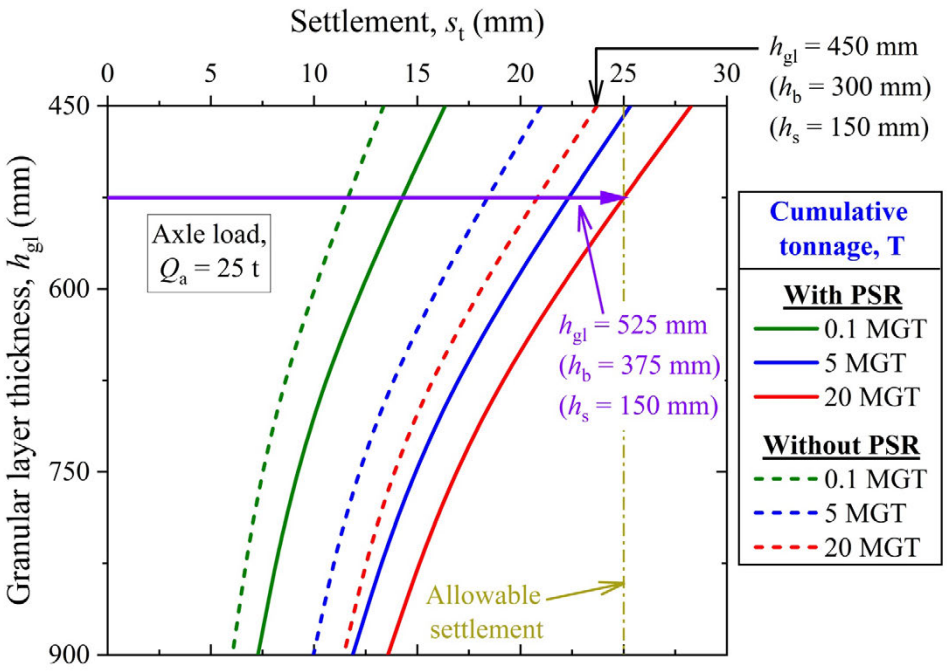

Figure 5.12 Effect of considering PSR on the selection of granular layer thickness

5.5 Application to Transition Zones

The previous sections demonstrated the importance of including the effect of PSR for an accurate prediction of track response. The present approach with enhanced capabilities of including the PSR effect may prove beneficial for evaluating the performance of transition zones in railway tracks, for which the prediction of accurate track response is paramount. Therefore, the computational approach discussed in previous sections is extended to investigate the behaviour of railway tracks in the transition zones. This is done by including the heterogeneous support conditions in the geotechnical rheological model, which are continually encountered in the track transitions. **Figure 5.13** shows the resulting rheological track model for a typical open track-bridge transition zone in which the track is supported by a concrete deck on one side (stiffer side) and soil layers on the other (softer side). The substructure comprises ballast, subballast, and subgrade layers on the softer side, while the ballast layer supported on the concrete deck constitutes the substructure of the stiffer side. The concrete bridge deck and abutment are simulated as fixed supports owing to their negligible deformation as compared to the geotechnical layers. Note that a region adjacent to the bridge abutment, termed as improved zone, can also be provided to simulate the transitions in which engineered backfills or other mitigation strategies are employed to enhance the performance of the critical zones.

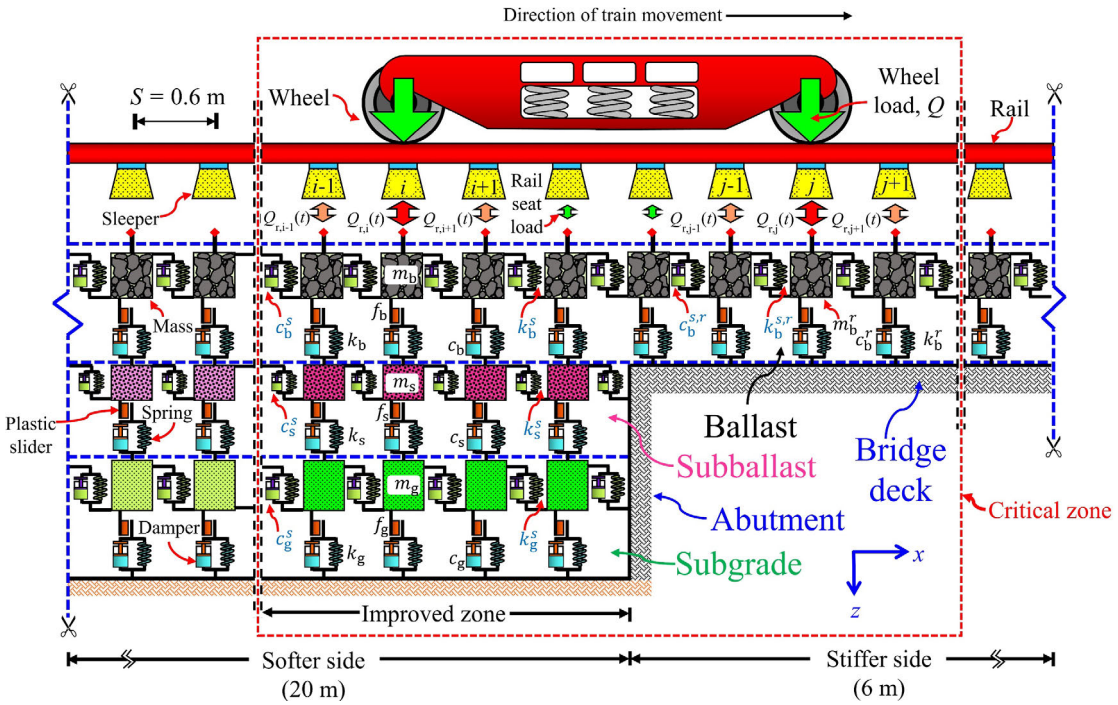

Figure 5.13 Geotechnical rheological model for an open track-bridge transition

On applying the dynamic equilibrium condition in this model, the equations of motion can be obtained [see Equations 4.2(a) and 4.2(b)]. The response of the transition zone is evaluated by solving these equations of motion at each time instant for all the sleeper locations considered. Note that the origin of the coordinate system is considered to be at the onset of the stiffer side.

5.5.1 Validation of Methodology

The validity of the present methodology to accurately simulate the behaviour of critical zones with heterogeneous track support conditions is investigated by comparing the predicted results with the field data reported by Paixão et al. (2014b) for a bridge approach in Portugal. **Table 5.2** shows the value of the input parameters used in the simulation. **Figure 5.14** shows the variation of vertical track displacement with time during a single pass of the Alfa Pendular train at two different locations of the transition zone. The field data (Paixão et al. 2014b) and results predicted using the present method are shown by dotted and solid lines, respectively. It is evident that the predicted results are in very good agreement with the field data in both sections 2 and 4 (located at 14.7 m and 0.9 m from the bridge, respectively). The track displacement decreases slightly as the train moves from section 2 (supported by UGM) towards section 4 (supported by CBM). Thus, the

present approach accurately simulates the response variation along the track length as observed in the field investigations.

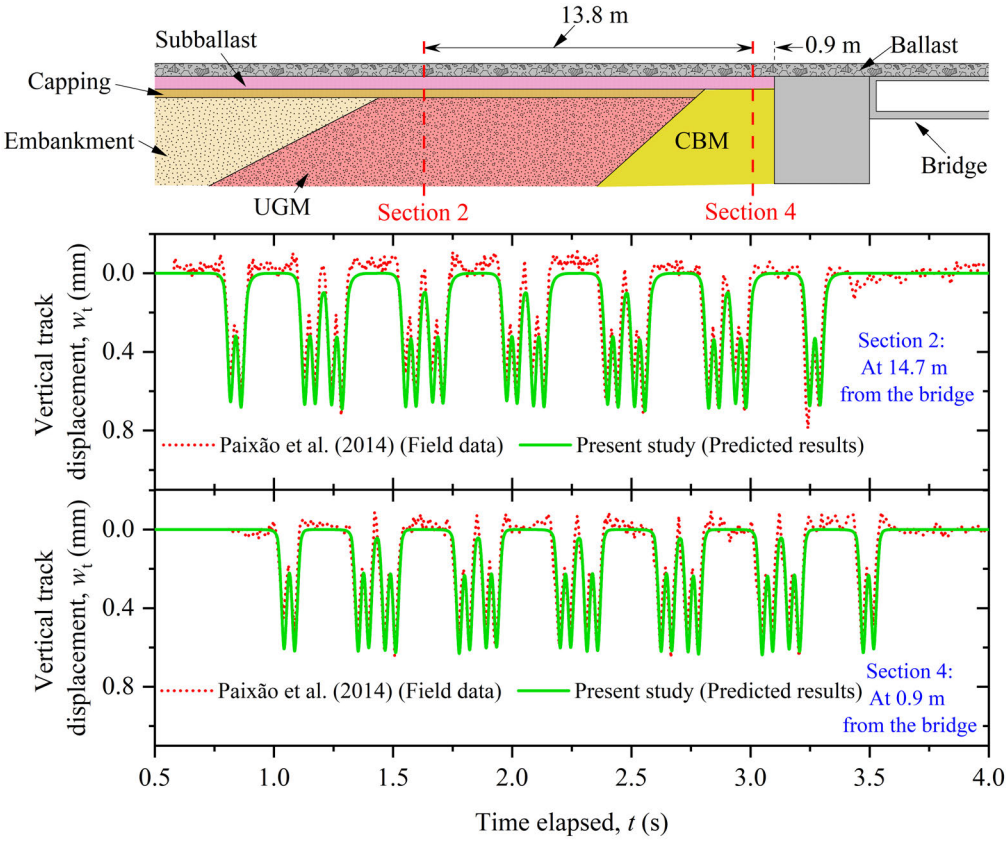

Figure 5.14 Comparison of predicted vertical track displacement with the field data reported by Paixão et al. (2014b) at 0.9 m and 14.7 m from the bridge

This validated model is now employed to investigate the performance of a typical open track-bridge transition shown in **Figure 5.13**. The values of the parameters used in the analysis are listed in **Tables 3.4, 5.1**, and **5.2.** As mentioned in Section 5.4, the constitutive parameters for the slider elements of granular layers have been derived from the cyclic triaxial tests conducted by Suiker et al. (2005) and Z is considered as 10 and 20 for ballast and subballast, respectively. Note that the nominal value of Q_a is 25 t unless otherwise specified. Firstly, the behaviour of a transition zone without any mitigation measure is studied at different axle loads. This investigation is particularly important for the transitions in which heavier axle loads are anticipated in the future. Subsequently, the practical utility of the present approach is demonstrated by investigating the effectiveness of two mitigation strategies in improving the performance of the transition zone. The

effects of ignoring the deformations due to PSR are also highlighted by comparing the results with and without the inclusion of PSR.

5.5.2 Performance at Different Axle Loads

The Q_a is varied from 20 t – 27 t to study its influence on the response of the transition zone. **Figure 5.15** shows the effect of Q_a on the settlement accumulated along the track length in the open track-bridge transition after a cumulative tonnage of 20 MGT for two cases: i) when PSR is considered and ii) when PSR is neglected. It can be observed that the differential settlement in the transition zone rises continuously with increasing Q_a. When PSR is considered, the differential settlement between the softer and stiffer side increases by 46.1% on increasing Q_a from 20 t – 27 t. The excessive differential settlement at higher axle loads is presumably due to an increase in the stresses in the substructure layers with Q_a (as observed in CHAPTER 4). In general, the track geometry degradation at the transition zones aggravates with an increase in Q_a. Consequently, the remedial measures intended to reduce this differential settlement become essential for the transitions in which heavier axle loads are expected in the future. It is also apparent from **Figure 5.15** that PSR increases the differential settlement between the softer and stiffer side of the transition. At 25 t Q_a, the predicted differential settlement is 16.3% less if PSR is ignored. Thus, the differential settlement is significantly underestimated if the phenomenon of PSR is neglected.

5.5.3 Improving the Performance of the Transition Zones

The performance of a transition zone can be improved by reducing the differential settlement between the softer and stiffer side of the transition. However, the correct choice of the mitigation strategy is particularly crucial for achieving the desired performance (see CHAPTER 4). The geotechnical rheological model can be employed to study the efficacy of different countermeasures in alleviating the problems associated with the transition zones and furnish the most appropriate strategy. This capability of the rheological model is demonstrated by investigating the adequacy of two different mitigation strategies: i) using thicker granular layers to limit the stresses transmitted to the subgrade on the softer side and ii) increasing the subgrade strength. These countermeasures are aimed to reduce the subgrade deformation in the softer side of the transition, which is the key contributor to the differential settlement in this study.

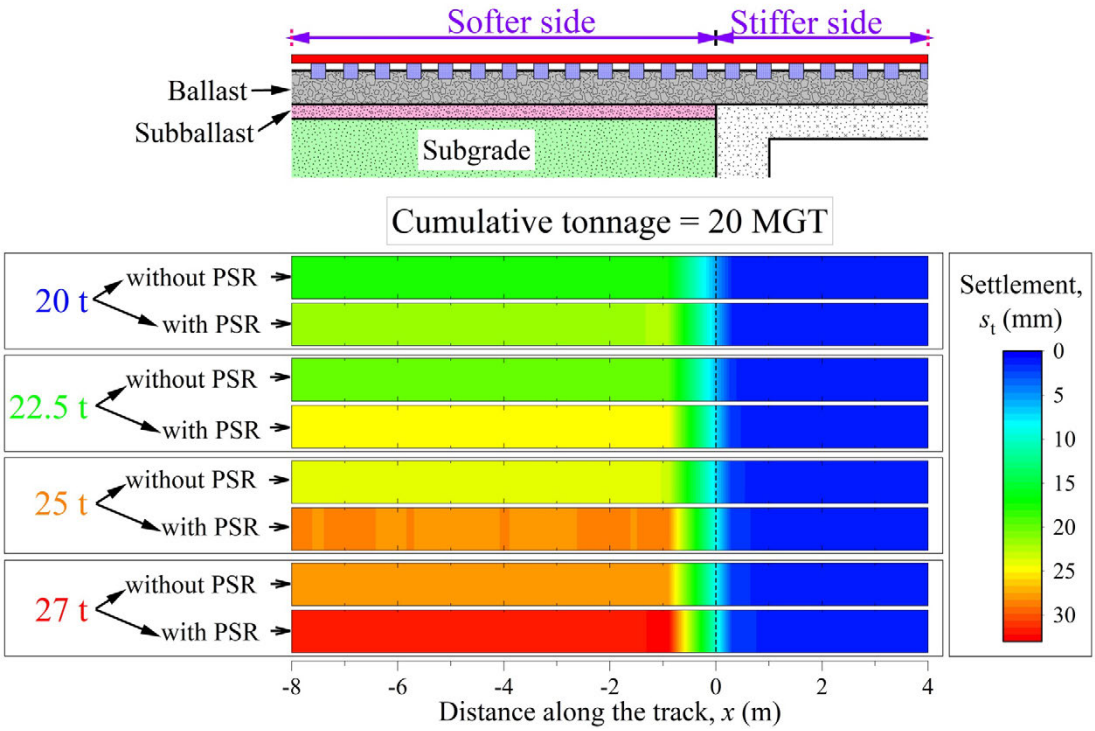

Figure 5.15 Effect of axle load on the behaviour of transition zone with and without the inclusion of PSR

5.5.3.1 Using Thicker Granular Layers

The h_{gl} in the softer side of the transition is varied from 450 mm – 900 mm to investigate its influence on the response of the transition zone. The required h_{gl} is achieved by either increasing h_b from 300 mm – 750 mm or by increasing the h_s from 150 mm – 600 mm. The thickness of only one layer is varied for an analysis, while the other layer is assigned a nominal value (see **Table 5.2**). Note that the thickness of the ballast layer at both the softer and stiffer side is kept identical. In the field, a thicker subballast layer can be furnished by replacing the underlying substructure layer with subballast to maintain the track level. The results are expressed in terms of the variation of settlement with distance along the track (x) for different granular layer thickness. **Figure 5.16(a)** shows the influence of h_b on the response of the transition zone with and without the inclusion of PSR. It can be observed that the differential settlement between the softer and stiffer side decreases with an increase in h_b. The differential settlement decreases by 86%, with an increase in h_b from 300 mm – 750 mm. This reduction is due to the fact that a thicker ballast layer spreads the load to a wider area; consequently, the stresses transferred to the underlying layers decrease (Selig & Waters 1994). This stress reduction leads to a

decrease in the accumulated settlement. Nonetheless, the differential settlement is significantly underestimated for each h_{gl} if PSR is disregarded.

Figure 5.16(b) shows the influence of h_s on the response of the transition zone with and without the inclusion of PSR. It can be observed that the differential settlement between the softer and stiffer side decreases with an increase in h_s. The differential settlement reduces by 41.6% with an increase in h_s from 150 mm – 600 mm. This observation is reasonable since a thicker subballast layer spreads the load to a wider subgrade area and reduces the stress transferred to the subgrade (Selig & Waters 1994). However, the reduction in the differential settlement is smaller than that observed when h_b is varied. This is presumably because the ballast material is much stronger than the subballast material. It is also evident that the differential settlement is much higher if PSR is included compared to the case when it is ignored.

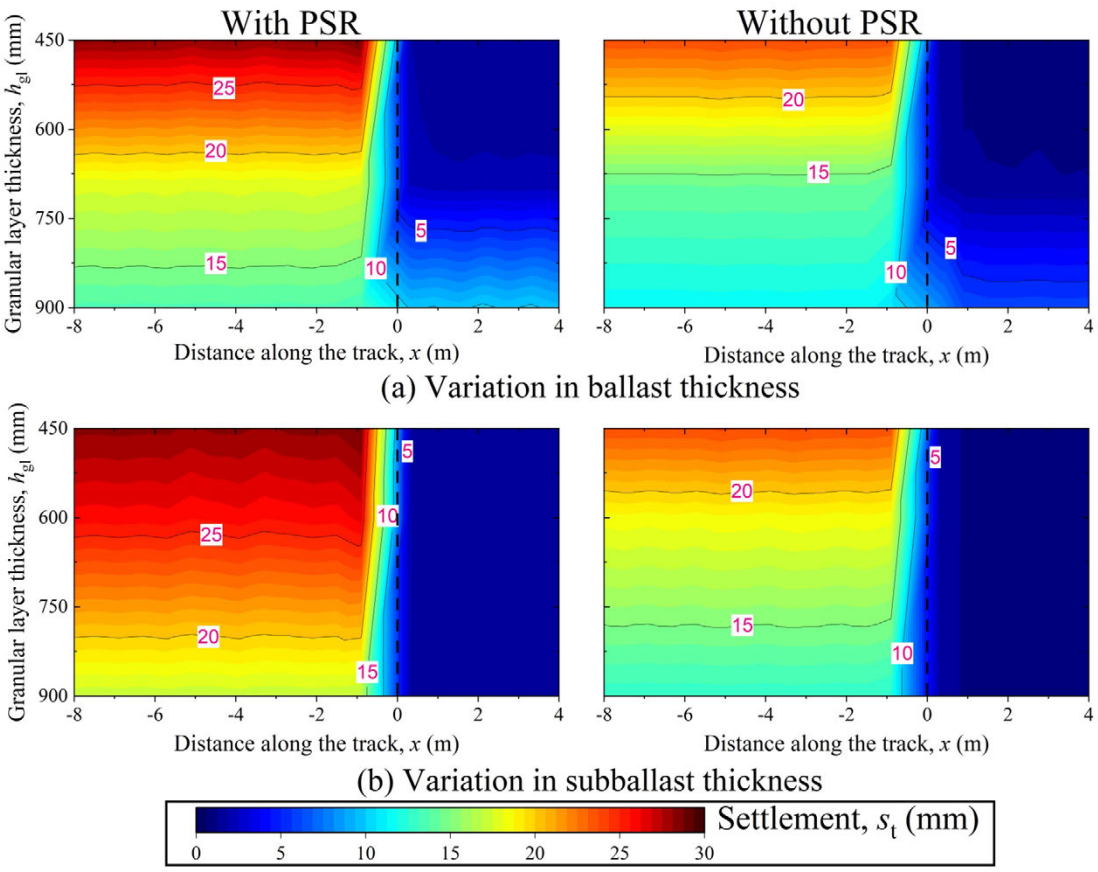

Figure 5.16 Effect of granular layer thickness on the behaviour of transition zone with and without considering the PSR: **(a)** for variation in ballast thickness; **(b)** for variation in subballast thickness

5.5.3.2 Improving the Subgrade Strength

The increment in subgrade strength (through ground improvement or geosynthetic reinforcement) is simulated by increasing the friction angle of the subgrade in the improved zone from 36° – 40°. **Figure 5.17(a)** shows the variation of settlement along the track length after a cumulative tonnage of 20 MGT. It can be seen that improving the strength of the subgrade adjacent to the bridge approach (in the improved zone) reduces the differential settlement between the softer and stiffer side. The differential settlement decreases by 23% with an increase in φ_c from 36° – 40°. **Figure 5.17(b)** shows the accumulation of settlement with tonnage in the softer side, improved zone and stiffer side of the transition. It can be observed that the settlement decreases along the length of the transition with the maximum settlement at the softer side (10.5 m from the bridge). It can also be seen that the settlement increases with PSR for all the three zones. However, the increment is much higher for the softer side than the stiffer side since the effect of PSR is more prominent in the subballast and subgrade layers as compared to the ballast layer (see section 5.4.1).

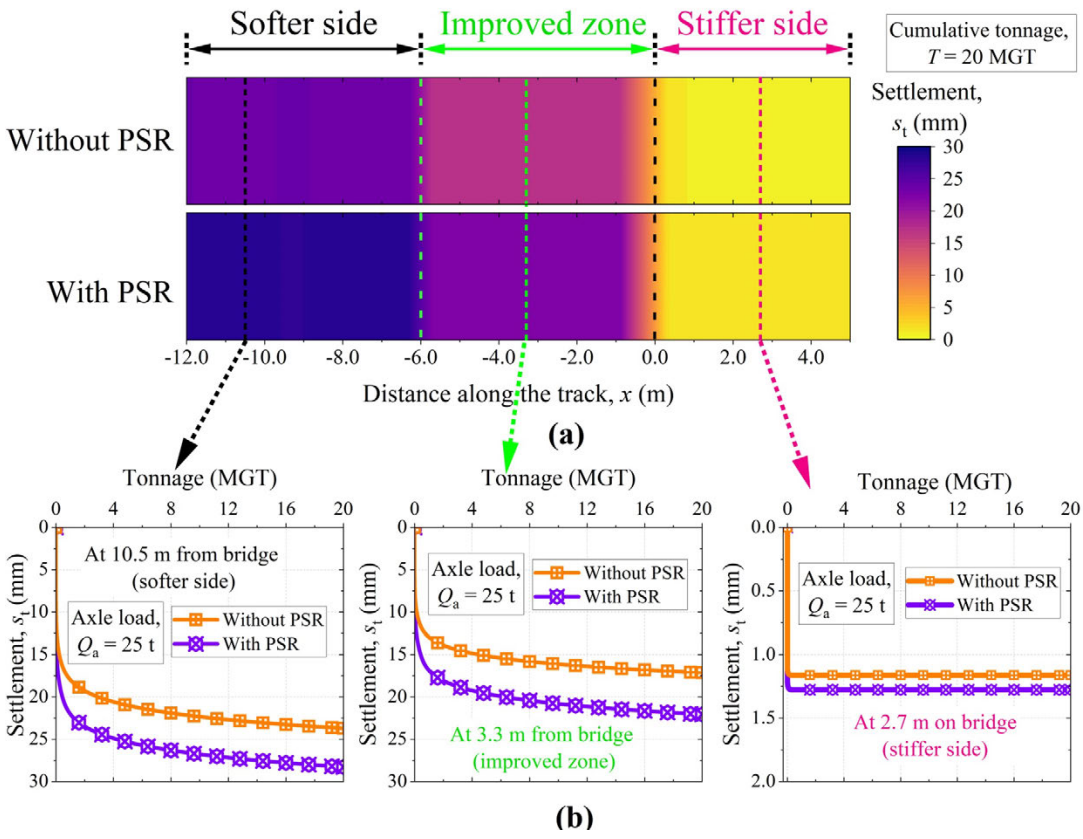

Figure 5.17 (a) Variation of settlement along the track length when subgrade friction angle in the improved zone is increased from 36° – 40°; **(b)** accumulation of settlement with tonnage at different sections of the transition zone

Thus, the results show that the techniques such as thicker granular layers and strengthened subgrade effectively decrease the differential settlement in the transition zone. Increasing h_b is more effective in reducing differential settlements than increasing h_s. Moreover, the results also reveal that strengthening the subgrade soil using ground improvement techniques or geosynthetic reinforcements may also be a viable alternative, but it is less effective than using thicker granular layers. Overall, for the open-track bridge transition considered in this study, a simple strategy of using a thick ballast layer turns out to be the most effective technique for reducing the differential settlements. Thus, the present approach can be used to compare the effectiveness of different mitigation strategies in improving the track performance and selecting the most suitable technique for a particular transition zone.

5.6 Practical Relevance, Potential Applications, Limitations, and Future Scope

The computational methodology proposed in this chapter provides a convenient means to evaluate the long-term performance of a ballasted railway track under train-induced repeated loading. Using this approach, a practicing railway engineer can evaluate the settlements accumulated at a section of a railway line over a specified amount of tonnage. This information would help in identifying the problematic sections along a railway line and in planning the maintenance cycles. The method can also be applied to transition zones to predict the magnitude of differential settlement accumulated after multiple train passages. Prior information of the differential settlements is crucial to optimize the design of the transition zones and improve the capacity of the track to allow heavier freight and high-speed passenger trains in the future. Moreover, as shown in the previous section, the proposed computational approach can be used to assess the adequacy of different countermeasures in improving the performance of the transition zones and select the most effective technique.

The limitations of the proposed computational approach are as follows:

- The present method considers train-induced loading only in the vertical direction. However, the ballasted railway tracks are also subjected to loading in longitudinal and transverse directions (Esveld 2001).
- In the present approach, the modified Boussinesq solutions are used to evaluate the stress distribution, which are based on the linear elasticity theory. However, the

present method considers the elastoplastic behavior of the track constituent materials. Therefore, the accuracy of the present approach can be improved by evaluating the stress distribution based on plasticity theory. Nevertheless, the author compared the stress distribution below a railway track, calculated using 3D finite element analyses, when the material behavior of substructure layers is considered as elastic and elastoplastic. It was observed that the stress distribution calculated by considering elastoplastic material behavior was similar to that determined by assuming elastic material behavior (difference of about 12%).

- The approach does not consider the effect of seasonal fluctuations in the water content in the form of wetting and drying cycles, frost heave, and unsaturated geomaterials on the response of the ballasted railway track.

Future investigations shall address these limitations to improve the accuracy of the present approach. Moreover, the experimental investigations to distinguish between the track settlements occurring with and without PSR constitute the future scope of this study.

5.7 Concluding Remarks

A computational approach is presented in this chapter, which employs a novel geotechnical rheological model to simulate the response of ballasted railway tracks under train-induced loads. The key highlights of this study include:

- A simplified yet effective geotechnical rheological model with enhanced capability of capturing the effect of PSR for an accurate prediction of the track response. This is also the essential methodological contribution of this chapter.
- Application of the rheological model to the transition zones by incorporating heterogeneous support conditions along the track length and predicting the magnitude of differential settlements accumulated over a specified period or tonnage.
- Using the computational approach to compare the effectiveness of different mitigation strategies in improving the performance of transition zones which helps in selecting the most appropriate strategy.

The rheological model used in this study considers the plasticity of track materials through plastic slider elements. The effect of PSR is accounted for in the model by modifying the constitutive relationship for the slider elements, which is successfully

validated against the experimental data reported in the literature. A parametric study is conducted to investigate the influence of Q_a and h_{gl} on track response, and the effect of PSR is highlighted by comparing the results with and without PSR inclusion. The results reveal that the deformation is significantly underestimated if PSR is neglected in the analysis, which may severely affect the selection of adequate h_{gl}. The settlement after a cumulative tonnage of 20 MGT at 25 t axle load is found to be underpredicted by 16% if PSR is disregarded.

The application of the rheological model to an open track-bridge transition showed that the PSR increases the differential settlement between the softer and stiffer side of the critical zone. Moreover, the track geometry deterioration in the transition zone aggravates with Q_a (46.1% increment with a rise in Q_a from 20 t – 27 t), suggesting the use of mitigation measures for the tracks in which heavier axle loads are anticipated in the future. An increase in h_{gl} reduced the differential settlement in the transition zone, with ballast thickness increment more effective (up to 86% reduction) than subballast thickness increment (up to 41.6% reduction). The capability of the present approach to examine the suitability of different countermeasures in improving the performance of the transition zone exhibits its practical utility. Finally, the findings from this study emphasise the inclusion of the PSR effect in the computational or predictive models for the accurate prediction of the behaviour of railway tracks.

This chapter improved the accuracy of the novel computational model by incorporating the influence of PSR on the cumulative deformation in the track layers. The effect of PSR was investigated on both the standard ballasted railway track and a typical open track-bridge transition. In the subsequent chapter, the revised computational model is used to assess the effectiveness of 3D cellular geoinclusions in improving the performance of the critical zones in railway tracks. First, a comprehensive review of literature is presented, followed by the development of a novel mathematical model to capture the magnitude of improvement provided by the artificial inclusion. Finally, the mathematical model is incorporated into the revised computational approach, and the adequacy of geoinclusions in mitigating the differential settlements near the transition zone is investigated.

CHAPTER 6 (PART-A)
IMPROVING THE PERFORMANCE OF RAILWAY TRACKS USING THREE-DIMENSIONAL CELLULAR GEOINCLUSIONS

6.1 General

In the previous chapters, a novel methodology to evaluate the mechanical behaviour of the ballasted railway tracks was developed. The approach was applied to investigate the performance of an open track-bridge transition zone, highlighting its practical relevance and potential applications. Subsequently, the accuracy of the predictions was enhanced by incorporating the effect of PSR on the track response. Furthermore, the previous chapters also highlighted the need to address the track geometry degradation problem at elevated axle loads and train speeds, especially at the transition zones. This chapter investigates the beneficial role of 3D cellular geoinclusions in reducing the settlement and thereby improving the performance of ballasted railway tracks. Firstly, the existing literature pertaining to the use of cellular inclusions in a railway track is comprehensively reviewed. Subsequently, a mathematical model is developed to evaluate the magnitude of improvement provided by the cellular inclusions. In the second part of this chapter, the mathematical model is combined with the geotechnical rheological track model to evaluate the magnitude of settlement reduction provided by the geoinclusion.

6.2 Beneficial Role of Cellular Geoinclusions in Railways

The conventional ballasted tracks require frequent maintenance due to the deterioration or degradation of the granular layers under repeated traffic loading (Esveld 2001). The degradation primarily involves the crushing or churning up of the ballast particles, which produces fines. The fines clog the voids and decrease the permeability of the ballast bed. Moreover, the track loses its geometry under repetitive loads due to inadequate confinement of the ballast/subballast bed. Additionally, the problems may arise due to mud pumping or the intrusion of clay and silt size particles from the subgrade (saturated, soft subgrade) into the ballast bed, lateral buckling of rails due to insufficient track confinement, among others (Indraratna et al. 2011). In **Figure 6.1**, a schematic diagram is shown, which illustrates the associated key issues governing the track instability during the normal track operations. The maintenance work is expensive and disrupts the traffic, and reduces the availability and operational efficiency of the track. Therefore, the rail

track designers are exploring suitable measures to improve the performance of the tracks and reduce the frequency of maintenance cycles. The 3D cellular geoinclusions such as geocells or scrap rubber tyres can provide a cost-effective solution in this aspect.

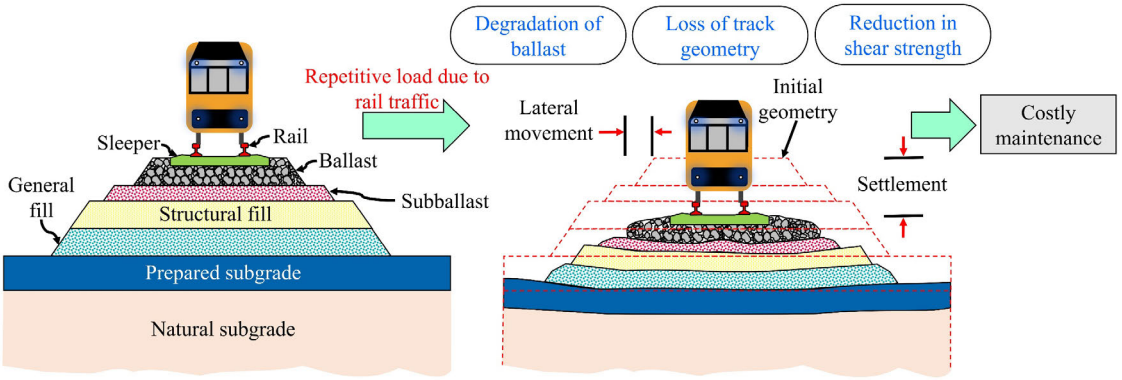

Figure 6.1 Key problems governing the instability of ballasted railway tracks

6.2.1 Potential Benefits of Using Geocells

The use of geocell can be highly beneficial for the long-term stability of the railway tracks. As discussed above, the traffic-induced load (moving static and dynamic) leads to the degradation of the constituent materials. Consequently, the track loses its geometry and operational efficiency and demands costly maintenance. The geocells provide confinement to the infill materials and may protect the track geometry for a long period and ultimately reduce the frequency of the maintenance cycles.

Numerous experimental, numerical, and analytical studies have indicated that the geocells can improve the performance of a ballasted track (Leshchinsky & Ling 2013a; Leshchinsky & Ling 2013b). The results of the studies show that:

- The geocell confines the infill material, which increases its strength and stiffness. Consequently, the traffic-induced stress gets uniformly distributed to a wide area (Chrismer 1997; Zhou & Wen 2008).
- The geocell confinement may reduce (redistribute) the shear stresses at the ballast (or subballast)-subgrade interface (Giroud & Han 2004b).
- The use of geocell preserves the track geometry by reducing the permanent deformation in the subgrade. Moreover, it increases the strength and resilience of the infill material under cyclic loading (Chrismer 1997; Raymond 2001; Indraratna et al. 2010).

- The confinement provided by the geocell reduces the lateral deformations in the track and thus, maintains the track shape (Satyal et al. 2018).

6.2.2 Factors Affecting Geocell Applications in Railways

The past studies indicate that the geocells can be effectively used to improve the stability of the railway tracks. However, the degree of improvement depends on a large number of parameters. Some of the crucial parameters are discussed below.

6.2.2.1 Geocell Properties

The stiffness, size, shape, seam strength are some of the properties that may influence the performance of the geocell. The stiffness of the geocell is crucial for the long-term stability and the overall cost of the reinforced track. The use of stiffer materials usually improves the confinement. However, stiffer materials may be more expensive as compared to soft materials. Moreover, large strains are generated in the soft material as compared to the stiff material for the same amount of vertical load (Leshchinsky & Ling 2013b). The strains may even exceed the elastic limit in soft material and prevent the geocell from performing its intended function.

The shape of the geocell significantly influences the response of the geocell reinforced layer. The layers with elliptical geocells are less stiff than the layers with circular geocells (Pokharel et al. 2010). Furthermore, the performance of the geocell reinforced layer decreases with an increase in the geocell pocket size (Yang & Han 2013).

6.2.2.2 Subgrade Properties

The subgrade strength and stiffness play a crucial role in the load-deformation behaviour of the geocell reinforced track. The total deformation in a railway track comprises ballast deformation (or subballast deformation) and subgrade deformation. For soft subgrades, the contribution of subgrade deformation is much higher as compared to the ballast deformation. However, for the stiff subgrades, the contribution of ballast deformation is significant (Doyle 1980). For stiff subgrade, the ballast (or subballast) layer tends to deform laterally, which leads to vertical track deformation. The geocells can significantly improve the performance of the track in this case by providing additional confinement to the ballast and reducing the lateral deformation. Moreover, for soft soils, the geocells

distribute the loads over a wider area and reduce the subgrade stress (Zhou & Wen 2008). Consequently, the settlement of subgrade decreases. Furthermore, the subgrade stiffness influences the magnitude of the strain developed in the geocell. A large amount of strain is developed in the geocell for very soft subgrades as compared to the soft subgrades (Leshchinsky & Ling 2013b).

6.2.2.3 Properties of Infill Materials

The performance of a geocell reinforced layer also depends on the properties of the infill soil. Pokharel et al. (2010) observed that the geocell confinement provides an apparent cohesion to the infill material. They reported that the benefit of using geocell reduces if the infill material contains a significant amount of cohesion. Conversely, repeated plate load tests by Pokharel et al. (2018) showed that the geocell reinforcement also reduces the cumulative deformation in infill with fines as compared to the unreinforced case. Moreover, the use of low strength materials as infill increases the effectiveness of geocell (Leshchinsky & Ling 2013b). Thus, the geocells may prove beneficial in the construction of tracks using inferior quality recycled and locally available materials.

6.2.2.4 Position of Geocells within the Rail Track

The amount of improvement in the track stability depends on the placement position of the geocell. Several researchers have studied the performance of the geocell reinforced infill layer at different locations within a track, such as in the ballast bed, the subballast bed, or in the soil subgrade (Leshchinsky & Ling 2013a; Indraratna et al. 2015; Satyal et al. 2018). The ideal location of the geocell layer is in the ballast bed immediately below the sleepers. However, a minimum gap of 15 cm – 25 cm has to be maintained below the sleeper for regular maintenance operations (Leshchinsky & Ling 2013b; Satyal et al. 2018). Furthermore, the service life of the geocell may reduce when it is placed near the top of the ballast bed due to a large amount of bending incurred from a high magnitude of vertical stress (Liu et al. 2018).

The presence of a reinforced layer in the track substructure reduces the vertical stress, which minimises the settlement and lateral spreading of the bottom layers (Liu et al. 2018). The effectiveness of geocell in reducing the settlement may decrease with an increase in depth of the reinforced layer from the top (or base of sleepers). **Figure 6.2** shows the variation of subgrade stress below a railway track with (a) unreinforced ballast

bed; (b) ballast bed reinforced with geocell near the sleeper base; (c) ballast bed reinforced with geocell at the bottom.

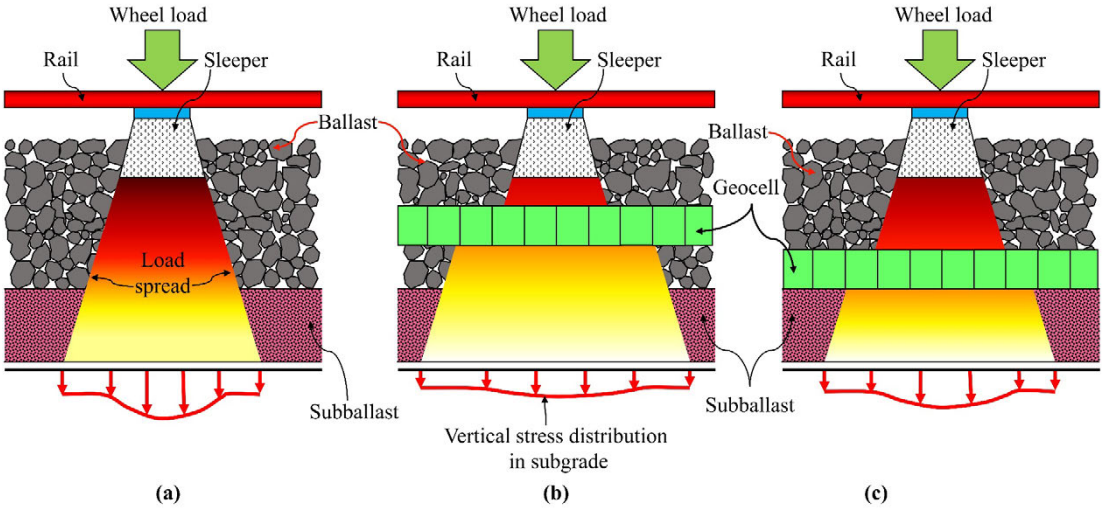

Figure 6.2 The vertical stress distribution in the subgrade for the ballasted track **(a)** without geocell; **(b)** geocell near the top of ballast layer; **(c)** geocell near the bottom of the ballast layer

It is apparent that the load is distributed uniformly over a wide area of the subgrade for reinforced ballast. Moreover, the load spread area is higher when the geocell is placed near the sleeper as compared to the case when it is situated near the subballast. This is because the reinforced ballast layer is subjected to a high magnitude of vertical stress when geocell is placed near the top. Consequently, more confinement is mobilised, and the load is spread over a wider area. Conversely, the high magnitude of vertical stress induces a large amount of bending in the geocell. Due to bending, high tensile stresses are generated near the bottom portion of the geocell layer (Leshchinsky & Ling 2013a). These stresses may exceed the seam strength (which is usually smaller than the tensile strength) and lead to wear and tear in the geocell. This wear and tear ultimately reduce the service life of geocell.

However, the reinforced layer is subjected to low vertical stress when the geocell is positioned near the base. Therefore, less confinement is mobilised, and the load is distributed over a small area. Nevertheless, the amount of load spread also depends on the relative stiffness between the subgrade and the reinforced layer (Leshchinsky & Ling 2013b). The stiffness ratio between the reinforced layer and subgrade must be large.

However, there is an upper limit to the stiffness ratio because Leshchinsky & Ling (2013b) observed a non-uniform stress distribution at the subgrade due to the use of rigid (steel) geocell. Thus, it is very challenging to decide the most suitable position of the geocell layer within the rail track. Factors such as the nature of subgrade, intended function of geocell (i.e., to reduce the subgrade stress or the lateral deformation of granular layers or both), and geocell material may govern the selection of the most appropriate placement location.

It is clear that the geocells can improve the performance of the railway tracks. However, it is essential to critically evaluate the improvement in terms of the parameters (or material properties) that are crucial for the track stability before their installation in the track. Therefore, the subsequent sections discuss the influence of geocells on the key parameters pertaining to track stability.

6.2.3 Influence of Geocell Reinforcement on Resilient Modulus

Several researchers have conducted experimental and numerical investigations to understand the effect of geocell reinforcement on the resilient modulus of geomaterials. Some of the investigations are briefly discussed below.

6.2.3.1 Experimental and Field Investigations

The geocell reinforcement generally improves the resilient modulus of the soil. However, the magnitude of improvement depends on the conditions such as the type of soil (fine-grained or coarse-grained), moisture content, confining pressure, deviator stress, frequency and number of load cycles (Mengelt et al. 2006; Indraratna et al. 2015). The experimental investigations by Edil & Bosscher (1994) revealed that the resilient modulus of sand increases with confinement. Moreover, the field investigations by Al-Qadi & Hughes (2000) on a pavement in Pennsylvania showed that the combination of geocell, geotextile, and geogrid could improve the resilient modulus of the aggregates. Mengelt et al. (2006) conducted cyclic triaxial tests to study the influence of geocell reinforcement on the resilient modulus and plastic deformation behaviour of the soil. The use of geocell increased the resilient modulus by 1.4% – 3.2% and 16.5% – 17.9% for the coarse-grained and fine-grained soils, respectively. Thus, the results indicated that the improvement is highly dependent on the soil type.

Tanyu et al. (2013) conducted large-scale repeated load tests (in a 3 m × 3 m × 3.5 m reinforced concrete pit) on geocell reinforced gravel (which represents granular sub-base layer for pavements). They observed a 40% – 50% increase in the resilient modulus on reinforcing the gravel with the geocell. Moreover, the increment was dependent on the thickness of the reinforced layer. They stated that a higher degree of improvement might be observed in thin layers as compared to thick layers. Indraratna et al. (2015) conducted repeated load tests on unreinforced and geocell reinforced subballast under plane-strain conditions. The use of plane-strain conditions gave a realistic approach to investigate the behaviour of the subballast. The use of geocell increased the resilient modulus of the unreinforced subballast by 10% – 18%. Moreover, the resilient modulus for both the reinforced and unreinforced specimens increased (about 20%) with an increase in the confining pressure and the loading frequency. Furthermore, the effect of frequency was more pronounced in the reinforced specimens.

6.2.3.2 Numerical and Analytical Investigations

Yang & Han (2013) observed that the use of geocell increases the resilient modulus of UGM. The amount of improvement in resilient modulus increased non-linearly with an increase in the tensile stiffness and the cyclic deviator stress. Moreover, the improvement also increased with a reduction in geocell pocket size and an increment in the dilation angle of the infill material. However, the improvement decreased with an increase in the resilient modulus of the infill material and the confining pressure.

Liu et al. (2018) studied the mechanical response of straight and curved geocell reinforced ballast embankment under monotonic and cyclic loading conditions using DEM. The results showed an increase in stiffness of the ballast bed under monotonic loading conditions and an increase in resilience under cyclic loading conditions.

Thus, the results from previous studies show that the geocells improve the resilient modulus of the granular materials. However, the degree of improvement depends on the parameters such as properties of the geocell, infill soil, subgrade, stress state, and the loading conditions.

6.3 Additional Confinement

6.3.1 General

The geocells provide an additional horizontal and vertical confinement to the infill material and restrain the upward movement of the underlying material (material below the geocell layer) outside the loaded area (mattress effect) (Pokharel et al. 2009; Pokharel et al. 2011). The horizontal confinement reduces the lateral deformation of the infill material. Moreover, the mattress effect results in a wider distribution of vehicle load, which prevents excessive deformation (or failure) in soft subgrades (Pokharel et al. 2011). However, the magnitude of additional confinement depends on the properties of the geocell, infill soil, and loading conditions. Yang & Han (2013) observed that the additional confining pressure provided by the geocell reinforcement decreases with an increase in the geocell pocket size. This reduction is because the quantity of geocell material that reinforces the infill decreases with an increase in pocket size.

The plane-strain cyclic loading tests by Indraratna et al. (2015) revealed that the loading frequency and external confining pressure significantly affect the extra confinement offered by the geocell. The additional confinement increased with an increase in loading frequency. However, it decreased with an increase in the external confining pressure at a particular loading frequency.

6.3.2 Models to Quantify Additional Confinement

The confinement provided by the geocells to the infill soil is identical to the confinement provided by the membrane to the soil sample in a triaxial test. Therefore, the magnitude of additional confinement can be evaluated using the classical work of Henkel & Gilbert (1952). Henkel & Gilbert (1952) quantified the additional confinement provided by the membrane (in a triaxial test) and its influence on the shear strength of the soil (Mengelt et al. 2006). Tanyu et al. (2013) used the theory developed by Henkel & Gilbert (1952) to evaluate the additional confining stress produced by the geocells on the soil (Equation 6.1). The geocell strain data collected from the experiments were used in Equation 6.1 to determine the additional confining pressure along the minor principal stress direction ($\Delta\sigma_3$):

$$\Delta\sigma_3 = \frac{2M_{\mathrm{m}}\varepsilon_{\mathrm{c}}}{d_{\mathrm{s}}(1-\varepsilon_{\mathrm{a}})} \qquad 6.1$$

where M_m is the mobilised modulus of the membrane (or geocell); d_s is the diameter of the specimen; ε_a is the axial strain; ε_c is the circumferential strain which can be calculated using Equation 6.2.

$$\varepsilon_c = \frac{1 - \sqrt{1 - \varepsilon_a}}{\sqrt{1 - \varepsilon_a}} \tag{6.2}$$

Yang & Han (2013) developed an analytical model to predict the additional confinement provided by the geocell in the repeated load triaxial tests. They suggested that the hoop stress developed in the geocell generates additional confining pressure within the infill material. Moreover, they assumed a uniform distribution of hoop stress along the height of the geocell. The additional confining pressure due to the incorporation of geocell was mathematically represented as:

$$\Delta\sigma_3 = \frac{M_t}{d_s}\left[\frac{-\Delta\sigma_3}{E_{R,1}} + \frac{\sigma_1 - (\sigma_3 + \Delta\sigma_3)}{E_{R,2}}\right]\left(\frac{\varepsilon_0}{\varepsilon_r}\right) e^{-\left(\frac{\rho_p}{N_{limit}}\right)^{\beta_p}} \left(\frac{1 + \sin\psi_d}{1 - \sin\psi_d}\right) \tag{6.3}$$

where M_t is the tensile stiffness of the geocell; ψ_d is the dilation angle; $\varepsilon_0/\varepsilon_r$, ρ_p and β_p are the fitting parameters that can be determined by using the permanent deformation test curve of UGM; N_{limit} is the number of load repetitions required to reach the resilient state; $E_{R,1}$ and $E_{R,2}$ are the resilient modulus of the granular material corresponding to the first and second stages of repeated load triaxial tests, respectively. The first stage corresponds to the condition when the axial stress increases from σ_3 to $\sigma_3 + \Delta\sigma_3$. The second stage corresponds to the increase of axial stress from $\sigma_3 + \Delta\sigma_3$ to σ_1.

However, Yang & Han (2013) ignored the influence of loading frequency on the additional confining pressure. Furthermore, the resilient modulus and mobilised dilation angle vary with the number of loading cycles (Indraratna et al. 2015). Therefore, using a constant value of resilient modulus and dilation angle can limit the accuracy of the proposed model.

Indraratna et al. (2015) derived a semi-empirical model using hoop tension theory to determine the additional confinement provided by the geocell to an infill soil under the plane-strain loading condition. They also incorporated the influence of loading frequency and load cycles on the mobilised modulus of geocell and the mobilised dilation angle for

the infill material. This was done by varying the mobilised geocell modulus and mobilised dilation angle in accordance with the strain reached during a particular loading cycle. The additional confinement was calculated as

$$\Delta\sigma_3' = \int_1^{N_{\text{lim}}} \left[\frac{2M_{\text{m}}}{D_{\text{g}}}\left\{\frac{(1-\nu_{\text{m}})k_{\text{c}}+\nu_{\text{m}}}{(1+\nu_{\text{m}})(1-2\nu_{\text{m}})}\right\}\left\{\frac{-\nu_{\text{m}}\sigma_{\text{cyc}}}{dE_{\text{R}}}+\varepsilon_{1,1}^{p}\left(\frac{a^*}{N}+\frac{b'}{N}\right)\left(\frac{1+\sin\psi_{\text{m}}}{1-\sin\psi_{\text{m}}}\right)\right\}\right] dN \quad 6.4$$

where N_{lim} is the number of cycles required to reach a stable zone; ν_{m} is the Poisson's ratio of the geocell; k_{c} is the ratio of circumferential strain to the radial strain in geocell; D_{g} is the diameter of the geocell opening (m) (the geocell opening is assumed circular); $\varepsilon_{1,1}^{p}$ is the permanent axial strain after the first load cycle; a^* and b' are the empirical coefficients; ψ_{m} is the mobilised dilation angle (°).

6.4 Irrecoverable Deformations

6.4.1 Influence of Geocell Reinforcement on Irrecoverable Deformations

Pokharel et al. (2009) conducted monotonic and repeated plate load tests on sand and reported that the geocell reinforcement reduces the permanent deformation and increases the stiffness and bearing capacity. Moreover, the moving wheel test conducted by Pokharel et al. (2011) revealed that the geocell reinforcement increases the confinement in infill and distributes the load over a wide area, which reduces subgrade stress and deformation.

The studies by Yang & Han (2013) revealed that the geocell reinforcement reduces the permanent deformation of the UGM. Moreover, they observed that the reduction in permanent deformation due to geocell reinforcement depends on the external confining pressure, tensile stiffness, and the opening size of the geocell. The reduction in permanent deformation:

- Increased non-linearly with an increase in the tensile stiffness of geocell.
- Increased with a reduction in geocell size.
- Increased with an increase in the dilation angle of the infill material.
- Decreased with an increase in the resilient modulus of the infill soil.
- Decreased with an increase in confining pressure and cyclic deviator stress.

Leshchinsky & Ling (2013a) conducted a series of model tests to investigate the influence of the number and location of the geocell layers on the strength and stiffness of an embankment of poorly graded gravel. The poorly graded gravel embankment was assumed representative of the ballast bed in railways. The gravel embankment was loaded both monotonically and cyclically, and the results of the tests with and without geocell reinforcement were compared. The experimental results showed that the reinforcement of gravel with geocell significantly reduces the vertical settlement and lateral deformation in both monotonic and repeated loading tests. Interestingly, the results showed that the maximum amount of lateral spreading occurred just above the geocell layer. Subsequently, a parametric study was conducted using FE analyses to investigate the influence of geocell stiffness, type of subgrade, and strength of gravel on the behaviour of reinforced gravel embankment. The results showed that the settlement and subgrade stress reduced significantly with an increase in the geocell stiffness. However, the magnitude of stress reduction was dependent on the stiffness of the subgrade. No significant stress reduction was observed for a stiff subgrade. Nevertheless, the settlement reduced considerably for the stiff subgrade. Thus, the authors stated that the geocell might have a beneficial effect on both the soft and stiff subgrade.

Leshchinsky & Ling (2013b) used 3D FE analyses to investigate the behaviour of ballasted railway track with and without geocell reinforcement under monotonic loading. The results showed that the reinforcement of ballast by geocell significantly reduces the vertical settlement of the track. However, the amount of reduction depends on the stiffness of geocell and subgrade in addition to the ballast strength. The decrease in the vertical settlement was more effective in the case of soft or stiff subgrade, however, in a very soft subgrade, there was a little benefit. This effect was probably due to the tendency of the ballast to undergo a significant amount of lateral deformation when a stiff subgrade underlies it. The geocell prevents this lateral deformation and hence, reduces the vertical settlement of the track. Furthermore, the decrease in settlement and lateral deformation was more significant for low strength ballast as compared to high strength ballast on soft subgrades.

The experimental investigation by Indraratna et al. (2015) showed that the addition of geocells in the subballast layer decreases the permanent axial strain. Moreover, this

beneficial role of geocell was more pronounced at low confining pressures (5 kPa – 10 kPa). Furthermore, the reduction in permanent axial strain increased with an increase in the loading frequency.

Satyal et al. (2018) conducted cyclic plate load tests and 3D FE analyses on geocell reinforced ballast over soft subgrade to assess the beneficial role of geocell in the railway tracks. They observed that the reinforced ballast layer distributes the traffic-induced load uniformly to a wide area in the subgrade soil and consequently reduces the plastic deformation. Moreover, the strain in the geocell was within the elastic range, and no significant damage was observed in geocells. Subsequently, they validated the numerical results with the experimental plate load tests and then conducted a parametric study. The parametric studies showed an overall 30% reduction in track settlement on reinforcing the ballast layer. Moreover, the amount of settlement reduction was dependent on the position and number of geocell layers. The use of two geocell layers, one above the other, produced the least settlement. Further, the effectiveness of geocell reinforcement decreased with an increase in the strength of subgrade soil.

The DEM analyses of geocell reinforced straight and curved embankments by Liu et al. (2018) showed that the application of geocell significantly reduces the vertical deformation of ballasted embankment under both monotonic and cyclic loading. This effect was more pronounced if the layer was placed at some distance above the subgrade. Moreover, it was observed that at the initial stages of monotonic loading, the geocell confinement was not mobilised, and both the unreinforced and reinforced embankments showed similar stiffness. However, after a particular value of the load, the stiffness of the reinforced embankment increased. Furthermore, the ballast inside the geocell tends to move downwards, however, the ballast for unreinforced case tends to move sideways in addition to the vertical movement. The repeated plate loading tests by Pokharel et al. (2018) also showed that the use of geocell reduces the permanent deformation of a layer as compared to the unreinforced case.

Thus, the results from the aforementioned studies indicate that the geocell reinforcement significantly decreases the lateral and vertical deformation of the infill materials.

However, the amount of reduction depends on the properties of the geocell, infill soil, subgrade, and loading conditions.

6.4.2 Empirical Models for Irrecoverable Deformations

Several mathematical models are available to predict the plastic deformations of the subgrade soil and the granular layers under repeated loading (Lekarp et al. 2000). Some of the models are discussed below.

Li & Selig (1996) gave a power model to predict the cumulative plastic deformation in fine-grained subgrade soils under repeated loading. The model considered the influence of the number of load cycles and the type, stress state (deviator stress) and physical state (dry density and moisture content) of the soil on the cumulative plastic strain (see Equation 3.24).

Yang & Han (2013) proposed an analytical model to evaluate the permanent deformation of geocell reinforced UGM under repeated load triaxial tests when it reaches the resilient state.

$$\varepsilon_{\mathrm{a}}^{p} = \left[-\frac{\Delta\sigma_3}{E_{\mathrm{R},1}} + \frac{\sigma_1 - (\sigma_3 + \Delta\sigma_3)}{E_{\mathrm{R},2}}\right]\left(\frac{\varepsilon_0}{\varepsilon_{\mathrm{r}}}\right) e^{-\left(\frac{\rho_{\mathrm{p}}}{N_{\mathrm{limit}}}\right)^{\beta_{\mathrm{p}}}} \tag{6.5}$$

The parameters have the same meaning as in Equation 6.3. Thus, to evaluate the permanent axial deformation, the additional confining pressure due to geocell need to be evaluated. Moreover, the parameters $E_{\mathrm{R},1}$ and $E_{\mathrm{R},2}$ can be calculated using the equations in **Table 2.2**.

Indraratna & Nimbalkar (2013) proposed a model to evaluate the variation of permanent axial strain in the ballast with the number of load cycles (Equation 6.6).

$$\varepsilon_1^p = \varepsilon_{1,1}^p[1 + a^* \ln N + 0.5b^*(\ln N)^2] \tag{6.6}$$

An attempt has been made to predict the variation of permanent deformation with N for different types of infill (for both unreinforced and geocell reinforced cases). The experimental data from the cyclic plate load tests conducted by different researchers were

used to derive the empirical coefficients a^* and b^*. The permanent deformation was then predicted using Equation 6.6. Subsequently, the accuracy of the coefficients was investigated by comparing the back-fitted data with the experimental data. **Table 6.1** gives the values of empirical coefficients (or model parameters) obtained for the unreinforced and geocell reinforced cases.

Table 6.1 Model parameters to predict permanent deformation

Reference	Infill	Condition	Model parameters	
			a^*	b^*
Thakur et al. (2012)	RAP	Unreinforced	0.148	1.820
Thakur et al. (2012)	RAP	Geocell reinforced	0.155	0.591
Leshchinsky & Ling (2013a)	Gravel	Unreinforced embankment	32.89	6.459
Leshchinsky & Ling (2013a)	Gravel	Geocell reinforced embankment (single layer)	0.1	122.5
Tanyu et al. (2013)	G2 gravel	Unreinforced	0.05	0.68
Tanyu et al. (2013)	G2 gravel	Reinforced (geocell with 200 mm diameter and 200 mm height)	1.386	0.461
Pokharel et al. (2018)	AB-3	Unreinforced (Maximum applied pressure : 552 kPa)	0.217	0.026
Pokharel et al. (2018)	AB-3	Geocell reinforced (single cell, maximum applied pressure : 552 kPa)	0.146	0.079
Pokharel et al. (2018)	AB-3	Geocell reinforced (multiple cells, maximum applied pressure : 552 kPa)	0.415	0.050

Note: RAP: Recycled asphalt pavement; AB-3: Aggregate base type 3; G2: Grade 2

Figure 6.3 shows the experimental versus predicted results for the tests conducted by Pokharel et al. (2018), Tanyu et al. (2013), Leshchinsky & Ling (2013a), and Thakur et al. (2012). The permanent deformation has been normalised with the layer/specimen thickness to compare results from the different studies. The figure shows that the geocell reinforcement significantly reduces the permanent deformation or settlement of the infill for all the cases. Moreover, the results from model predictions are in close agreement with the experimental results.

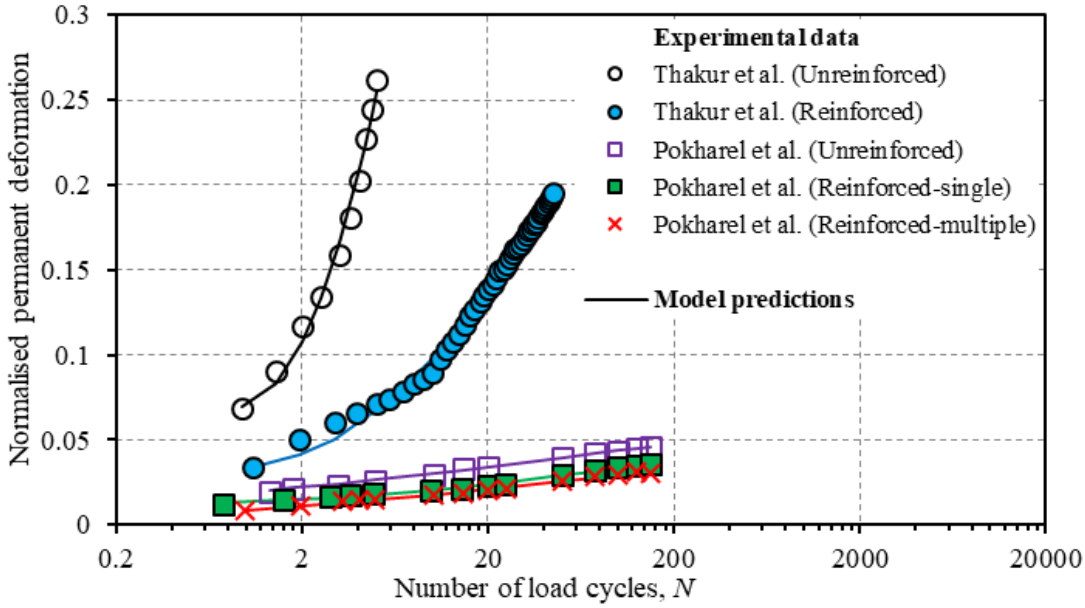

(a)

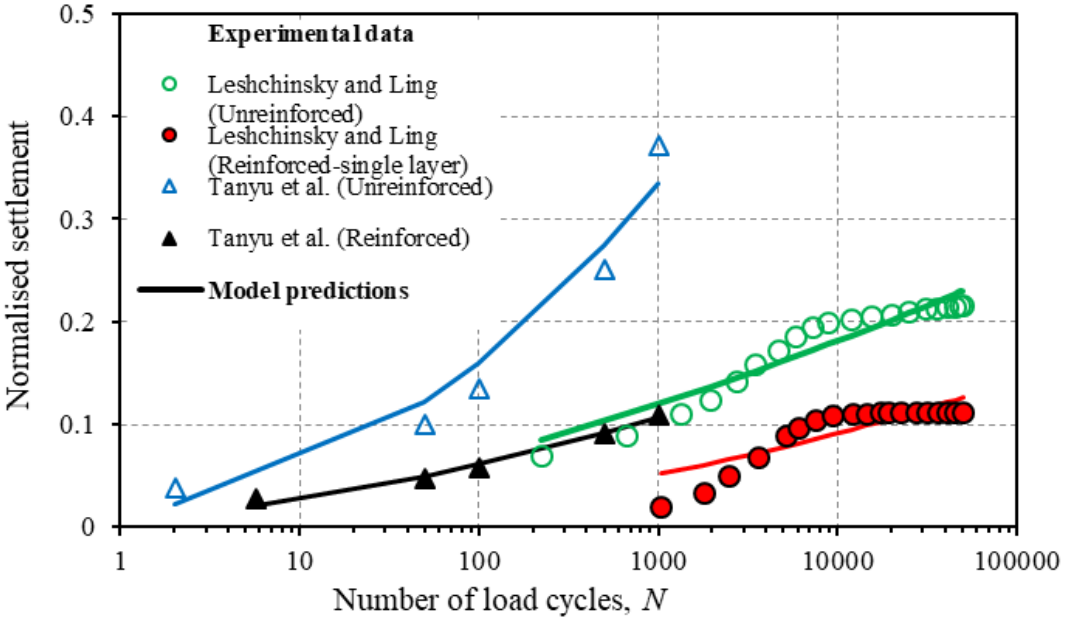

(b)

Figure 6.3 Comparison of predicted and experimental results from previous studies

6.5 Field Performance of Geocells

This section discusses a few case studies where geocells have been used to stabilise the railway tracks.

6.5.1 Reconstruction of Ballasted Track for Gantry Crane Using Geocells

Raymond (2001) reported the reconstruction of a ballasted track for a gantry crane in Canada. A 200 mm thick geocell reinforced subballast layer was provided below the

sleepers (with a gap of 200 mm between the sleeper and geocell layer) during the reconstruction. The use of geocell reduced the settlement and lateral deformation of the track significantly.

6.5.2 Retrofitting of a Portion of Amtrak's North East Corridor Railway Line Using Geocells

Zarembski et al. (2017) discussed the reconstruction of a portion of Amtrak's North East Corridor railway line using geocells. The presence of soft subgrade in the site and extensive ballast fouling resulted in a significant loss in track geometry which demanded frequent maintenance. Consequently, a layer of geocell was provided in the subballast to reduce the subgrade stress and the track geometry degradation. Furthermore, a part of the track was reconstructed without geocell to compare the results. The field investigations revealed that the geocell stabilised section showed a minimal amount of settlement and subgrade stress as compared to the unreinforced section. Moreover, the rate of track geometry degradation reduced for the reinforced track.

6.5.3 Construction of a Transition Zone near a Railway Bridge on the South Coast of New South Wales, Australia

Kaewunruen et al. (2016) investigated the performance of a transition zone near a railway bridge on the south coast of New South Wales, Australia. The transition zone comprised geocells along with track superstructure elements such as resilient baseplates and sleepers to mitigate the traffic-induced vibrations and increase the stiffness of the track. **Figure 6.4** shows the placement of the geocells below the ballast bed near the bridge end.

Additionally, stiffness transfer sleepers with rail pads were provided after the geocell reinforced section. The rail pads were employed to dampen the traffic-induced vibrations. Accelerometers were used to monitor the vibrations generated in the rail, sleepers, and the ballast at the bridge, the bridge ends, the transition zone, the section with stiffness transfer sleepers, and the region with ordinary sleepers. **Figure 6.5** shows the placement positions of the geocells and superstructure elements (pads, sleepers) along the track.

Figure 6.4 Installation of geocells at the railway bridge ends on the south coastline of New South Wales, Australia
[modified from Kaewunruen et al. (2016)]

Figures 6.6, **6.7** and **6.8** show the typical Fourier amplitude spectra of the acceleration recorded in different components of a railway track at different sections (for the passage of three different trains) (Kaewunruen et al. 2016). It is apparent from the figures that as the trains move from the region with ordinary sleepers towards the bridge, the vibration in the sleepers increases. However, the magnitude of rail vibration is almost identical at the bridge end and the reinforced zone. This behaviour may be attributed to the increased stiffness of the track by the use of geocells in the transition zone, which mitigated the impact loads on the track. As explained in Section 2.2.2, an abrupt change in track stiffness generates the impact loads near the bridge ends, which produce excessive vibrations and endangers the track stability (Nimbalkar et al. 2018). However, the geocells reduced the stiffness difference near the bridge end and consequently abated the magnitude of the impact loads.

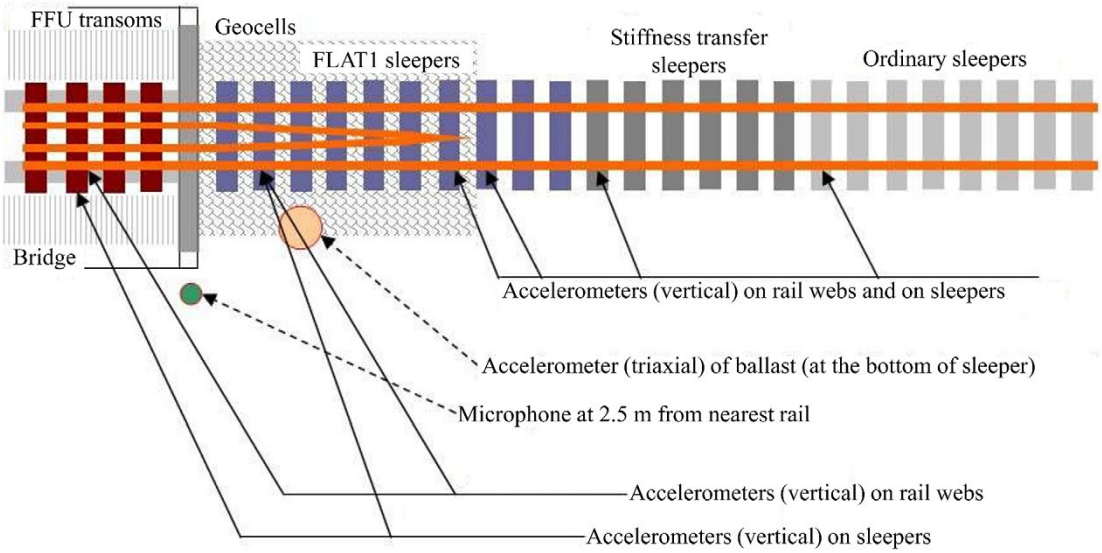

Figure 6.5 Track longitudinal profile showing the location of the geocells and superstructure elements (pads, sleepers)
[modified from Kaewunruen et al. (2016)]

Moreover, **Figure 6.8** shows that the magnitude of vibration in the ballast is very small as compared to the sleepers. The higher rate of vibration attenuation with depth could be attributed to the use of vibration isolation fastening systems such as resilient baseplates. Note that the transoms are structural members provided on top of the open deck bridges to support the rail or guard rails.

Figure 6.9 shows the deviations in track geometry along the bridge after the construction of the transition zone. The data has been obtained from the axle-box accelerometers installed in an inspection vehicle (Kaewunruen et al. 2016). The transition zone was constructed in late November 2012. The figure shows the track geometry measurements taken immediately after the construction, i.e., in December 2012 and after seven months of construction, i.e., in July 2013. The track was bidirectional, therefore, the data was taken in both up and down directions. The up and down directions correspond to the cases when the bridge end act as the exit and the entrance, respectively.

It is apparent in **Figure 6.9** that the deviation in the track is almost identical for both the measurements conducted in December 2012 and July 2013. This observation indicates that the rate of track geometry deterioration is very slow. This slow rate of deterioration is probably due to the gradual variation in track stiffness achieved by installing the geocell layer in the transition zone.

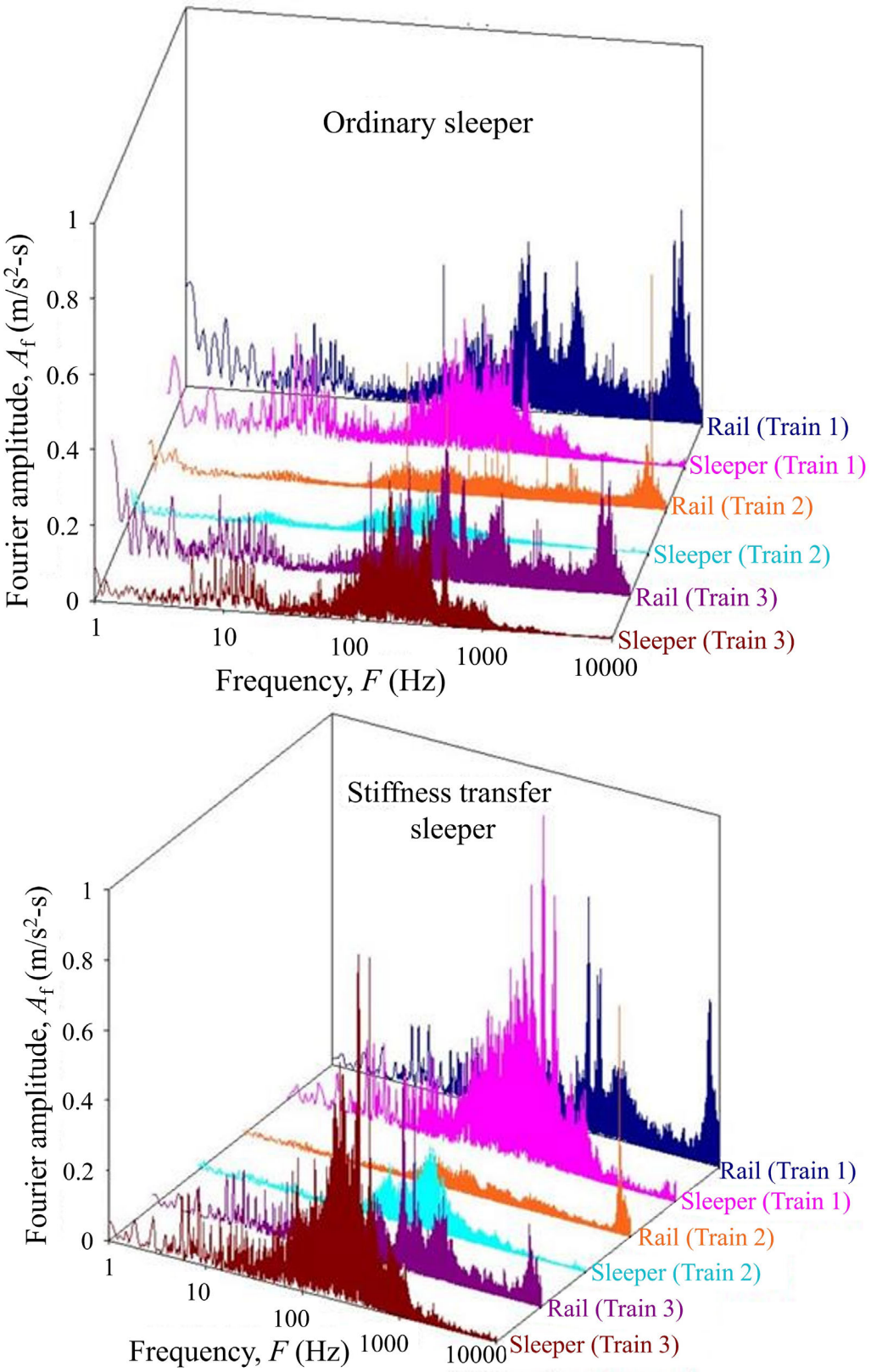

Figure 6.6 Typical Fourier amplitude spectrum for field accelerometer data recorded at the region with ordinary sleeper and stiffness transfer sleeper [adapted from Kaewunruen et al. (2016)]

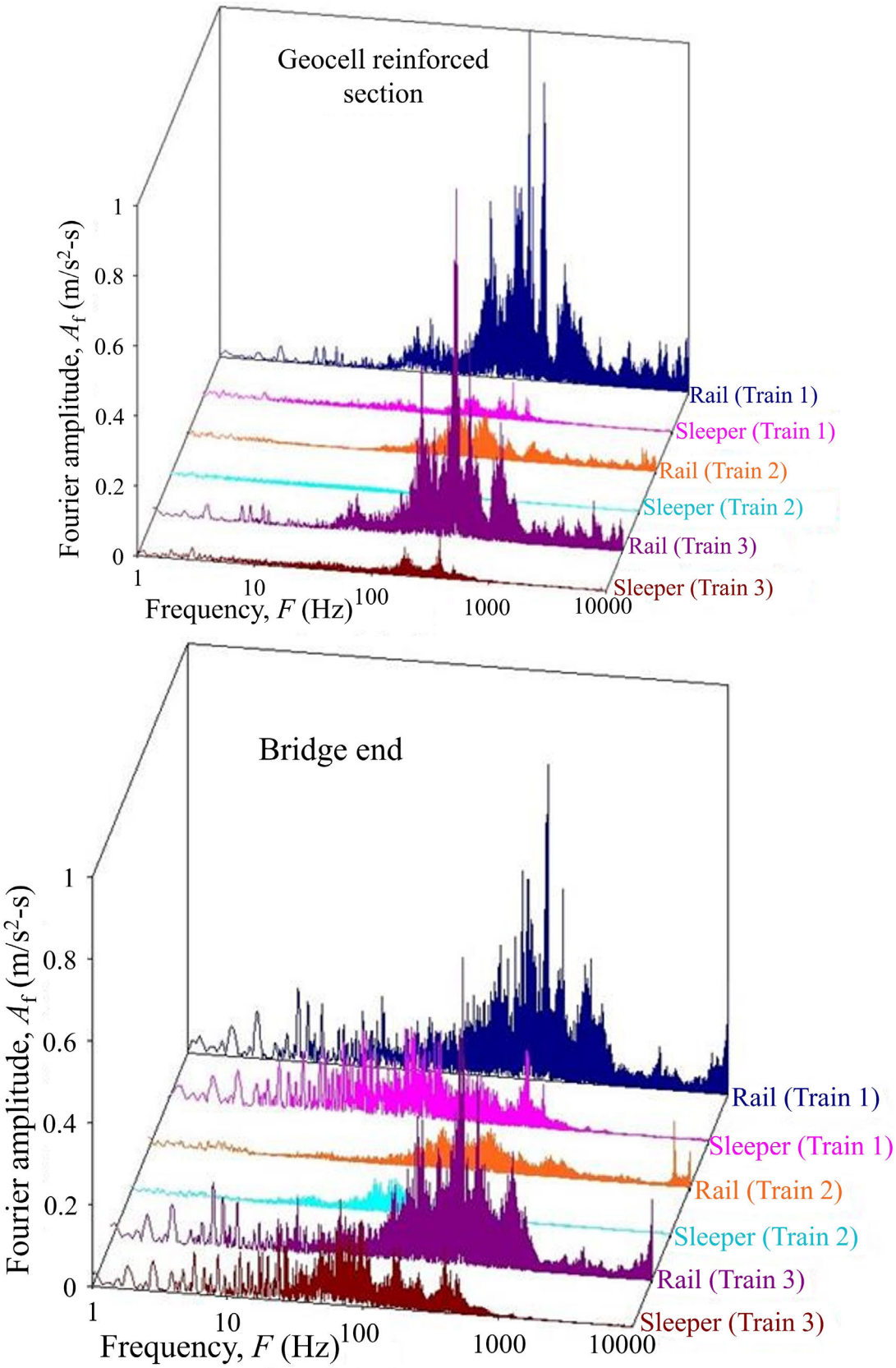

Figure 6.7 Fourier amplitude spectrum for field accelerometer data recorded in the geocell reinforced section and at the bridge end

[adapted from Kaewunruen et al. (2016)]

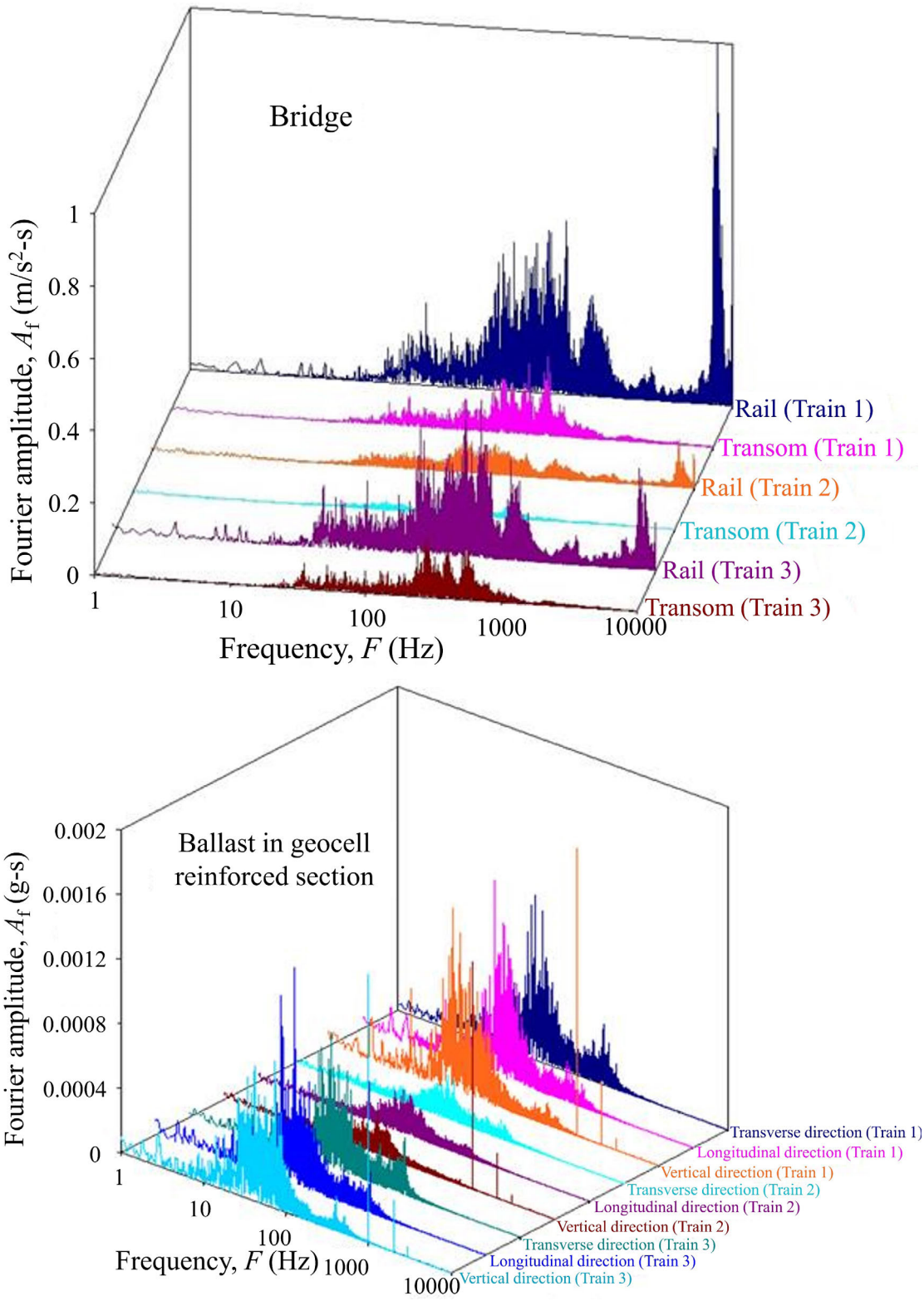

Figure 6.8 Fourier amplitude spectrum for field accelerometer data recorded at the bridge and the ballast in geocell reinforced section
[adapted from Kaewunruen et al. (2016)]

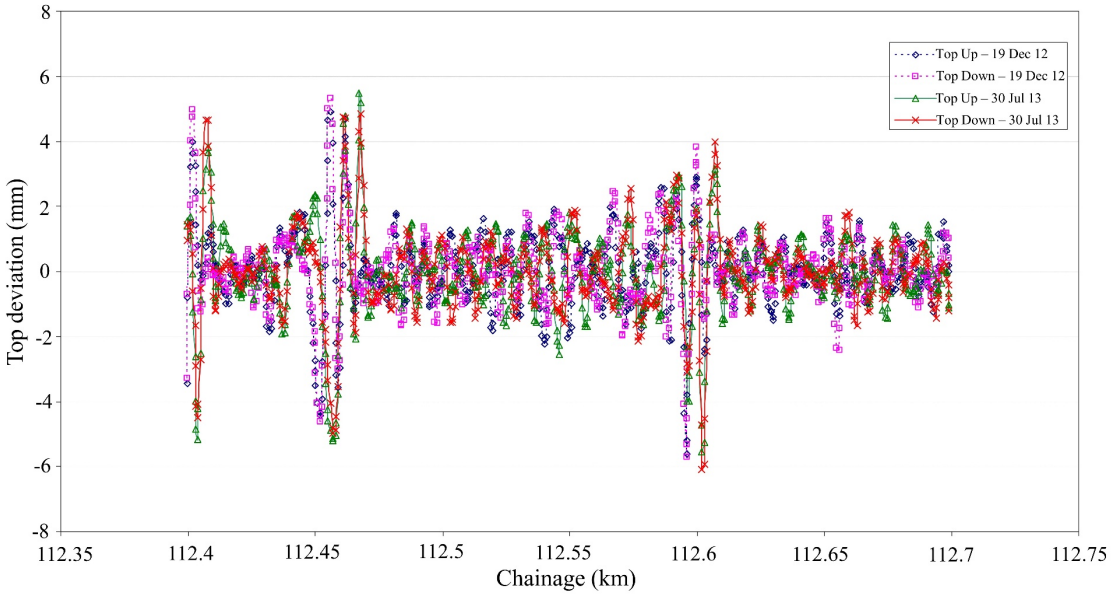

Figure 6.9 Variation in track geometry data along the rail bridge after the construction of the transition zone
[adapted from Kaewunruen et al. (2016)]

Thus, the geocell reinforcement possesses enormous applications in the railway tracks. Recently, the industry guidelines such as ARTC RTS 3430 (Australian Rail Track Corporation 2006) have recommended using geocell immediately below the ballast layer to stabilise the subgrade with a California Bearing Ratio (CBR) value of 1 or less. While Australia's coastal zone holds tremendous national significance, it also suffers from thick deposits of soft compressible clays. In view of this, ARTC recommendation is a testimony of interest among railway industries for the dissemination of geocell technology in Australasian track practice.

The subsequent section of this chapter deals with the development of a mathematical model that can predict the additional confinement provided by the geoinclusions under general loading conditions (or a 3D stress state). This is because the geoinclusion is likely to be subjected to a 3D stress state in a railway track.

6.6 Evaluation of Additional Confinement for 3D Geoinclusions under General Stress State

6.6.1 General

The lateral spreading of UGM under train-induced loading poses a severe challenge to the stability of the ballasted railway tracks (Selig & Waters 1994). This lateral movement is often associated with insufficient confinement of UGM layers overlying stiff subgrade soils (Sun et al. 2018). **Figure 6.10(a)** shows the loss in track geometry due to the lateral spreading of UGM under the train traffic-induced loads. The 3D cellular geoinclusions such as geocells and scrap rubber tyres can be employed in the ballasted railway tracks to provide additional confinement and consequently improve the track stability. As shown in **Figure 6.10(b)**, these cellular geoinclusions surround the UGM and create a stiff structure that resists the lateral spreading of UGM (Koerner 2012). Consequently, the loss in track geometry can be minimised.

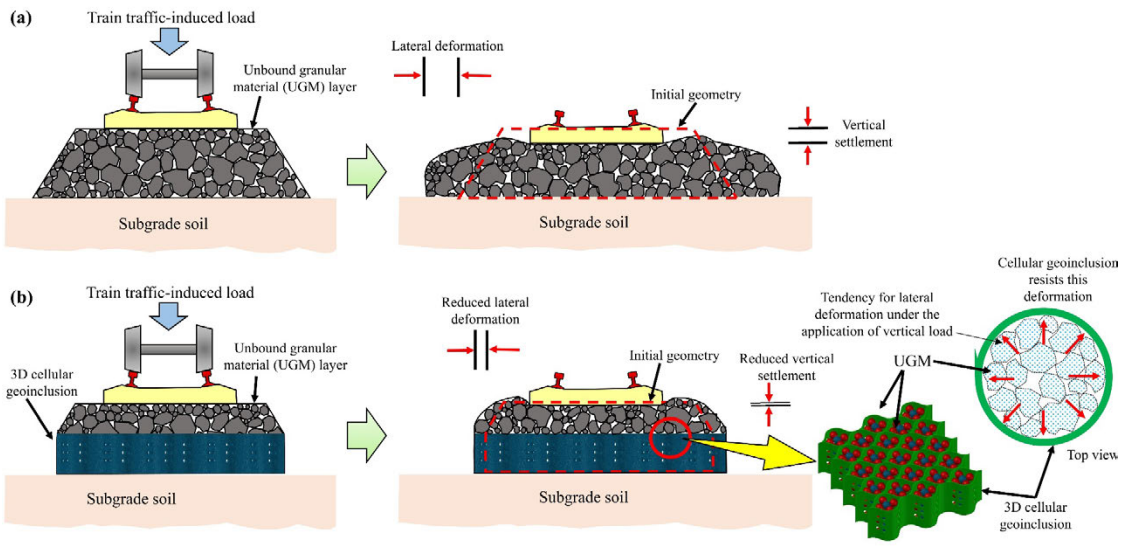

Figure 6.10 The behaviour of railway embankment under train traffic-induced loads: **(a)** without cellular geoinclusion; **(b)** with cellular geoinclusion

The 3D cellular geoinclusions are increasingly being used to improve the mechanical properties of granular infill materials. These geoinclusions provide all-around confinement to the infill soil and consequently, prevent its lateral spreading under loads (Zhou & Wen 2008; Leshchinsky & Ling 2013a). The investigations in the past have demonstrated the beneficial role of geocells (e.g., Raymond 2001; Satyal et al. 2018) and scrap tyres (e.g., Forsyth & Egan 1976; Garga & O'Shaughnessy 2000; Indraratna et al.

2017) in improving the stability of railway tracks and embankments. However, the lack of a well-established method to evaluate the magnitude of additional confinement provided by these geoinclusions has limited their application in the railway tracks.

An insight into the load transfer mechanism, quantification of the benefits and the full-scale performance data is inevitable to develop the design methods for cellular geoinclusions in railway applications. Although experimental and field studies are reliable techniques to gain insight into the behaviour of 3D artificial inclusions, these investigations require a considerable amount of time and efforts. On the other hand, the analytical and numerical simulations offer cost-effective alternatives to study and predict the response of the cellular geoinclusion reinforced soil. Therefore, researchers have conducted 2D (e.g., Bathurst & Knight 1998) and 3D numerical analyses (e.g., Han et al. 2008; Leshchinsky & Ling 2013a; Leshchinsky & Ling 2013b; Liu et al. 2018) on geoinclusion reinforced soil and have reported that the artificial inclusions significantly improve the strength and stiffness of the infill soil. However, the magnitude of improvement or modification depends on the stress state, properties of the infill and the geoinclusions.

Several researchers have attempted to evaluate the extra confinement offered by the cellular geoinclusions under static (Bathurst & Rajagopal 1993; Rajagopal et al. 1999) and cyclic or repeated loading conditions (Yang & Han 2013; Indraratna et al. 2015). These models are applicable to the 2D (plane-strain or axisymmetric) stress state. However, the 3D cellular geosynthetics are more likely to be subjected to a general stress state (3D) in a real track (e.g., at turnouts, intersections). Therefore, the additional confinement provided by the cellular geoinclusions under the general stress state may significantly differ from the plane-strain or triaxial (axisymmetric) stress state.

This section of the chapter describes the theoretical development of a semi-empirical model for evaluating the additional confinement provided by cellular geoinclusions under the 3D stress state. A parametric study is conducted to investigate the influence of infill soil properties, geoinclusion type and stress levels on additional confinement. Moreover, the proposed model is validated against the experimental data available in the literature.

This study is inevitable for assessing the performance of cellular geoinclusion-stabilised infills under the 3D stress state resembling actual track environment.

6.6.2 Development of Model

6.6.2.1 General Loading Condition

When the cellular geoinclusion-reinforced UGM is loaded vertically, the infill material deforms in vertical and lateral directions. The geoinclusion resists the lateral deformation of the infill material, which generate circumferential stresses (tension) along its periphery. These circumferential stresses provide additional confinement to the infill. The magnitude of additional confinement can be evaluated using the hoop tension theory as:

$$\Delta\sigma_2' = \frac{2\sigma_{C,2}t_g}{D_g} \qquad 6.7(a)$$

$$\Delta\sigma_3' = \frac{2\sigma_{C,3}t_g}{D_g} \qquad 6.7(b)$$

where $\Delta\sigma'_2$ and $\Delta\sigma'_3$ are the additional confining pressures in the direction of intermediate (σ'_2) and minor principal stresses (σ'_3), respectively; $\sigma_{C,2}$ and $\sigma_{C,3}$ are the circumferential stresses in the direction of σ'_2 and σ'_3, respectively; D_g and t_g are diameter and thickness of geoinclusion, respectively. The derivation of Equations 6.7(a) and 6.7(b) is given in APPENDIX I.

The circumferential stress is determined using Hooke's law (Timoshenko & Goodier 1970):

$$\sigma_C = \frac{M_m}{t_g}\left[\frac{(1-\nu_m)\varepsilon_c + \nu_m\varepsilon_r}{(1+\nu_m)(1-2\nu_m)}\right] \qquad 6.8$$

where ε_c and ε_r are circumferential and radial strains in the geoinclusion, respectively.

Figures 6.11(a), **6.11(b)** and **6.11(c)** show the deformation profiles of the cellular geoinclusions for general ($\sigma'_1 \neq \sigma'_2 \neq \sigma'_3$ and $\varepsilon_2 \neq \varepsilon_3 \neq 0$), plane-strain ($\sigma'_1 \neq \sigma'_2 \neq \sigma'_3$ and $\varepsilon_2 = 0$) and axisymmetric stress state ($\sigma'_1 \neq \sigma'_2 = \sigma'_3$ and $\varepsilon_2 = \varepsilon_3$), respectively. In general loading condition, the geoinclusion-reinforced soil is subjected to a 3D stress state. In other words, under the general loading condition, all the three principal stresses or strains can

vary independently. Assuming that the geoinclusion deforms as an ellipse with a uniform tensile stress distribution along its height, the additional confinement can be calculated as (combining Equations 6.7 and 6.8):

$$\Delta\sigma_2' = -\frac{2M_m}{D_g}\left[\frac{(1-\nu_m)k_c+\nu_m}{(1+\nu_m)(1-2\nu_m)}\right]\varepsilon_2 \qquad 6.9(a)$$

$$\Delta\sigma_3' = -\frac{2M_m}{D_g}\left[\frac{(1-\nu_m)k_c+\nu_m}{(1+\nu_m)(1-2\nu_m)}\right]\varepsilon_3 \qquad 6.9(b)$$

where ε_2 and ε_3 are the intermediate and minor principal strains in infill (assuming that the geocell and infill soil deform together).

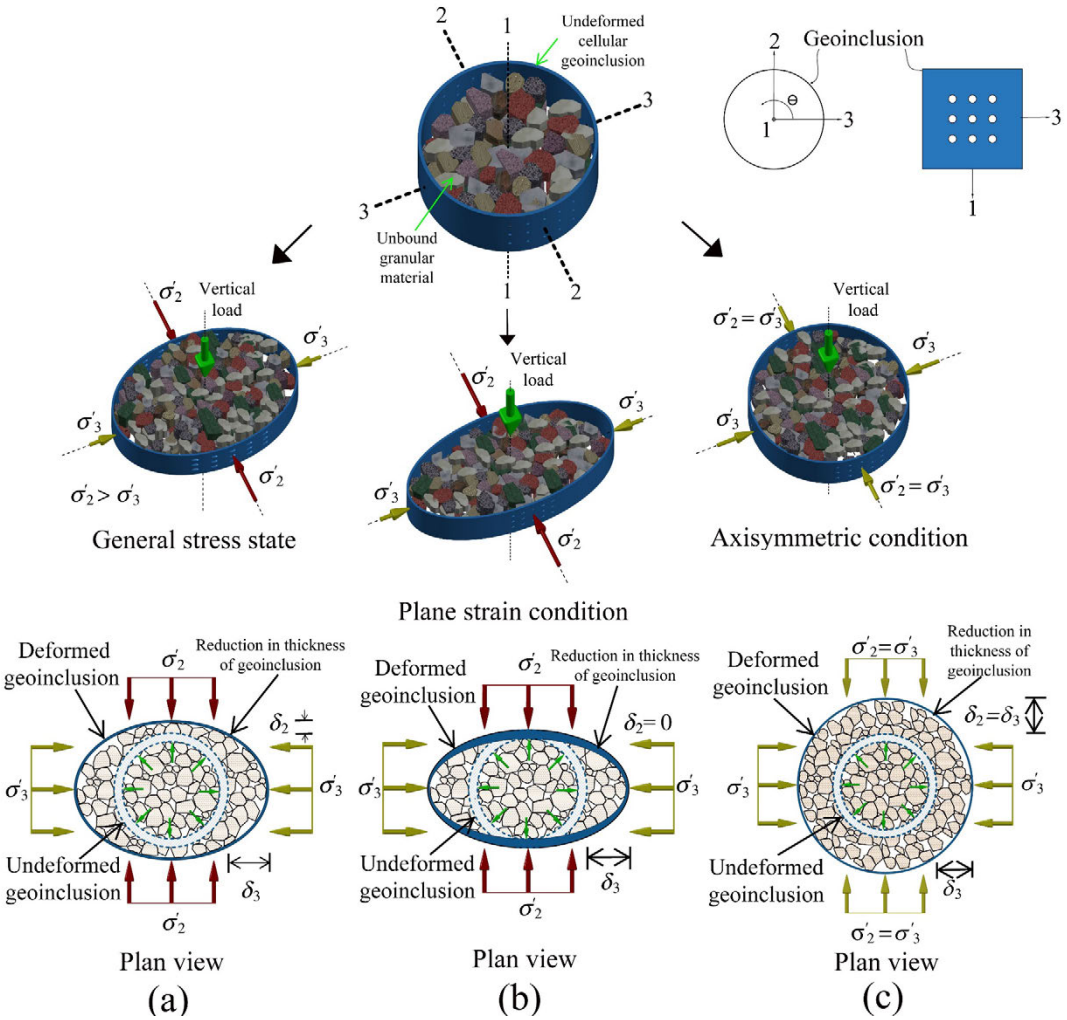

Figure 6.11 Deformation of cellular geoinclusion under different stress states: **(a)** general; **(b)** plane-strain; **(c)** axisymmetric

Equations 6.9(a) and 6.9(b) can be employed to calculate the additional confinement provided by cellular geoinclusions under both static and repeated loading conditions. The parameters M_m, D_g, and v_m are the material properties of geoinclusions, and these can be evaluated easily. Moreover, the lateral principal strains (ε_2 and ε_3) in UGM usually comprises recoverable and irrecoverable components that can be calculated using the procedure described in the subsequent sections. The cellular geoinclusion and the infill soil deform together under the applied loading. The irrecoverable component of deformation for the infill soil is primarily attributed to the reorientation or rearrangement of the particles to a denser packing arrangement under loading. The geoinclusion undergoes recoverable deformation until the yield strain of the geoinclusion material is reached. However, the infill deformation usually comprises both recoverable and irrecoverable components due to the elastoplastic nature of granular materials.

Recoverable Deformation of Infill.

The recoverable strains for the static loading case can be determined as follows (Timoshenko & Goodier 1970):

$$\varepsilon_2^e = \frac{1}{E}[\sigma'_2 - \nu_i(\sigma'_1 + \sigma'_3)] \quad 6.10(a)$$

$$\varepsilon_3^e = \frac{1}{E}[\sigma'_3 - \nu_i(\sigma'_1 + \sigma'_2)] \quad 6.10(b)$$

where $\varepsilon_2{}^e$ and $\varepsilon_3{}^e$ are the recoverable components of intermediate and minor principal strains, respectively; σ'_1, σ'_2 and σ'_3 are the major, intermediate and minor principal stresses; v_i is the Poisson's ratio of the infill material; E is Young's modulus of the infill material.

Similarly, for the repeated loading condition:

$$\varepsilon_2^e = \frac{\sigma_{cyc}}{E_R}\left[\frac{\sigma'_2 - \nu_i(\sigma'_1 + \sigma'_3)}{\sigma'_1 - \nu_i(\sigma'_2 + \sigma'_3)}\right] \quad 6.11(a)$$

$$\varepsilon_3^e = \frac{\sigma_{cyc}}{E_R}\left[\frac{\sigma'_3 - \nu_i(\sigma'_1 + \sigma'_2)}{\sigma'_1 - \nu_i(\sigma'_2 + \sigma'_3)}\right] \quad 6.11(b)$$

Irrecoverable Deformation of Infill.

The irrecoverable components of intermediate and minor principal strains (ε_2^p, ε_3^p) can be evaluated by using the 3D stress-dilatancy relationship (Schanz & Vermeer 1996). This relationship is given as:

$$\frac{1}{K} = \left(\frac{\sigma_3'}{\sigma_1'}\right)\left(-\frac{d\varepsilon_3^p}{d\varepsilon_1^p}\right) + \left(\frac{\sigma_2'}{\sigma_1'}\right)\left(-\frac{d\varepsilon_2^p}{d\varepsilon_1^p}\right) \qquad 6.12$$

where $d\varepsilon_1^p$, $d\varepsilon_2^p$, $d\varepsilon_3^p$ are the irrecoverable major, intermediate and minor principal strain increments, respectively; K is the coefficient representing the internal friction [$K = (1+\sin\varphi'_m)/(1-\sin\varphi'_m)$]; φ'_m is the mobilised friction angle.

On rearranging Equation 6.12, $d\varepsilon_2^p$ and $d\varepsilon_3^p$ can be expressed in terms of $d\varepsilon_1^p$ as:

$$-\frac{d\varepsilon_2^p}{d\varepsilon_1^p} = \frac{(1-R_s)^{-1}}{b}\left(1 - D_r - \frac{R_s}{K}\right) \qquad 6.13(a)$$

$$-\frac{d\varepsilon_3^p}{d\varepsilon_1^p} = \left[1 - \frac{(1-R_s)^{-1}}{b}\right]\left\{1 - D_r - \frac{[R_s^{-1} + b(1-R_s^{-1})]^{-1}}{K}\right\} \qquad 6.13(b)$$

where D_r is the dilatancy rate ($d\varepsilon_v^p/d\varepsilon_1^p$); R_s is the stress ratio (σ'_1/σ'_3); b is the intermediate principal stress ratio [$b=(\sigma'_2-\sigma'_3)/(\sigma'_1-\sigma'_3)$].

Thus, ε_2^p and ε_3^p can be calculated by integrating Equations 6.13(a) and 6.13(b), respectively.

$$\varepsilon_2^p = -\int \frac{(1-R_s)^{-1}}{b}\left(1 - D_r - \frac{R_s}{K}\right) d\varepsilon_1^p \qquad 6.14(a)$$

$$\varepsilon_3^p = -\int \left[1 - \frac{(1-R_s)^{-1}}{b}\right]\left\{1 - D_r - \frac{[R_s^{-1} + b(1-R_s^{-1})]^{-1}}{K}\right\} d\varepsilon_1^p \qquad 6.14(b)$$

Additional Confinement.

The additional confinement ($\Delta\sigma'_2$ and $\Delta\sigma'_3$) provided by the cellular geoinclusions for static loading condition (loading in the vertical direction) can be evaluated by combining Equations 6.9(a), 6.9(b), 6.10(a), 6.10(b), 6.14(a) and 6.14(b).

$$\Delta\sigma_2' = -\frac{2M_{\mathrm{m}}}{D_{\mathrm{g}}}\left[\frac{(1-\nu_{\mathrm{m}})k_{\mathrm{c}}+\nu_{\mathrm{m}}}{(1+\nu_{\mathrm{m}})(1-2\nu_{\mathrm{m}})}\right]\left\{\frac{\sigma_3'}{E}[1-b(1-R_{\mathrm{s}})-\nu_{\mathrm{i}}(1+R_{\mathrm{s}})] - \int\frac{(1-R_{\mathrm{s}})^{-1}}{b}\left[1-D_{\mathrm{r}}-\frac{R_{\mathrm{s}}}{K}\right]d\varepsilon_1^{p}\right\} \quad 6.15(a)$$

$$\Delta\sigma_3' = -\frac{2M_{\mathrm{m}}}{D_{\mathrm{g}}}\left[\frac{(1-\nu_{\mathrm{m}})k_{\mathrm{c}}+\nu_{\mathrm{m}}}{(1+\nu_{\mathrm{m}})(1-2\nu_{\mathrm{m}})}\right]\left\{\frac{\sigma_3'}{E}[1+\nu_{\mathrm{i}}b(1-R_{\mathrm{s}})-\nu_{\mathrm{i}}(1+R_{\mathrm{s}})] - \int\left[1-\frac{(1-R_{\mathrm{s}})^{-1}}{b}\right]\left\{1-D_{\mathrm{r}}-\frac{[R_{\mathrm{s}}^{-1}+b(1-R_{\mathrm{s}}^{-1})]^{-1}}{K}\right\}d\varepsilon_1^{p}\right\} \quad 6.15(b)$$

Thus, for static loading conditions, the additional confinement at a given value of major principal strain (ε_1) can be calculated by using Equations 6.15(a) and 6.15(b). However, under repeated or cyclic vertical loading conditions, the strain in UGM also varies with the number of load cycles (Dahlberg 2001). Several models have been developed to predict the behaviour of UGM under cyclic loading conditions (Lekarp et al. 2000). In the present study, a power model has been used which incorporates the influence of the stress state and loading conditions on the irrecoverable deformation of UGM (e.g., Puppala et al. 2009).

$$\varepsilon_1{}^{p} = k_1\left(\frac{\sigma_{\mathrm{oct}}}{P_{\mathrm{a}}}\right)^{k_2}\left(\frac{\tau_{\mathrm{oct}}}{P_{\mathrm{a}}}\right)^{k_3}N^{k_4} \quad 6.16$$

where k_1, k_2, k_3, k_4 are the empirical parameters. The parameter k_1 represents the influence of the infill type on the magnitude of $\varepsilon_1{}^{\mathrm{p}}$ corresponding to the first load cycle. Parameters k_2 and k_3 represent the influence of octahedral normal and shear stresses on the magnitude of $\varepsilon_1{}^{\mathrm{p}}$ corresponding to the first load cycle. The parameter k_4 shows the dependency of $\varepsilon_1{}^{\mathrm{p}}$ on the number of load cycles. It governs the variation of $\varepsilon_1{}^{\mathrm{p}}$ with N.

Differentiating Equation 6.16 with respect to N and substituting the value of $d\varepsilon_1{}^{p}$ in Equations 6.14(a) and 6.14(b) gives:

$$\varepsilon_2^{p} = -\int_0^{N_{\mathrm{lim}}}\frac{k_1k_4(1-R_{\mathrm{s}})^{-1}}{b}\left[1-D_{\mathrm{r}}-\frac{R_{\mathrm{s}}}{K}\right]\left(\frac{\sigma_{\mathrm{oct}}}{P_{\mathrm{a}}}\right)^{k_2}\left(\frac{\tau_{\mathrm{oct}}}{P_{\mathrm{a}}}\right)^{k_3}N^{k_4-1}\,dN \quad 6.17(a)$$

$$\varepsilon_3^p = -\int_0^{N_{\lim}} k_1 k_4 \left[1 - \frac{(1-R_s)^{-1}}{b}\right]\left\{1 - D_r - \frac{[R_s^{-1} + b(1-R_s^{-1})]^{-1}}{K}\right\} \times \left(\frac{\sigma_{oct}}{P_a}\right)^{k_2}\left(\frac{\tau_{oct}}{P_a}\right)^{k_3} N^{k_4-1} dN \quad 6.17(b)$$

Similarly, Equations 6.11(a) and 6.11(b) can be modified to incorporate the variation of E_R with N:

$$\varepsilon_2^e = \int_0^{N_{\lim}} \left\{\sigma_{cyc}\left[\frac{\sigma_3' + b(\sigma_1' - \sigma_3') - \nu_i(\sigma_1' + \sigma_3')}{\sigma_1' - \nu_i b(\sigma_1' - \sigma_3') - 2\nu_i\sigma_3'}\right]\left(\frac{dE_R^{-1}}{dN}\right)\right\} dN \quad 6.18(a)$$

$$\varepsilon_3^e = \int_0^{N_{\lim}} \left\{\sigma_{cyc}\left[\frac{\sigma_3' - \nu_i(\sigma_1' + \sigma_3') - \nu_i b(\sigma_1' - \sigma_3')}{\sigma_1' - \nu_i b(\sigma_1' - \sigma_3') - 2\nu_i\sigma_3'}\right]\left(\frac{dE_R^{-1}}{dN}\right)\right\} dN \quad 6.18(b)$$

Therefore, the additional confinement ($\Delta\sigma'_2$ and $\Delta\sigma'_3$) offered by the geoinclusions for repeated loading condition can be evaluated by combining Equations 6.9(a), 6.9(b), 6.17(a), 6.17(b), 6.18(a) and 6.18(b).

$$\Delta\sigma_2' = \int_0^{N_{\lim}} -\frac{2M_m}{D_g}\left[\frac{(1-\nu_m)k_c + \nu_m}{(1+\nu_m)(1-2\nu_m)}\right]\left\{\sigma_{cyc}\left[\frac{1 - b(1-R_s) - \nu_i(1+R_s)}{R_s + \nu_i b(1-R_s) - 2\nu_i}\right]\left(\frac{dE_R^{-1}}{dN}\right) - \frac{k_1 k_4 (1-R_s)^{-1}}{b}\left[1 - D_r - \frac{R_s}{K}\right]\left(\frac{\sigma_{oct}}{P_a}\right)^{k_2}\left(\frac{\tau_{oct}}{P_a}\right)^{k_3} N^{k_4-1}\right\} dN \quad 6.19(a)$$

$$\Delta\sigma_3' = \int_0^{N_{\lim}} -\frac{2M_m}{D_g}\left[\frac{(1-\nu_m)k_c + \nu_m}{(1+\nu_m)(1-2\nu_m)}\right]\left\{\sigma_{cyc}\left[\frac{1 + \nu_i b(1-R_s) - \nu_i(1+R_s)}{R_s + \nu_i b(1-R_s) - 2\nu_i}\right]\left(\frac{dE_R^{-1}}{dN}\right) - k_1 k_4\left[1 - \frac{(1-R_s)^{-1}}{b}\right]\left\{1 - D_r - \frac{[R_s^{-1} + b(1-R_s^{-1})]^{-1}}{K}\right\}\left(\frac{\sigma_{oct}}{P_a}\right)^{k_2}\left(\frac{\tau_{oct}}{P_a}\right)^{k_3} N^{k_4-1}\right\} dN \quad 6.19(b)$$

Thus, for repeated loading conditions, the extra confinement offered by geoinclusions after the completion of a given number of load cycles (N_{lim}), can be calculated by using

Equations 6.19(a) and 6.19(b). The proposed model can also be simplified to cater for the axisymmetric and the plane-strain cases.

6.6.2.2 Axisymmetric Condition

For the axisymmetric condition [$\sigma'_2 = \sigma'_3$ (or $b = 0$), $d\varepsilon_2 = d\varepsilon_3$ and $k_c = 1$], Equation 6.13(a) is deduced to:

$$R_s = K(1 - D_r) \tag{6.20}$$

Upon simplification, Equation 6.20 becomes

$$d\varepsilon_3^p = -d\varepsilon_1^p \frac{R_s}{2K} \tag{6.21}$$

Thus, $\Delta\sigma'_3$ for the axisymmetric condition can be given by:

$$\Delta\sigma'_3 = \int_0^{N_{lim}} -\frac{2M_m}{D_g}\left[\frac{1}{(1+\nu_m)(1-2\nu_m)}\right]\left\{\sigma_{cyc}\left[\frac{1-\nu_i(1+R_s)}{R_s-2\nu_i}\right]\left(\frac{dE_R^{-1}}{dN}\right) - \frac{k_1 k_4 R_s}{2K}\left(\frac{\sigma_{oct}}{P_a}\right)^{k_2}\left(\frac{\tau_{oct}}{P_a}\right)^{k_3} N^{k_4-1}\right\} dN \tag{6.22}$$

6.6.2.3 Plane-Strain Condition

For the plane-strain condition ($d\varepsilon_2 = 0$), Equation 6.13(a) can be simplified as:

$$d\varepsilon_3^p = -d\varepsilon_1^p \frac{R_s}{K} \tag{6.23}$$

The $\Delta\sigma'_3$ for the plane-strain condition can thus be expressed as:

$$\Delta\sigma'_3 = \int_0^{N_{lim}} -\frac{2M_m}{D_g}\left[\frac{(1-\nu_m)k_c+\nu_m}{(1+\nu_m)(1-2\nu_m)}\right]\left\{\sigma_{cyc}\left[\frac{(1-\nu_i)-\nu_i R_s}{R_s(1-\nu_i)-\nu_i}\right]\left(\frac{dE_R^{-1}}{dN}\right) - \frac{k_1 k_4 R_s}{K}\left(\frac{\sigma_{oct}}{P_a}\right)^{k_2}\left(\frac{\tau_{oct}}{P_a}\right)^{k_3} N^{k_4-1}\right\} dN \tag{6.24}$$

6.6.3 Identification of Model Parameters

The present model comprises the following parameters: M_m, D_g, ν_m, b, E_R, E, ν_i, k_1, k_2, k_3, k_4, φ'_m, and D_r. The first three parameters are the geoinclusion properties. The parameter

b depends on the external loading conditions. The parameters E_R, E and ν_i for a particular cellular geoinclusion reinforced UGM can be determined from conventional laboratory experiments. The empirical parameters k_1, k_2, k_3 and k_4 can be determined by fitting the experimental curves of irrecoverable vertical strain with N for reinforced UGM at different loading conditions. Furthermore, parameters φ'_m and D_r can be determined by conducting true-triaxial tests ($\sigma'_1 \neq \sigma'_2 \neq \sigma'_3$) on geoinclusion reinforced UGM. Moreover, φ'_m and D_r depend on the parameter b (Wang & Lade 2001). However, a unique relationship between these parameters is not yet established. Therefore, the values of b, φ'_m and D_r are varied to investigate their influence on the additional confinement.

6.6.4 Results and Discussion

Using the present approach, the influence of infill properties, stress levels and geoinclusion type on additional confinement are investigated. **Table 6.2** lists the parameters used in the analysis. The results are expressed in terms of normalised additional confinement ($k_{\sigma,2} = \Delta\sigma'_2/\sigma'_2$ and $k_{\sigma,3} = \Delta\sigma'_3/\sigma'_3$) and additional confinement ratio (ACR). The ACR is the ratio of extra confinement offered by the geoinclusions in lateral orthogonal directions (i.e., $\Delta\sigma'_2/\Delta\sigma'_3$). These normalised ratios are used to present the results in a concise form. Moreover, the use of ACR allows efficient comparison of $\Delta\sigma'_2$ with $\Delta\sigma'_3$. The value of ACR ranges between 0 and 1 corresponding to the cases when $\Delta\sigma'_2 = 0$ and $\Delta\sigma'_2 = \Delta\sigma'_3$, respectively.

6.6.4.1 Influence of Infill Properties and Stress Levels

Figure 6.12(a) shows the variation of ACR with the mobilised friction angle (φ'_m) and dilatancy rate (D_r). It can be observed that ACR increases with a decrease in D_r (e.g. 370% increment when D_r decreases from -1 to -0.2, for $\varphi'_m = 40°$). Moreover, it decreases with an increase in φ'_m for a particular value of D_r (e.g. 98% reduction when φ'_m increases from 40° to 60° for D_r = -0.2). This variation is probably due to a reduction in ε_2 with an increase in D_r and K [refer to Equation 6.14(a)]. Consequently, a smaller magnitude of confinement ($\Delta\sigma'_2$) is mobilised in the direction of σ'_2 for higher values of D_r and K. Thus, a weak infill (exhibited by small φ'_m) with a smaller D_r may mobilise more confinement, $\Delta\sigma'_2$, than a strong infill with a greater D_r (for a particular value of b). On the contrary, ε_3 increases with an increase in D_r and K [refer to Equation 6.14(b)]. This increases the

magnitude of $\Delta\sigma'_3$. Therefore, an optimum value of φ'_m and D may be required to derive maximum benefits from geoinclusion reinforcement.

Table 6.2 Input parameters for the parametric study

Parameter	Value
Test type	Repeated load test
Loading condition	General
Geoinclusion material	HDPE (unless stated otherwise)
Infill material	Subballast
Frequency, F (Hz)	10
D_g (m)	0.24, 0.54 (for rubber tyre)
σ'_1 (kPa)	160
σ'_3 (kPa)	15, 20, 25, 30
σ_{cyc} (kPa)	145, 140, 135, 130
P_a (kPa)	101.325
N_{lim}	500,000
ν_m	0.3
ν_i	0.35
D_r*	-0.2, -0.4, -0.6, -0.8, -1.0
k_1	19.12
k_2	-3
k_3	8.42
k_4	0.129
φ'_m (°)	40, 45, 50, 55, 60

*Negative sign is assigned for dilative behaviour; HDPE: High-density polyethylene.

Nevertheless, this variation also depends on stress levels. **Figure 6.12(b)** shows the influence of parameter b on ACR. It is observed that ACR decreases with an increase in b (e.g. 92% reduction when b increases from 0.1 to 0.3 for $D_r = –0.2$). This is because ε_2 reduces with an increase in b. As a consequence, the extra confinement $\Delta\sigma'_2$ undergoes substantial reduction. Thus, σ'_2 significantly influences the magnitude of extra confinement offered by the geoinclusion.

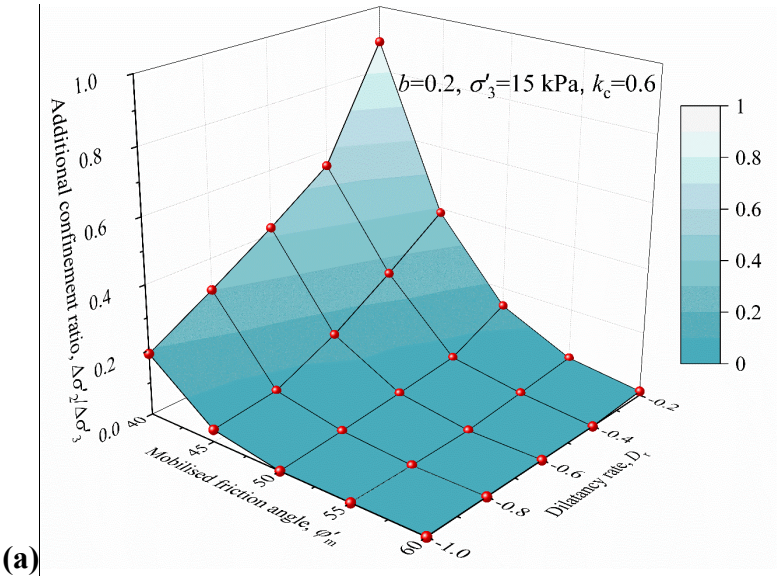

(a)

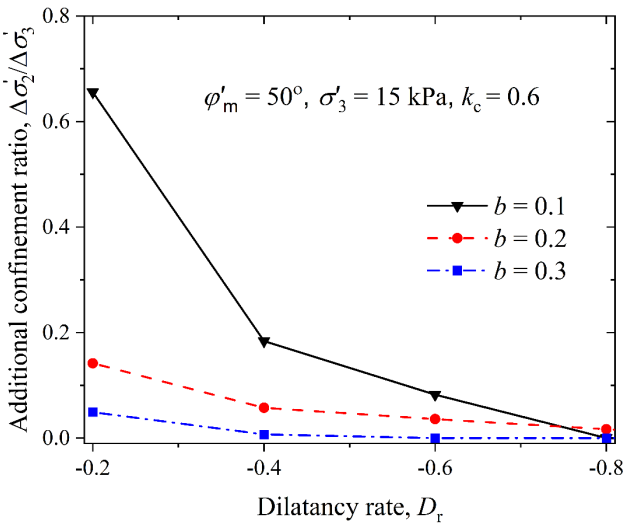

(b)

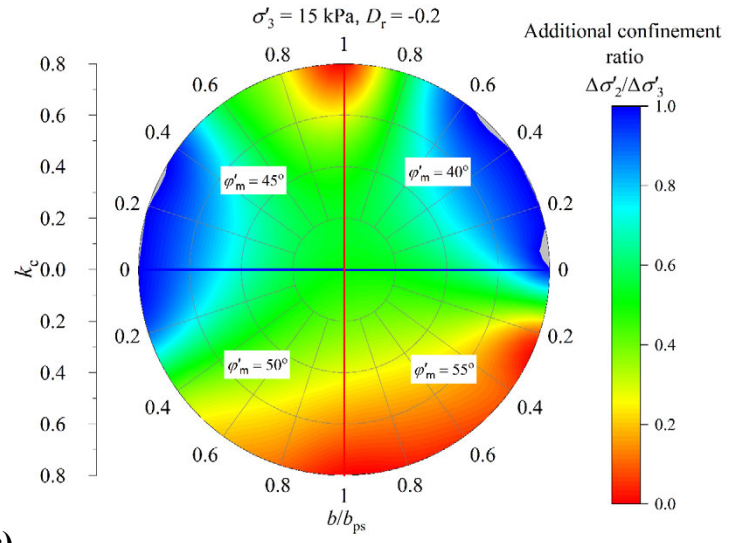

(c)

Figure 6.12 Variation of additional confinement ratio (ACR) with **(a)** mobilised friction angle (φ'_m) and dilatancy rate (D_r); **(b)** dilatancy rate (D_r) for b = 0.1, 0.2 and 0.3; **(c)** b/b_{ps} ratio and φ'_m

It can be noted that parameter b at the plane-strain condition (b_{ps}) for the preceding case is 0.32. Therefore, the magnitude of ACR is nearly equal to 0 for b = 0.3. Moreover, ACR becomes 0 for $b \geq b_{ps}$ because ε_2 becomes compressive if b exceeds b_{ps}. Due to a lack of experimental or field data, it is very difficult at this stage to visualise the deformation behaviour of geoinclusion once b exceeds b_{ps}. Therefore, b has been normalised with b_{ps} in the subsequent section to show its influence on additional confinement. **Figure 6.12(c)** shows the polar contour plot of ACR for σ'_3 = 15 kPa and D_r = –0.2 to elucidate the influence of φ'_m and b/b_{ps} ratio on ACR. The radial and polar coordinates in the plot correspond to the values of parameters k_c and b/b_{ps} ratio, respectively. The four different sectors in the plot represent the ACR values for φ'_m = 40°, 45°, 50°, and 55°. The radial boundary of each sector is marked by the plane-strain (b/b_{ps} = 1) and the axisymmetric conditions (b/b_{ps} = 0). It can be observed that ACR decreases with an increase in b/b_{ps} and φ'_m. This may be attributed to the reduction in the magnitude of ε_2 with an increase in φ'_m and b/b_{ps}.

6.6.4.2 Influence of Geoinclusion Type

The geoinclusion type may influence the magnitude of additional confinement. Therefore, five different types of geoinclusion materials, namely, HDPE, woven coir geotextile, nonwoven polypropylene (PP) geotextile, rubber membrane (with three different thicknesses) and rubber tyre, have been used in the analysis. **Figure 6.13(a)** shows the load versus strain curves of the five materials obtained from tension tests (Henkel & Gilbert 1952; Koerner 2012; Biabani 2015; Indraratna et al. 2017; Lal et al. 2017). It can be observed that each material exhibits a distinct load-strain response. HDPE shows an elastic-perfectly plastic response with high initial modulus, while nonwoven PP geotextile shows a strain hardening response with progressively increasing modulus. The secant modulus of woven coir geotextile is initially intermediate to that of HDPE and nonwoven PP geotextile. However, after 12.5% strain, the secant modulus of coir geotextile exceeds the modulus of HDPE. Furthermore, the rubber tyre and rubber membranes have the maximum and minimum modulus among all the materials, respectively.

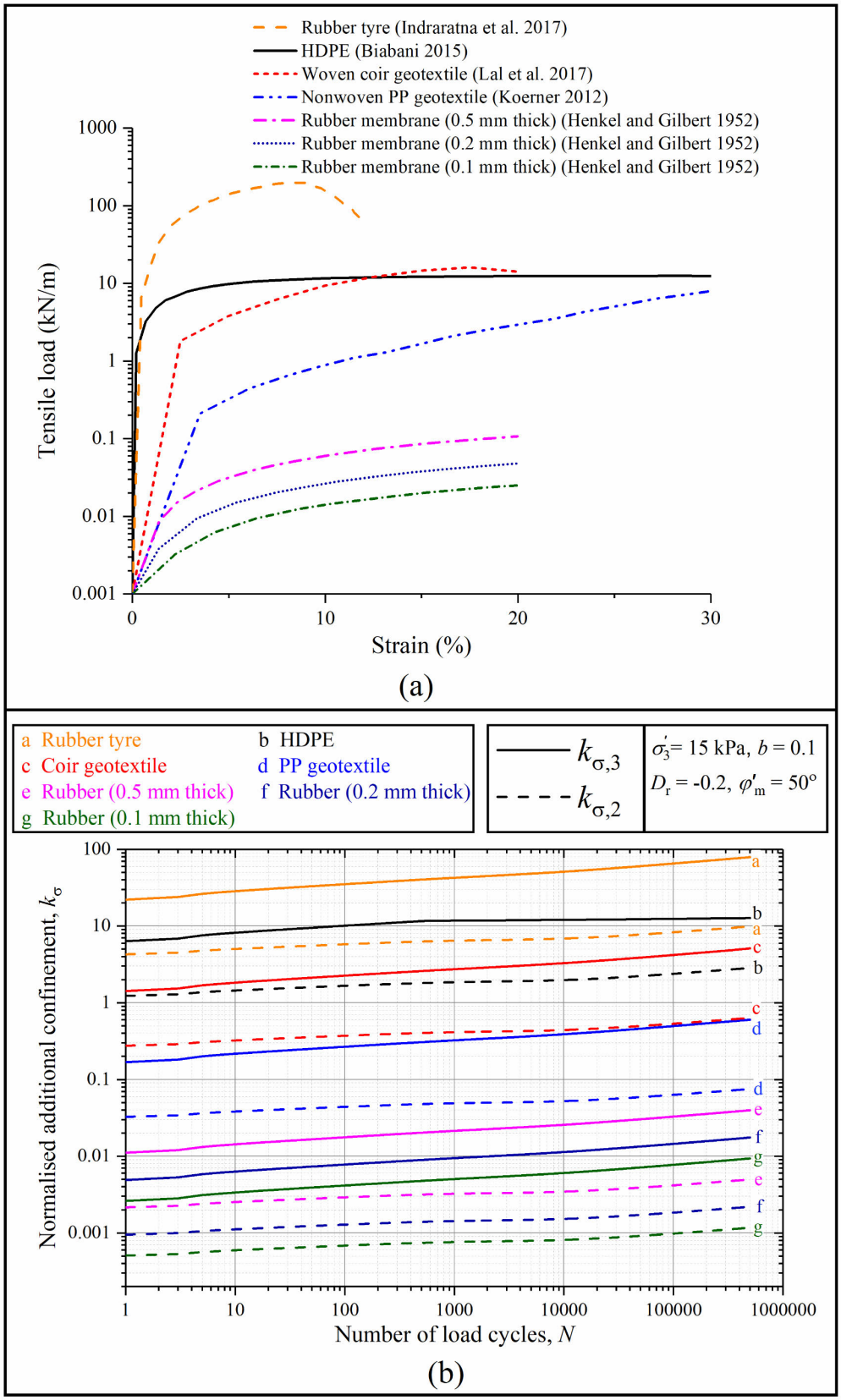

Figure 6.13 (a) Tensile load-strain curves for five different types of cellular geoinclusion materials; **(b)** variation of normalised additional confinement ($k_{\sigma,2}$ and $k_{\sigma,3}$) with the number of load cycles (N)

Figure 6.13(b) shows the variation of normalised additional confinement with N for the five different geoinclusion materials at σ'_3 = 15 kPa, b = 0.1, D_r = -0.2 and $\varphi'_m = 50^\circ$. It can be observed that the rubber tyre provides the maximum confinement to the infill in the direction of σ'_3. This is reasonable since the modulus of rubber tyre is the maximum among the five materials at a particular magnitude of strain. HDPE provides higher confinement than coir geotextile, PP geotextile and rubber membranes. However, if the mobilised strain increases beyond 12.5%, the magnitude of confinement provided by coir geotextile may exceed that provided by HDPE [refer to **Figure 6.13(a)**]. Nevertheless, the mobilised strain, in this case, is below 12.5%. Consequently, HDPE provides higher confinement than coir geotextile throughout the loading schedule. The extra confinement offered by PP geotextile and rubber membranes is very small as compared to the rubber tyre, HDPE and woven coir geotextile due to their low secant modulus. Similar behaviour is observed in the direction of σ'_2. The magnitude of $k_{\sigma,2}$ is the highest for rubber tyre, followed by HDPE, coir geotextile, PP geotextile and rubber membranes. However, $k_{\sigma,2}$ is smaller than $k_{\sigma,3}$ for all the materials. This is due to the mobilisation of a small magnitude of strain in the direction of σ'_2.

Hence, the additional confinement provided by the geoinclusion significantly depends on the type of the constituent material. Usually, the confinement increases with an increase in geoinclusion modulus. However, the selection of an appropriate geoinclusion must be based on its intended function and the scope of the project. Moreover, the additional confinement ($\Delta\sigma'_2$ and $\Delta\sigma'_3$) is not only directionally sensitive but also sensitive to parametric variations. Therefore, simplification of 3D into 2D (axisymmetric or plane-strain) stress state may result into either over-predictive or conservative estimates. Thus, the present model yields more accurate results as compared to the existing models.

In practice, the geoinclusion-stabilised soil is more likely to be subjected to a complex 3D stress state. The present model evaluates the extra confinement offered by the cellular geoinclusions in the directions of σ'_2 and σ'_3. Moreover, it can capture the variations in the confinement mobilised in the two orthogonal directions due to changes in stress levels, infill and geoinclusion properties. Thus, the model can also help in the selection of

adequate material parameters for deriving maximum potential benefits from geoinclusion reinforcement.

6.6.5 Model Validation

Limited laboratory or field data are available on the magnitude of additional confinement provided by the cellular geoinclusions in the 3D ($\sigma'_1 \neq \sigma'_2 \neq \sigma'_3$) loading conditions. Nevertheless, the present model is validated against the results of the static triaxial tests on geocell-reinforced soils conducted by Bathurst & Rajagopal (1993) and Rajagopal et al. (1999), and the repeated load triaxial tests conducted by Mengelt et al. (2006). **Table 6.3** lists the input parameters used in the predictions. **Figure 6.14(a)** compares the additional confinement calculated using the present model with the experimental data. It is observed that the predicted values vary by 1% to 20% from the experimental results.

The model is also used to predict the extra confinement offered by geocells for the plane-strain repeated load tests conducted by Indraratna et al. (2015). The values of the parameters used in the prediction are listed in **Table 6.3**. **Figure 6.14(b)** compares the predicted and experimentally observed results. The results are expressed in terms of normalised additional confinement ($k_{\sigma,3}$). The predicted results are in a good agreement with the experimental data. A slight deviation from the experimental data can occur if the value of modulus is arbitrarily selected. In fact, the modulus needs careful evaluation by conducting the tensile tests or junction peel tests. This is because, it depends on the type of test arrangement (i.e. specimen with or without welds) and the nature of the test (i.e. wide width, junction peel, split). Nevertheless, it is apparent that the present approach can provide reliable estimates of the extra confinement offered by geoinclusions.

6.6.6 Limitations and Future Scope

The limitations of the novel semi-empirical model are as follows:

- The additional confining pressure is assumed to be constant along the height of the geoinclusion as opposed to the actual non-uniform distribution.
- The bending of geoinclusions under the application of vertical loads is ignored.
- The shape of geoinclusions is assumed to be circular in contrast to their actual shape which can be a 3D honeycomb.

These limitations shall be addressed in future investigations.

Table 6.3 Parameters for predicting the additional confinement under the plane-strain and axisymmetric conditions

Parameter	Axisymmetric			Plane-strain
	Bathurst and Rajagopal (1993)	**Rajagopal et al. (1999)**	**Mengelt et al. (2006)**	**Indraratna et al. (2015)**
Infill material	Dense SS	Sand	Sand	Subballast
Geocell material	PE	PP-W, PP-NW	HDPE	HDPE
Frequency, F (Hz)	Not applicable	Not applicable	1	10–30
D_g (m)	0.2	0.1	0.25	0.24
σ'_1 (kPa)	1,050	550–860	25–100	166
σ'_3 (kPa)	25	100	1	5–30
N_{lim}	Not applicable	Not applicable	1,500	500,000
φ'_m (°)	72.5	44.1–52.4	67.4–78.6	Varies with N
E (MPa)	46.2	21.9–38.2	Not applicable	Not applicable
E_R (MPa)	Not applicable	Not applicable	16–41	Varies with N
v_m	0.30	0.30	0.30	0.30
v_i	0.35	0.35	0.35	0.35
k_c	1	1	1	0.075
k_1	Not applicable	Not applicable	Not applicable	19.12–72.17
k_2	Not applicable	Not applicable	Not applicable	-3
k_3	Not applicable	Not applicable	Not applicable	8.42
k_4	Not applicable	Not applicable	Not applicable	0.129–0.156

Note: Geocell modulus is the secant modulus corresponding to the magnitude of mobilised strain; SS = silica sand; PP-W = polypropylene woven geotextile; PP-NW = polypropylene nonwoven geotextile; PE = polyethylene.

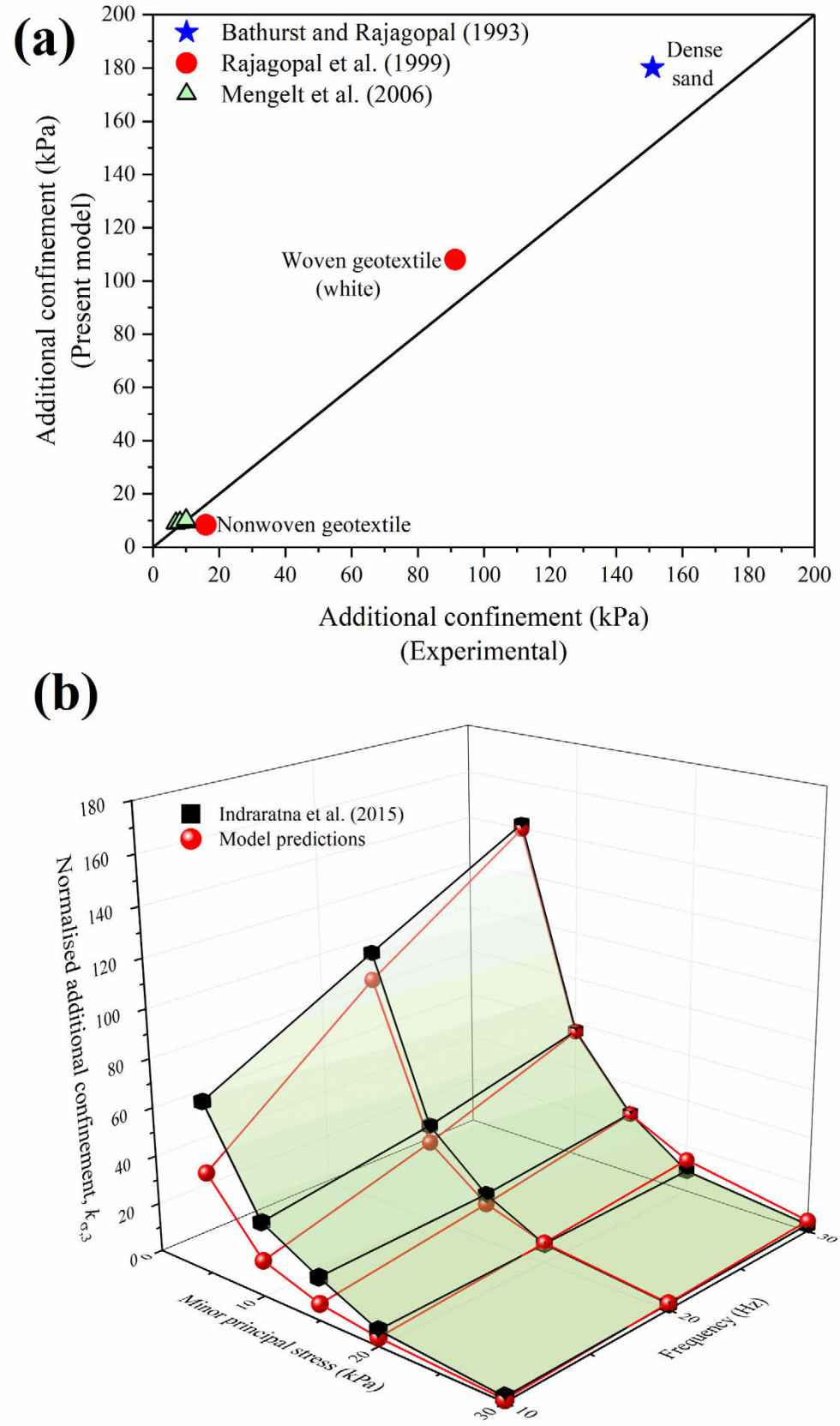

Figure 6.14 Comparison of the additional confinement computed using the present model with the experimental data under **(a)** axisymmetric condition; **(b)** plane-strain condition

6.7 Concluding Remarks

This part of the chapter examined the potential for the use of 3D cellular geoinclusions in the railway tracks. A semi-empirical model is also developed to evaluate the extra confinement offered by the cellular geoinclusions under the 3D stress state ($\sigma'_1 \neq \sigma'_2 \neq \sigma'_3$). The following concluding remarks may be drawn from this part:

6.7.1 Based on Literature Review

- The geocell confinement significantly improves the strength and stiffness of the granular infill materials in the track. The confinement reduces the track deformations in both lateral and vertical directions. Moreover, the geocell reinforced granular layer behaves as a rigid slab and distributes the train-induced loads uniformly over a wide area of the subgrade. Consequently, the settlement in the subgrade reduces, and the track geometry is retained over an extended period.
- The performance of a geocell reinforced layer depends on the properties of the geocell, infill soil, subgrade, location of the layer within the track, and the loading conditions. A thorough analysis of these parameters is essential for selecting a suitable type of geocell.
- The geocells increase the strength and resilience of the geomaterials under cyclic loading. However, the amount of improvement depends on the properties of geocell, infill soil, and the loading conditions such as frequency and magnitude of the vertical load.
- The geocell reinforcement decreases the magnitude and rate of plastic deformations in the track. This effect is beneficial for maintaining the track geometry over an extended period and reducing the frequency of maintenance cycles. However, the reduction in permanent deformation depends on several parameters such as the magnitude and frequency of load, and the properties of the geocell, infill, and subgrade soil.
- Several analytical models have been developed to evaluate the increase in confining pressure due to geocell reinforcement under axisymmetric or plane-strain loading conditions. These models can be used effectively to predict the improvement in the performance of a track layer when it is reinforced with the geocells.

- The geocells can be provided in the transition zones near the railway bridges to gradually increase the stiffness of the track and prevent the track geometry degradation.

6.7.2 Based on Novel Semi-Empirical Model

- The results from the developed model indicate that the magnitude of additional confinement is sensitive to the stress state (axisymmetric, plane-strain and 3D), type of inclusion and the parametric variations. The ACR varies between 0 and 1 for the 3D stress state, which indicates that the simplification of the 3D stress state to plane-strain or axisymmetric stress states yields conservative or over-predicted results, respectively.
- In comparison to $\Delta\sigma'_3$, the additional confinement in the direction of σ'_2 ($\Delta\sigma'_2$) decreases with an increase in D_r, φ'_m and b.
- The magnitude of extra confinement increases with an increase in geoinclusion modulus.
- The developed model provides a realistic assessment of additional confinement for deriving maximum potential benefits from geoinclusion reinforcement with a convenient selection of adequate material parameters.

In this part of the chapter, an exhaustive review of existing literature pertaining to the use of cellular geoinclusions in a railway track is presented first. Subsequently, a mathematical model is developed to predict the magnitude of improvement provided by the cellular geoinclusions. In the next part of this chapter, the developed mathematical model is incorporated into the geotechnical rheological track model, and the efficacy of geoinclusion reinforcement in mitigating the differential settlement problem of a transition zone is investigated.

CHAPTER 6 (PART-B)
ASSESSING THE EFFECTIVENESS OF GEOINCLUSION IN IMPROVING THE PERFORMANCE OF TRANSITION ZONE USING GEOTECHNICAL RHEOLOGICAL MODEL

6.8 General

The railway engineers have long been pursuing for tools to assist them in assessing the effectiveness of various countermeasures for improving the performance of the transition zones in railway tracks. **Figure 6.15** illustrates the differential settlement problem encountered in a typical open track-bridge transition without any countermeasure. As can be seen from the figure, the track supported by soil layers (softer side) settles more than that founded on the bridge (stiffer side) after several load repetitions. As discussed in Section 6.4, 3D cellular geoinclusions can reduce the plastic deformation in the soil layers by providing additional confinement. Consequently, employing these inclusions to strengthen the softer side of the transition zone may reduce the uneven track displacement and improve their performance in a cost-effective manner.

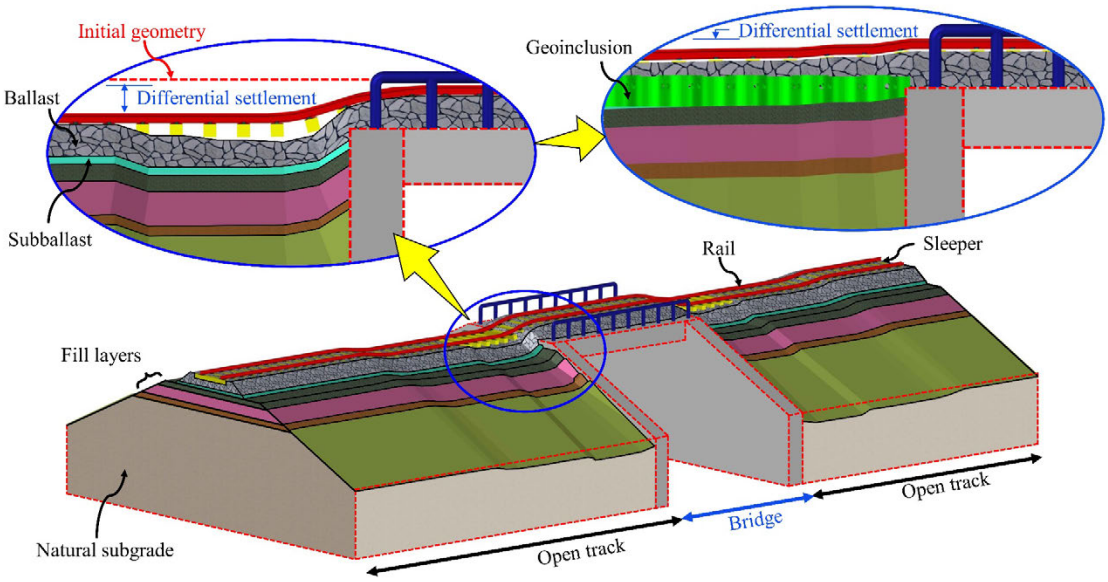

Figure 6.15 Differential settlement in an open track-bridge transition and its potential mitigation using 3D cellular geoinclusion

Despite the immense potential, the application of 3D artificial inclusions in railway tracks is still minimal due to the lack of a well-established method to evaluate the magnitude of improvement provided by these geoinclusions. Although the researchers have resorted to

FE and DE analyses to explore the beneficial aspects of geoinclusions in improving track performance (e.g., Leshchinsky & Ling 2013b; Liu et al. 2018; Banerjee et al. 2020a), these analyses are computationally intensive and may require a relatively large amount of time to accurately predict the track response, especially when the number of load repetitions or train passages is huge. The analytical approaches offer comparatively faster and computationally more efficient alternatives to DE or FE analyses for evaluating the performance of reinforced railway tracks; however, such methods are relatively scarce.

In view of the above discussion, this part of the chapter provides a novel computational methodology that incorporates the effect of geoinclusion on the behaviour of a ballasted railway track. The proposed method is an integrated approach that combines the additional confinement model (see Section 6.6) with the geotechnical rheological model for a railway track (see CHAPTER 5). The accuracy of the approach is verified by comparing the predicted results against the data reported in the literature. The proposed methodology is applied to an open track-bridge transition to demonstrate its practical applicability, and the adequacy of artificial inclusions in mitigating the differential settlements is investigated. Finally, a parametric study is conducted to assess the influence of factors such as axle load, subgrade properties, placement location, type and opening size of geoinclusion on the track settlement. This study provides a computational tool that the practising railway engineers can use to improve the performance of the ballasted railway tracks, especially in the transition zones.

6.9 Response Prediction for Reinforced Track

The proposed computational method is an integrated approach that combines the loading model (CHAPTER 3), geotechnical rheological track model (CHAPTER 5) and additional confinement model (Section 6.6) to predict the response of railway tracks reinforced with 3D cellular inclusions. The proposed method involves the following steps:

Step 1: Determine the effective region of substructure layers below individual sleepers using the input data for the entire section of a railway line simulated by the geotechnical rheological model (see Section 3.2.2.2).

Step 2: Calculate the vibrating mass (m), spring stiffness (k) and viscous damping coefficient (c) for the substructure layers (see Section 3.2.2.2).

Step 3: Compute the rail seat load-time history for all the sleepers under consideration (see Section 3.2.1 and APPENDIX F).

Step 4: Evaluate the stress distribution in the substructure layers at each time instant using the modified Boussinesq approach (see Section 3.9.1.1).

Step 5: For each time instant, check whether the yield criterion of the slider element for any substructure layer is met. If the yield is reached and loading conditions are satisfied, compute the plastic deformations using the constitutive relations for the slider element (see Sections 3.9.2.2 and 5.3.1). Moreover, calculate the additional confinement mobilised by the cellular geoinclusion using the strain accumulated in the lateral and longitudinal directions (see Section 6.6.2.1). If the yield is not reached, no plastic deformation occurs, consequently, no additional confinement is mobilised.

Step 6: Solve the dynamic equilibrium equation using Newmark's β-numerical integration scheme to compute the total displacement of the track layers at that time instant.

Step 7: Update the stress state using the magnitude of additional confinement provided by geoinclusion in the lateral and longitudinal direction.

Step 8: Repeat steps 5 to 7 till the desired number of axles have passed the section of a railway line simulated by the geotechnical rheological model.

Step 9: Calculate the total displacement-time history.

6.10 Validation of Methodology

Limited field data is available on the behaviour of ballasted railway tracks reinforced with cellular geoinclusions under train-induced repetitive loading. Nevertheless, the validity of the proposed computational methodology to accurately simulate the behaviour of reinforced railway tracks is investigated by comparing the predicted results with 3D FE analyses conducted by Satyal et al. (2018). Satyal et al. (2018) developed FE models of ballasted railway tracks with and without geocell reinforcement and studied the effect of factors such as geocell configuration, ballast thickness and subgrade type on the track performance. These FE models were previously validated against the experimental plate loading tests on unreinforced and geocell-reinforced ballast overlying weak subgrade soil (Satyal et al. 2018). The 3D FE model of the ballasted railway track for the unreinforced case is shown in **Figure 6.16**. The model consists of a ballast layer overlying a 2 m thick

subgrade. The model length along the longitudinal and transverse directions is 1.485 m and 5 m, respectively. The nodes at the bottom boundary of the model were completely fixed, while the nodes along the side boundaries were normally fixed. Only one half of the track was modelled due to symmetry. For the reinforced case, the geocell was modelled as an embedded element inside the ballast layer. Other details of the model can be found in Satyal et al. (2018).

Figure 6.16 compares the results predicted using the present method and that using FE analyses by Satyal et al. (2018). **Table 6.4** lists the values of the parameters used in the simulation. It can be observed that the results predicted using the proposed approach agree reasonably well with the predictions from the FE analyses. The settlement values evaluated using the present method vary by 1% – 13% from the FE results. The proposed model can accurately predict the reduction in track settlement achieved by reinforcing the bottom of the ballast layer with a geocell. Moreover, the performance of the reinforced track at various subgrade conditions and ballast thicknesses is also predicted satisfactorily.

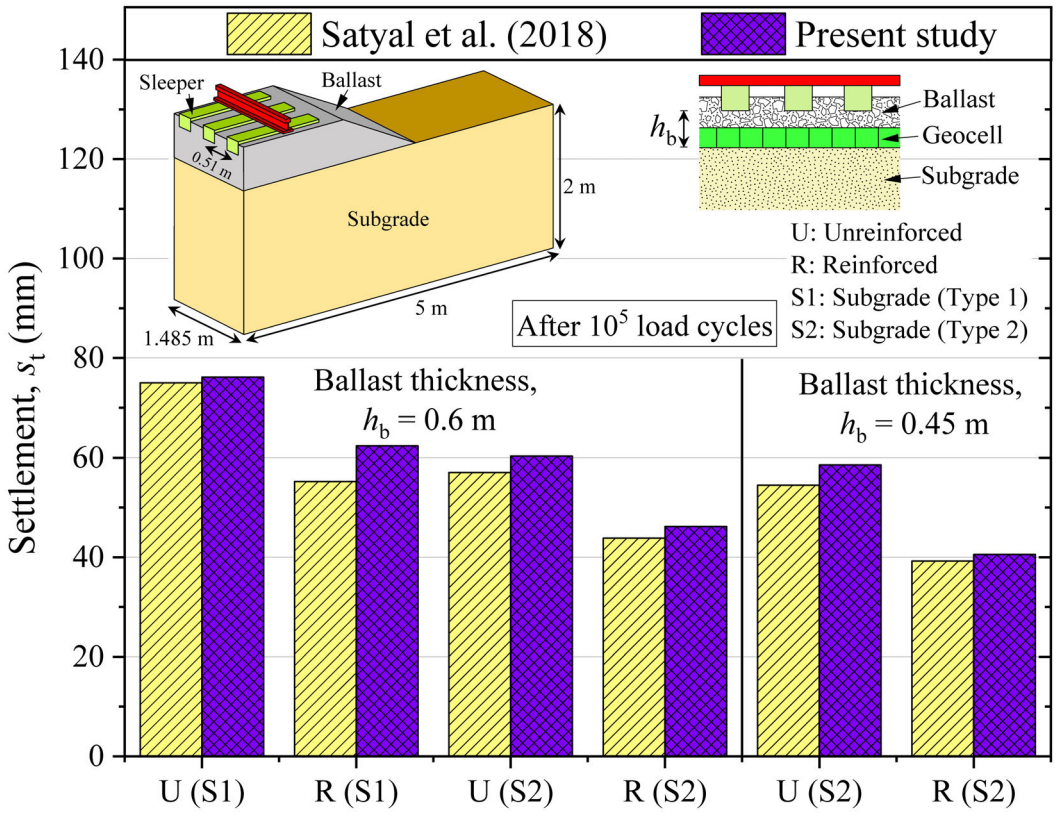

Figure 6.16 Comparison of track settlement computed using the present method with results from FE analyses conducted by Satyal et al. (2018)

Table 6.4 Input parameters used in the validation

Layer	Variable	Symbol	Unit	Satyal et al. (2018)	Banerjee et al. (2020a)
Ballast	Resilient modulus	E_b	MPa	30	5.99
	Poisson's ratio	ν_b	–	0.4	0.35
	Shear stiffness	k_b^s	MN/m	78.4	78.4
	Density	ρ_b	kg/m^3	1,500	1,621
	Thickness	h_b	m	0.45 – 0.6	0.0875
	Reference void ratio on CSL	Γ	–	1.4	1.4
	Slope of CSL	λ	–	0.1	0.1
	Critical stress ratio	M_{tc}	–	1.42	1.25
	Volumetric coupling parameter	N_v	–	0.2	0.2
	State-dilatancy parameter	χ_{tc}	–	3	3
	Cyclic hardening parameter	a_h	–	0.32	–
	Plastic hardening parameter	H	–	50-250×ψ	50-250×ψ
Subballast	Resilient modulus	E_s	MPa	–	1.48 – 1.54
	Poisson's ratio	ν_s	–	–	0.32
	Shear stiffness	k_s^s	MN/m	–	476
	Density	ρ_s	kg/m^3	–	1,417
	Thickness	h_s	m	–	0.1125 – 0.15
	Reference void ratio on CSL	Γ	–	–	1.2$^{\#}$
	Slope of CSL	λ	–	–	0.05$^{\#}$
	Critical stress ratio	M_{tc}	–	–	1.65$^{\#}$
	Volumetric coupling parameter	N_v	–	–	0.5$^{\#}$
	State-dilatancy parameter	χ_{tc}	–	–	2.5$^{\#}$
	Plastic hardening parameter	H	–	–	80-260×$\psi^{\#}$
Subgrade	Resilient modulus	E_g	MPa	8.5	1.07 – 1.14
	Poisson's ratio	ν_g	–	0.35	0.49
	Shear stiffness	k_g^s	MN/m	1,600	1,600
	Density	ρ_g	kg/m^3	2,162	1,551
	Thickness	h_g	m	2	0.3625 – 0.4
	Slope of CSL	λ	–	0.0041	0.06
	Slope of swelling line	κ	–	0.002	0.03
	Critical state friction angle	φ_c	°	37.5 (S1) 42.5 (S2)	42.5
	Characteristic stress parameter	ξ	–	0.1	0.1
	Spacing parameter	A	–	0.1	0.15
	Cyclic hardening parameter	a_h	–	0.09	–
Geoinclusion	Material (or component)	–	–	PE*	Geogrid
	Diameter	D_g	m	0.3	0.1 – 0.165
	Poisson's ratio	ν_m	–	0.35	0.2

*Polyethylene; $^{\#}$calibrated using triaxial test data reported by Banerjee et al. (2020b)

The validity of the proposed computational methodology is also investigated by comparing the predicted results with the reduced scale model tests conducted by Banerjee et al. (2020a). The values of the parameters used in the simulation are listed in **Table 6.4**. **Figure 6.17** compares the results predicted using the present method with the data reported by Banerjee et al. (2020a). It is apparent that the predicted results are in a reasonable agreement with the model test data. The present method can satisfactorily simulate the settlement reduction caused by reinforcing the subballast layer with geocell at different subballast layer thicknesses. Moreover, it can also capture the improvement in settlement reduction with a decrease in geocell pocket size.

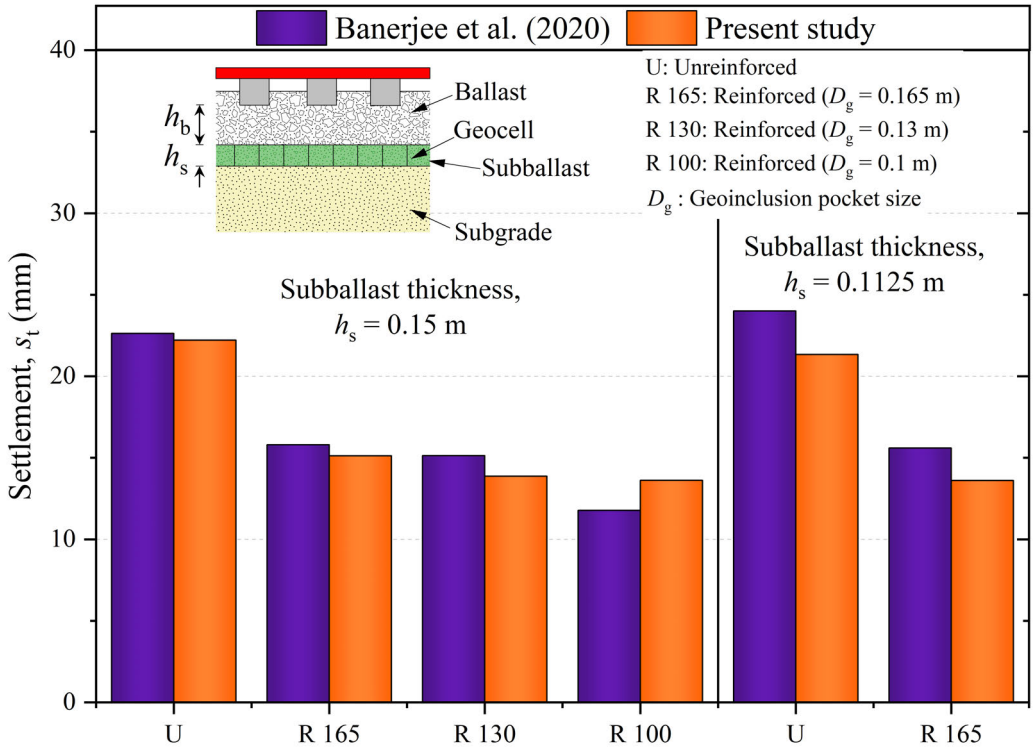

Figure 6.17 Comparison of results computed using the present method with experimental data reported by Banerjee et al. (2020a)

6.11 Results and Discussion

A parametric analysis is carried out to investigate the influence of geoinclusion properties, subgrade properties and axle load on the performance of a reinforced ballasted railway track. Subsequently, the effectiveness of 3D cellular and planar (2D) geosynthetics in reducing the track settlement is compared. **Tables 4.1** and **6.5** list the values of input parameters used in the analysis. The nominal values of the variables are provided in the parenthesis. The values of constitutive parameters for ballast, subballast and subgrade are

given in **Tables 4.2, 3.4** and **5.1**, respectively. The value of Z is assumed as 10 and 20 for ballast and subballast, respectively. The results are computed for multiple passages of a train comprising 32 axles with a configuration identical to the Acela express passenger train at a speed of 100 km/h. Only one variable is changed for each analysis, while other parameters are allocated nominal values. The nominal value of Q_a is taken as 25 t. The depth of cellular geoinclusion is considered as 150 mm, and it is provided at the bottom of the ballast layer.

Table 6.5 Input parameters for parametric study

Variable	Symbol	Unit	Present study
Subgrade:			
Resilient modulus	E_g	MPa	20
Poisson's ratio	v_g	–	0.45
Thickness	h_g	m	6
Geoinclusion:			
Material	–	–	HDPE (unless otherwise stated)
Diameter†	D_g	m	0.25 – 0.4 (0.25)
Poisson's ratio	v_m	–	0.3

†D_g = 1 m for rubber tyre

6.11.1 Influence of Geoinclusion Material

The magnitude of additional confinement provided by a 3D cellular geosynthetic depends on the type of material used for its manufacture. Hence, the material type may influence the inelastic deformation or settlement accumulated in a reinforced track layer. To study its effect, five different types of materials, namely, HDPE, nonwoven PP geotextile, woven coir geotextile, geocomposite (PP biaxial geogrid with PP fabric) and rubber tyre, are considered in the analysis. **Figure 6.18(a)** shows the load-strain curves for the five different materials obtained using tension tests (Koerner 2012; Gonzalez-Torre et al. 2014; Biabani 2015; Indraratna et al. 2017; Lal et al. 2017). **Figure 6.18(b)** shows the accumulation of track settlement with tonnage when the cellular geoinclusion manufactured using different materials is provided at the bottom of the ballast layer. It can be observed that the track settlement decreases on reinforcing the substructure layer.

However, the magnitude of settlement reduction depends on the material used to manufacture the artificial inclusion. The maximum reduction in track settlement is provided by the rubber tyre (32%), followed by geocomposite (30%), HDPE (22%), woven coir geotextile (12.5%) and nonwoven PP geotextile (4%). This observation is reasonable as the rubber tyre provides the maximum confinement among all the materials tested, which is apparent in **Figure 6.19**.

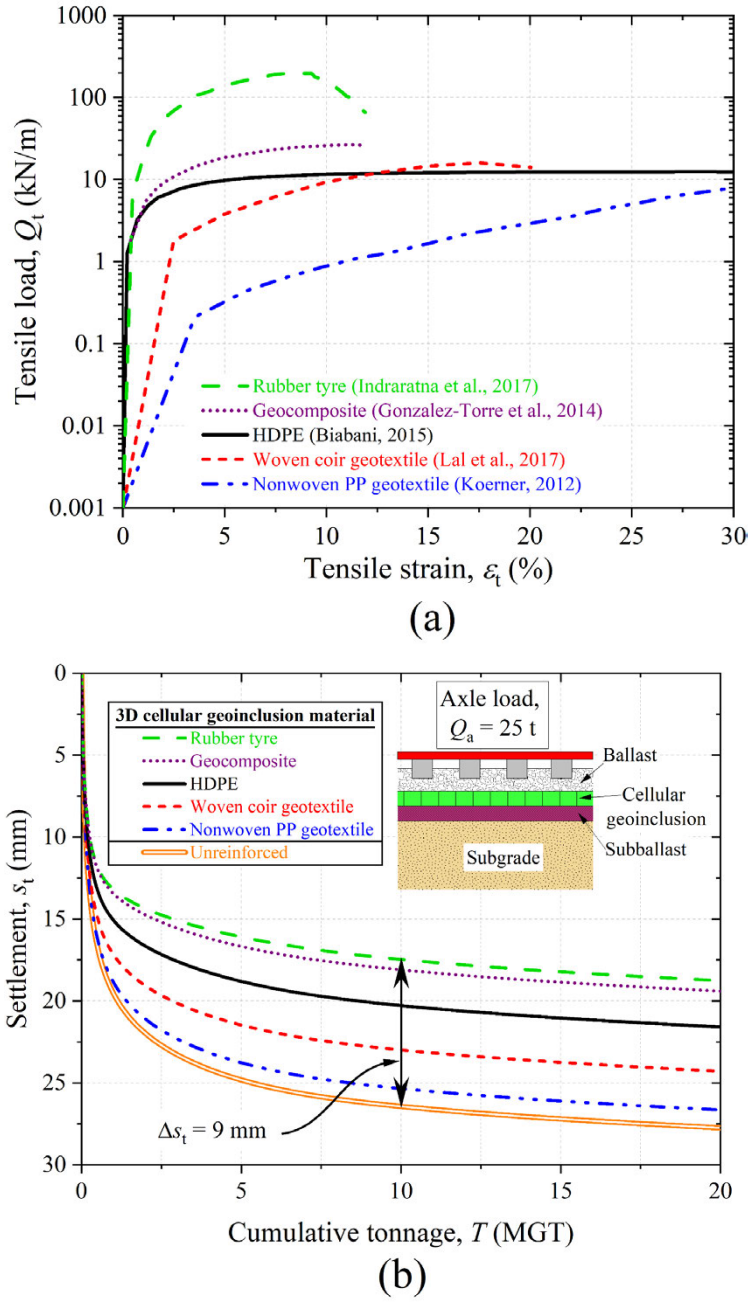

Figure 6.18 (a) Load versus strain curves for five geoinclusion materials obtained from tension tests; **(b)** accumulation of settlement with tonnage for tracks reinforced with cellular inclusions manufactured using different materials

Figure 6.19 shows the variation of additional confinement with cumulative tonnage provided by five different materials along the longitudinal, $\Delta\sigma_x$, and transverse directions, $\Delta\sigma_y$. The rubber tyre provides the maximum confinement because the modulus of the rubber tyre is the highest among the five materials considered [see **Figure 6.18(a)**]. It is also apparent that the geocomposite provides more confinement than HDPE, woven coir geotextile and nonwoven PP geotextile. This observation is reasonable as the modulus of geocomposite is higher than HDPE, woven coir and nonwoven PP geotextiles [see **Figure 6.18(a)**]. Moreover, the confinement provided along the transverse direction (represented by solid lines) is much higher than that in the longitudinal direction (represented by dashed lines) for all the materials tested. This trend may be attributed to the fact that the deformation is higher in the transverse direction, and consequently, more confinement is mobilised in this direction compared to the longitudinal direction.

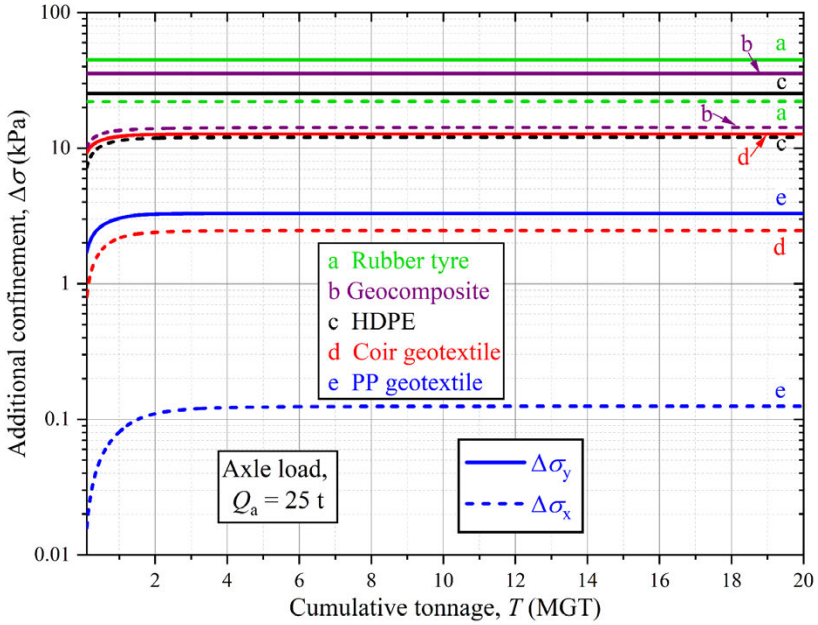

Figure 6.19 Variation of additional confinement with tonnage for tracks reinforced with 3D artificial inclusions manufactured using different materials

Thus, it is apparent that stiffer materials offer more confinement than softer materials. Consequently, cellular geoinclusions made up of stiffer materials provide more improvement in the track performance than those manufactured using softer materials. Nonetheless, the selection of a particular geosynthetic material must be based on factors such as its intended role, the scope of the project, and the costs associated with the fabrication and installation.

6.11.2 Influence of Pocket Size

D_g is varied between 0.25 m and 0.4 m to investigate its effect on the settlement reduction. **Figure 6.20(a)** shows the variation of settlement with depth when the bottom of the ballast layer is reinforced with cellular HDPE inclusion having different diameter or pocket sizes. It can be observed that the track settlement increases with an increase in D_g. The settlement increases by 6% on increasing D_g from 0.25 m to 0.4 m. This observation is reasonable since more material is available per unit area for providing confinement when D_g is smaller. Nonetheless, the track settlement is 17.4% less than the unreinforced case, even when D_g is 0.4 m. **Figures 6.20(b)** and **6.20(c)** show similar trends for geoinclusions manufactured using woven coir and nonwoven PP geotextiles, respectively. Thus, the performance of a reinforced track is somewhat sensitive to the diameter or pocket size. Cellular inclusions with smaller pocket size provide better confinement and more settlement reduction than those with larger pocket size.

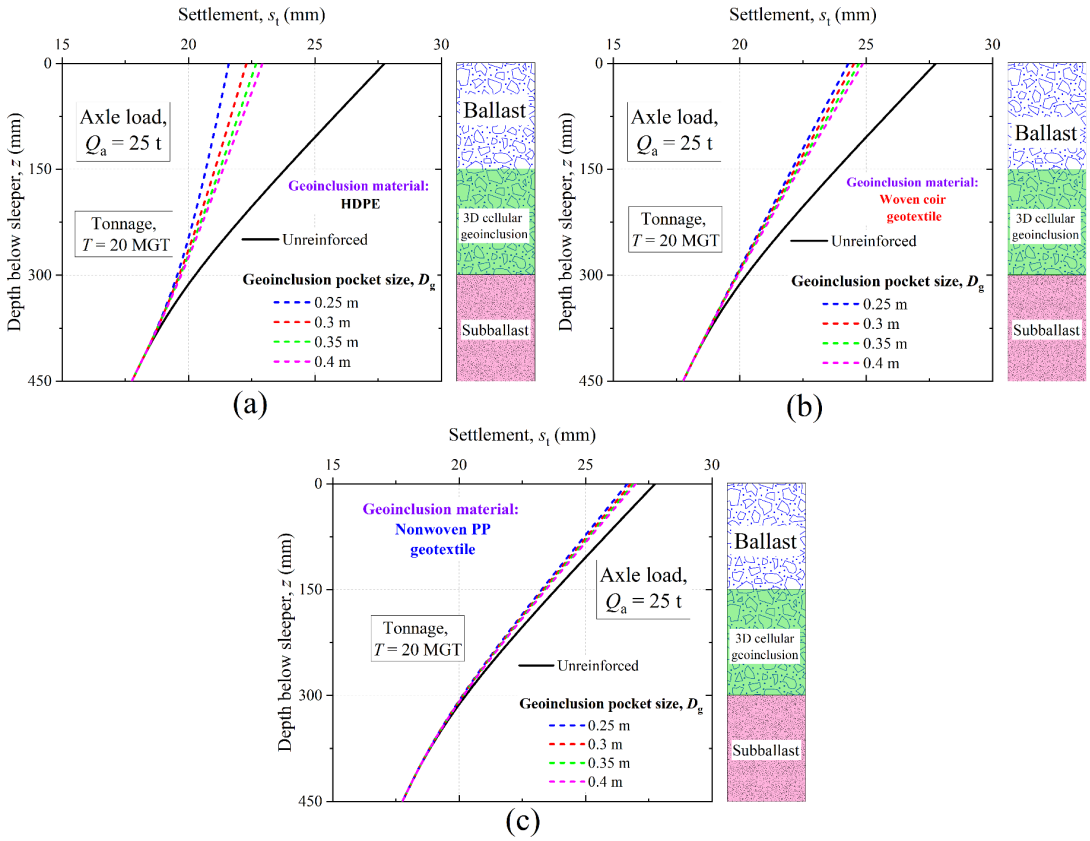

Figure 6.20 Influence of opening or pocket size on track response for 3D cellular inclusions manufactured using **(a)** HDPE; **(b)** woven coir geotextile; **(c)** nonwoven PP geotextile

6.11.3 Influence of Axle Load

Q_a is varied from 20 t – 30 t to investigate its influence on the effectiveness of the reinforcement. **Figure 6.21** shows the effect of axle load on the accumulation of track settlement with tonnage for different geoinclusion materials, viz. HDPE, woven coir geotextile and nonwoven PP geotextile. It can be observed that the settlement increases for all the cases with an increase in Q_a. For the unreinforced case, the cumulative settlement after 20 MGT increases by 41.3% on increasing Q_a from 20 t – 30 t. For HDPE inclusion reinforced track, the settlement increases by 37.9% with an increase in Q_a from 20 t – 30 t. This trend is reasonable because the stress transferred to the substructure layers rises on increasing the axle load, leading to an increment in deformation.

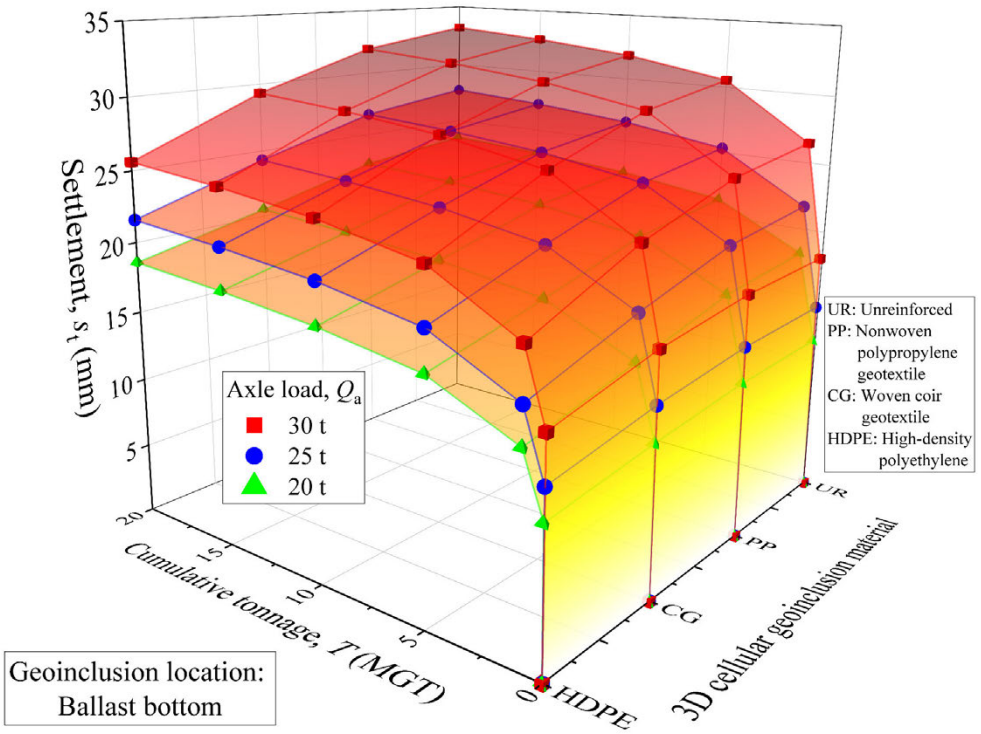

Figure 6.21 Influence of axle load on settlement for track reinforced with different cellular inclusion types

It is interesting to note that the effectiveness of reinforcement in reducing the track settlement is relatively constant at the three axle loads. After a cumulative tonnage of 20 MGT, HDPE geoinclusion reduced the settlement by 21%, 22% and 23% for 20 t, 25 t and 30 t axle loads, respectively. Similar behaviour is observed for cellular inclusions manufactured using coir and PP geotextiles. Thus, the results imply that the geoinclusions would maintain their effectiveness in those railway tracks where heavier axle loads are anticipated in the future.

6.11.4 Comparison with Planar Geosynthetic Reinforcement

This section compares the effectiveness of a 3D-cellular inclusion with a planar (2D) geosynthetic such as geogrid or geotextile. **Figure 6.22(a)** shows the equivalence of stress generated in a planar geosynthetic to the extra confining pressure provided to the surrounding soil. The magnitude of additional confinement provided by the planar inclusion can be determined following a similar approach as proposed by Yang & Han (2013) for axisymmetric loading conditions. Since a planar geosynthetic is subjected to 3D loading conditions in a railway track, the additional confinement provided under a 3D stress state can be computed using the following equations:

$$\Delta\sigma_{\mathrm{x}} = -\frac{M_{\mathrm{m}}\alpha_{\mathrm{m}}}{H_{\mathrm{m}}(1-\nu_{\mathrm{m}}^2)}(\varepsilon_{\mathrm{x}} + \nu_{\mathrm{m}}\varepsilon_{\mathrm{y}}) \tag{6.25}$$

$$\Delta\sigma_{\mathrm{y}} = -\frac{M_{\mathrm{m}}\alpha_{\mathrm{m}}}{H_{\mathrm{m}}(1-\nu_{\mathrm{m}}^2)}(\varepsilon_{\mathrm{y}} + \nu_{\mathrm{m}}\varepsilon_{\mathrm{x}}) \tag{6.26}$$

where α_{m} and H_{m} are the bonding coefficient and influence height of planar geosynthetic, respectively. The derivation of Equations 6.25 and 6.26 is provided in APPENDIX J. H_{m} is assumed as 150 mm in this study, which is equal to the height of 3D cellular geoinclusion. The value of α_{m} depends on several factors, such as stiffness and Poisson's ratio of geosynthetic and soil-geosynthetic interface stiffness (see Yang & Han 2013). For simplicity, α_{m} is varied from 0.25 to 0.75 in the analysis to show its influence on the benefits provided by planar geosynthetics.

Figure 6.22(b) shows the effectiveness of planar and 3D cellular geosynthetics in reducing the track settlement. For planar case, PP, coir and HDPE may represent nonwoven PP geotextile, woven coir geotextile and biaxial HDPE geogrid, respectively. It can be observed that the use of both 3D and planar geosynthetics decrease the track settlement; however, the 3D inclusions are more effective in reducing the settlement as compared to planar geosynthetics. After a cumulative tonnage of 20 MGT, the planar PP, coir and HDPE inclusions reduce the track settlement by 2%, 8.6% and 15.3%, respectively, for α_{m} = 0.25. Whereas the 3D geoinclusions manufactured using PP, coir, and HDPE reduce the track settlement by 4%, 12.5% and 22%, respectively. This finding is reasonable because a 3D cellular inclusion provides confinement to the infill material by resisting its lateral deformation throughout the inclusion height, whereas the confinement provided by a planar geosynthetic depends on the frictional interaction and

interlocking with the soil at the interface. It is also apparent that the effectiveness of planar geosynthetic increases with an increase in α_m. The higher the frictional interaction between soil and planar geosynthetic (large value of α_m), the higher is the mobilised confinement and consequently, more settlement is reduced.

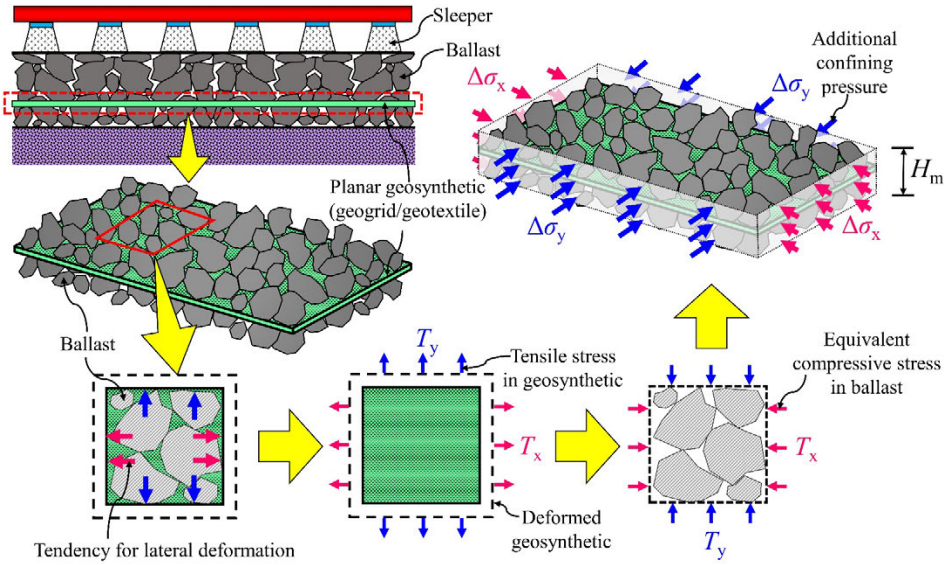

(a)

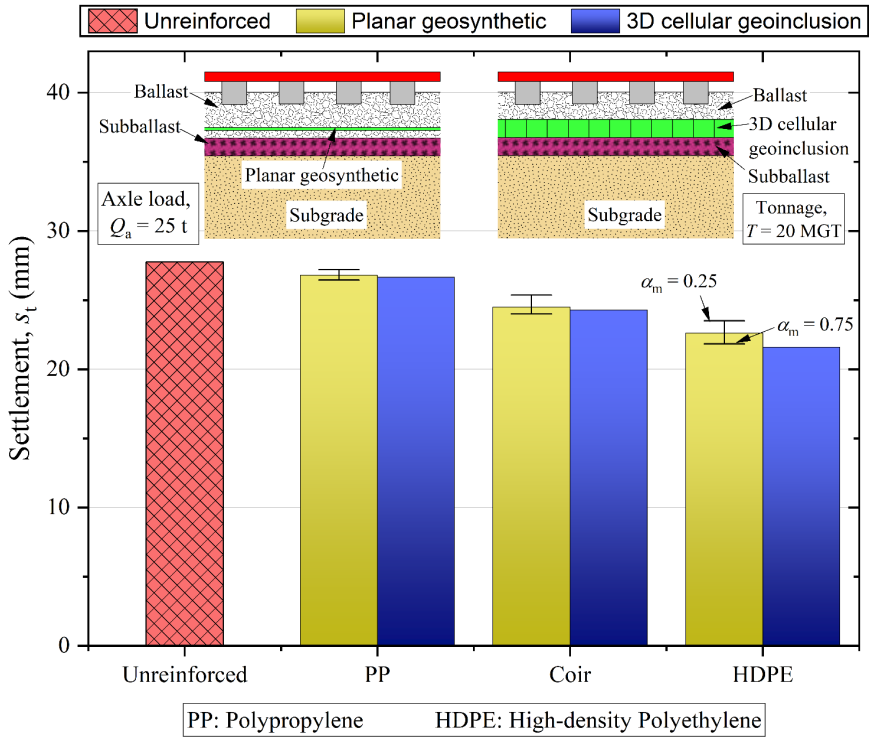

(b)

Figure 6.22 (a) Equivalence of stresses in planar geosynthetic to additional confining pressure in soil; **(b)** comparison of settlement accumulated in the unreinforced track and track reinforced using planar and 3D geosynthetics

6.12 Application to Transition Zones

The previous section demonstrated that a considerable reduction in track settlement could be achieved when the granular track layers are reinforced with 3D cellular inclusions. The adequacy of geoinclusions in reducing the differential settlement at the transition zones is investigated in this section. **Figure 6.23** shows the geotechnical rheological model of the open track-bridge transition considered in this analysis. The substructure of the softer side of the transition consists of three layers (ballast, subballast and subgrade), while the ballast layer supported by concrete bridge deck forms the substructure on the stiffer side.

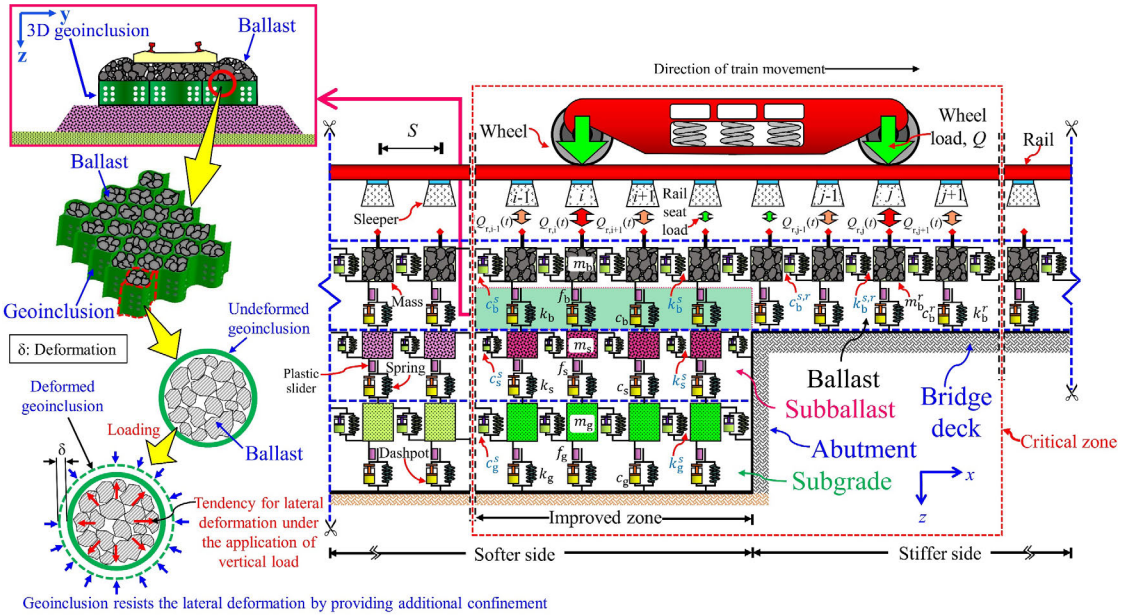

Figure 6.23 Geotechnical rheological model of a typical open track-bridge transition with 3D cellular geosynthetic reinforcement

The geosynthetic layer is provided up to a distance of 6 m from the bridge (i.e., in the improved zone). The height of the inclusion is considered as 150 mm and is provided at the bottom of the ballast layer (as illustrated in **Figure 6.23**). The effect of reinforcement is simulated using a similar procedure as described in Section 6.9.

The subsequent sections investigate the efficacy of 3D geoinclusions in improving the performance of transition zones through parametric analyses. **Tables 4.1** and **6.5** list the values of input parameters used in the analysis. The values of constitutive parameters for ballast, subballast and subgrade are given in **Tables 4.2, 3.4** and **5.1**, respectively.

6.12.1 Effect of Geoinclusion Material

Figure 6.24 shows the variation of settlement along the track length when 3D geoinclusions manufactured using different materials are provided in the bottom portion of the ballast layer near the bridge approach (improved zone). The results of the unreinforced track are also provided for comparison. Note that the origin of the *x*-coordinate is at the onset of the stiffer side. It can be observed that the differential settlement accumulated after a cumulative tonnage of 20 MGT is the maximum for the unreinforced case. On reinforcing the track, the differential settlement between the stiffer and softer side decreases. The rubber tyre provides the maximum benefit among all the materials tested, followed by geocomposite, HDPE, woven coir geotextile and nonwoven PP geotextile. As discussed in Section 6.11.1, the modulus of rubber tyre at a particular strain value is the highest among all the materials considered; consequently, it provides maximum confinement and improvement in track performance. The reduction in the differential settlement is 5.4%, 16.7%, 29.8%, 40.3% and 43.4% for nonwoven PP geotextile, woven coir geotextile, HDPE, geocomposite and rubber tyre, respectively. Thus, the material used to manufacture the artificial inclusion significantly influences the magnitude of differential settlement at the open track-bridge transition. Stiffer materials provide more performance improvement (or differential settlement reduction) than softer materials.

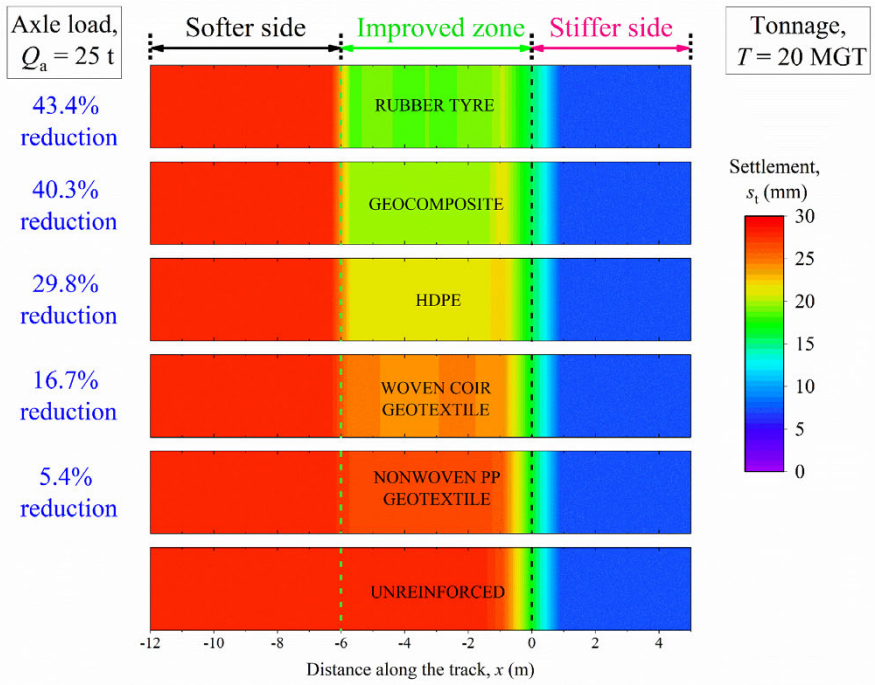

Figure 6.24 Variation of settlement along the length for unreinforced and reinforced track

6.12.2 Influence of Subgrade Strength

The subgrade strength is varied by changing φ_c between 36° and 45°. **Figure 6.25(a)** shows the settlement accumulated along the length of the track when cellular HDPE inclusion is provided at the bottom of the ballast layer, and φ_c in the improved zone is varied between 36° and 45°. It can be observed that the reinforcement is more effective when the subgrade strength is high. The differential settlement decreases by 45.3% and 55.6% for φ_c = 40° and 45°, respectively. **Figures 6.25(b)** and **6.25(c)** show that the 3D geoinclusions manufactured using woven coir and nonwoven PP geotextiles are also more effective when subgrade strength is high. The differential settlement in the transition zone in the case of coir geotextile decreases by 32.3% and 42.6% for φ_c = 40° and 45°, respectively [see **Figure 6.25(b)**]. Similarly, the differential settlement in the case of PP geotextile decreases by 19.4% and 31.2% for φ_c = 40° and 45°, respectively. Thus, the effectiveness of reinforcement significantly depends on the subgrade strength. For critical zones with low subgrade strength, the use of cellular geoinclusion in the ballast layer coupled with subgrade strength increment through ground improvement techniques may prove to be very effective.

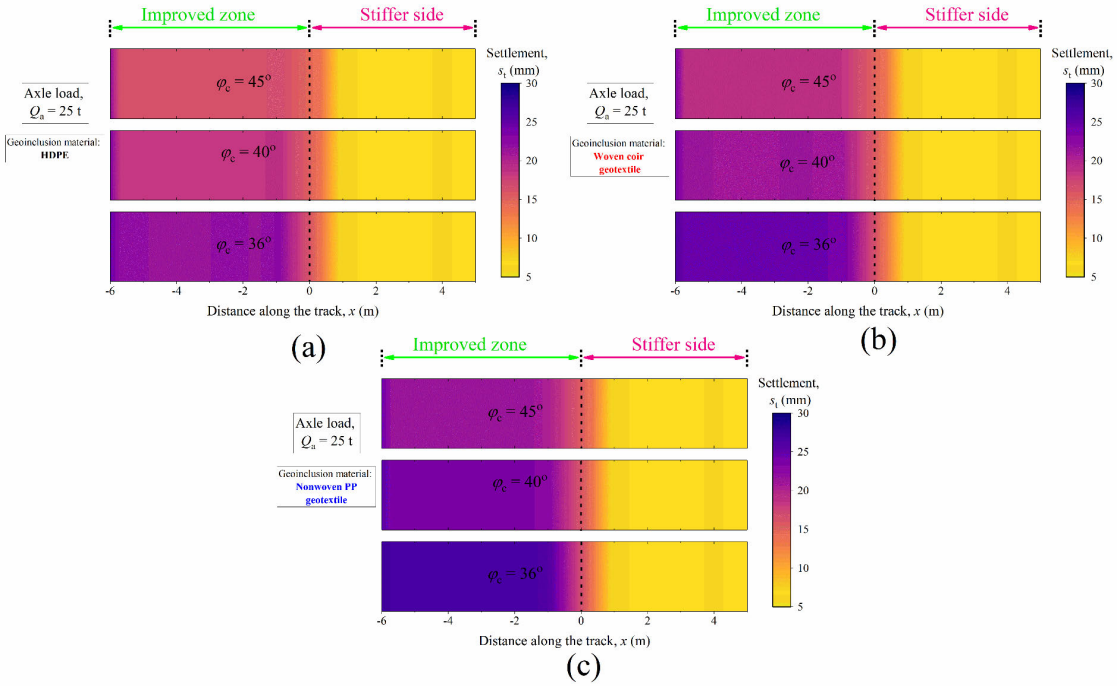

Figure 6.25 Influence of subgrade strength on the effectiveness of artificial inclusions manufactured using: **(a)** HDPE; **(b)** woven coir geotextile; **(c)** nonwoven PP geotextile

6.12.3 Influence of Geoinclusion Location

The magnitude of settlement reduction provided by the geosynthetic reinforcement also depends on its location within the rail track. To investigate its most effective placement position, the 3D geoinclusion is provided at three locations in the track, viz., ballast bottom, subballast and subgrade top. **Figure 6.26** shows the variation of settlement along the track length accumulated after a cumulative tonnage of 10 MGT when reinforcement is provided at different locations within the track. As expected, the differential settlement decreases on reinforcing the track layers in the improved zone. The maximum reduction is obtained for the case when the bottom of the ballast layer is reinforced. After a cumulative tonnage of 10 MGT, the differential settlement reduces by 31.6%, 7.4% and 9.7% when the HDPE geoinclusion is provided in the ballast bottom, subballast and subgrade top, respectively. This behaviour may be ascribed to a smaller confining pressure acting on the ballast layer prior to the reinforcement (Selig & Waters 1994). The extra confinement provided by the geoinclusion significantly decreases the deformations in the ballast layer, and consequently, the differential settlement is reduced. The improvement is much smaller when the geoinclusion is provided at the top of the subgrade layer than at the ballast bottom because only the top 150 mm of the 6,000 mm thick subgrade layer is reinforced. The contribution of the remaining 5,850 mm to total settlement is still very high.

Nonetheless, a similar trend is observed for inclusions manufactured using coir geotextile (CG). However, as expected, the HDPE geoinclusion provides more improvement in track performance than the inclusion manufactured using coir geotextile. Thus, the results demonstrate that the performance of a transition zone can be improved with the strategic placement of 3D cellular inclusion in the track.

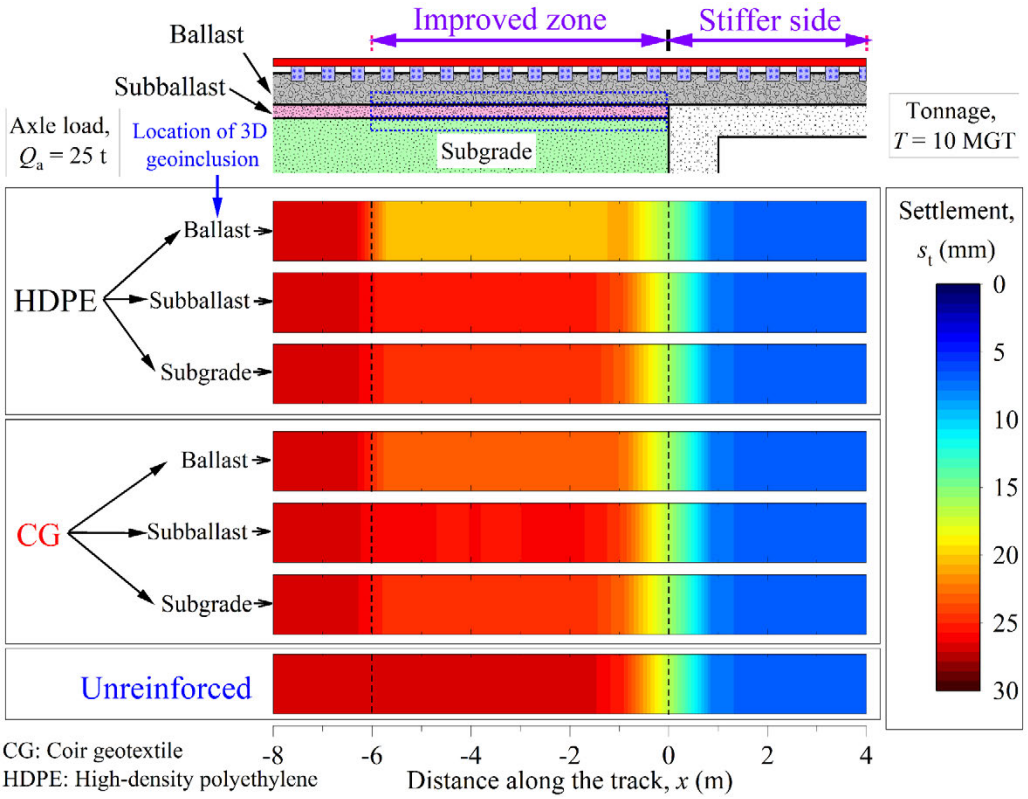

Figure 6.26 Variation of settlement along the track length when 3D cellular inclusion is provided at different positions within the track

6.13 Economic and Environmental Aspects of 3D Cellular Geoinclusion Reinforcement

The results from this study demonstrate that the use of 3D cellular geoinclusions improves the track performance by reducing the settlement and decreasing the track geometry degradation rate. Consequently, the frequency of periodic maintenance operations can be decreased, leading to significant cost savings. By employing 3D cellular geoinclusions into the track, it is feasible to reduce the thickness of granular layers (such as subballast) without compromising track performance, as illustrated in **Figure 6.27**. As evident, the reduction in subgrade settlement is identical when the HDPE geoinclusion is provided at the top of the subgrade and when h_s is increased from 0.15 m to 0.2 m. Thus, by reinforcing the top of the subgrade layer with geoinclusion, the subballast thickness could be reduced by 25%, thereby mitigating the environmental impact while lowering overall costs. This is especially true when a sufficient supply of good quality subballast material is unavailable near the construction site, leading to significant economic and environmental consequences (Sol-Sánchez & D'Angelo 2017).

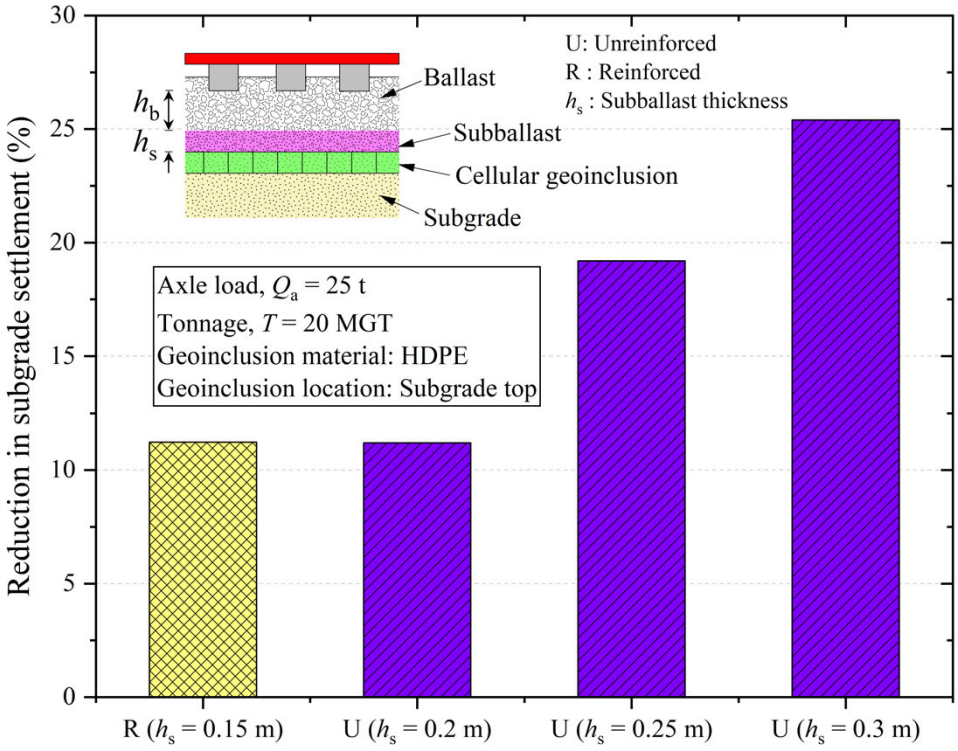

Figure 6.27 Reduction in subgrade settlement when cellular geoinclusion is provided at the top of the subgrade and when subballast thickness is increased from 0.15 m to 0.3 m.

The results from this study also revealed that rubber tyres could significantly improve the track performance. The use of scrap rubber tyres as cellular reinforcement can be considered an environment friendly alternative for enhancing track performance because these tyres have become a major source of pollution on a global scale. Around 50 million tyre equivalent passenger units are estimated to be discharged annually in Australia (Farooq et al. 2021). Therefore, reusing these tyres in the railway tracks may be an appealing solution.

Despite these environmental and economic benefits, there are a few issues pertaining to the use of 3D cellular inclusions in railway tracks. One major concern is the initial cost of synthetic inclusions (made up of HDPE). In this regard, the geoinclusions made of coir geotextile can serve as low-cost alternatives to their synthetic counterparts.

6.14 Limitations and Future Scope

The limitations of the novel computational methodology are as follows:

- The train-induced loading is considered only along the vertical direction.
- The additional confining pressure is assumed to be constant along the height of the cellular geoinclusion.
- The shape of the cellular geoinclusion is assumed to be circular as opposed to their actual shape, which can be a 3D honeycomb.
- Long-term performance of geoinclusions, particularly their fatigue life is ignored.
- Behaviour of geoinclusions under train-induced impact loading in the transition zones is not studied.

The future investigations shall address these limitations.

6.15 Concluding Remarks

In this section of the chapter, a novel computational methodology is developed by combining the loading, additional confinement and geotechnical rheological models to investigate the efficacy of 3D cellular inclusions in improving the performance of ballasted railway tracks. The primary features of the method include:

- Use of simplified yet effective geotechnical rheological model which can incorporate inhomogeneous support conditions along the track length, capture the effect of PSR due to moving wheel loads and accurately predict the cumulative settlement.
- The utilisation of the additional confinement model derived from hoop stress theory and Hooke's law that can evaluate the magnitude of extra confinement offered by cellular geosynthetics under 3D loading conditions (or general stress state).
- Provides a simple yet elegant analytical framework (which involves solving governing equations in a step-by-step manner) to evaluate the response of ballasted railway tracks at normal and transition zones while incorporating the effect of geosynthetic reinforcement in contrast to previous studies that relied on the use of commercial software packages, which were often computationally intensive.

The methodology is successfully validated against the results of FE analyses reported in the literature. A parametric study is carried out to investigate the influence of axle load and geosynthetic properties on the performance of reinforced railway tracks. Subsequently, the methodology is applied to a typical open track-bridge transition, and

the adequacy of cellular inclusion in mitigating the differential settlement at the transition is investigated. Finally, the effect of placement location, geosynthetic and subgrade properties on the performance of the transition zone is discussed. The following conclusions can be drawn from this study:

- The material used to manufacture the 3D cellular inclusion significantly influences the reduction in the differential settlement at the open track-bridge transition. Stiffer materials such as rubber tyre, geocomposite and HDPE reduced the differential settlement by 43.4%, 40.3% and 29.8%, respectively. In contrast, softer materials such as woven coir and nonwoven PP geotextiles reduced the differential settlement by 16.7% and 5.4%, respectively.
- Geoinclusions with smaller pocket size are more effective than those with large pocket size.
- The effectiveness of artificial inclusions in reducing the differential settlement depends on the subgrade strength. The reinforcement is more effective when the subgrade strength is high compared to the case when subgrade strength is low.
- The improvement in track performance provided by the cellular geoinclusion also depends on its placement location within the track. In this study, the bottom of the ballast layer is found to be the most effective location for reinforcement.

Thus, the present study demonstrates that 3D cellular geoinclusions effectively reduce the settlement in ballasted railway tracks and possess enormous potential for future use. The essential contribution of this study is the development of a technique that can assist railway engineers in assessing the efficacy of artificial inclusions in enhancing the performance of railway tracks, especially in transition zones. This method may help select the most appropriate placement location, size and type of geoinclusion for deriving maximum potential benefits and optimising the track performance.

This chapter elucidated the beneficial role of 3D cellular geoinclusions in improving the performance of the ballasted railway tracks, especially in the transition zones. The modified computational approach was used to evaluate the effectiveness of these geoinclusions in mitigating the differential settlement at the track transitions. The next chapter discusses the development of 3D FE models of the standard ballasted rail track and the transition zones. The FE analyses complement the findings of the mathematical models developed in this and previous chapters.

CHAPTER 7
NUMERICAL MODELLING OF BALLASTED RAILWAY TRACKS WITH SPECIAL REFERENCE TO TRANSITION ZONES

7.1 General

In the previous chapters, computational methodologies were developed to predict the recoverable and irrecoverable response of the ballasted tracks under train-induced repeated loads. These techniques were successfully validated using the published field data. The developed approaches are computationally efficient, do not require any commercial FE-based software and can facilitate the interpretation of results obtained from other techniques (such as FEM, DEM and BEM). These methodologies also allow the visualisation of the physical laws that are responsible for the observed response. Indeed, the developed computational modelling techniques may prove indispensable tools to quickly obtain accurate and reliable solutions for the engineering problem.

Nonetheless, for a comprehensive analysis of the transition zone problems, the developed computational methodology can be used in conjugation with a numerical technique. The numerical techniques, such as the FE method, offer some features that may complement the results obtained from the methods described in the previous chapters. Some of these features include:

- Incorporation of actual track geometry in the analysis.
- Realistic simulation of the 3D loading due to moving train.
- Availability of a vast range of material models.
- Detailed visualisation of results.

Therefore, FE modelling is deemed necessary in this study for a comprehensive analysis of the behaviour of the transition zone in a railway track. In this chapter, 3D FE models for a standard track and an open track-bridge transition are developed. These models can realistically simulate complex geometries such as ballast profile, rail fasteners and the actual shape of the 3D cellular geoinclusions, and 3D loading due to a moving train.

7.2 3D FE Modelling of Ballasted Railway Track: Case Study of High-Speed Track in Sweden

7.2.1 General

The case study of a high-speed ballasted railway track in Sweden has been used to investigate the reliability and accuracy of the 3D FE modelling in predicting the track response. The track is located along the West Coast Line between Göteborg and Malmö in Sweden. To study the influence of V on the track response, trial test runs of Swedish X-2000 passenger train were made at V ranging between 10 km/h and 200 km/h (Kaynia et al. 2000). The displacement, velocity and acceleration were recorded at different depth of the track and the nearby ground during the individual train passage.

A 3D FE model of the track is developed using ABAQUS (Dassault Systèmes 2018) to predict the transient deformation of the different track layers during the passage of the X-2000 train. **Figure 7.1** shows the FE mesh of the track and nearby ground. The track comprises rail, sleeper, ballast, interface and subgrade layers. The plan dimensions of the model are 40 m (width) × 78.65 m (length), and it consists of 158,309 elements. The mesh comprises of 8-noded linear hexahedral elements of type C3D8R to model the sleeper, track layers and ground. The rail is modelled using Timoshenko beam elements of type B31 with properties identical to UIC 60 rail. The rail is connected to the sleepers (of size 1.25 m × 0.26 m × 0.2 m) using springs (with stiffness 480 MN/m) that represent the rail pad. The sleepers rest on the ballast layers: ballast #1 and ballast #2 of thickness 0.5 and 0.8 m, respectively. A 0.3 m thick interface zone underlies the ballast #2 layer. The subgrade comprises of 3.2 m thick mud layer and multiple clay layers with a combined thickness of 25 m. Only one half of the track is modelled owing to the symmetry. The nodes along the side boundaries are normally fixed, while those along the bottom boundary are fully fixed. A total of 120 sleepers are considered, and the results are reported for the 60^{th} sleeper.

Table 7.1 shows the material properties used in this study for the simulation of track response. The properties of the track components are selected based on the published literature (Hall 2003; Sayeed & Shahin 2016). The behaviour of each component is simulated using a linear-elastic model as a first estimate. A damping ratio of 4% is used for the geotechnical layers.

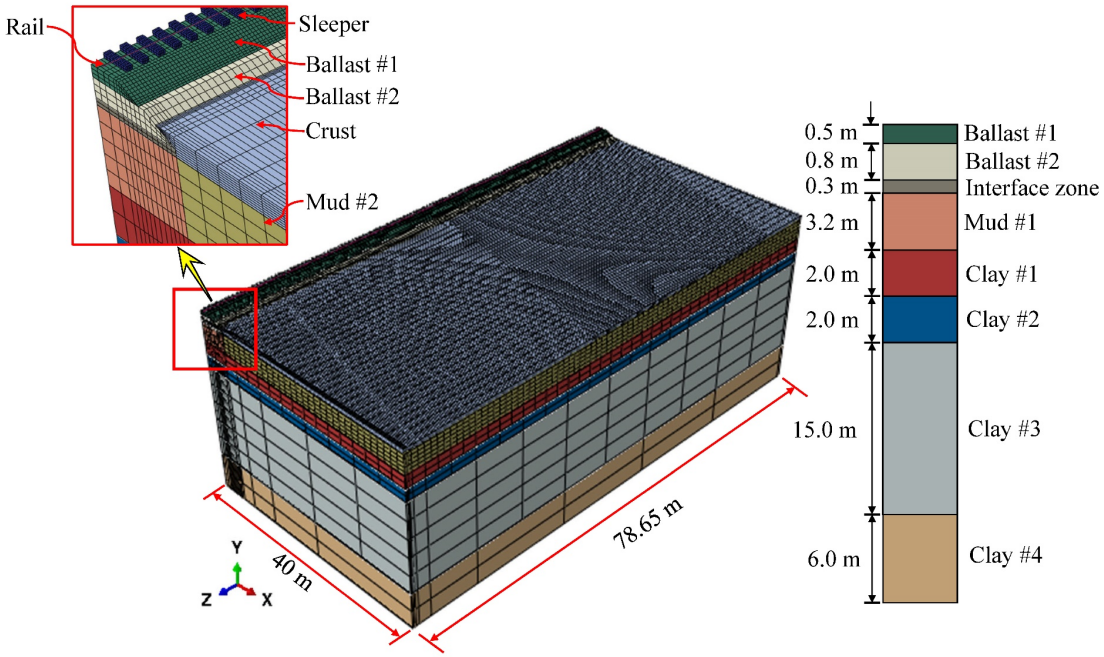

Figure 7.1 3D FE model of the high-speed railway track in Sweden

Table 7.1 Material parameters used for the simulation of the track response

Component	Young's modulus, E (MPa)	Poisson's ratio, ν	Density, ρ (kg/m^3)
Rail	210,000	0.3	7,800
Sleeper	30,000	0.2	2,500
Ballast	134.5	0.3	1,900
Interface	10	0.45	1,700
Crust layer	18	0.45	1,700
Mud layer #1	2.55	0.45	1,260
Mud layer #2	7.3	0.45	1,260
Clay layer #1	10.5	0.45	1,450
Clay layer #2	13.6	0.45	1,450
Clay layer #3	25.26	0.45	1,500
Clay layer #4	53	0.45	1,600

7.2.2 Train-Induced Loading

The moving train load is simulated by applying a time-varying vertical load at different nodes of the rail (known as loading nodes) (Hall 2003). **Figure 7.2** shows the procedure used to calculate the moving wheel loads. In this method, the wheel load is assumed as a

triangular pulse distributed among three loading nodes. With reference to **Figure 7.2**, consider that the wheel is located at the loading node, 'n' at time instant 't_0'. The magnitude of load at nodes n, n+1 and n+2 are Q, 0 and 0, respectively. As the wheel moves towards node n+1, the magnitude of the load at node n decreases, while it increases for node n+1 and reaches a maximum value of Q when the wheel is directly above node n+1 (i.e., at time instant t_1). Similarly, as the wheel approaches node n+2, the load at n+1 decreases and becomes equal to zero as soon as the wheel reaches the node n+2 (at time instant t_2). The resulting load-time history at the three nodes is also shown in **Figure 7.2**. Using a similar procedure, the load-time history during a train passage is calculated at each loading node along the entire track length. In this study, the loading nodes are spaced at equal intervals of 0.65 m, which is the same as the sleeper spacing. The load time history during the passage of Swedish X-2000 high-speed train is first calculated using this procedure and then applied at each node.

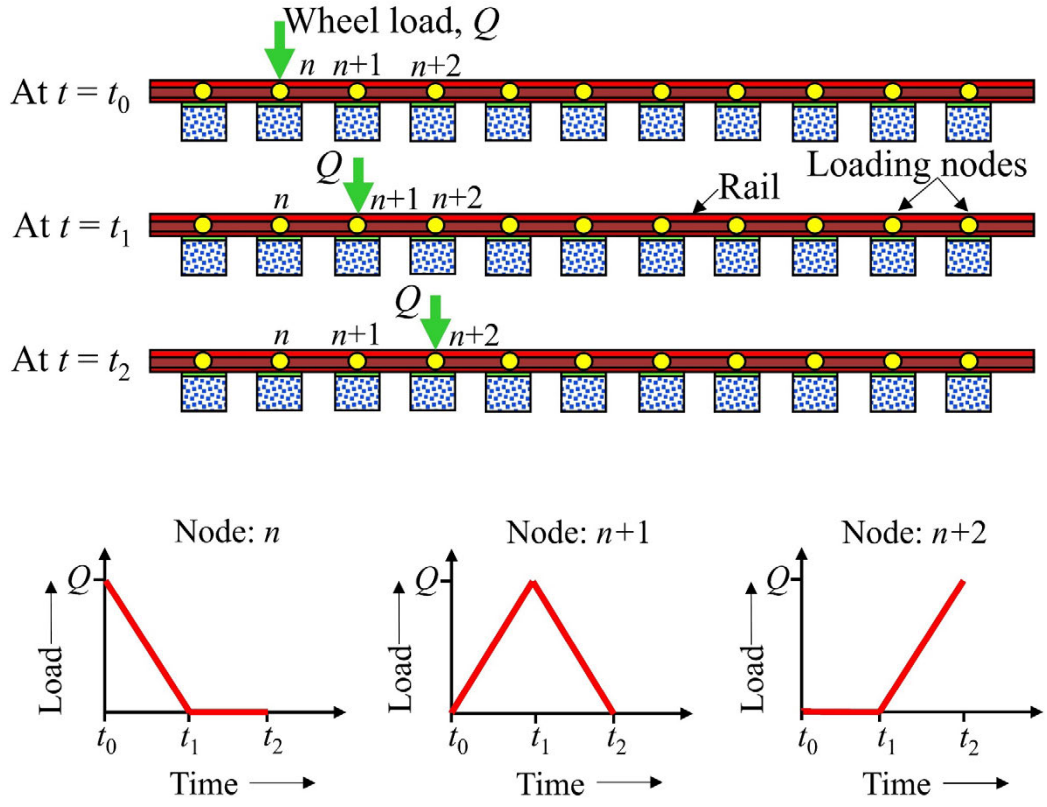

Figure 7.2 Procedure used to calculate the moving wheel loads

7.2.3 Model Validation

The 3D FE model of the high-speed rail track is validated by comparing its results with the field measurements reported by Kaynia et al. (2000). **Figure 7.3** compares the vertical

displacement time-history during the train passage at speed of 70 km/h, 185 km/h, and 200 km/h predicted using the present model with the data recorded in the field investigations. It can be observed that the model predictions are in good agreement with the field measurements. At low speed, 70 km/h, only downward displacement of the track is observed. However, as V increases, the upward displacement becomes apparent. The magnitude of vertical displacement increases with an increase in V in both upward and downward directions. Thus, the FE modelling process adopted in this study is reliable and can be used to predict the response of the railway track accurately.

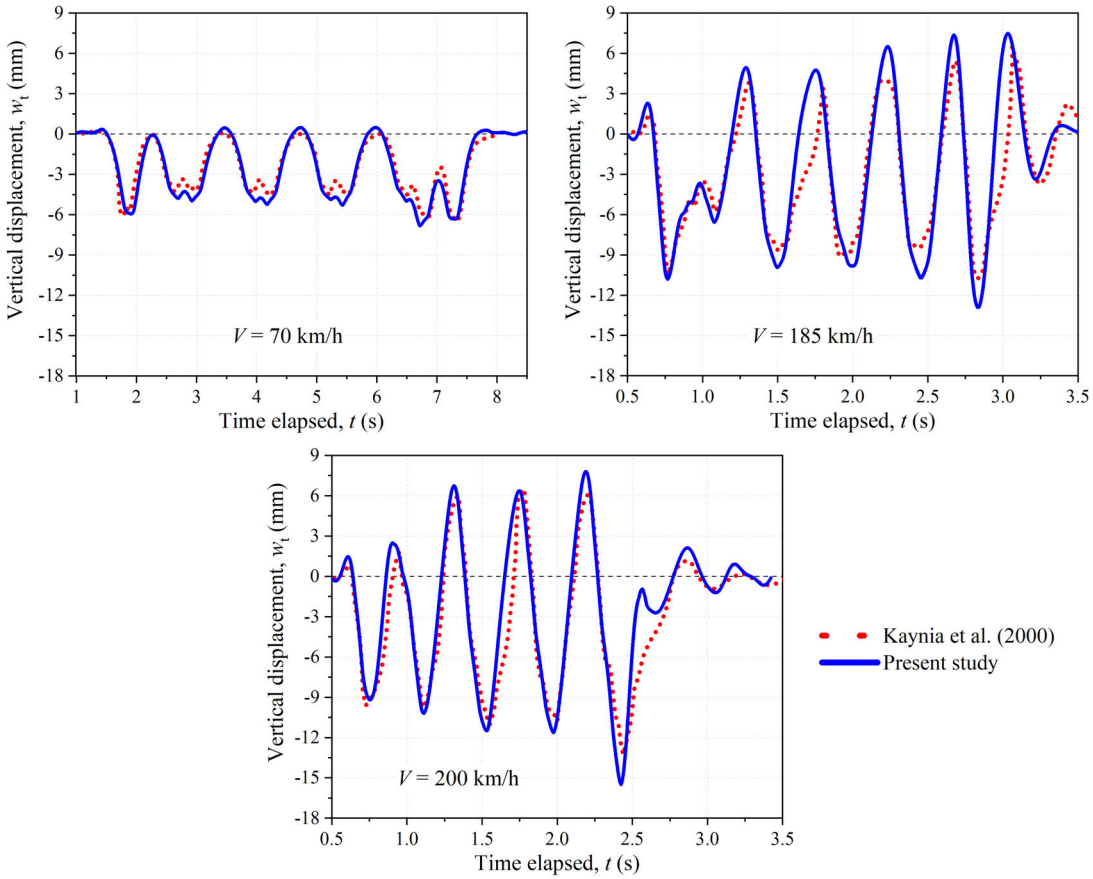

Figure 7.3 Comparison of FE model results with the field data at different train speed

7.3 FE Modelling of Ballasted Railway Track: Case Study of a Bridge Approach along Amtrak's North East Corridor

7.3.1 General

The case study of a bridge approach along Amtrak's North East Corridor in the United States has been used to investigate the reliability and accuracy of the 3D FE modelling technique in predicting the track response near the transition zones. Boler et al. (2018a)

conducted extensive field instrumentation that included MDDs to monitor the displacement of the substructure layers, and strain gauges to measure the wheel load and reaction from the sleeper.

A 3D FE model of the track is developed using ABAQUS (Dassault Systèmes 2018) to predict the transient deformation of the track layers during the passage of the Acela express train. **Figure 7.4** shows the FE mesh of the track and the nearby ground. The track comprises of rail, sleeper, ballast, subballast [referred to as fouled ballast in Boler et al. (2018a)] and subgrade layers. The plan dimensions of the model are 18.2 m (width) × 25 m (length), and it consists of 131,876 elements. The mesh comprises of 8-noded linear hexahedral elements of type C3D8R to model the sleeper, track layers and the ground. The rail is modelled using Timoshenko beam elements of type B32 with properties identical to UIC 60 rail. The rail is connected to the sleepers (of size 1.295 m × 0.274 m × 0.177 m) using springs (with stiffness 480 MN/m) that represent the rail pad. The sleepers rest on the ballast layer of thickness 0.305 m. A 0.127 m thick subballast layer underlies the ballast layer. The subgrade comprises of sandy loam, clayey silt and sandy loam #2 layers of thickness 0.508 m, 0.721 m and 18.938 m, respectively. Only one half of the track is modelled owing to the symmetry. The nodes along the side boundaries are normally fixed, while those along the bottom boundary are fully fixed. A total of 21 sleepers are considered, and the results are reported for the 11th sleeper.

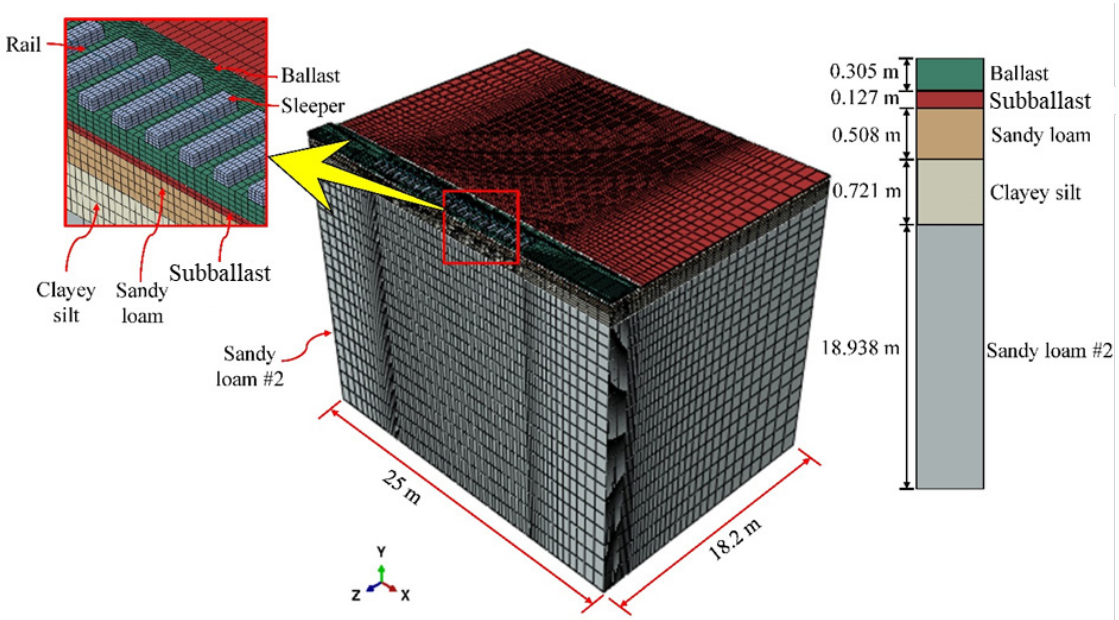

Figure 7.4 3D FE model of the ballasted track near the bridge approach

Table 7.2 shows the material parameters used in the analysis. The properties of the track components are selected based on the published literature (Mishra et al. 2014a; Boler et al. 2018a). The behaviour of each element is simulated using a linear-elastic model as a first estimate. The elastoplastic constitutive models are used in the later analyses to simulate the behaviour of the track substructure layers more realistically. The moving train load is simulated by applying time-varying vertical load at different nodes of the rail, as described in Section 7.2.2. The loading nodes are equally spaced at 0.61 m intervals.

Table 7.2 Material parameters used for the simulation of the response of track near the bridge approach

Component	Young's modulus, E (MPa)	Poisson's ratio, ν	Density, ρ (kg/m^3)
Rail	207,000	0.25	7,850
Sleeper	20,700	0.15	2,500
Ballast	184	0.3	1,990*
Subballast	19	0.4	2,090*
Sandy loam	31	0.4	2,090*
Clayey silt	37	0.4	2,090*
Sandy loam #2	70	0.4	2,090*

*Values taken from Mishra et al. (2014a)

7.3.2 Model Validation

The FE model is validated by comparing the predicted results with the field data reported by Boler et al. (2018a). **Figure 7.5** compares the vertical displacement time-history during the passage of two axles of the Acela express train. It can be observed that the model predictions are consistent with the field measurements. The model slightly overpredicts the displacement of the sandy loam #2 layer; however, the predicted trend is similar to the field measurements. It must be noted that the predicted variation of displacement with time for the ballast layer is slightly different from the field data. This difference may be attributed to the fact that Boler et al. (2018a) modified the actual field data by subtracting the sleeper-ballast gap from ballast displacement. Nevertheless, the FE modelling process adopted in this study is reliable and can be used to predict the

response of the railway track accurately. This model is extended in the subsequent sections to include the bridge and its approach.

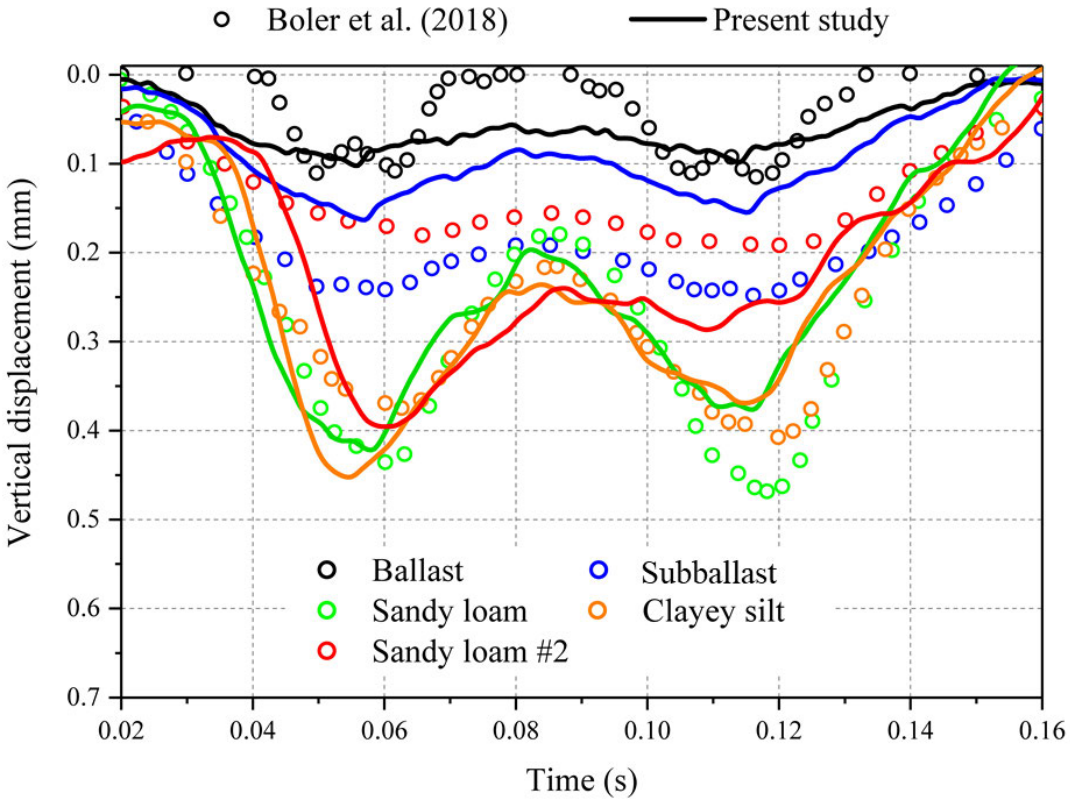

Figure 7.5 Comparison of model predictions with the field data reported by Boler et al. (2018a)

7.4 3D FE Modelling of Transition Zones

7.4.1 General

A 3D FE model of a typical open track-bridge transition is developed using ABAQUS (Dassault Systèmes 2018). The geometry of the transition is based on a section of a railway line along Amtrak's North East Corridor in the United States. The details of the model have been discussed in Section 4.4.1.1. To validate the FE model, the predicted results are compared against the field data reported by Boler et al. (2018a). Subsequently, a parametric study is conducted to investigate the influence of Q_a, V and subgrade properties on the track response.

7.4.2 Model Validation

Figure 7.6 shows a comparison of the predicted results with the field data reported by Boler et al. (2018a) for the track at the open track and near bridge locations. **Table 7.3** lists the values of the parameters used in the analysis. It can be observed that the predicted

vertical deformation for the layers in the open track and near bridge is in close agreement with the field data. The predicted results vary by 1% – 16% from the field data. Thus, the 3D FE model can accurately predict the behaviour of the open track-bridge transition.

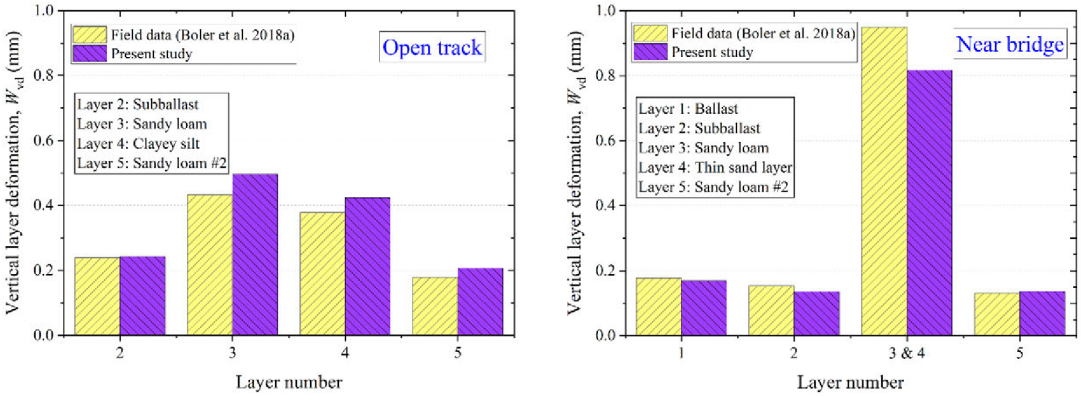

Figure 7.6 Comparison of predicted vertical layer deformation with the field data reported by Boler et al. (2018a)

7.4.3 Results and Discussion

A parametric analysis is conducted to study the influence of Q_a and V on the track response. The values of the parameters used in the analysis are provided in **Tables 7.3** and **7.4**. The behaviour of the ballast layer is simulated using the Drucker-Prager model with a non-associated flow rule. The behaviour of other substructure layers is simulated using the Mohr-Coulomb model with a non-associated flow rule. The values of the constitutive parameters for the substructure layers are selected based on published literature and engineering judgement (Karasev et al. 1977; Rybnikov 1990; Carter & Bentley 2016). The results are reported for a single passage of two bogies from adjacent wagons.

7.4.3.1 Influence of Axle Load

The Q_a is varied from 25.5 t – 30 t to study its effect on the behaviour of the transition zone. **Figure 7.7** shows the variation of vertical displacement with depth at different axle loads. It can be observed that the displacement increases with an increase in Q_a. The vertical displacement at the ballast top for both open track and near bridge sections increases by 17.5%, with an increase in Q_a from 25.5 t to 30 t. This increment in displacement is reasonable as the stresses in the substructure layers increase with an increase in Q_a.

Table 7.3 Material parameters used in the analysis

Component	Young's modulus, E (MPa)	Poisson's ratio, ν	Density, ρ (kg/m^3)
Rail	207,000	0.25	7,850
Sleeper	20,700	0.15	2,500
Rail pad	100	0.45	1,000
Geocell	2,070	0.35	950
Open track:			
Ballast	184	0.3	1,990*
Subballast	19	0.4	2,090*
Sandy loam	31	0.4	2,090*
Clayey silt	37	0.4	2,090*
Sandy loam #2	70	0.4	2,090*
Near bridge:			
Ballast	153	0.3	1,990*
Subballast	80	0.4	2,090*
Sandy loam	33	0.4	2,090*
Thin sand layer	33	0.4	2,090*
Sandy loam #2	123	0.4	2,090*

*Values taken from Mishra et al. (2014a)

Table 7.4 Constitutive parameters for substructure layers

Layer	Constitutive model	Friction angle, φ (°)	Cohesion, c (kPa)	Dilation angle, ψ_d (°)
Ballast	Drucker-Prager	45	1	15
Subballast	Mohr-Coulomb	35	1	5
Sandy loam	Mohr-Coulomb	19	12	1
Clayey silt	Mohr-Coulomb	25	10	0
Sandy loam #2	Mohr-Coulomb	18	18	1
Thin sand	Mohr-Coulomb	24	1	1
Sandy loam #3	Mohr-Coulomb	18	18	1

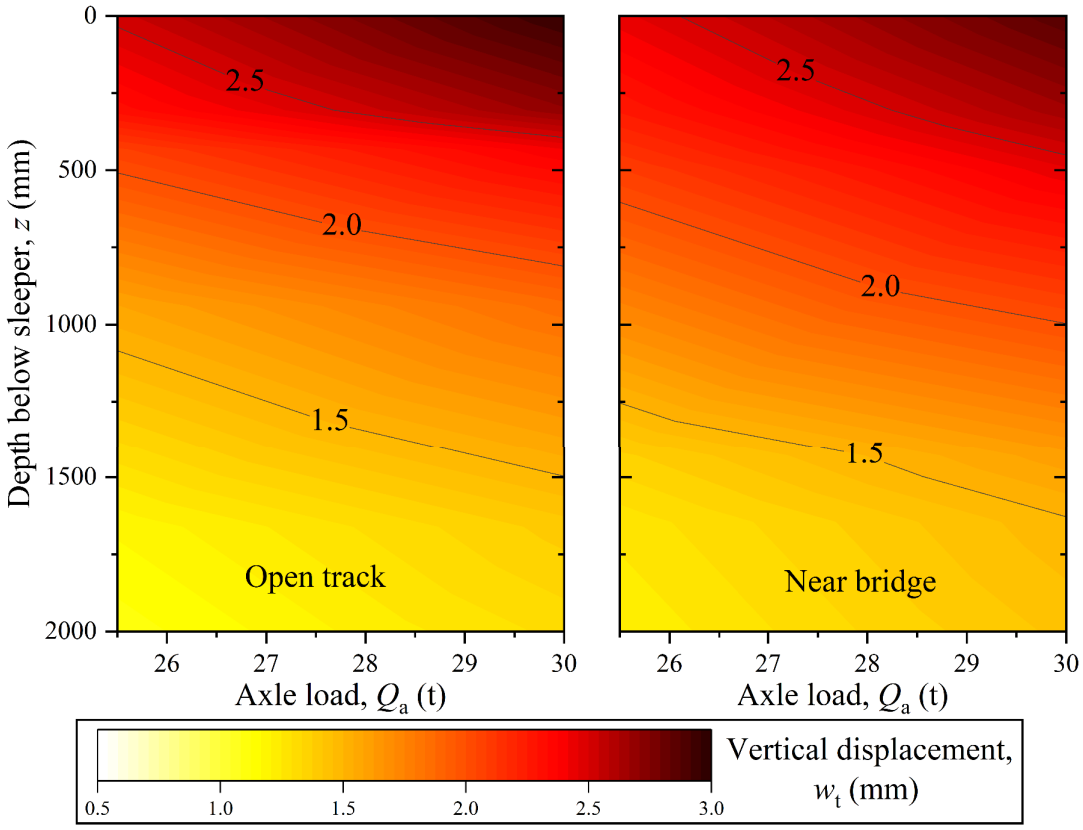

Figure 7.7 Variation of vertical displacement with depth at different axle loads

7.4.3.2 Influence of Train Speed

V is varied from 177 km/h to 250 km/h to study its effect on the behaviour of the open track-bridge transition. **Figure 7.8** shows the variation of maximum vertical displacement along the track length for the two train speeds. It can be observed that the displacement increases with an increase in V. The average displacement increments in open track, near bridge and above bridge sections are 12.2%, 11.8% and 11%, respectively, when V increases from 177 km/h to 250 km/h. Moreover, the differential displacement between near bridge and bridge increases by 11.8% with an escalation in V from 177 km/h to 250 km/h. This amplification in track displacement occurs due to dynamic vehicle-track interaction (which is simulated in this 3D model) and relative velocity of the vehicle with respect to the critical wave propagation velocity of the track-ground system.

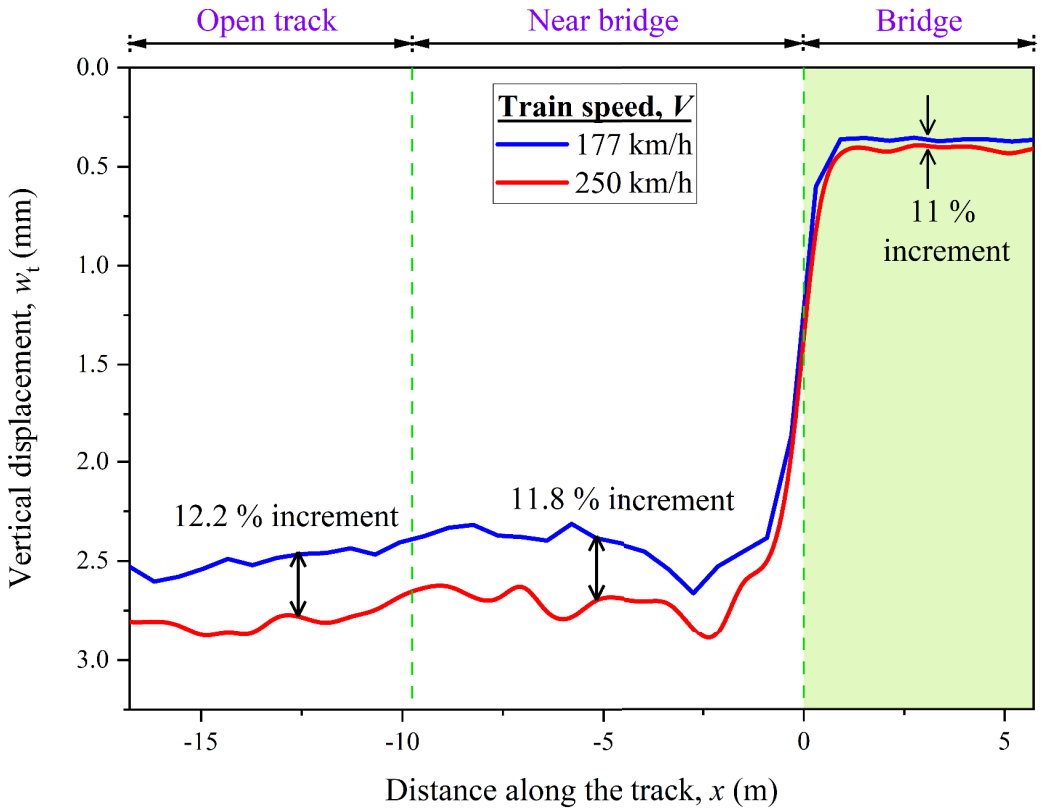

Figure 7.8 Variation of displacement along the length of the track at different train speeds

7.4.3.3 Influence of Subgrade Properties

To study the influence of subgrade properties on track response, the sandy loam layer in the track model is replaced with a loose sand layer, which represents a weak subgrade. The behaviour of weak subgrade is reproduced using the Mohr-Coulomb constitutive model. The values of elastic modulus, Poisson's ratio, friction angle and cohesion of the soft subgrade layer are 15 MPa, 0.3, 36°, 1 kPa, respectively (Hegde & Sitharam 2015). **Figure 7.9** shows the variation of vertical displacement along the track length for the two different types of subgrade. It can be observed that the vertical displacement is much higher for the track with a weak subgrade (loose sand) than that with a relatively strong subgrade (sandy loam). The differential displacement between the stiffer (bridge) and softer side (near bridge) for the track with loose sand is 51.2% higher than the track with sandy loam. Therefore, the subgrade soil in the softer side of the transition must be strengthened using ground improvement techniques for improving the performance of the transition zone.

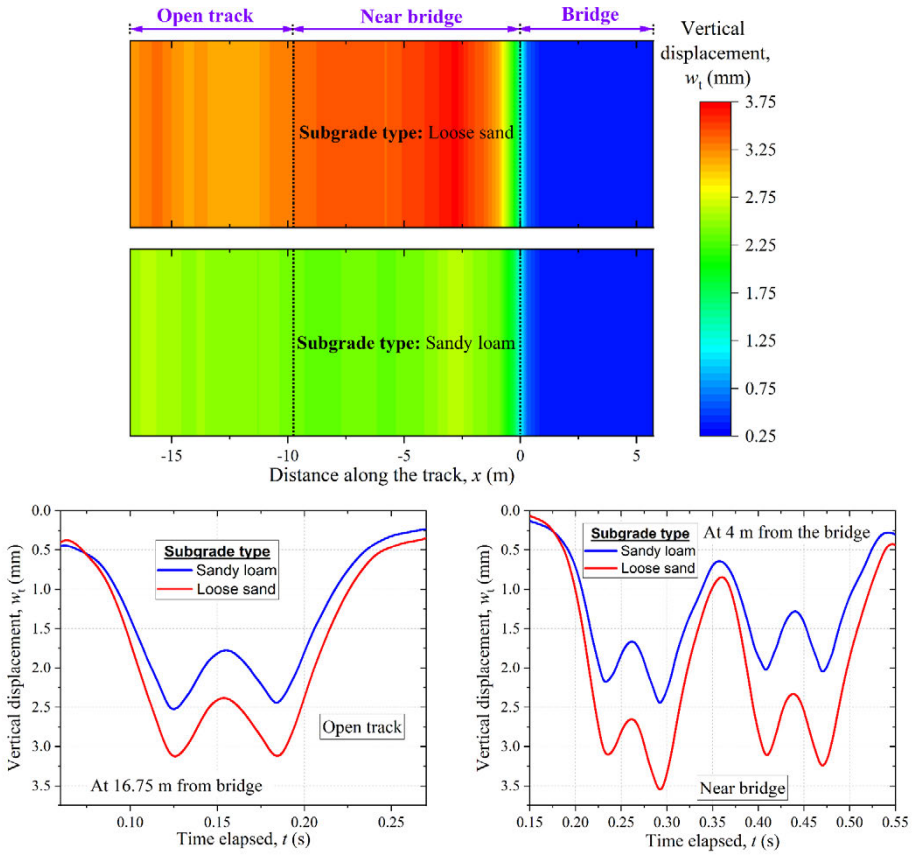

Figure 7.9 Variation of vertical displacement along the track length for different subgrade types

7.5 Assessing the Adequacy of Geocells in Improving the Performance of an Open Track-Bridge Transition Using 3D FE Modelling

7.5.1 General

The primary cause of the geometry degradation problem in the critical regions of a railway line is the uneven displacement, which occurs due to the inhomogeneous support conditions along the track length. Previous studies have demonstrated that cellular geoinclusions such as geocells or scrap rubber tyres can be employed to improve the strength and stiffness of the granular materials (Leshchinsky & Ling 2013b; Yang & Han 2013). Consequently, employing geoinclusions in the critical zones may reduce the uneven track displacement and improve their performance. This section of the chapter examines the adequacy of reinforcing the track substructure layers using 3D cellular geoinclusions in mitigating the differential movement in the critical zones. Note that a comprehensive review of existing literature on the beneficial aspects of employing cellular geoinclusions in the railway tracks was presented in CHAPTER 6.

To assess the efficacy of employing 3D cellular geoinclusions in improving the performance of the transition zones, a 3D FE model of a typical open track-bridge transition is developed (see Section 7.4). The numerical model is successfully validated using the data available in the literature. Subsequently, a parametric study is conducted to investigate the influence of geoinclusion material type and its location within the track on the behaviour of the transition zone.

7.5.2 Model Development

A 3D FE model of an open track-bridge transition zone is developed using ABAQUS (Dassault Systèmes 2018). This section describes the modelling of the geocells that are used in the transition, and the details of the other parts of the model have been discussed elsewhere (see Sections 4.4.1 and 7.4). **Figure 7.10** shows the placement location for the geocell layer in the transition zone, which include the bottom of the ballast layer, inside the subballast layer and at the top of the subgrade. The thickness of the geocell layer in this study is considered as 150 mm. The width and length of the geocell layer are taken as 2.2 m and 9.75 m, respectively. The actual shape of the geocell is modelled and is discretised using eight-noded 3D brick elements of type C3D8R. The entire geocell layer comprises 44,146 elements, and it is simulated as an embedded part inside the substructure layer in which it is placed. **Table 7.3** shows the material parameters used in the simulation. The geocell is modelled as a linear-elastic material similar to the previous studies (see Han et al. 2011; Leshchinsky & Ling 2013b; Satyal et al. 2018).

7.5.3 Results and Discussion

7.5.3.1 Location of Geocell

The effectiveness of geocell in reducing the differential movement at a transition zone depends on its location within the track. Therefore, the geocell layer is provided at the ballast bottom, within subballast and subgrade top (as shown in **Figure 7.10**) to investigate its most effective position for the open track-bridge transition considered in this study. **Figure 7.11** shows the variation of vertical displacement along the track when geocell is provided at different locations within the track. It can be observed that the geocell reinforcement reduces the differential displacement at the track transition. However, the reduction is very small. Note that in Section 6.12, it was shown that the geocells significantly reduce the differential movement at the transition zone. This

contrasting behaviour may be due to the fact that the results presented in this section are for a single passage of two bogies (cumulative tonnage of 0.00012 MGT), whereas the results in Section 6.12 are for a cumulative tonnage of 10 MGT – 20 MGT. As the number of bogie passages increase, more reduction in the differential settlement is expected for the geocell reinforced track transition. Nonetheless, providing the geocell at the subgrade top leads to the highest reduction in the differential settlement, in this case, followed by geocell at the subballast and ballast top. This is because the contribution of the top layer of the subgrade is greater than that of the overlying ballast and subballast layers. Consequently, the subgrade top proved to be the most effective location for geocell reinforcement in this case.

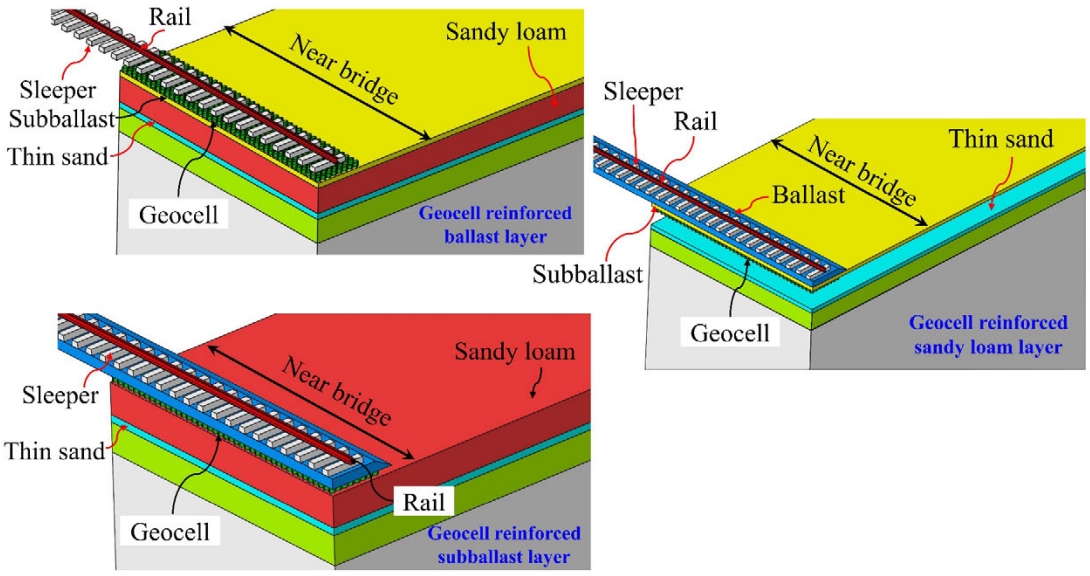

Figure 7.10 Details of the placement of geocells in the transition zone

7.5.3.2 Effect of Geocell Material

The magnitude of improvement provided by a geocell depends on the material used for its manufacture. To investigate the influence of geocell material on track response, the elastic modulus, E_m of the geocell is varied between 2 GPa to 200 GPa. The geocell in this study is provided at the top of the subgrade, which is the most effective location, as observed in the previous section. **Figure 7.12** shows a comparison of the performance improvement provided by geocells with different stiffness. The displacement has been normalised with respect to the mean value of track displacement in the stiffer zone (bridge). It can be observed that the differential displacement decreases with an increase in E_m. This indicates that the geocells manufactured using stiffer materials provide more

improvement in track response as compared to the softer materials. Similar results were also obtained in Section 6.11.1.

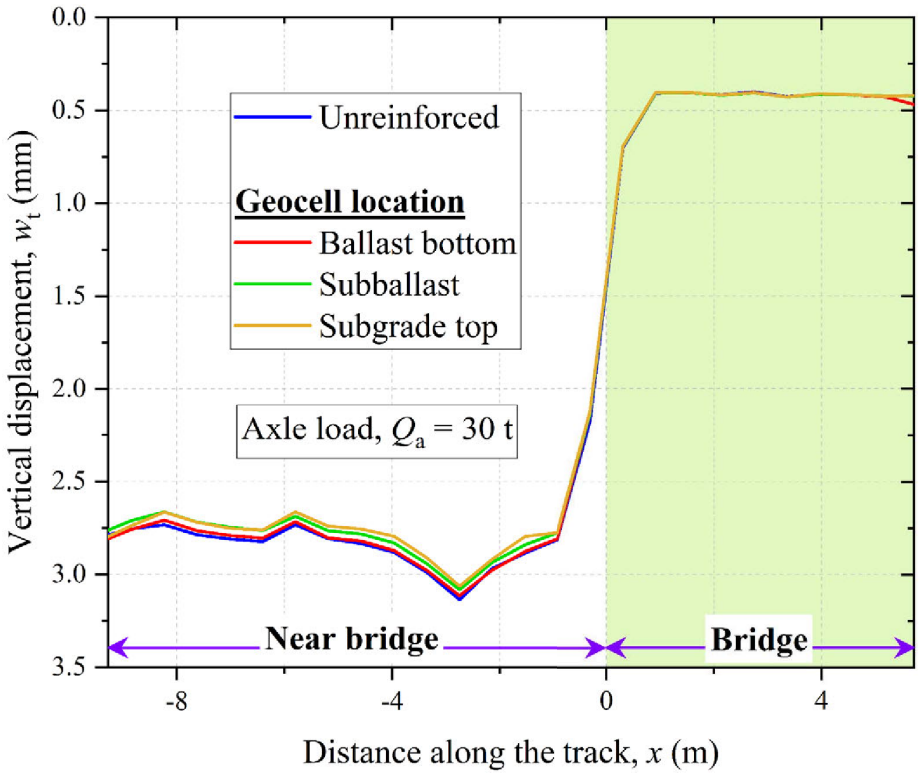

Figure 7.11 Variation of vertical displacement along the track length when geocell is provided at different locations

7.5.3.3 Analysis of Sleeper-Ballast Gap

One of the main advantages of 3D FE modelling is its capability to capture the formation of sleeper-ballast gaps near the bridge approach. **Figure 7.13** shows the generation of sleeper-ballast gaps in the near bridge region at different axle loads (within 3 m from the bridge). It can be observed that a gap of 0.61 mm is formed at the final sleeper of the softer zone (near bridge region) after single passage of two bogies. This gap is formed in the last five sleepers of the softer zone, and its size decreases with an increase in distance from the bridge. With an increase in Q_a from 25.5 t – 30 t, the maximum gap size increases by 13%.

It can also be observed that the geocell is effective in reducing the size of the sleeper-ballast gap. At 30 t axle load, the gap size reduces by 29% on reinforcing the substructure

layers using geocell. Thus, the geocells also help in reducing the size of the sleeper-ballast gap formed in the final sleepers of the softer side.

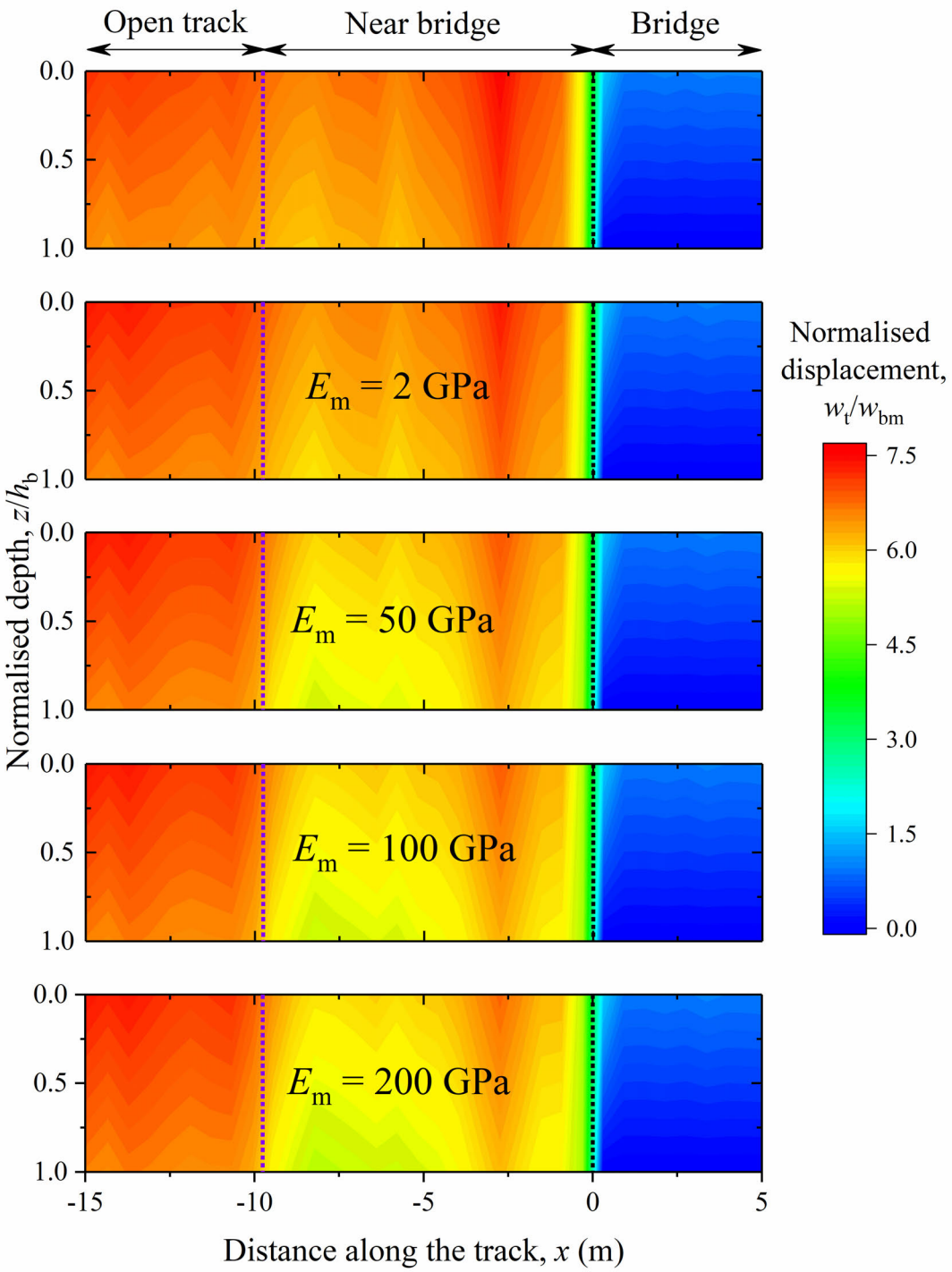

Figure 7.12 Variation of vertical displacement along the track length when geocell with different stiffness are provided in the subgrade

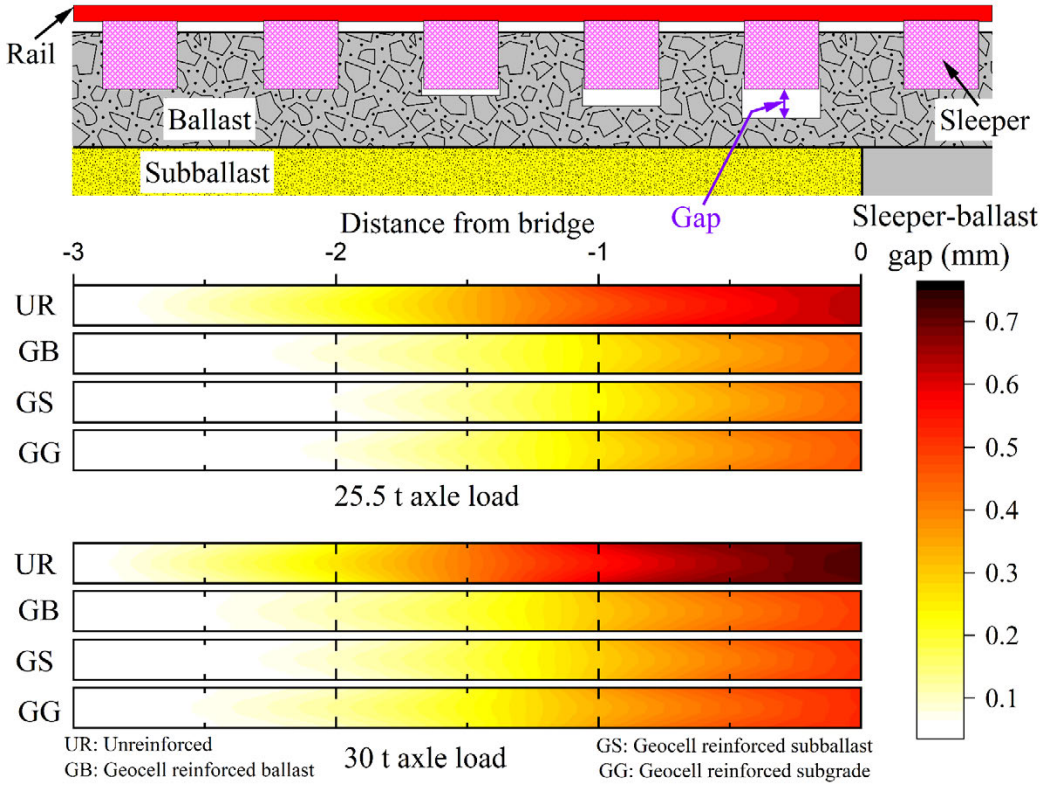

Figure 7.13 Formation of sleeper-ballast gaps near the bridge approach

7.5.4 Model Validation

To validate the ability of FEM in accurately simulating the improvement provided by the geocells, the results predicted from the FE analysis are compared with the experimental data reported by Satyal et al. (2018). **Table 7.5** lists the input parameters used in the simulations. Satyal et al. (2018) conducted plate loading tests on a large-scale soil box comprising a layer of soft subgrade overlain by a ballast layer with and without geocell reinforcement. A woven PE geotextile was also provided at the ballast-subgrade interface for the tests involving geocell reinforcement. **Figure 7.14** shows a comparison of the results predicted using the 3D FE model with those obtained through experiments by Satyal et al. (2018). It can be observed that the predicted plate settlement and ballast-subgrade interface pressure are in a good agreement with the experimental data for both unreinforced and geocell reinforced ballast cases. The discrepancies between the predicted and experimental data at the subgrade centre and 200 mm from the centre may be due to the inability of the selected constitutive model to accurately predict the response of the ballast and subgrade soil. The accuracy of the predictions may be increased further by employing advanced constitutive models. Nevertheless, the settlement trends matched reasonably well for both the unreinforced and reinforced cases.

Table 7.5 Constitutive parameters for substructure layers (Satyal et al. 2018)

Layer	Constitutive model	Young's modulus, E (MPa)	Poisson's ratio, ν	Friction angle, φ (°)	Dilation angle, ψ_d (°)
Ballast	Drucker-Prager	30	0.4	45	10
Subgrade	Drucker-Prager	8.5	0.35	1	1
Geocell	Linear elastic	380	0.35	–	–
Geotextile	Linear elastic	380	0.35	–	–

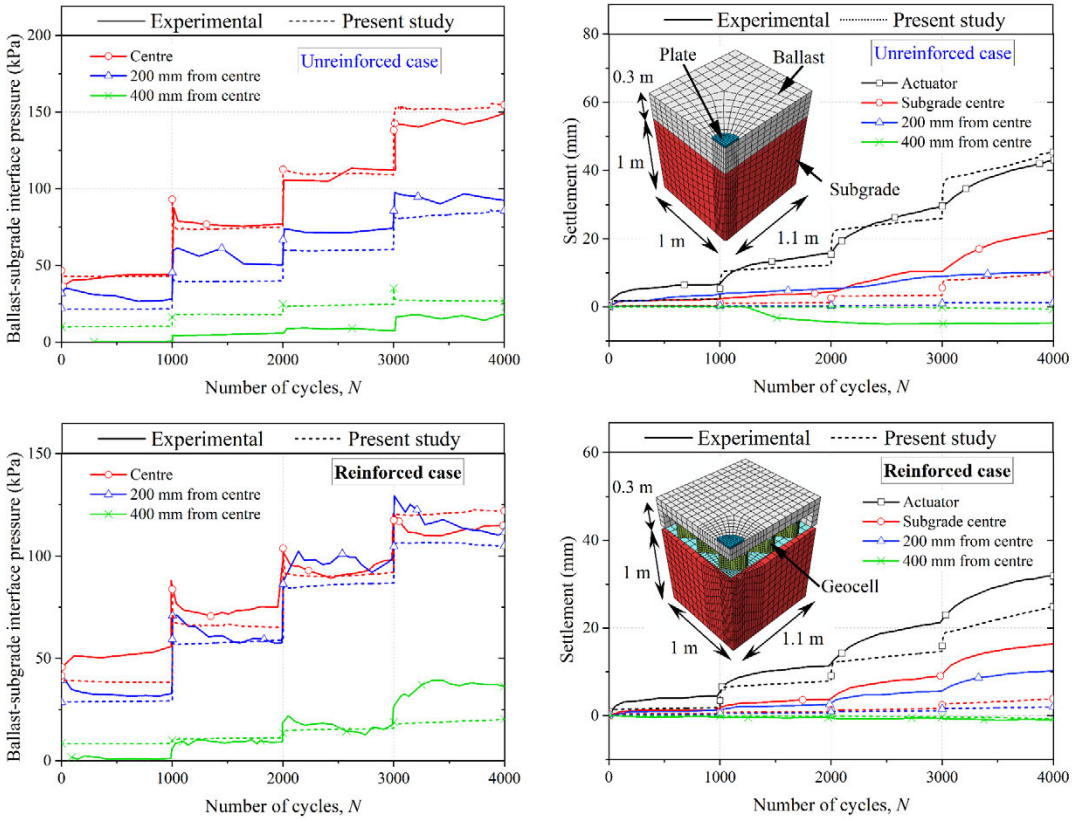

Figure 7.14 Comparison of predicted results with the experimental data reported by Satyal et al. (2018)

7.5.5 Limitations

The following are the limitations of the 3D FE analyses:

- The non-linear elasticity observed in the geomaterials is ignored.
- The effect of seasonal fluctuations in the water content in the form of wetting and drying cycles, mud pumping, unsaturated track materials is neglected.
- Computationally intensive and require huge data storage capability.

- Interpretation of predicted results is difficult.

7.5.6 Concluding Remarks

The results from the study suggest that the use of geocells may improve the performance of the railway tracks in the transition zones. However, the magnitude of improvement depends on several factors, such as the material used to manufacture the geocells and their location within the track. The study also highlighted the capability of the 3D FE modelling technique to:

- Simulate the formation of sleeper-ballast gaps on the softer side of the transition.
- Incorporate the effect of dynamic wheel-rail interaction in the analysis.
- Model the actual honeycomb shape of the geocells.

The mathematical models developed in the previous chapters are unable to simulate these aspects. Therefore, the numerical modelling techniques developed in this chapter complement the results obtained from the mathematical models.

CHAPTER 8
CONCLUSIONS

In this thesis, a novel computational methodology is developed for evaluating the performance of ballasted railway tracks under train-induced repeated loading. This methodology is applied to predict the behaviour of the transition zones, which are one of the weakest locations along a railway line. The effectiveness of various countermeasures in improving the performance of the transition zones is then assessed. The accuracy of the predictions is subsequently improved by incorporating the effect of PSR on the track response under moving train loads. The beneficial role of 3D cellular geoinclusions in improving the track performance is also comprehensively studied. To this end, a novel semi-empirical model is developed for computing the additional confinement provided by these cellular inclusions. Subsequently, this approach is incorporated into the computational methodology developed for evaluating the track behaviour and the performance improvement provided by geoinclusions is investigated. 3D FE analyses of the standard railway track and transition zones are conducted to complement the findings from the computational model and gain insight into the aspects that the mathematical approach is unable to simulate. The outcomes of this study have huge potential to influence the real-world design implications and maintenance planning of a standard ballasted rail track as well as the transition zones along the railway line. The approaches developed in this study are original, simple yet elegant, and can enhance, if not fully replace, present complex track modelling procedures for anticipating the behaviour of ballasted rail tracks at normal and transition zones. The methodologies illustrated in this thesis can also be used for selecting appropriate strategies to improve the track performance.

The subsequent sections highlight the conclusions that can be drawn from the present study:

8.1 Computational Methodology for Evaluating the Transient and Long-Term Performance of Railway Tracks

8.1.1 Track Response Prediction Using Integrated Loading, Resiliency and Settlement Models

- The behaviour of the ballasted railway tracks under train-induced repetitive loading can be accurately evaluated by combining the track loading, resiliency and settlement models. The simplistic representation of substructure layers as lumped masses connected by springs and dashpots (termed as track resiliency model) is adequate for evaluating the transient response of the track. Whilst the empirical settlement models can be integrated with the track resiliency model to compute the irrecoverable deformations accumulated in the substructure layers and thus, evaluate the long-term track performance.
- A parametric investigation using this integrated approach reveals that the irrecoverable deformation in the substructure layers is sensitive to the resilient modulus and thickness of individual layers. For instance, the cumulative average irrecoverable strain in the subgrade layer (after a tonnage of 100 MGT) decreased by 9%, 3.5% and 99% with an increase in ballast (138 MPa to 551 MPa), subballast (69 MPa to 276 MPa) and subgrade modulus (14 MPa to 276 MPa), respectively. Similarly, the cumulative average irrecoverable strain in the subgrade layer (after a tonnage of 100 MGT) decreased by 31%, 29 % and 87% with an increase in ballast (0.15 m to 0.6 m), subballast (0.15 m to 0.45 m) and subgrade thickness (1 m to 10 m), respectively.
- The response of each track substructure layer to train-induced loading is affected by the neighbouring layers, and the incorporation of a multi-layered track structure enables a more accurate prediction of track behaviour.

8.1.2 Track Response Prediction Using Geotechnical Rheological Model

- A mechanistic approach involving plastic slider elements for computing the irrecoverable deformations accumulated in the substructure layers can accurately predict the long-term performance of the ballasted railway tracks. The addition of slider elements in the track model is a significant improvement over the aforementioned integrated approach that relies on empirical settlement models for evaluating the cumulative deformations.

- Using the geotechnical rheological track model, a parametric investigation elucidates the significant influence of axle load, train speed and granular layer thickness on the track behaviour. An increase in the axle load can substantially increase the cumulative deformation in the existing tracks (143% increase in settlement on increasing axle load from 20 t to 30 t), resulting in track geometry degradation. The magnitude of settlement accumulated in a track also increases with an increase in train speed (50% increase in settlement on increasing train speed from 100 km/h to 200 km/h). Moreover, an increment in the total thickness of the granular layers considerably reduces the settlement accumulated in the subgrade layer (56% reduction in subgrade settlement with an increase in granular layer thickness from 0.45 m to 0.9 m).

8.1.3 Application of the Geotechnical Rheological Model to Transition Zones

- The novel geotechnical rheological model can accurately simulate the behaviour of the tracks with varied support conditions along the longitudinal direction that are encountered in the transition zones. This computational approach can also predict the differential settlements, which are major concerns for track transitions.
- The developed approach is a quick and straightforward technique that does not require any commercial FE based software in contrast to existing approaches that rely on these software.
- The developed methodology serves as a tool to assess the performance of different remedial measures in mitigating the differential settlement at the transition zone.
- The application of the rheological model to a typical open track-bridge transition highlighted that an increase in axle load exacerbates the track geometry degradation problem. For instance, the differential settlement between the softer and stiffer side of the transition increased by 25% and 26 % with an increase in axle load from 20 t to 25 t and from 25 t to 30 t, respectively, after a cumulative tonnage of 25 MGT. Therefore, it is essential to provide remedial strategies in the transitions on which heavier trains are anticipated in future.
- The use of thicker granular layers reduced the differential settlement at the open track-bridge transition considered in this study. This technique performed well because the subgrade layer was the primary contributor to the differential settlement, and a thick granular layer reduced the cumulative subgrade deformation.

- The countermeasures intended to enhance the subgrade strength may be more effective than the techniques aimed to improve the stiffness of granular layers for transition zones with weak/soft subgrade. However, this countermeasure (subgrade strength increment) may be inappropriate for the transition zones where the granular layers are major contributors to the differential settlement.
- Accurate identification of the primary cause of the differential settlement problem in a transition zone is crucial for selecting the most appropriate mitigation strategy.

8.2 Improving the Accuracy of the Computational Methodology by Incorporating the Effect of Principal Stress Rotation

- The effect of PSR on track response can be adequately incorporated by modifying the constitutive relationship for the plastic slider elements. This modification is achieved by rendering the yield surface, potential surface, and hardening rule as a function of the angle between major principal stress direction and vertical.
- This analysis revealed that the cumulative track deformation is significantly underestimated if PSR is disregarded in the analysis, which may have severe consequences while selecting an adequate granular layer thickness. In this study, the settlement after a cumulative tonnage of 20 MGT at 25 t axle load is underestimated by 16% if PSR is disregarded.
- PSR increases the cumulative differential settlement at a transition zone, which aggravates with an increase in the axle load (46% increment in differential settlement with an increase in axle load from 20 t to 27 t).
- The findings from this study emphasised the inclusion of the PSR effect in the computational models for accurate prediction of the behaviour of railway tracks, especially at the transition zones.

8.3 Performance Improvement of Ballasted Rail Tracks Using 3D Cellular Geoinclusions

8.3.1 Semi-Empirical Model for Evaluating Extra Confinement Offered by Geoinclusions

- A semi-empirical model based on Hooke's law and hoop tension theory can adequately evaluate the additional confinement provided by the cellular geoinclusions under a 3D stress state.

- The magnitude of additional confinement provided by a geoinclusion is highly sensitive to the stress state (axisymmetric, plane-strain and 3D), the material used to manufacture the inclusion and the infill properties.
- The simplification of the 3D stress state to plane-strain or axisymmetric stress states yields conservative or over-predicted results, respectively.

8.3.2 Influence of Geoinclusion Reinforcement on Track Performance

- The geoinclusion reinforcement possesses enormous applications in the railway tracks and can be employed to improve the performance of the transition zones. However, the magnitude of improvement provided by the inclusions depends on several factors such as its location within a track, size and material used for its manufacture, axle load and subgrade properties.
- Stiffer materials such as rubber tyre, geocomposite and HDPE reduced the differential settlement at the open track-bridge transition considered in this study by 43.4%, 40.3% and 29.8%, respectively. In contrast, softer materials such as woven coir and nonwoven PP geotextiles reduced the differential settlement by 16.7% and 5.4%, respectively.
- Geoinclusions with small pocket size are found to be more effective than those with large pocket size. Moreover, the geoinclusions are more potent when the subgrade strength is high.

8.4 Numerical Modelling of the Ballasted Rail Tracks

- The 3D FE modelling of the ballasted rail tracks showed similar trends as those predicted using the novel computational methodology developed in this study. The track displacement increased with an increase in axle load and train speed. For instance, the vertical displacement increased by 17.5% and 12% with an increase in axle load (25.5 t to 30 t) and train speed (177 km/h to 250 km/h), respectively.
- The results showed that the subgrade soil in the softer side of a transition must be strengthened using ground improvement techniques for improving the performance of the transition zone.
- In addition to reducing the differential movement between the stiffer and softer side of a transition zone, the use of geocells also decreases the size of the sleeper-ballast gaps that form in the final sleepers of the softer side.

8.5 Recommendations for Future Work

This thesis provides novel methodologies for computing the transient and long-term performance of the railway tracks under repeated train loads with particular reference to transition zones. These methodologies are validated using the field data and complemented with the findings of 3D FE analyses. This work includes the first-ever attempt to incorporate the plastic slider elements to simulate the material plasticity in a railway track model. Since it is the first-ever attempt, there is ample scope for future research work to improve the accuracy of the predictions further. The future scope of this research work includes:

- Incorporation of the vehicle-track interaction in the geotechnical rheological model for more accurate simulation of the loads transmitted to the track.
- Consideration of train-induced loads in the longitudinal and transverse track directions.
- Consideration of the non-uniform distribution of sleeper-ballast contact pressure. The sleeper-ballast contact pressure in this study is assumed to be uniformly distributed. However, in real tracks, the contact pressure distribution is highly non-uniform and time-dependent, i.e., it depends on the cumulative tonnage that the track has experienced.
- Replacing viscous damping with hysteretic damping, which is a more realistic representation of the behaviour of geomaterials.
- Incorporating the non-linear elasticity observed in the geomaterials. The present approach considers constant values of elastic modulus and Poisson's ratio to represent material elasticity. However, for geomaterials, these parameters are generally non-linear with respect to strain.
- Incorporating the variation in stiffness and damping of the track substructure layers on account of cumulative deformations.
- Addressing the effect of seasonal fluctuations in the water content in the form of wetting and drying cycles, frost heave, mud pumping, unsaturated track materials and consolidation on the response of the ballasted railway tracks.
- Considering the non-uniform distribution of additional confining pressure with depth provided by the cellular geoinclusions. In this study, the additional confining pressure is assumed to be constant along the height of the geoinclusion. However, in reality, this distribution is non-uniform.

- Considering the bending of geoinclusions under the application of vertical loads in the additional confinement model.

REFERENCES

Ahlbeck, D.R., Meacham, H.C. & Prause, R.H. 1978, 'The development of analytical models for railroad track dynamics', in A.D. Kerr (ed.), *Railroad Track Mechanics and Technology*, Pergamon, London, pp. 239-63.

Ahlvin, R.G. & Ulery, H.H. 1962, 'Tabulated values for determining the complete pattern of stresses, strains, and deflections beneath a uniform circular load on a homogeneous half space', *Highway Research Board Bulletin*, no. 342, pp. 1-13.

Al-Qadi, I. & Hughes, J.J. 2000, 'Field evaluation of geocell use in flexible pavements', *Transportation Research Record*, vol. 1709, no. 1, pp. 26-35. https://doi.org/10.3141/1709-04.

Altaee, A., Evgin, E. & Fellenius, B. 1992, 'Finite element validation of a bounding surface plasticity model', *Computers & structures*, vol. 42, no. 5, pp. 825-32. https://doi.org/10.1016/0045-7949(92)90193-4.

Altuhafi, F.N., Jardine, R.J., Georgiannou, V.N. & Moinet, W.W. 2018, 'Effects of particle breakage and stress reversal on the behaviour of sand around displacement piles', *Géotechnique*, vol. 68, no. 6, pp. 546-55. https://doi.org/10.1680/jgeot.17.P.117.

Ansell, P. & Brown, S.F. 1978, 'A cyclic simple shear apparatus for dry granular materials', *Geotechnical Testing Journal*, vol. 1, no. 2, pp. 82-92.

AREA 1978, *Manual of recommended practice*, American Railway Engineering Association, Washington D.C., USA.

Asset Standards Authority 2018, *T HR CI 12110 ST-Earthworks and Formation*, Transport for NSW, New South Wales.

Australian Rail Track Corporation 2006, *RTS 3430 - Track Reconditioning Guidelines*, Australian Rail Track Corporation, NSW.

Banerjee, L., Chawla, S. & Dash, S.K. 2020a, 'Application of geocell reinforced coal mine overburden waste as subballast in railway tracks on weak subgrade', *Construction and Building Materials*, vol. 265, p. 120774. https://doi.org/10.1016/j.conbuildmat.2020.120774.

Banerjee, L., Chawla, S. & Dash, S.K. 2020b, 'Performance Evaluation of Coal Mine Overburden as a Potential Subballast Material in Railways with Additional Improvement Using Geocell', *Journal of Materials in Civil Engineering*, vol. 32, no. 8, p. 04020200. https://doi.org/doi:10.1061/(ASCE)MT.1943-5533.0003269.

Banimahd, M., Woodward, P., Kennedy, J. & Medero, G. 2013, 'Three-dimensional modelling of high speed ballasted railway tracks', *Proceedings of the Institution of Civil Engineers - Transport*, vol. 166, no. 2, pp. 113-23. https://doi.org/10.1680/tran.9.00048.

Banimahd, M., Woodward, P.K., Kennedy, J. & Medero, G.M. 2012, 'Behaviour of train–track interaction in stiffness transitions', *Proceedings of the Institution of Civil Engineers - Transport*, vol. 165, no. 3, pp. 205-14. https://doi.org/10.1680/tran.10.00030.

Basu, D. & Kameswara Rao, N.S.V. 2013, 'Analytical solutions for Euler-Bernoulli beam on visco-elastic foundation subjected to moving load', *International Journal for Numerical and Analytical Methods in Geomechanics*, vol. 37, no. 8, pp. 945-60. https://doi.org/10.1002/nag.1135.

Bathurst, R.J. & Knight, M.A. 1998, 'Analysis of geocell reinforced-soil covers over large span conduits', *Computers and Geotechnics*, vol. 22, no. 3-4, pp. 205-19. https://doi.org/10.1016/S0266-352X(98)00008-1.

Bathurst, R.J. & Rajagopal, K. 1993, 'Large-scale triaxial compression testing of geocell-reinforced granular soils', *Geotechnical Testing Journal*, vol. 16, no. 3, pp. 296-303.

Biabani, M.M. 2015, 'Behaviour of geocell-reinforced subballast under cyclic loading in plane strain condition', PhD thesis, University of Wollongong, Wollongong, Australia.

Bian, X., Jiang, H. & Chen, Y. 2010, 'Accumulative deformation in railway track induced by high-speed traffic loading of the trains', *Earthquake Engineering and Engineering Vibration*, vol. 9, no. 3, pp. 319-26. https://doi.org/10.1007/s11803-010-0016-2.

Bian, X., Li, W., Qian, Y. & Tutumluer, E. 2020, 'Analysing the effect of principal stress rotation on railway track settlement by discrete element method', *Géotechnique*, vol. 70, no. 9, pp. 803-21. https://doi.org/10.1680/jgeot.18.P.368.

Boler, H., Mishra, D., Hou, W. & Tutumluer, E. 2018a, 'Understanding track substructure behavior: Field instrumentation data analysis and development of numerical models', *Transportation Geotechnics*, vol. 17, pp. 109-21. https://doi.org/10.1016/j.trgeo.2018.10.001.

Boler, H., Mishra, D., Tutumluer, E., Chrismer, S. & Hyslip, J.P. 2018b, 'Stone blowing as a remedial measure to mitigate differential movement problems at railroad bridge approaches', *Proceedings of the Institution of Mechanical Engineers, Part F: Journal of Rail and Rapid Transit*, vol. 233, no. 1, pp. 63-72. https://doi.org/10.1177/0954409718778654.

Briaud, J.L., James, R.W. & Hoffman, S.B. 1997, *Settlement of bridge approaches (the bump at the end of the bridge)*, NCHRP Synthesis of Highway Practice 234, Transportation Research Board, Washington DC.

British Railways Board 1993, *GM/TT0088 - Permissible track forces for railway vehicles*, Group Standards, Railway Technical Centre, Derby.

British Railways Board 1995, *GM/RC2513 - Commentary on permissible track forces for railway vehicles*, Safety & Standards Directorate, Railtrack, Railway Technical Centre, London.

Brown, S.F. 1996, 'Soil mechanics in pavement engineering', *Géotechnique*, vol. 46, no. 3, pp. 383-426. https://doi.org/10.1680/geot.1996.46.3.383.

Brown, S.F., Lashine, A.K.F. & Hyde, A.F.L. 1975, 'Repeated load triaxial testing of a silty clay', *Géotechnique*, vol. 25, no. 1, pp. 95-114. https://doi.org/10.1680/geot.1975.25.1.95.

Budhu, M. 2015, *Soil mechanics fundamentals*, John Wiley & Sons.

Burmister, D.M. 1958, 'Evaluation of pavement systems of the WASHO road test by layered system methods', *Highway Research Board Bulletin*, no. 177, pp. 26-54.

Cai, Y., Sun, Q., Guo, L., Juang, C.H. & Wang, J. 2015, 'Permanent deformation characteristics of saturated sand under cyclic loading', *Canadian Geotechnical Journal*, vol. 52, no. 6, pp. 795-807. https://doi.org/10.1139/cgj-2014-0341.

Carter, J.P., Booker, J.R. & Wroth, C.P. 1982, 'A critical state soil model for cyclic loading', in G.N. Pande & O.C. Zienkiewicz (eds), *Soil mechanics - transient and cyclic loads*, John Wiley and Sons Ltd, pp. 219-52.

Carter, M. & Bentley, S.P. 2016, *Soil properties and their correlations, 2nd Edition*, John Wiley & Sons, West Sussex, United Kingdom.

Chebli, H., Clouteau, D. & Schmitt, L. 2008, 'Dynamic response of high-speed ballasted railway tracks: 3D periodic model and in situ measurements', *Soil Dynamics and Earthquake Engineering*, vol. 28, no. 2, pp. 118-31. https://doi.org/10.1016/j.soildyn.2007.05.007.

Chen, C. & McDowell, G.R. 2016, 'An investigation of the dynamic behaviour of track transition zones using discrete element modelling', *Proceedings of the Institution of Mechanical Engineers, Part F: Journal of Rail and Rapid Transit*, vol. 230, no. 1, pp. 117-28. https://doi.org/10.1177/0954409714528892.

Chen, G. & Zhai, W.M. 2004, 'A new wheel/rail spatially dynamic coupling model and its verification', *Vehicle System Dynamics*, vol. 41, no. 4, pp. 301-22. https://doi.org/10.1080/00423110412331315178.

Chen, J. & Zhou, Y. 2018, 'Dynamic responses of subgrade under double-line high-speed railway', *Soil Dynamics and Earthquake Engineering*, vol. 110, pp. 1-12. https://doi.org/10.1016/j.soildyn.2018.03.028.

Chen, Y.H. & Huang, Y.H. 2000, 'Dynamic stiffness of infinite Timoshenko beam on viscoelastic foundation in moving co-ordinate', *International Journal for Numerical Methods in Engineering*, vol. 48, no. 1, pp. 1-18.

Choudhury, D., Bharti, R.K., Chauhan, S. & Indraratna, B. 2008, 'Response of multilayer foundation system beneath railway track under cyclic loading', *Journal of Geotechnical and Geoenvironmental Engineering*, vol. 134, no. 10, pp. 1558-63. https://doi.org/10.1061/(ASCE)1090-0241(2008)134:10(1558)

Chrismer, S. 1997, *Test of Geoweb to improve track stability over soft subgrade*, TD 97-045, Association of American Railroads, Washington DC.

Christopher, B.R., Schwartz, C. & Boudreau, R. 2006, *Geotechnical aspects of pavements* FHWA NHI-05-037, Washington, D.C.

Coelho, B., Hölscher, P., Priest, J., Powrie, W. & Barends, F. 2011, 'An assessment of transition zone performance', *Proceedings of the Institution of Mechanical Engineers, Part F: Journal of Rail and Rapid Transit*, vol. 225, no. 2, pp. 129-39. https://doi.org/10.1177/09544097jrrt389.

Connolly, D., Giannopoulos, A. & Forde, M.C. 2013, 'Numerical modelling of ground borne vibrations from high speed rail lines on embankments', *Soil Dynamics and Earthquake Engineering*, vol. 46, pp. 13-9. https://doi.org/10.1016/j.soildyn.2012.12.003.

Connolly, D.P., Kouroussis, G., Laghrouche, O., Ho, C.L. & Forde, M.C. 2015, 'Benchmarking railway vibrations – Track, vehicle, ground and building effects', *Construction and Building Materials*, vol. 92, pp. 64-81. https://doi.org/10.1016/j.conbuildmat.2014.07.042.

Connolly, D.P., Kouroussis, G., Woodward, P.K., Alves Costa, P., Verlinden, O. & Forde, M.C. 2014, 'Field testing and analysis of high speed rail vibrations', *Soil Dynamics and Earthquake Engineering*, vol. 67, pp. 102-18. https://doi.org/10.1016/j.soildyn.2014.08.013.

Costa, P.A., Calçada, R., Cardoso, A.S. & Bodare, A. 2010, 'Influence of soil non-linearity on the dynamic response of high-speed railway tracks', *Soil Dynamics and Earthquake Engineering*, vol. 30, no. 4, pp. 221-35. https://doi.org/10.1016/j.soildyn.2009.11.002.

Dahlberg, T. 2001, 'Some railroad settlement models – A critical review', *Proceedings of the Institution of Mechanical Engineers, Part F: Journal of Rail and Rapid Transit*, vol. 215, no. 4, pp. 289-300. https://doi.org/10.1243/0954409011531585.

Dassault Systèmes 2018, 'Abaqus', 2018 edn, Dassault Systèmes Simulia Corp, Providence, RI.

Degrande, G. & Schillemans, L. 2001, 'Free field vibrations during the passage of a Thalys high-speed train at variable speed', *Journal of Sound and Vibration*, vol. 247, no. 1, pp. 131-44. https://doi.org/10.1006/jsvi.2001.3718.

Di Prisco, C. & Vecchiotti, M. 2006, 'A rheological model for the description of boulder impacts on granular strata', *Géotechnique*, vol. 56, no. 7, pp. 469-82. https://doi.org/10.1680/geot.2006.56.7.469.

Dieterman, H.A. & Metrikine, A.V. 1996, 'The equivalent stiffness of a half space interacting with a beam. Critical velocities of a moving load along the beam', *European Journal of Mechanics - A/Solids*, vol. 15, no. 1, pp. 67-90.

Dieterman, H.A. & Metrikine, A.V. 1997, 'Steady-state displacements of a beam on an elastic half-space due to a uniformly moving constant load', *European Journal of Mechanics - A/Solids*, vol. 16, no. 2, pp. 295-306.

Dimitrovová, Z. & Varandas, J.N. 2009, 'Critical velocity of a load moving on a beam with a sudden change of foundation stiffness: Applications to high-speed trains', *Computers and Structures*, vol. 87, no. 19-20, pp. 1224-32. https://doi.org/10.1016/j.compstruc.2008.12.005.

Doyle, N.F. 1980, *Railway track design: A review of current practice*, Bureau of Transport Economics, Australian government publishing service, Canberra, Australia.

Drumm, E.C., Boateng-Poku, Y. & Johnson Pierce, T. 1990, 'Estimation of subgrade resilient modulus from standard tests', *Journal of Geotechnical Engineering*, vol. 116, no. 5, pp. 774-89. https://doi.org/10.1061/(ASCE)0733-9410(1990)116:5(774).

Edil, T.B. & Bosscher, P.J. 1994, 'Engineering properties of tire chips and soil mixtures', *Geotechnical Testing Journal*, vol. 17, no. 4, pp. 453-64. https://doi.org/10.1520/GTJ10306J.

Eisenmann, J. 1972, 'Germans gain a better understanding of track structure', *Railway Gazette International*, vol. 128, no. 8, pp. 305-8.

Elliott, R.P. & Thornton, S.I. 1988, 'Resilient modulus and AASHTO pavement design', *Transportation Research Record*, no. 1196, pp. 116-24.

Esveld, C. 2001, *Modern railway track*, MRT-Productions, Delft, The Netherlands.

Farooq, M.A., Nimbalkar, S. & Fatahi, B. 2021, 'Three-dimensional finite element analyses of tyre derived aggregates in ballasted and ballastless tracks', *Computers and Geotechnics*, vol. 136, p. 104220. https://doi.org/10.1016/j.compgeo.2021.104220.

Forsyth, R.A. & Egan, J.P. 1976, 'Use of waste materials in embankment construction', *Transportation Research Record*, no. 593, pp. 3-8.

Fredlund, D.G., Bergan, A.T. & Sauer, E.K. 1975, 'Deformation characterization of subgrade soils for highways and runways in northern environments', *Canadian Geotechnical Journal*, vol. 12, no. 2, pp. 213-23. https://doi.org/10.1139/t75-026.

Galvín, P. & Domínguez, J. 2009, 'Experimental and numerical analyses of vibrations induced by high-speed trains on the Córdoba–Málaga line', *Soil Dynamics and Earthquake Engineering*, vol. 29, no. 4, pp. 641-57. https://doi.org/10.1016/j.soildyn.2008.07.001.

Galvín, P., Maestre, J. & Romero, A. 2014, 'A 3D time domain numerical model based on half-space Green's function for soil–structure interaction analysis', *Computational Mechanics*, vol. 53, no. 5, pp. 1073-85. https://doi.org/10.1007/s00466-013-0949-1.

Galvín, P., Mendoza, D.L., Connolly, D.P., Degrande, G., Lombaert, G. & Romero, A. 2018, 'Scoping assessment of free-field vibrations due to railway traffic', *Soil Dynamics and Earthquake Engineering*, vol. 114, pp. 598-614. https://doi.org/10.1016/j.soildyn.2018.07.046.

Galvín, P., Romero, A. & Domínguez, J. 2010, 'Fully three-dimensional analysis of high-speed train–track–soil-structure dynamic interaction', *Journal of Sound and Vibration*, vol. 329, no. 24, pp. 5147-63. https://doi.org/10.1016/j.jsv.2010.06.016.

Gao, Y., Qian, Y., Stoffels, S.M., Huang, H. & Liu, S. 2017, 'Characterization of railroad crosstie movements by numerical modeling and field investigation', *Construction and Building Materials*, vol. 131, pp. 542-51. https://doi.org/10.1016/j.conbuildmat.2016.11.067.

Garga, V.K. & O'Shaughnessy, V. 2000, 'Tire-reinforced earthfill. Part 1: Construction of a test fill, performance, and retaining wall design', *Canadian Geotechnical Journal*, vol. 37, no. 1, pp. 75-96. https://doi.org/10.1139/t99-084.

Giroud, J.P. & Han, J. 2004a, 'Design method for geogrid-reinforced unpaved roads. I. Development of design method', *Journal of Geotechnical and Geoenvironmental Engineering*, vol. 130, no. 8, pp. 775-86. https://doi.org/10.1061/(asce)1090-0241(2004)130:8(775).

Giroud, J.P. & Han, J. 2004b, 'Design method for geogrid-reinforced unpaved roads. II. Calibration and applications', *Journal of Geotechnical and Geoenvironmental Engineering*, vol. 130, no. 8, pp. 787-97. https://doi.org/10.1061/(ASCE)1090-0241(2004)130:8(787).

Gonzalez-Torre, I., Calzada-Perez, M.A., Vega-Zamanillo, A. & Castro-Fresno, D. 2014, 'Damage evaluation during installation of geosynthetics used in asphalt pavements', *Geosynthetics International*, vol. 21, no. 6, pp. 377-86. https://doi.org/10.1680/gein.14.00025.

Gräbe, P.J. & Clayton, C.R.I. 2009, 'Effects of principal stress rotation on permanent deformation in rail track foundations', *Journal of Geotechnical and Geoenvironmental Engineering*, vol. 135, no. 4, pp. 555-65. https://doi.org/10.1061/(ASCE)1090-0241(2009)135:4(555).

Gräbe, P.J., Clayton, C.R.I. & Shaw, F.J. 2005, 'Deformation measurement on a heavy haul track formation', paper presented to the *8th International Heavy Haul Conference*, Rio de Janeiro, Brazil.

Gräbe, P.J. & Shaw, F.J. 2010, 'Design life prediction of a heavy haul track foundation', *Proceedings of the Institution of Mechanical Engineers, Part F: Journal of Rail and Rapid Transit*, vol. 224, no. 5, pp. 337-44. https://doi.org/10.1243/09544097jrrt371.

Grossoni, I., Powrie, W., Zervos, A., Bezin, Y. & Le Pen, L. 2021, 'Modelling railway ballasted track settlement in vehicle-track interaction analysis', *Transportation Geotechnics*, vol. 26, p. 100433. https://doi.org/10.1016/j.trgeo.2020.100433.

Guo, L., Cai, Y., Jardine, R.J., Yang, Z. & Wang, J. 2018, 'Undrained behaviour of intact soft clay under cyclic paths that match vehicle loading conditions', *Canadian Geotechnical Journal*, vol. 55, no. 1, pp. 90-106. https://doi.org/10.1139/cgj-2016-0636.

Guo, Y. & Zhai, W. 2018, 'Long-term prediction of track geometry degradation in high-speed vehicle–ballastless track system due to differential subgrade settlement', *Soil Dynamics and Earthquake Engineering*, vol. 113, pp. 1-11. https://dx.doi.org/10.1016/j.soildyn.2018.05.024.

Hall, L. 2003, 'Simulations and analyses of train-induced ground vibrations in finite element models', *Soil Dynamics and Earthquake Engineering*, vol. 23, no. 5, pp. 403-13. https://doi.org/10.1016/s0267-7261(02)00209-9.

Han, J., Acharya, R., Parsons, R.L. & Khatri, D. 2013, *Improved load distribution for load rating of low-fill box structures*, K-TRAN: KU12-3, Kansas Department of Transportation, Kansas.

Han, J., Pokharel, S.K., Yang, X., Manandhar, C., Leshchinsky, D., Halahmi, I. & Parsons, R.L. 2011, 'Performance of geocell-reinforced RAP bases over weak subgrade under full-scale moving wheel loads', *Journal of Materials in Civil Engineering*, vol. 23, no. 11, pp. 1525-34. https://doi.org/10.1061/(asce)mt.1943-5533.0000286.

Han, J., Yang, X., Leshchinsky, D. & Parsons, R.L. 2008, 'Behavior of geocell-reinforced sand under a vertical load', *Transportation Research Record*, vol. 2045, no. 1, pp. 95-101. https://doi.org/10.3141/2045-11.

Hashiguchi, K. 1989, 'Subloading surface model in unconventional plasticity', *International Journal of Solids and Structures*, vol. 25, no. 8, pp. 917-45. https://doi.org/10.1016/0020-7683(89)90038-3.

Heath, D.L., Waters, J.M., Shenton, M.J. & Sparrow, R.W. 1972, 'Design of conventional rail track foundations', *Proceedings of the Institution of Civil Engineers*, vol. 51, no. 2, pp. 251-67. https://doi.org/10.1680/iicep.1972.5952.

Hegde, A. & Sitharam, T.G. 2015, '3-Dimensional numerical modelling of geocell reinforced sand beds', *Geotextiles and Geomembranes*, vol. 43, no. 2, pp. 171-81. https://doi.org/10.1016/j.geotexmem.2014.11.009.

Henkel, D.J. & Gilbert, G.D. 1952, 'The effect measured of the rubber membrane on the triaxial compression strength of clay samples', *Géotechnique*, vol. 3, no. 1, pp. 20-9. https://doi.org/10.1680/geot.1952.3.1.20.

Hight, D.W., Gens, A. & Symes, M.J. 1983, 'The development of a new hollow cylinder apparatus for investigating the effects of principal stress rotation in soils', *Géotechnique*, vol. 33, no. 4, pp. 355-83. https://doi.org/10.1680/geot.1983.33.4.355.

Hirai, H. 2008, 'Settlements and stresses of multi-layered grounds and improved grounds by equivalent elastic method', *International Journal for Numerical and Analytical Methods in Geomechanics*, vol. 32, no. 5, pp. 523-57. https://doi.org/10.1002/nag.636.

Hung, H.H., Chen, G.H. & Yang, Y.B. 2013, 'Effect of railway roughness on soil vibrations due to moving trains by 2.5D finite/infinite element approach', *Engineering Structures*, vol. 57, pp. 254-66. https://doi.org/10.1016/j.engstruct.2013.09.031.

Hunt, H.E. 1997, 'Settlement of railway track near bridge abutments', *Proceedings of the Institution of Civil Engineers - Transport*, vol. 123, no. 1, pp. 68-73. https://doi.org/10.1680/itran.1997.29182.

Indraratna, B., Biabani, M.M. & Nimbalkar, S. 2015, 'Behavior of geocell-reinforced subballast subjected to cyclic loading in plane-strain condition', *Journal of Geotechnical and Geoenvironmental Engineering*, vol. 141, no. 1, p. 04014081. https://doi.org/10.1061/(asce)gt.1943-5606.0001199.

Indraratna, B. & Nimbalkar, S. 2013, 'Stress-strain degradation response of railway ballast stabilized with geosynthetics', *Journal of Geotechnical and Geoenvironmental Engineering*, vol. 139, no. 5, pp. 684-700. https://doi.org/10.1061/(asce)gt.1943-5606.0000758.

Indraratna, B., Nimbalkar, S., Christie, D., Rujikiatkamjorn, C. & Vinod, J. 2010, 'Field assessment of the performance of a ballasted rail track with and without geosynthetics', *Journal of Geotechnical and Geoenvironmental Engineering* vol. 136, no. 7, pp. 907-17. https://doi.org/10.1061/(ASCE)GT.1943-5606.0000312.

Indraratna, B., Salim, W. & Rujikiatkamjorn, C. 2011, *Advanced rail geotechnology – Ballasted track*, CRC Press/Balkema, The Netherlands.
Indraratna, B., Sun, Q. & Grant, J. 2017, 'Behaviour of subballast reinforced with used tyre and potential application in rail tracks', *Transportation Geotechnics*, vol. 12, pp. 26-36. https://doi.org/10.1016/j.trgeo.2017.08.006.
Ishikawa, T., Sekine, E. & Miura, S. 2011, 'Cyclic deformation of granular material subjected to moving-wheel loads', *Canadian Geotechnical Journal*, vol. 48, no. 5, pp. 691-703. https://doi.org/10.1139/t10-099.
Janardhanam, R. & Desai, C.S. 1983, 'Three-dimensional testing and modeling of ballast', *Journal of Geotechnical Engineering*, vol. 109, no. 6, pp. 783-96. https://doi.org/10.1061/(ASCE)0733-9410(1983)109:6(783).
Jefferies, M., Shuttle, D. & Been, K. 2015, 'Principal stress rotation as cause of cyclic mobility', *Geotechnical Research*, vol. 2, no. 2, pp. 66-96. https://doi.org/10.1680/gr.15.00002.
Jefferies, M.G. 1993, 'Nor-Sand: a simple critical state model for sand', *Géotechnique*, vol. 43, no. 1, pp. 91-103. https://doi.org/10.1680/geot.1993.43.1.91.
Jefferies, M.G. & Been, K. 2015, *Soil liquefaction: a critical state approach*, CRC press, Boca Raton, FL.
Jefferies, M.G. & Shuttle, D.A. 2002, 'Dilatancy in general Cambridge-type models', *Géotechnique*, vol. 52, no. 9, pp. 625-38. https://doi.org/10.1680/geot.2002.52.9.625.
Kaewunruen, S., Remennikov, A.M., Nguyen, P. & Aikawa, A. 2016, 'Field performance to mitigate impact vibration at railway bridge ends using soft baseplates', *The 11th World Congress on Railway Research*, vol. 2, WCRR2016, Milan, Italy, pp. 1-10.
Karasev, O.V., Talanov, G.P. & Benda, S.F. 1977, 'Investigation of the work of single situ-cast piles under different load combinations', *Soil Mechanics and Foundation Engineering*, vol. 14, pp. 173-7. https://doi.org/10.1007/BF02092686.
Karlström, A. & Boström, A. 2006, 'An analytical model for train-induced ground vibrations from railways', *Journal of Sound and Vibration*, vol. 292, no. 1-2, pp. 221-41. https://doi.org/10.1016/j.jsv.2005.07.041.
Katou, M., Matsuoka, T., Yoshioka, O., Sanada, Y. & Miyoshi, T. 2008, 'Numerical simulation study of ground vibrations using forces from wheels of a running high-speed train', *Journal of Sound and Vibration*, vol. 318, no. 4-5, pp. 830-49. https://doi.org/10.1016/j.jsv.2008.04.053.
Kaynia, A.M., Madshus, C. & Zackrisson, P. 2000, 'Ground vibration from high-speed trains: Prediction and countermeasure', *Journal of Geotechnical and Geoenvironmental Engineering*, vol. 126, no. 6, pp. 531-7. https://doi.org/10.1061/(asce)1090-0241(2000)126:6(531).
Kennedy, J., Woodward, P.K., Medero, G. & Banimahd, M. 2013, 'Reducing railway track settlement using three-dimensional polyurethane polymer reinforcement of the ballast', *Construction and Building Materials*, vol. 44, pp. 615-25. https://doi.org/10.1016/j.conbuildmat.2013.03.002.
Kerr, A.D. & Moroney, B.E. 1993, 'Track transition problems and remedies', *Proceedings of AREA*, vol. 94, pp. 267-98.
Knothe, K.L. & Grassie, S.L. 1993, 'Modelling of railway track and vehicle/track interaction at high frequencies', *Vehicle System Dynamics*, vol. 22, no. 3-4, pp. 209-62. https://doi.org/10.1080/00423119308969027.
Koerner, R.M. 2012, *Designing with geosynthetics*, vol. 1, Xlibris Corporation.

Kong, Y., Zhou, A., Shen, F. & Yao, Y. 2019, 'Stress–dilatancy relationship for fiber-reinforced sand and its modeling', *Acta Geotechnica*, vol. 14, no. 6, pp. 1871-81. https://doi.org/10.1007/s11440-019-00834-6.

Krylov, V.V. 2001, *Noise and vibration from high-speed trains*, Thomas Telford, London.

Kuo, C.M. & Huang, C.H. 2009, 'Two approaches of finite-element modeling of ballasted railway track', *Journal of Geotechnical and Geoenvironmental Engineering*, vol. 135, no. 3, pp. 455-8. https://doi.org/10.1061/(ASCE)1090-0241(2009)135:3(455).

Lal, D., Sankar, N. & Chandrakaran, S. 2017, 'Effect of reinforcement form on the behaviour of coir geotextile reinforced sand beds', *Soils and Foundations*, vol. 57, no. 2, pp. 227-36. https://doi.org/10.1016/j.sandf.2016.12.001.

Lei, X. & Mao, L. 2004, 'Dynamic response analyses of vehicle and track coupled system on track transition of conventional high speed railway', *Journal of Sound and Vibration*, vol. 271, no. 3-5, pp. 1133-46. https://doi.org/10.1016/s0022-460x(03)00570-4.

Lekarp, F., Isacsson, U. & Dawson, A. 2000, 'State of the art - II: Permanent strain response of unbound aggregates', *Journal of Transportation Engineering*, vol. 126, no. 1, pp. 76-83. https://doi.org/10.1061/(asce)0733-947x(2000)126:1(76).

Leshchinsky, B. & Ling, H. 2013a, 'Effects of geocell confinement on strength and deformation behavior of gravel', *Journal of Geotechnical and Geoenvironmental Engineering*, vol. 139, no. 2, pp. 340-52. https://doi.org/10.1061/(asce)gt.1943-5606.0000757.

Leshchinsky, B. & Ling, H.I. 2013b, 'Numerical modeling of behavior of railway ballasted structure with geocell confinement', *Geotextiles and Geomembranes*, vol. 36, pp. 33-43. https://doi.org/10.1016/j.geotexmem.2012.10.006.

Li, D. & Davis, D. 2005, 'Transition of railroad bridge approaches', *Journal of Geotechnical and Geoenvironmental Engineering*, vol. 131, no. 11, pp. 1392-8. https://doi.org/10.1061/(ASCE)1090-0241(2005)131:11(1392).

Li, D., Hyslip, J., Sussmann, T. & Chrismer, S. 2016, *Railway geotechnics*, Taylor and Francis, Boca Raton, USA.

Li, D. & Selig, E.T. 1994, 'Resilient modulus for fine-grained subgrade soils', *Journal of Geotechnical Engineering*, vol. 120, no. 6, pp. 939-57. https://doi.org/10.1061/(ASCE)0733-9410(1994)120:6(939).

Li, D. & Selig, E.T. 1996, 'Cumulative plastic deformation for fine-grained subgrade soils', *Journal of Geotechnical Engineering* vol. 122, no. 12, pp. 1006-13. https://doi.org/10.1061/(asce)0733-9410(1996)122:12(1006).

Li, D. & Selig, E.T. 1998, 'Method for railroad track foundation design. I: Development', *Journal of Geotechnical and Geoenvironmental Engineering*, vol. 124, no. 4, pp. 316-22. https://doi.org/10.1061/(asce)1090-0241(1998)124:4(316)

Li, L., Nimbalkar, S. & Zhong, R. 2018, 'Finite element model of ballasted railway with infinite boundaries considering effects of moving train loads and Rayleigh waves', *Soil Dynamics and Earthquake Engineering*, vol. 114, pp. 147-53. https://doi.org/10.1016/j.soildyn.2018.06.033.

Liu, Y., Deng, A. & Jaksa, M. 2018, 'Three-dimensional modeling of geocell-reinforced straight and curved ballast embankments', *Computers and Geotechnics*, vol. 102, pp. 53-65. https://doi.org/10.1016/j.compgeo.2018.05.011.

López-Pita, A., Teixeira, P.F., Casas, C., Ubalde, L. & Robusté, F. 2007, 'Evolution of track geometric quality in high-speed lines: Ten years experience of the Madrid-Seville line', *Proceedings of the Institution of Mechanical Engineers, Part F:*

Journal of Rail and Rapid Transit, vol. 221, no. 2, pp. 147-55. https://doi.org/10.1243/0954409jrrt62.

Lu, D., Li, X., Du, X. & Liang, J. 2019, 'A simple 3D elastoplastic constitutive model for soils based on the characteristic stress', *Computers and Geotechnics*, vol. 109, pp. 229-47. https://doi.org/10.1016/j.compgeo.2019.02.001.

Lu, D., Ma, C., Du, X., Jin, L. & Gong, Q. 2017, 'Development of a new nonlinear unified strength theory for geomaterials based on the characteristic stress concept', *International Journal of Geomechanics*, vol. 17, no. 2, p. 04016058. https://doi.org/10.1061/(asce)gm.1943-5622.0000729.

Luenberger, D.G. 1973, *Introduction to linear and nonlinear programming*, Addison-wesley, Reading, MA.

Lundqvist, A. & Dahlberg, T. 2005, 'Load impact on railway track due to unsupported sleepers', *Proceedings of the Institution of Mechanical Engineers, Part F: Journal of Rail and Rapid Transit*, vol. 219, no. 2, pp. 67-77. https://doi.org/10.1243/095440905x8790.

Ma, C., Lu, D., Du, X. & Zhou, A. 2017, 'Developing a 3D elastoplastic constitutive model for soils: A new approach based on characteristic stress', *Computers and Geotechnics*, vol. 86, pp. 129-40. https://doi.org/10.1016/j.compgeo.2017.01.003.

Mamou, A., Powrie, W., Clayton, C.R.I. & Priest, J.A. 2021, 'Suitability of empirical equations for estimating permanent settlement of railway foundation materials subjected to cyclic loading with principal stress rotation', *Canadian Geotechnical Journal*, vol. 58, no. 10, pp. 1603-10. https://doi.org/10.1139/cgj-2020-0183.

Mamou, A., Powrie, W., Priest, J.A. & Clayton, C. 2017, 'The effects of drainage on the behaviour of railway track foundation materials during cyclic loading', *Géotechnique*, vol. 67, no. 10, pp. 845-54. https://doi.org/10.1680/jgeot.15.P.278.

MathWorks Inc. 2021, 'MATLAB version 2021a', MathWorks Inc., Natick, Massachusetts.

Mauer, L. 1995, 'An interactive track-train dynamic model for calculation of track error growth', *Vehicle System Dynamics*, vol. 24, no. sup1, pp. 209-21. https://doi.org/10.1080/00423119508969626.

McDonald, L.M. & Raymond, G.P. 1984, 'Repetitive load testing: reversal or rotation', *Canadian Geotechnical Journal*, vol. 21, no. 3, pp. 456-74. https://doi.org/10.1139/t84-050.

Mengelt, M., Edil, T.B. & Benson, C.H. 2006, 'Resilient modulus and plastic deformation of soil confined in a geocell', *Geosynthetics International*, vol. 13, no. 5, pp. 195-205. https://doi.org/10.1680/gein.2006.13.5.195.

Metrikine, A.V. & Popp, K. 1999, 'Vibration of a periodically supported beam on an elastic half-space', *European Journal of Mechanics - A/Solids*, vol. 18, no. 4, pp. 679-701. https://doi.org/10.1016/s0997-7538(99)00141-2.

Metrikine, A.V. & Verichev, S.N. 2001, 'Instability of vibrations of a moving two-mass oscillator on a flexibly supported Timoshenko beam', *Archive of Applied Mechanics*, vol. 71, pp. 613-24 https://doi.org/10.1007/s004190100177.

Metrikine, A.V., Wolfert, A.R.M. & Dieterman, H.A. 1998, 'Transition radiation in an elastically supported string. Abrupt and smooth variations of the support stiffness', *Wave Motion*, vol. 27, no. 4, pp. 291-305. https://doi.org/10.1016/s0165-2125(97)00055-3.

Mishra, D., Boler, H., Tutumluer, E., Hou, W. & Hyslip, J.P. 2017, 'Deformation and dynamic load amplification trends at railroad bridge approaches: Effects caused by high-speed passenger trains', *Transportation Research Record*, vol. 2607, no. 1, pp. 43-53. https://doi.org/10.3141/2607-07.

Mishra, D., Qian, Y., Huang, H. & Tutumluer, E. 2014a, 'An integrated approach to dynamic analysis of railroad track transitions behavior', *Transportation Geotechnics*, vol. 1, no. 4, pp. 188-200. https://doi.org/10.1016/j.trgeo.2014.07.001.

Mishra, D., Tutumluer, E., Boler, H., Hyslip, J.P. & Sussmann, T.R. 2014b, 'Railroad track transitions with multidepth deflectometers and strain gauges', *Transportation Research Record*, vol. 2448, no. 1, pp. 105-14. https://doi.org/10.3141/2448-13.

Mishra, D., Tutumluer, E., Stark, T.D., Hyslip, J.P., Chrismer, S.M. & Tomas, M. 2012, 'Investigation of differential movement at railroad bridge approaches through geotechnical instrumentation', *Journal of Zhejiang University SCIENCE A*, vol. 13, no. 11, pp. 814-24. https://doi.org/10.1631/jzus.A12ISGT7.

Miura, S., Takai, H., Uchida, M. & Fukada, Y. 1998, 'The mechanism of railway tracks', *Japan Railway and Transport Review*, vol. 3, pp. 38-45.

Momoya, Y., Sekine, E. & Tatsuoka, F. 2005, 'Deformation characteristics of railway roadbed and subgrade under moving-wheel load', *Soils and Foundations*, vol. 45, no. 4, pp. 99-118. https://doi.org/10.3208/sandf.45.4_99.

Moossazadeh, J. & Witczak, M.W. 1981, 'Prediction of subgrade moduli for soil that exhibits nonlinear behavior', *Transportation Research Record*, no. 810, pp. 9-17.

Namura, A. & Suzuki, T. 2007, 'Evaluation of countermeasures against differential settlement at track transitions', *Quarterly Report of RTRI*, vol. 48, no. 3, pp. 176-82.

Nguyen, K., Villalmanzo, D.I., Goicolea, J.M. & Gabaldon, F. 2016, 'A computational procedure for prediction of ballasted track profile degradation under railway traffic loading', *Proceedings of the Institution of Mechanical Engineers, Part F: Journal of Rail and Rapid Transit*, vol. 230, no. 8, pp. 1812-27. https://doi.org/10.1177/0954409715615374.

Nielsen, J.C.O. & Li, X. 2018, 'Railway track geometry degradation due to differential settlement of ballast/subgrade – Numerical prediction by an iterative procedure', *Journal of Sound and Vibration*, vol. 412, pp. 441-56. https://doi.org/10.1016/j.jsv.2017.10.005.

Nimbalkar, S., Dash, S.K. & Indraratna, B. 2018, 'Performance of ballasted track under impact loading and applications of recycled rubber inclusion', *Geotechnical Engineering Journal of the SEAGS & AGSSEA*, vol. 49, no. 4, pp. 79-91.

Nimbalkar, S. & Indraratna, B. 2016, 'Improved performance of ballasted rail track using geosynthetics and rubber shockmat', *Journal of Geotechnical and Geoenvironmental Engineering*, vol. 142, no. 8, p. 04016031. https://doi.org/10.1061/(asce)gt.1943-5606.0001491.

Nimbalkar, S., Indraratna, B., Dash, S.K. & Christie, D. 2012, 'Improved performance of railway ballast under impact loads using shock mats', *Journal of Geotechnical and Geoenvironmental Engineering*, vol. 138, no. 3, pp. 281-94. https://doi.org/10.1061/(asce)gt.1943-5606.0000598.

Nova, R. 1982, 'A constitutive model for soil under monotonic and cyclic loading', in G.N. Pande & O.C. Zienkiewicz (eds), *Soil Mechanics Transient and Cyclic Loads* Wiley, Chichester, pp. 343-73.

O'Brien, J. & Rizos, D.C. 2005, 'A 3D BEM-FEM methodology for simulation of high speed train induced vibrations', *Soil Dynamics and Earthquake Engineering*, vol. 25, no. 4, pp. 289-301. https://doi.org/10.1016/j.soildyn.2005.02.005.

Odemark, N. 1949, 'Investigations as to the elastic properties of soils and design of pavements according to the theory of elasticity', *Statens Vaginstitut, Meddelande* vol. 77.

ORE 1968, *Stresses in the rails*, Report D 71/RP8/E, Utrecht.

Oscarsson, J. & Dahlberg, T. 1998, 'Dynamic train/track/ballast interaction - computer models and full-scale experiments', *Vehicle System Dynamics*, vol. 29, no. S1, pp. 73-84. https://doi.org/10.1080/00423119808969553.

Paixão, A., Alves Ribeiro, C., Pinto, N., Fortunato, E. & Calçada, R. 2014a, 'On the use of under sleeper pads in transition zones at railway underpasses: experimental field testing', *Structure and Infrastructure Engineering*, vol. 11, no. 2, pp. 112-28. https://doi.org/10.1080/15732479.2013.850730.

Paixão, A., Fortunato, E. & Calçada, R. 2014b, 'Transition zones to railway bridges: Track measurements and numerical modelling', *Engineering Structures*, vol. 80, pp. 435-43. https://doi.org/10.1016/j.engstruct.2014.09.024.

Paixão, A., Fortunato, E. & Calçada, R. 2015a, 'Design and construction of backfills for railway track transition zones', *Proceedings of the Institution of Mechanical Engineers, Part F: Journal of Rail and Rapid Transit*, vol. 229, no. 1, pp. 58-70. https://doi.org/10.1177/0954409713499016.

Paixão, A., Fortunato, E. & Calçada, R. 2015b, 'A numerical study on the influence of backfill settlements in the train/track interaction at transition zones to railway bridges', *Proceedings of the Institution of Mechanical Engineers, Part F: Journal of Rail and Rapid Transit*, vol. 230, no. 3, pp. 866-78. https://doi.org/10.1177/0954409715573289.

Palmer, L.A. & Barber, E.S. 1941, 'Soil displacement under a circular loaded area', *Highway Research Board Bulletin*, vol. 20, pp. 279-86.

Pokharel, S.K., Han, J., Leshchinsky, D. & Parsons, R.L. 2018, 'Experimental evaluation of geocell-reinforced bases under repeated loading', *International Journal of Pavement Research and Technology*, vol. 11, no. 2, pp. 114-27. https://doi.org/10.1016/j.ijprt.2017.03.007.

Pokharel, S.K., Han, J., Leshchinsky, D., Parsons, R.L. & Halahmi, I. 2009, 'Behavior of geocell-reinforced granular bases under static and repeated loads', *Contemporary Topics in Ground Modification, Problem Soils, and Geo-Support*, pp. 409-16.

Pokharel, S.K., Han, J., Leshchinsky, D., Parsons, R.L. & Halahmi, I. 2010, 'Investigation of factors influencing behavior of single geocell-reinforced bases under static loading', *Geotextiles and Geomembranes*, vol. 28, no. 6, pp. 570-8. https://doi.org/10.1016/j.geotexmem.2010.06.002.

Pokharel, S.K., Han, J., Manandhar, C., Yang, X., Leshchinsky, D., Halahmi, I. & Parsons, R.L. 2011, 'Accelerated pavement testing of geocell-reinforced unpaved roads over weak subgrade', *Transportation Research Record*, vol. 2204, no. 1, pp. 67-75. https://doi.org/10.3141/2204-09.

Poulos, H.G. & Davis, E.H. 1974, *Elastic solutions for soil and rock mechanics*, John Wiley & Sons, New York.

Powrie, W., Le Pen, L., Milne, D. & Thompson, D. 2019, 'Train loading effects in railway geotechnical engineering: Ground response, analysis, measurement and interpretation', *Transportation Geotechnics*, vol. 21, p. 100261. https://doi.org/10.1016/j.trgeo.2019.100261.

Powrie, W., Yang, L.A. & Clayton, C.R.I. 2007, 'Stress changes in the ground below ballasted railway track during train passage', *Proceedings of the Institution of Mechanical Engineers, Part F: Journal of Rail and Rapid Transit*, vol. 221, no. 2, pp. 247-62. https://doi.org/10.1243/0954409jrrt95.

Prause, R.H., Meacham, H.C., Harrison, H.D., Johns, T.G. & Glaeser, W.A. 1974, *Assessment of design tools and criteria for urban rail track structures*, Report no. UMTA-MA-06-0025-74-3, Urban Mass Transportation Administration, Office of Research and Development, Washington, DC.

Priest, J.A., Powrie, W., Yang, L., Grabe, P.J. & Clayton, C.R.I. 2010, 'Measurements of transient ground movements below a ballasted railway line', *Géotechnique*, vol. 60, no. 9, pp. 667-77. https://doi.org/10.1680/geot.7.00172.

Puppala, A.J., Saride, S. & Chomtid, S. 2009, 'Experimental and modeling studies of permanent strains of subgrade soils', *Journal of Geotechnical and Geoenvironmental engineering*, vol. 135, no. 10, pp. 1379-89. https://doi.org/10.1061/(ASCE)GT.1943-5606.0000163.

Rajagopal, K., Krishnaswamy, N.R. & Latha, G.M. 1999, 'Behaviour of sand confined with single and multiple geocells', *Geotextiles and Geomembranes*, vol. 17, no. 3, pp. 171-84. https://doi.org/10.1016/S0266-1144(98)00034-X.

Raymond, G.P. 2001, 'Failure and reconstruction of a gantry crane ballasted track', *Canadian Geotechnical Journal*, vol. 38, no. 3, pp. 507-29. https://doi.org/10.1139/t00-121.

Raymond, G.P., Gaskin, P.N. & Addo-Abedi, F.Y. 1979, 'Repeated compressive loading of Leda clay', *Canadian Geotechnical Journal*, vol. 16, no. 1, pp. 1-10. https://doi.org/10.1139/t79-001.

Read, D. & Li, D. 2006, *Design of track transitions*, Transportation Research Board, United States.

Remennikov, A.M. & Kaewunruen, S. 2008, 'A review of loading conditions for railway track structures due to train and track vertical interaction', *Structural Control and Health Monitoring*, vol. 15, no. 2, pp. 207-34. https://doi.org/10.1002/stc.227.

Ribeiro, C.A., Calçada, R. & Delgado, R. 2017, 'Experimental assessment of the dynamic behaviour of the train-track system at a culvert transition zone', *Engineering Structures*, vol. 138, pp. 215-28. https://doi.org/10.1016/j.engstruct.2017.02.020.

Roscoe, K.H. & Burland, J.B. 1968, 'On the generalized stress-strain behaviour of wet clay', in J. Heyman & F. Leckie (eds), *Engineering Plasticity*, Cambridge University Press, Cambridge, pp. 535-609.

Rybnikov, A.M. 1990, 'Experimental investigations of bearing capacity of bored-cast-in-place tapered piles', *Soil Mechanics and Foundation Engineering*, vol. 27, no. 2, pp. 48-52. https://doi.org/10.1007/BF02306100.

Sadri, M. & Steenbergen, M. 2018, 'Effects of railway track design on the expected degradation: Parametric study on energy dissipation', *Journal of Sound and Vibration*, vol. 419, pp. 281-301. https://doi.org/10.1016/j.jsv.2018.01.029.

Sañudo, R., dell'Olio, L., Casado, J.A., Carrascal, I.A. & Diego, S. 2016, 'Track transitions in railways: A review', *Construction and Building Materials*, vol. 112, pp. 140-57. https://doi.org/10.1016/j.conbuildmat.2016.02.084.

Sassa, S. & Sekiguchi, H. 2001, 'Analysis of wave-induced liquefaction of sand beds', *Géotechnique*, vol. 51, no. 2, pp. 115-26. https://doi.org/10.1680/geot.2001.51.2.115.

Satyal, S.R., Leshchinsky, B., Han, J. & Neupane, M. 2018, 'Use of cellular confinement for improved railway performance on soft subgrades', *Geotextiles and Geomembranes*, vol. 46, no. 2, pp. 190-205. https://doi.org/10.1016/j.geotexmem.2017.11.006.

Sayeed, M.A. & Shahin, M.A. 2016, 'Three-dimensional numerical modelling of ballasted railway track foundations for high-speed trains with special reference to

critical speed', *Transportation Geotechnics*, vol. 6, pp. 55-65. https://doi.org/10.1016/j.trgeo.2016.01.003.
Schanz, T. & Vermeer, P.A. 1996, 'Angles of friction and dilatancy of sand', *Géotechnique*, vol. 46, no. 1, pp. 145-51. https://doi.org/10.1680/geot.1996.46.1.145.
Selig, E.T. & Waters, J.M. 1994, *Track geotechnology and substructure management*, Thomas Telford, London.
Shackel, B. 1973, 'The derivation of complex stress–strain relations', *Proceedings of the 8th International Conference on Soil Mechanics and Foundation Engineering*, pp. 353-9.
Shahraki, M., Warnakulasooriya, C. & Witt, K.J. 2015, 'Numerical study of transition zone between ballasted and ballastless railway track', *Transportation Geotechnics*, vol. 3, pp. 58-67. https://doi.org/10.1016/j.trgeo.2015.05.001.
Shahu, J.T., Kameswara Rao, N.S.V. & Yudhbir 1999, 'Parametric study of resilient response of tracks with a sub-ballast layer', *Canadian Geotechnical Journal*, vol. 36, no. 6, pp. 1137-50. https://doi.org/10.1139/t99-054.
Shan, Y., Zhou, S., Wang, B. & Ho, C.L. 2020, 'Differential settlement prediction of ballasted tracks in bridge–embankment transition zones', *Journal of Geotechnical and Geoenvironmental Engineering*, vol. 146, no. 9, p. 04020075. https://doi.org/10.1061/(asce)gt.1943-5606.0002307.
Shan, Y., Zhou, S., Zhou, H., Wang, B., Zhao, Z., Shu, Y. & Yu, Z. 2017, 'Iterative method for predicting uneven settlement caused by high-speed train loads in transition-zone subgrade', *Transportation Research Record*, vol. 2607, no. 1, pp. 7-14. https://doi.org/10.3141/2607-02.
Sheng, X., Jones, C.J.C. & Petyt, M. 1999, 'Ground vibration generated by a harmonic load acting on a railway track', *Journal of Sound and Vibration*, vol. 225, no. 1, pp. 3-28. https://doi.org/10.1006/jsvi.1999.2232.
Sheng, X., Jones, C.J.C. & Thompson, D.J. 2006, 'Prediction of ground vibration from trains using the wavenumber finite and boundary element methods', *Journal of Sound and Vibration*, vol. 293, no. 3-5, pp. 575-86. https://doi.org/10.1016/j.jsv.2005.08.040.
Shih, J.Y., Grossoni, I. & Bezin, Y. 2019, 'Settlement analysis using a generic ballasted track simulation package', *Transportation Geotechnics*, vol. 20, p. 100249. https://doi.org/10.1016/j.trgeo.2019.100249.
Shih, J.Y., Thompson, D.J. & Zervos, A. 2016, 'The effect of boundary conditions, model size and damping models in the finite element modelling of a moving load on a track/ground system', *Soil Dynamics and Earthquake Engineering*, vol. 89, pp. 12-27. https://doi.org/10.1016/j.soildyn.2016.07.004.
Shin, E.C., Kim, D.H. & Das, B.M. 2002, 'Geogrid-reinforced railroad bed settlement due to cyclic load', *Geotechnical & Geological Engineering*, vol. 20, no. 3, pp. 261-71. https://doi.org/10.1023/A:1016040414725.
Sim, W.W., Aghakouchak, A. & Jardine, R.J. 2013, 'Cyclic triaxial tests to aid offshore pile analysis and design', *Proceedings of the Institution of Civil Engineers - Geotechnical Engineering*, vol. 166, no. 2, pp. 111-21. https://doi.org/10.1680/geng.12.00056.
Simo, J.C. & Hughes, T.J.R. 1998, *Computational inelasticity*, Springer, New York.
Sol-Sánchez, M. & D'Angelo, G. 2017, 'Review of the design and maintenance technologies used to decelerate the deterioration of ballasted railway tracks', *Construction and Building Materials*, vol. 157, pp. 402-15. https://doi.org/10.1016/j.conbuildmat.2017.09.007.

Sol-Sánchez, M., Moreno-Navarro, F. & Rubio-Gámez, M.C. 2016, 'Analysis of ballast tamping and stone-blowing processes on railway track behaviour: the influence of using USPs', *Géotechnique*, vol. 66, no. 6, pp. 481-9. https://doi.org/10.1680/jgeot.15.P.129.

Stark, T.D. & Wilk, S.T. 2015, 'Root cause of differential movement at bridge transition zones', *Proceedings of the Institution of Mechanical Engineers, Part F: Journal of Rail and Rapid Transit*, vol. 230, no. 4, pp. 1257-69. https://doi.org/10.1177/0954409715589620.

Stark, T.D., Wilk, S.T. & Rose, J.G. 2016, 'Design and performance of well-performing railway transitions', *Transportation Research Record*, vol. 2545, no. 1, pp. 20-6. https://doi.org/10.3141/2545-03.

Stewart, H.E. & Selig, E.T. 1982, 'Predicted and measured resilient response of track', *Journal of Geotechnical Engineering Division*, vol. 108, no. 11, pp. 1423-42. https://doi.org/10.1061/AJGEB6.0001369.

Suiker, A.S.J. & de Borst, R. 2003, 'A numerical model for the cyclic deterioration of railway tracks', *International Journal for Numerical Methods in Engineering*, vol. 57, no. 4, pp. 441-70. https://doi.org/10.1002/nme.683.

Suiker, A.S.J., de Borst, R. & Esveld, C. 1998, 'Critical behaviour of a Timoshenko beam-half plane system under a moving load', *Archive of Applied Mechanics*, vol. 68, pp. 158-68. https://doi.org/10.1007/s004190050153.

Suiker, A.S.J., Metrikine, A.V. & de Borst, R. 2001a, 'Dynamic behaviour of a layer of discrete particles, Part 1: Analysis of body waves and eigenmodes', *Journal of Sound and Vibration*, vol. 240, no. 1, pp. 1-18. https://doi.org/10.1006/jsvi.2000.3202.

Suiker, A.S.J., Metrikine, A.V. & de Borst, R. 2001b, 'Dynamic behaviour of a layer of discrete particles, Part 2: Response to a uniformly moving, harmonically vibrating load', *Journal of Sound and Vibration*, vol. 240, no. 1, pp. 19-39. https://doi.org/10.1006/jsvi.2000.3203.

Suiker, A.S.J., Selig, E.T. & Frenkel, R. 2005, 'Static and cyclic triaxial testing of ballast and subballast', *Journal of Geotechnical and Geoenvironmental Engineering*, vol. 131, no. 6, pp. 771-82. https://doi.org/10.1061/(ASCE)1090-0241(2005)131:6(771).

Sun, Q.D., Indraratna, B. & Nimbalkar, S. 2016, 'Deformation and degradation mechanisms of railway ballast under high frequency cyclic loading', *Journal of Geotechnical and Geoenvironmental Engineering*, vol. 142, no. 1, p. 04015056. https://doi.org/10.1061/(asce)gt.1943-5606.0001375.

Sun, Y., Chen, C. & Nimbalkar, S. 2017, 'Identification of ballast grading for rail track', *Journal of Rock Mechanics and Geotechnical Engineering*, vol. 9, no. 5, pp. 945-54. https://doi.org/10.1016/j.jrmge.2017.04.006.

Sun, Y., Nimbalkar, S. & Chen, C. 2018, 'Grading and frequency dependence of the resilient modulus of ballast', *Géotechnique Letters*, vol. 8, no. 4, pp. 305-9. https://doi.org/10.1680/jgele.18.00084.

Sun, Y.Q. & Dhanasekar, M. 2002, 'A dynamic model for the vertical interaction of the rail track and wagon system', *International Journal of Solids and Structures*, vol. 39, no. 5, pp. 1337-59. https://doi.org/10.1016/s0020-7683(01)00224-4.

Symes, M.J., Gens, A. & Hight, D.W. 1988, 'Drained principal stress rotation in saturated sand', *Géotechnique*, vol. 38, no. 1, pp. 59-81. https://doi.org/10.1680/geot.1988.38.1.59.

Takemiya, H. & Bian, X. 2005, 'Substructure simulation of inhomogeneous track and layered ground dynamic interaction under train passage', *Journal of Engineering*

Mechanics, vol. 131, no. 7, pp. 699-711. https://doi.org/10.1061/(ASCE)0733-9399(2005)131:7(699).

Tanyu, B.F., Aydilek, A.H., Lau, A.W., Edil, T.B. & Benson, C.H. 2013, 'Laboratory evaluation of geocell-reinforced gravel subbase over poor subgrades', *Geosynthetics International*, vol. 20, no. 2, pp. 47-61. https://doi.org/10.1680/gein.13.00001.

Thakur, J.K., Han, J., Pokharel, S.K. & Parsons, R.L. 2012, 'Performance of geocell-reinforced recycled asphalt pavement (RAP) bases over weak subgrade under cyclic plate loading', *Geotextiles and Geomembranes*, vol. 35, pp. 14-24. https://doi.org/10.1016/j.geotexmem.2012.06.004.

Thompson, M.R. & Robnett, Q.L. 1976, *Resilient properties of subgrade soils*, FHWA-IL-U1-160, University of Illinois, Urbana, United States.

Thornely-Taylor, R.M. 2004, 'The prediction of vibration, groundborne noise and structure radiated noise using finite difference methods', *Proceedings of the 8th International Workshop on Railway Noise, Buxton, England*.

Timoshenko, S.P. & Goodier, J.N. 1970, *Theory of elasticity*, McGraw Hill, New York.

Tutumluer, E., Qian, Y., Hashash, Y.M.A., Ghaboussi, J. & Davis, D.D. 2013, 'Discrete element modelling of ballasted track deformation behaviour', *International Journal of Rail Transportation*, vol. 1, no. 1-2, pp. 57-73. https://doi.org/10.1080/23248378.2013.788361.

Uzan, J. 1985, 'Characterization of granular material', *Transportation Research Record*, vol. 1022, no. 1, pp. 52-9.

Uzan, J. 1992, 'Resilient characterization of pavement materials', *International Journal for Numerical and Analytical Methods in Geomechanics*, vol. 16, no. 6, pp. 453-9. https://doi.org/10.1002/nag.1610160605.

Van Dyk, B.J., Edwards, J.R., Dersch, M.S., Ruppert, C.J. & Barkan, C.P.L. 2016, 'Evaluation of dynamic and impact wheel load factors and their application in design processes', *Proceedings of the Institution of Mechanical Engineers, Part F: Journal of Rail and Rapid Transit*, vol. 231, no. 1, pp. 33-43. https://doi.org/10.1177/0954409715619454.

Varandas, J.N., Hölscher, P. & Silva, M.A.G. 2013, 'Settlement of ballasted track under traffic loading: Application to transition zones', *Proceedings of the Institution of Mechanical Engineers, Part F: Journal of Rail and Rapid Transit*, vol. 228, no. 3, pp. 242-59. https://doi.org/10.1177/0954409712471610.

Varandas, J.N., Paixão, A., Fortunato, E., Zuada Coelho, B. & Hölscher, P. 2020, 'Long-term deformation of railway tracks considering train-track interaction and non-linear resilient behaviour of aggregates – a 3D FEM implementation', *Computers and Geotechnics*, vol. 126, p. 103712. https://doi.org/10.1016/j.compgeo.2020.103712.

Vostroukhov, A.V. & Metrikine, A.V. 2003, 'Periodically supported beam on a visco-elastic layer as a model for dynamic analysis of a high-speed railway track', *International Journal of Solids and Structures*, vol. 40, no. 21, pp. 5723-52. https://doi.org/10.1016/s0020-7683(03)00311-1.

Wang, H. & Markine, V. 2018a, 'Corrective countermeasure for track transition zones in railways: Adjustable fastener', *Engineering Structures*, vol. 169, pp. 1-14. https://doi.org/10.1016/j.engstruct.2018.05.004.

Wang, H. & Markine, V. 2018b, 'Methodology for the comprehensive analysis of railway transition zones', *Computers and Geotechnics*, vol. 99, pp. 64-79. https://doi.org/10.1016/j.compgeo.2018.03.001.

Wang, H. & Markine, V. 2018c, 'Modelling of the long-term behaviour of transition zones: Prediction of track settlement', *Engineering Structures*, vol. 156, pp. 294-304. https://doi.org/10.1016/j.engstruct.2017.11.038.

Wang, H., Markine, V. & Liu, X. 2018, 'Experimental analysis of railway track settlement in transition zones', *Proceedings of the Institution of Mechanical Engineers, Part F: Journal of Rail and Rapid Transit*, vol. 232, no. 6, pp. 1774-89. https://doi.org/10.1177/0954409717748789.

Wang, Q. & Lade, P.V. 2001, 'Shear banding in true triaxial tests and its effect on failure in sand', *Journal of Engineering Mechanics*, vol. 127, no. 8, pp. 754-61. https://doi.org/10.1061/(ASCE)0733-9399(2001)127:8(754).

Wang, Z., Yang, Y., Lu, N., Li, Y. & Yu, H.S. 2019, 'Effects of the principal stress rotation in numerical simulations of geotechnical laboratory cyclic tests', *Computers and Geotechnics*, vol. 109, pp. 220-8. https://doi.org/10.1016/j.compgeo.2019.01.023.

Waterways Experiment Station 1954, *Investigations of pressures and deflections for flexible pavements: Report no. 4: Homogeneous sand test section*, 3-323, U.S. Waterways Experiment Station, Vicksburg, Mississippi.

Wichtmann, T. 2005, 'Explicit accumulation model for non-cohesive soils under cyclic loading', PhD thesis, Ruhr-Universität Bochum, Germany.

Wijewickreme, D. & Vaid, Y.P. 2008, 'Experimental observations on the response of loose sand under simultaneous increase in stress ratio and rotation of principal stresses', *Canadian Geotechnical Journal*, vol. 45, no. 5, pp. 597-610. https://doi.org/10.1139/t08-001.

Winkler, E. 1867, *Die Lehre von der Elastizität und Festigkeit*, Dominicus publishing, Prague.

Wong, R.K.S. & Arthur, J.R.F. 1986, 'Sand sheared by stresses with cyclic variations in direction', *Geotechnique*, vol. 36, no. 2, pp. 215-26. https://doi.org/10.1680/geot.1986.36.2.215.

Wu, Z.X., Yin, Z.Y., Dano, C. & Hicher, P.Y. 2020, 'Cyclic volumetric strain accumulation for sand under drained simple shear condition', *Applied Ocean Research*, vol. 101, p. 102200. https://doi.org/10.1016/j.apor.2020.102200.

Yang, L. 2013, 'Experimental study of soil anisotropy using hollow cylinder testing', PhD thesis thesis, University of Nottingham.

Yang, L.A., Powrie, W. & Priest, J.A. 2009, 'Dynamic stress analysis of a ballasted railway track bed during train passage', *Journal of Geotechnical and Geoenvironmental Engineering*, vol. 135, no. 5, pp. 680-9. https://doi.org/10.1061/(ASCE)GT.1943-5606.0000032.

Yang, X. & Han, J. 2013, 'Analytical model for resilient modulus and permanent deformation of geosynthetic-reinforced unbound granular material', *Journal of Geotechnical and Geoenvironmental Engineering*, vol. 139, no. 9, pp. 1443-53. https://doi.org/10.1061/(asce)gt.1943-5606.0000879.

Yang, Y.B. & Hung, H.H. 2001, 'A 2.5D finite/infinite element approach for modelling visco-elastic bodies subjected to moving loads', *International Journal for Numerical Methods in Engineering*, vol. 51, no. 11, pp. 1317-36. https://doi.org/10.1002/nme.208.

Yoo, T.S. & Selig, E.T. 1979, 'Field observations of ballast and subgrade deformations in track', *Transportation Research Record*, no. 733, pp. 6-12.

Zarembski, A.M., Palese, J., Hartsough, C.M., Ling, H.I. & Thompson, H. 2017, 'Application of geocell track substructure support system to correct surface degradation problems under high-speed passenger railroad operations',

Transportation Infrastructure Geotechnology, vol. 4, no. 4, pp. 106-25. https://dx.doi.org/10.1007/s40515-017-0042-x.

Zhai, W., Wang, K. & Cai, C. 2009, 'Fundamentals of vehicle–track coupled dynamics', *Vehicle System Dynamics*, vol. 47, no. 11, pp. 1349-76. https://doi.org/10.1080/00423110802621561.

Zhai, W.M., Wang, K.Y. & Lin, J.H. 2004, 'Modelling and experiment of railway ballast vibrations', *Journal of Sound and Vibration*, vol. 270, no. 4-5, pp. 673-83. https://doi/org/10.1016/s0022-460x(03)00186-x.

Zhang, T.W., Cui, Y.J., Lamas-Lopez, F., Calon, N. & Costa D'Aguiar, S. 2016, 'Modelling stress distribution in substructure of French conventional railway tracks', *Construction and Building Materials*, vol. 116, pp. 326-34. https://doi.org/10.1016/j.conbuildmat.2016.04.137.

Zhang, X., Zhao, C. & Zhai, W. 2017, 'Dynamic behavior analysis of high-speed railway ballast under moving vehicle loads using discrete element method', *International Journal of Geomechanics*, vol. 17, no. 7, p. 04016157. https://doi.org/10.1061/(ASCE)GM.1943-5622.0000871.

Zhou, H. & Wen, X. 2008, 'Model studies on geogrid-or geocell-reinforced sand cushion on soft soil', *Geotextiles and Geomembranes*, vol. 26, no. 3, pp. 231-8. https://doi.org/10.1016/j.geotexmem.2007.10.002.

APPENDICES

APPENDIX A Calculation of Mass and Stiffness of Substructure Layers

The mass of the effective region of the substructure layers is calculated by multiplying the density of each layer with its volume. **Figures A.1(a)**, **A.1(b)** and **A.1(c)** show the effective portion of ballast, subballast and subgrade layers, respectively, in the case of no overlapping. Consider a small element *dz* at a depth *z* from the top of the ballast layer. The area of the element [A_b (z)] is given by:

$$A_b(z) = (b_{sl} + 2z\tan\alpha)(l_e + 2z\tan\alpha) \quad \text{A.1}$$

The mass of this element is calculated as:

$$dm_b = \rho_b(b_{sl} + 2z\tan\alpha)(l_e + 2z\tan\alpha)dz \quad \text{A.2}$$

The mass of the total effective region of ballast can then be calculated by integrating Equation A.2:

$$m_b = \rho_b \int_{z=0}^{z=h_b} (b_{sl} + 2z\tan\alpha)(l_e + 2z\tan\alpha)dz \quad \text{A.3}$$

Similarly, the mass of subballast and subgrade layers can be determined as:

$$m_s = \rho_s \int_{z=0}^{z=h_s} (b_{sl} + 2h_b\tan\alpha + 2z\tan\beta)(l_e + 2h_b\tan\alpha + 2z\tan\beta)dz \quad \text{A.4}$$

$$m_g = \rho_g \int_{z=0}^{z=h_g} (b_{sl} + 2h_b\tan\alpha + 2h_s\tan\beta + 2z\tan\gamma)(l_e + 2h_b\tan\alpha + 2h_s\tan\beta + 2z\tan\gamma)dz \quad \text{A.5}$$

The stiffness of ballast, subballast and subgrade layers is calculated using the analogy between the effective region of substructure layers and an axially loaded bar with variable cross-sectional area as:

$$k_b = \frac{E_b}{\int \frac{dz}{A_b(z)}} = E_b\left[\int_{z=0}^{z=h_b} \frac{dz}{(b_{sl} + 2z\tan\alpha)(l_e + 2z\tan\alpha)}\right]^{-1} \quad \text{A.6}$$

$$k_s = E_s \left[\int_{z=0}^{z=h_s} \frac{dz}{(b_{sl} + 2h_b \tan\alpha + 2z\tan\beta)(l_e + 2h_b \tan\alpha + 2z\tan\beta)} \right]^{-1} \quad \text{A.7}$$

$$k_g = E_g \left[\int_{z=0}^{z=h_g} \frac{dz}{(b_{sl} + 2h_b \tan\alpha + 2h_s \tan\beta + 2z\tan\gamma)(l_e + 2h_b \tan\alpha + 2h_s \tan\beta + 2z\tan\gamma)} \right]^{-1} \quad \text{A.8}$$

A similar procedure is employed to evaluate the mass and stiffness of the substructure layers in case of overlapping along the longitudinal and transverse directions.

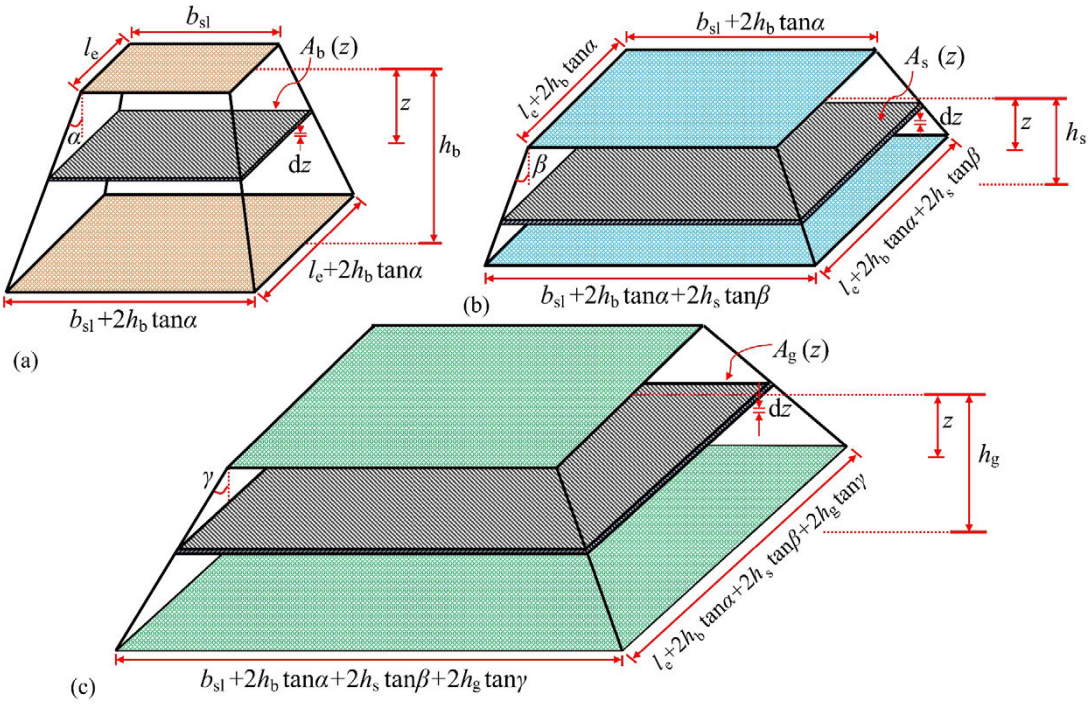

Figure A.1 Effective region of **(a)** ballast; **(b)** subballast; **(c)** subgrade layers

APPENDIX B Stress Calculations

The vertical stress in the ballast, subballast and subgrade at any depth can be calculated using Equations B.1, B.2 and B.3, respectively.

$$\sigma'_{\mathrm{z,b}}(t) = \frac{F_{\mathrm{b,n}}(t)}{A_{\mathrm{b}}(z)} \tag{B.1}$$

$$\sigma'_{\mathrm{z,s}}(t) = \frac{c_{\mathrm{b}}\left[\dot{z}_{\mathrm{b,n}}(t) - \dot{z}_{\mathrm{s,n}}(t)\right] + k_{\mathrm{b}}\left[z_{\mathrm{b,n}}(t) - z_{\mathrm{s,n}}(t)\right]}{A_{\mathrm{s}}(z)} \tag{B.2}$$

$$\sigma'_{\mathrm{z,g}}(t) = \frac{c_{\mathrm{s}}\left[\dot{z}_{\mathrm{s,n}}(t) - \dot{z}_{\mathrm{g,n}}(t)\right] + k_{\mathrm{s}}\left[z_{\mathrm{s,n}}(t) - z_{\mathrm{g,n}}(t)\right]}{A_{\mathrm{g}}(z)} \tag{B.3}$$

where $\sigma'_{\mathrm{z,b}}(t)$, $\sigma'_{\mathrm{z,s}}(t)$, and $\sigma'_{\mathrm{z,g}}(t)$ are the vertical stresses (N/m^2) in the ballast, subballast and subgrade layers, respectively at depth z and time t; $A_{\mathrm{b}}(z)$, $A_{\mathrm{s}}(z)$ and $A_{\mathrm{g}}(z)$ are the equivalent area (m^2) of ballast, subballast and subgrade layers at depth z, respectively (refer to **Figure 3.4**). The lateral stresses (σ'_{x}, σ'_{y}) for each layer are calculated by multiplying the vertical stress with the coefficient of lateral earth pressure [k_0, (k_0=1–sin φ'_{m})]. The average shear stress acting at each substructure layer can be evaluated as:

$$\boldsymbol{T}_n^s = 0.5\begin{bmatrix} \frac{k_{\mathrm{g}}^s}{A_{\mathrm{g}}^s} & 0 & 0 \\ 0 & \frac{k_{\mathrm{s}}^s}{A_{\mathrm{s}}^s} & 0 \\ 0 & 0 & \frac{k_{\mathrm{b}}^s}{A_{\mathrm{b}}^s} \end{bmatrix} \begin{Bmatrix} z_{\mathrm{g,n-1}}(t) + z_{\mathrm{g,n+1}}(t) - 2z_{\mathrm{g,n}}(t) \\ z_{\mathrm{s,n-1}}(t) + z_{\mathrm{s,n+1}}(t) - 2z_{\mathrm{s,n}}(t) \\ z_{\mathrm{b,n-1}}(t) + z_{\mathrm{b,n+1}}(t) - 2z_{\mathrm{b,n}}(t) \end{Bmatrix}$$
$$+ 0.5\begin{bmatrix} \frac{c_{\mathrm{g}}^s}{A_{\mathrm{g}}^s} & 0 & 0 \\ 0 & \frac{c_{\mathrm{s}}^s}{A_{\mathrm{s}}^s} & 0 \\ 0 & 0 & \frac{c_{\mathrm{b}}^s}{A_{\mathrm{b}}^s} \end{bmatrix} \begin{Bmatrix} \dot{z}_{\mathrm{g,n-1}}(t) + \dot{z}_{\mathrm{g,n+1}}(t) - 2\dot{z}_{\mathrm{g,n}}(t) \\ \dot{z}_{\mathrm{s,n-1}}(t) + \dot{z}_{\mathrm{s,n+1}}(t) - 2\dot{z}_{\mathrm{s,n}}(t) \\ \dot{z}_{\mathrm{b,n-1}}(t) + \dot{z}_{\mathrm{b,n+1}}(t) - 2\dot{z}_{\mathrm{b,n}}(t) \end{Bmatrix} \tag{B.4}$$

where $\boldsymbol{T}_{\mathrm{n}}^s$ is the average shear stress vector at n^{th} sleeper point in yz plane; A^s_{b}, A^s_{s} and A^s_{g} are the equivalent shear area (m^2) of ballast, subballast and subgrade layers, respectively. The shear stress is assumed to be uniformly distributed along the entire thickness of the individual substructure layers. **Figure 3.4** shows the equivalent normal and shear area of the substructure layers considered in the present method. The equations to evaluate the octahedral normal and shear stresses, and deviator stress can be found in Timoshenko & Goodier (1970).

APPENDIX C Vertical Load Transfer from Superstructure to Substructure

Figure C.1 illustrates the transfer of train-induced loading from the superstructure to the substructure layers of the track. The vertical wheel load (Q) is transmitted from the rails to multiple sleepers via the rail seats. This load is termed as the rail seat load (Q_r). The rail seat load is applied to the ballast surface over a circular sleeper-ballast contact area, whose size depends on the sleeper dimensions. The sleeper-ballast contact pressure (σ_{sb}) is considered to be uniformly distributed and is calculated by dividing the rail seat load with the sleeper-ballast contact area. The stress distribution in the track substructure layers is then calculated using the Boussinesq solutions (after transforming multiple substructure layers into a single layer) for a uniformly loaded circular footing.

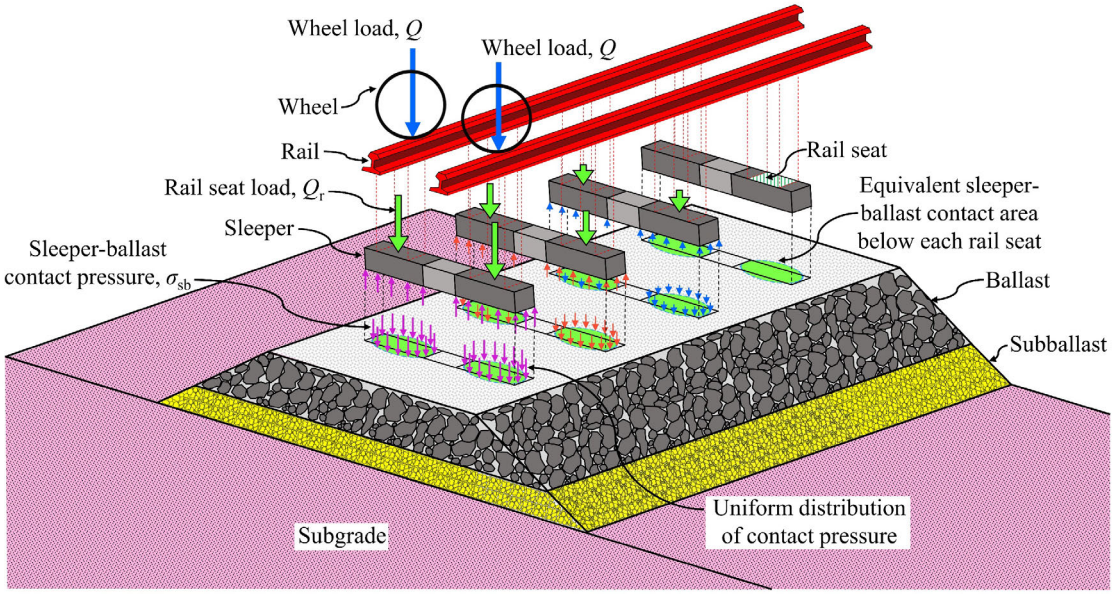

Figure C.1 Transfer of train-induced load from superstructure to the substructure layers

APPENDIX D Incremental Equivalent Force Vector

The incremental equivalent force vector is determined as:

$$d\bar{\boldsymbol{F}} = d\boldsymbol{F} - \boldsymbol{M}d\ddot{\boldsymbol{z}} - \boldsymbol{C}d\dot{\boldsymbol{z}} - \boldsymbol{C^p}d\dot{\boldsymbol{z}}^{\boldsymbol{p}} - \boldsymbol{K^p}d\boldsymbol{z}^{\boldsymbol{p}} + \boldsymbol{C'}\{d\dot{\boldsymbol{z}}_{\mathbf{n+1}} + d\dot{\boldsymbol{z}}_{\mathbf{n-1}}\} + \boldsymbol{K'}\{d\boldsymbol{z}_{\mathbf{n+1}} + d\boldsymbol{z}_{\mathbf{n-1}}\} - \boldsymbol{C^{p'}}\{d\dot{\boldsymbol{z}}^{\boldsymbol{p}}_{\mathbf{n+1}} + d\dot{\boldsymbol{z}}^{\boldsymbol{p}}_{\mathbf{n-1}}\} - \boldsymbol{K^{p'}}\{d\boldsymbol{z}^{\boldsymbol{p}}_{\mathbf{n+1}} + d\boldsymbol{z}^{\boldsymbol{p}}_{\mathbf{n-1}}\} \quad \text{D.1}$$

where:

$$d\mathbf{z} = \begin{Bmatrix} dz_{\mathrm{g,n}} \\ dz_{\mathrm{s,n}} \\ dz_{\mathrm{b,n}} \end{Bmatrix}; d\dot{\boldsymbol{z}} = \begin{Bmatrix} d\dot{z}_{\mathrm{g,n}} \\ d\dot{z}_{\mathrm{s,n}} \\ d\dot{z}_{\mathrm{b,n}} \end{Bmatrix};\ d\ddot{\boldsymbol{z}} = \begin{Bmatrix} d\ddot{z}_{\mathrm{g,n}} \\ d\ddot{z}_{\mathrm{s,n}} \\ d\ddot{z}_{\mathrm{b,n}} \end{Bmatrix}; d\boldsymbol{z^p} = \begin{Bmatrix} dz^p_{\mathrm{g,n}} \\ dz^p_{\mathrm{s,n}} \\ dz^p_{\mathrm{b,n}} \end{Bmatrix};\ d\dot{\boldsymbol{z}}^{\boldsymbol{p}} = \begin{Bmatrix} d\dot{z}^p_{\mathrm{g,n}} \\ d\dot{z}^p_{\mathrm{s,n}} \\ d\dot{z}^p_{\mathrm{b,n}} \end{Bmatrix} \quad \text{D.2}$$

$$d\dot{\boldsymbol{z}}_{\mathbf{n+1}} = \begin{Bmatrix} d\dot{z}_{\mathrm{g,n+1}} \\ d\dot{z}_{\mathrm{s,n+1}} \\ d\dot{z}_{\mathrm{b,n+1}} \end{Bmatrix}; d\dot{\boldsymbol{z}}_{\mathbf{n-1}} = \begin{Bmatrix} d\dot{z}_{\mathrm{g,n-1}} \\ d\dot{z}_{\mathrm{s,n-1}} \\ d\dot{z}_{\mathrm{b,n-1}} \end{Bmatrix}; d\boldsymbol{z}_{\mathbf{n+1}} = \begin{Bmatrix} dz_{\mathrm{g,n+1}} \\ dz_{\mathrm{s,n+1}} \\ dz_{\mathrm{b,n+1}} \end{Bmatrix}; d\boldsymbol{z}_{\mathbf{n-1}} = \begin{Bmatrix} dz_{\mathrm{g,n-1}} \\ dz_{\mathrm{s,n-1}} \\ dz_{\mathrm{b,n-1}} \end{Bmatrix} \quad \text{D.3}$$

$$d\dot{\boldsymbol{z}}^{\boldsymbol{p}}_{\mathbf{n+1}} = \begin{Bmatrix} d\dot{z}^p_{\mathrm{g,n+1}} \\ d\dot{z}^p_{\mathrm{s,n+1}} \\ d\dot{z}^p_{\mathrm{b,n+1}} \end{Bmatrix}; d\dot{\boldsymbol{z}}^{\boldsymbol{p}}_{\mathbf{n-1}} = \begin{Bmatrix} d\dot{z}^p_{\mathrm{g,n-1}} \\ d\dot{z}^p_{\mathrm{s,n-1}} \\ d\dot{z}^p_{\mathrm{b,n-1}} \end{Bmatrix};\ d\boldsymbol{z}^{\boldsymbol{p}}_{\mathbf{n+1}} = \begin{Bmatrix} dz^p_{\mathrm{g,n+1}} \\ dz^p_{\mathrm{s,n+1}} \\ dz^p_{\mathrm{b,n+1}} \end{Bmatrix}; d\boldsymbol{z}^{\boldsymbol{p}}_{\mathbf{n-1}} = \begin{Bmatrix} dz^p_{\mathrm{g,n-1}} \\ dz^p_{\mathrm{s,n-1}} \\ dz^p_{\mathrm{b,n-1}} \end{Bmatrix} \quad \text{D.4}$$

$$\boldsymbol{K} = \begin{bmatrix} k_{\mathrm{g}} + k_{\mathrm{s}} + 2k^s_{\mathrm{g}} & -k_{\mathrm{s}} & 0 \\ -k_{\mathrm{s}} & k_{\mathrm{s}} + k_{\mathrm{b}} + 2k^s_{\mathrm{s}} & -k_{\mathrm{b}} \\ 0 & -k_{\mathrm{b}} & k_{\mathrm{b}} + 2k^s_{\mathrm{b}} \end{bmatrix}; \boldsymbol{K^p} = \begin{bmatrix} -k_{\mathrm{g}} - 2k^s_{\mathrm{g}} & k_{\mathrm{s}} & 0 \\ -2k^s_{\mathrm{s}} & -k_{\mathrm{s}} - 2k^s_{\mathrm{s}} & k_{\mathrm{b}} \\ -2k^s_{\mathrm{b}} & -2k^s_{\mathrm{b}} & -k_{\mathrm{b}} - 2k^s_{\mathrm{b}} \end{bmatrix} \quad \text{D.5}$$

$$\boldsymbol{C} = \begin{bmatrix} c_{\mathrm{g}} + c_{\mathrm{s}} + 2c^s_{\mathrm{g}} & -c_{\mathrm{s}} & 0 \\ -c_{\mathrm{s}} & c_{\mathrm{s}} + c_{\mathrm{b}} + 2c^s_{\mathrm{s}} & -c_{\mathrm{b}} \\ 0 & -c_{\mathrm{b}} & c_{\mathrm{b}} + 2c^s_{\mathrm{b}} \end{bmatrix};\ \boldsymbol{C^p} = \begin{bmatrix} -c_{\mathrm{g}} - 2c^s_{\mathrm{g}} & c_{\mathrm{s}} & 0 \\ -2c^s_{\mathrm{s}} & -c_{\mathrm{s}} - 2c^s_{\mathrm{s}} & c_{\mathrm{b}} \\ -2c^s_{\mathrm{b}} & -2c^s_{\mathrm{b}} & -c_{\mathrm{b}} - 2c^s_{\mathrm{b}} \end{bmatrix} \quad \text{D.6}$$

$$d\boldsymbol{F} = \begin{Bmatrix} dF_{\mathrm{g,n}} \\ dF_{\mathrm{s,n}} \\ dF_{\mathrm{b,n}} \end{Bmatrix}; \boldsymbol{M} = \begin{bmatrix} m_{\mathrm{g}} & 0 & 0 \\ 0 & m_{\mathrm{s}} & 0 \\ 0 & 0 & m_{\mathrm{b}} \end{bmatrix}; \boldsymbol{K'} = \begin{bmatrix} k^s_{\mathrm{g}} & 0 & 0 \\ 0 & k^s_{\mathrm{s}} & 0 \\ 0 & 0 & k^s_{\mathrm{b}} \end{bmatrix}; \boldsymbol{K^{p\prime}} = \begin{bmatrix} k^s_{\mathrm{g}} & 0 & 0 \\ k^s_{\mathrm{s}} & k^s_{\mathrm{s}} & 0 \\ k^s_{\mathrm{b}} & k^s_{\mathrm{b}} & k^s_{\mathrm{b}} \end{bmatrix}; \boldsymbol{C'} = \begin{bmatrix} c^s_{\mathrm{g}} & 0 & 0 \\ 0 & c^s_{\mathrm{s}} & 0 \\ 0 & 0 & c^s_{\mathrm{b}} \end{bmatrix}; \boldsymbol{C^{p\prime}} = \begin{bmatrix} c^s_{\mathrm{g}} & 0 & 0 \\ c^s_{\mathrm{s}} & c^s_{\mathrm{s}} & 0 \\ c^s_{\mathrm{b}} & c^s_{\mathrm{b}} & c^s_{\mathrm{b}} \end{bmatrix} \quad \text{D.7}$$

APPENDIX E Calculation of Mass and Stiffness for Stiffer Side

The vibrating mass and stiffness of the track layers in the stiffer side for the non-overlapped case (see **Figure E.1)** can be determined using the following equations:

$$m_{\mathrm{b}}^{r} = \rho_{\mathrm{b}}^{r} h_{\mathrm{b}}^{r} \left[b_{\mathrm{sl}} l_{\mathrm{e}} + (b_{\mathrm{sl}} + l_{\mathrm{e}}) h_{\mathrm{b}}^{r} \tan \alpha^{r} + \frac{4}{3} (h_{\mathrm{b}}^{r})^{2} \tan^{2} \alpha^{r} \right] \quad \text{E.1}$$

$$k_{\mathrm{b}}^{r} = E_{\mathrm{b}}^{r} \frac{2(l_{\mathrm{e}} - b_{\mathrm{sl}}) \tan \alpha^{r}}{\ln \left[\frac{l_{\mathrm{e}}}{b_{\mathrm{sl}}} \left(\frac{b_{\mathrm{sl}} + 2h_{\mathrm{b}}^{r} \tan \alpha^{r}}{l_{\mathrm{e}} + 2h_{\mathrm{b}}^{r} \tan \alpha^{r}} \right) \right]} \quad \text{E.2}$$

A similar approach can be followed to derive these parameters for the overlapped case. Moreover, the parameters for the softer side can be computed using a similar approach as described in Section 3.2.2.2.

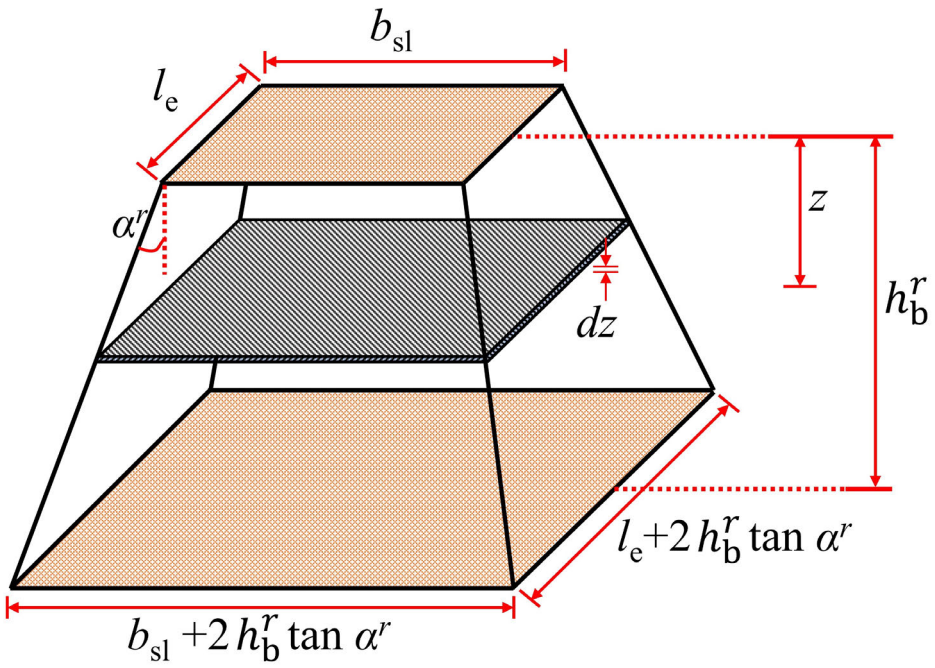

Figure E.1 Effective region of ballast in stiffer side for non-overlapped case

The load distribution angle for the track layer in the stiffer side is calculated as follows:

$$\alpha^{r} = \tan^{-1} \left\{ \frac{a^{r}}{h_{\mathrm{b}}^{r}} \left[\sqrt{\frac{\sigma_{\mathrm{sb}}^{r}}{\sigma_{\mathrm{bb}}^{r}}} - 1 \right] \right\} \quad \text{E.3}$$

where σ_{bb}^{r} is the vertical stress (N/m^2) at the bottom of the substructure layer in the stiffer side of the transition.

APPENDIX F Determination of Rail Seat Load

As per the BoEF method, the rail seat load is simply the product of track modulus, sleeper spacing and track deflection. The vertical track deflection is obtained from Equation 3.2, and the track modulus for the stiffer zone of the track is given by:

$$\frac{1}{k^r} = S\left(\frac{1}{k_{\mathrm{p}}^r} + \frac{1}{k_{\mathrm{b}}^r}\right) \qquad \text{F.1}$$

Note that the track modulus for the softer side can be computed using Equation 3.21.

Figure F.1 demonstrates the evaluation of rail seat load and its variation with time at m^{th} and n^{th} sleeper locations during the passage of the Acela Express passenger train. **Figure F.1(a)** shows the train configuration. The train is assumed to be travelling from the softer to the stiffer side of the transition. **Figure F.1(b)** shows the vertical track deflection at time instant t_1 calculated using Equation 3.2 for wheels Q_1 and Q_2. It is apparent that only the leading wheel Q_1 contributes to the track deflection at the m^{th} sleeper. The deflection at the n^{th} sleeper, which lies in the stiffer zone, is zero since it is far from the influence of wheels Q_1 and Q_2 at time instant t_1.

At time instant t_2, the total vertical track deflection at the m^{th} sleeper is the sum of contributions from both Q_1 and Q_2 [see **Figure F.1(c)**]. In contrast, the deflection at the n^{th} sleeper is still zero since it is far away from the influence of wheels Q_1 and Q_2. **Figure F.1(d)** shows the vertical track deflection at time instant t_3 for wheels Q_1, Q_2, Q_3 and Q_4. It can be seen that the wheels Q_3 and Q_1 contribute to the track deflection at the m^{th} and n^{th} sleepers, respectively. Since the stiffness of the stiffer zone is much higher, it follows that the magnitude of track deflection is lower at the n^{th} sleeper than the m^{th} sleeper. Using a similar procedure, the vertical track deflection at other sleeper locations is calculated. Finally, the variation of rail seat load with time is computed for all the sleeper positions considered in the analysis.

Figures F.1(e) and **F.1(f)** show the variation of vertical rail seat load with time for m^{th} and n^{th} sleepers, respectively, computed for one passage of the train at a speed of 150 km/h. It can be seen that the magnitude of rail seat load is much higher at the stiffer side of the track [see **Figure F.1(f)**] as compared to the softer side [see **Figure F.1(e)**]. This

increment in rail seat load is plausible since the track modulus of the stiffer side is much higher than the softer side.

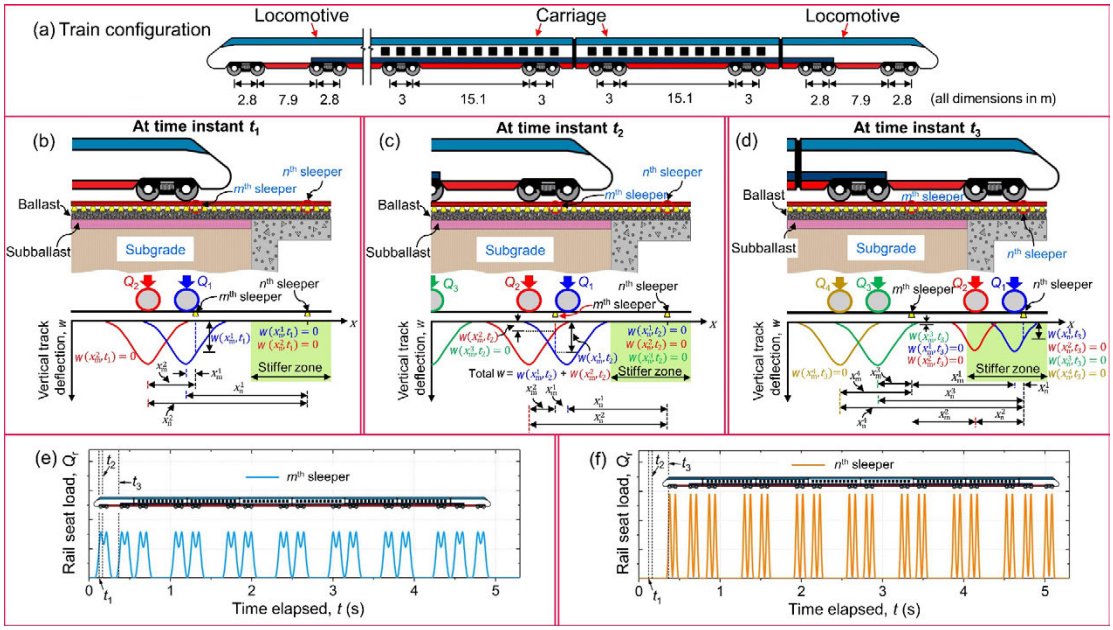

Figure F.1 (a) Train configuration; track response at time instant **(b)** t_1; **(c)** t_2; **(d)** t_3; variation of rail seat load with time at **(e)** m^{th} sleeper; **(f)** n^{th} sleeper during one complete train passage

APPENDIX G Vehicle and Wheel-Rail Contact Modelling

In the FE model, the vehicle is modelled as a multi-body system consisting of two bogies from adjacent wagons, four axles and four wheels in this analysis (see **Figure 4.4**). Two levels of suspensions are considered: one between the bogie and the wheel (primary suspension) and the other between the car body and bogie (secondary suspension). The car body, bogie and wheels are simulated as rigid bodies, while the suspensions are modelled using springs and dashpots. The vertical stiffness of primary and secondary suspensions are considered as 1400 kN/m and 450 kN/m, respectively. The damping coefficient of the primary and secondary suspensions are taken as 120 kNs/m and 40 kNs/m, respectively. The wheel-rail contact is simulated using the Hertzian non-linear contact theory, following Zhai et al. (2009). According to this theory, the wheel-rail contact force, F_{wr}, is given by (Chen & Zhai 2004):

$$F_{\mathrm{wr}}(t) = \left[\frac{1}{G} W_{\mathrm{wr}}(t)\right]^{\frac{3}{2}} \qquad \text{G.1}$$

where G is the wheel-rail contact constant (m/N$^{2/3}$); $W_{\mathrm{wr}}(t)$ is the deformation at the wheel-rail contact point (m) at time instant t. The value of G is calculated using the following expression (Chen & Zhai 2004):

$$G = 3.86 R_{\mathrm{w}}^{-0.115} \times 10^{-8} \qquad \text{G.2}$$

where R_{w} is the nominal radius of the wheel (m).

APPENDIX H Yield Surface during Unloading

In the present approach, it is assumed that the size of the yield surface shrinks isotropically during unloading. This approach of reducing the yield surface size during the unloading stage was originally proposed by Carter et al. (1982). Since the parameter p_{i} controls the size of the yield surface, its value is reduced using the following expression:

$$\frac{dp_{\mathrm{i}}}{p_{\mathrm{i}}} = \theta^* \frac{dp_{\mathrm{l}}}{p_{\mathrm{l}}} \tag{H.1}$$

where,

$$p_{\mathrm{l}} = pe^{\left(\frac{q}{M_{\mathrm{i}}p}-1\right)} \tag{H.2}$$

If the value of θ^* is taken as unity, the yield surface will shrink in such a way that it would always pass the current stress state. Carter et al. (1982) suggested that the value of θ^* must be less than unity. This is achieved by reducing the size of the yield surface in such a manner that the ratio $\frac{p_{\mathrm{i}}}{p}$ is constant during unloading and equal to the value attained at the end of the loading stage.

Figure H.1 shows the evolution of the yield surface during loading and unloading. Suppose the geomaterial is first loaded along the path A to B and then unloaded along the path B to E. During unloading, both the yield surface and loading surface (which passes through the current stress state) shrink. However, the yield surface shrinks less than that of the loading surface. Now, if the geomaterial is unloaded to point D, both yield and loading surfaces will shrink further. If the geomaterial is reloaded from point C to point B through point E, it will show elastic behavior till point E is reached. Subsequently, the yield and loading surfaces will expand together until point B is reached, thereby generating plastic deformations.

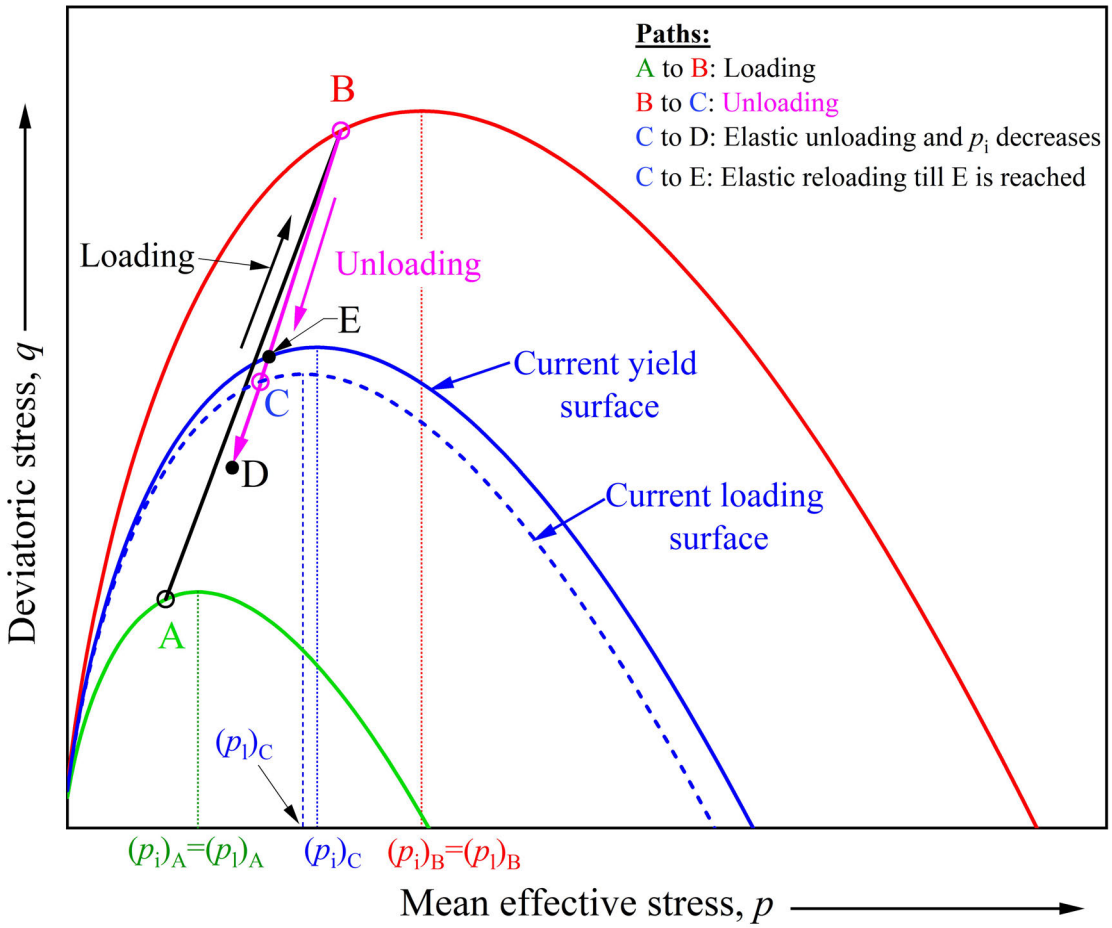

Figure H.1 Yield surface during loading and unloading

APPENDIX I Calculation of Additional Confinement under General Stress State

Figure I.1 shows the stress profile of the 3D cellular geoinclusion under the general stress state. Taking equilibrium of forces along the directions 2 and 3 gives:

$$(\sigma_2' + \Delta\sigma_2')D_g - \sigma_2' D_g - 2\sigma_{C,2} t_g = 0 \qquad \text{I.1(a)}$$

$$(\sigma_3' + \Delta\sigma_3')D_g - \sigma_3' D_g - 2\sigma_{C,3} t_g = 0 \qquad \text{I.1(b)}$$

On simplification, $\Delta\sigma'_2$ and $\Delta\sigma'_3$ can be expressed as:

$$\Delta\sigma_2' = \frac{2\sigma_{C,2} t_g}{D_g} \qquad \text{I.2(a)}$$

$$\Delta\sigma_3' = \frac{2\sigma_{C,3} t_g}{D_g} \qquad \text{I.2(b)}$$

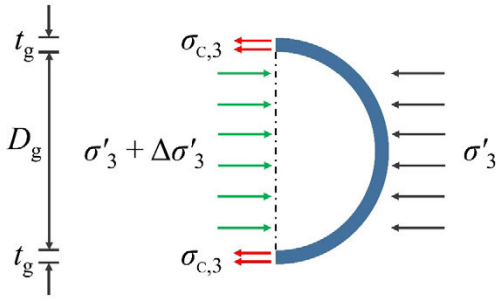

Taking equilibrium of forces along direction 3:

$(\sigma'_3 + \Delta\sigma'_3)\cdot D_g = \sigma'_3 \cdot D_g + 2\cdot\sigma_{C,3}\cdot t_g$

$\Delta\sigma'_3 = (2\cdot\sigma_{C,3}\cdot t_g)/D_g$

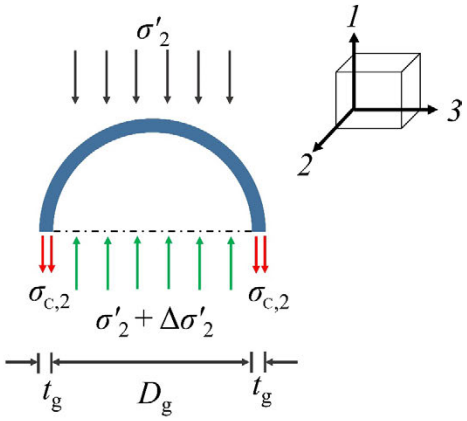

Taking equilibrium of forces along direction 2:

$(\sigma'_2 + \Delta\sigma'_2)\cdot D_g = \sigma'_2 \cdot D_g + 2\cdot\sigma_{C,2}\cdot t_g$

$\Delta\sigma'_2 = (2\cdot\sigma_{C,2}\cdot t_g)/D_g$

Figure I.1 Stress profile of 3D cellular geoinclusion under general stress state

APPENDIX J Calculation of Additional Confinement Provided by Planar Geosynthetic

In planar geosynthetic-reinforced soil, the lateral deformation of the soil under the application of vertical loads generates tensile stresses in the geosynthetic [see **Figure 6.22(a)**]. The magnitude of these tensile stresses (T_x and T_y) along *x* and *y* directions can be computed as:

$$T_x = \frac{M_m}{(1-\nu_m^2)}(\varepsilon_x^m + \nu_m \varepsilon_y^m) \quad \text{J.1}$$

$$T_y = \frac{M_m}{(1-\nu_m^2)}(\varepsilon_y^m + \nu_m \varepsilon_x^m) \quad \text{J.2}$$

where $\varepsilon_x^m$and ε_y^m are strains in geosynthetic in *x* and *y* directions, respectively. These tensile stresses can be considered as equivalent compressive stresses applied to the soil at the reinforcement location [see **Figure 6.22(a)**]. If the equivalent compressive stress is assumed to be distributed uniformly over a thickness of H_m, the extra confining pressure applied to the soil can be computed as:

$$\Delta\sigma_x = \frac{T_x}{H_m} \quad \text{J.3}$$

$$\Delta\sigma_y = \frac{T_y}{H_m} \quad \text{J.4}$$

Substitution of the values of T_x and T_y from Equations (J.1) and (J.2) to Equations (J.3) and (J.4), and considering $\alpha_m = -\varepsilon_x^m/\varepsilon_x = -\varepsilon_y^m/\varepsilon_y$ yields Equations 6.25 and 6.26.